OXYGEN ASSISTED FOCUSED ELECTRON BEAM INDUCED DEPOSITION OF SILICON DIOXIDE

PAR

Alexandre PERENTES

ingénieur en microtechnique diplômé EPF
de nationalité suisse et originaire de Attalens (FR)

EPFL
ÉCOLE POLYTECHNIQUE
FÉDÉRALE DE LAUSANNE

Suisse
2007

To my Mother

ABSTRACT

Focused Electron Beam Induced Deposition (FEBID) is a rapid prototyping technique for the investigation, production and modification of 2 and 3-D nanostructures. The process takes place at room temperature, in the high-vacuum chamber of a Scanning Electron Microscope (SEM). The principle is based on the local FEB decomposition of molecules injected in the chamber and adsorbed on a surface. These molecules, called the precursors, are specifically chosen to contain the element of interest to be deposited. However, the electron induced decomposition results in contaminated materials containing additional parasitic elements from the precursor molecule. These contaminants are incorporated with the element of interest, and downgrade the properties of the materials and prevent therefore their use for many applications.

Gas-assisted FEBID, the subject of this thesis, is a promising evolution and solution to the problem that was never extensively studied in literature. It consists in injecting a reactive gas simultaneously to the precursors, which will react in real time with the deposited contaminants to form volatile products, leaving ideally only the interesting material on the surface. This work focused on the Oxygen assisted FEBID of Silicon dioxide (SiO_2) and on the understanding of the deposition process. SiO_2 it is a high performance material for nano-optic and electronic applications, widely used in research and industry. Modifications were brought to an existing SEM to allow the simultaneous injection of two different and controlled gases, and to allow the *in-situ* control of growth of optical materials. Si-precursors of three families (alkoxy-, alkyl- and isocyanato-silanes) were compared.

The FEBID material could be gradually converted from contaminated Si-materials to pure SiO_2, above a [O_2]/[precursor] ratio specific to each precursor chemistry and precursor flow. The SiO_2 deposited was stoichiometric, C and OH–free, had an estimated density of 2.2, was amorphous and had optical properties close to that of fused silica. Optical structures for nano-optics and plasmonics were produced.

Compared to traditional FEBID, O_2 assisted FEBID required much lower energy to induce a decomposition reaction, and secondary electrons achieved 90 % of the deposition process in our setup. The electron efficiency could be multiplied by 20 compared to conventional FEBID. O_2 assisted FEBID was insensitive to electron density in our setup.

The conditions for no C and large deposition rates during O_2 assisted FEBID were high molecule reactivity to O_2, low sticking coefficient, low acceleration voltage and dwell time (< 6 μs), and large replenishment time (> 60 μs). As function of the precursor chemistry and flow, additional O_2 influenced the deposition rate, which could be increased it by a factor of 7. The O_2 and precursor molecules co-adsorption resulted in a surface coverage competition, which determined the deposition efficiencies

Limitations due to the residual water in the SEM were demonstrated and characterized. They appeared as Oxygen incorporation in the deposited materials, which influenced the deposition process. Residual water impinging flow was demonstrated to be responsible of the FEBID process deposition efficiency when no Oxygen was injected.

KEY–WORDS

FEB deposition, local nano-scale deposition, pure materials, gas assistance, deposition efficiency, deposition mechanism, precursor chemistry.

RESUME

La Déposition Induite par Faisceau d'Electrons Focalisé (FEBID) est une technique de prototypage rapide permettant la fabrication et la modification de nanostructures 2- et 3-D. Le procédé a lieu à température ambiante, dans un Microscope Electronique à Balayage (MEB) sous haut-vide. Le principe est basé sur la décomposition locale par le FEB de molécules injectées dans la chambre et adsorbées sur un échantillon. Ces molécules, appelées les précurseurs, sont choisies de telle sorte à contenir l'élément d'intérêt à déposer. Toutefois, la réaction de décomposition produit des matériaux contaminés par des éléments parasites provenant du précurseur qui sont déposés en même temps que l'élément d'intérêt. Ceci dégrade les propriétés des matériaux et en entrave l'emploi pour des applications concrètes.

La FEBID assistée par gaz, le sujet de cette thèse, est une solution prometteuse et évolution de la FEBID de base, qui n'a toutefois jamais été étudiée en détail. Elle consiste à injecter un gaz réactif simultanément au précurseur, qui va réagir en temps réel avec les contaminants du matériau en cours de déposition pour former des entités volatiles, laissant idéalement uniquement le matériau d'intérêt à la surface. Ce travail a focalisé sur la FEBID assistée par Oxygène d'oxyde de Silicium (SiO_2), et sur la compréhension du processus de déposition. Le SiO_2 est largement utilisé en recherche et en industrie pour des applications nano-optiques et électroniques. Des modifications ont été apportées à un MEB afin de permettre l'injection simultanée de deux flux différents et contrôlés, ainsi que le contrôle *in-situ* de la croissance de matériaux optiques. Des précurseurs de Si provenant de trois familles (alkoxy-, aklyl- et isocyanatosilanes) ont été comparés.

Les matériaux déposés ont pu être graduellement convertis de matériaux contaminés contenant du Si à du SiO_2 pur, au-delà d'un rapport [O_2]/[précurseur] spécifique à chaque molécule. Le SiO_2 était stœchiométrique, avait une densité estimée de 2.2, était amorphe, et possédait des propriétés optiques comparables à de la silice commerciale. Des structures nano-optiques et plasmoniques ont été produites.

Comparée à la FEBID traditionnelle, la FEBID assistée par O_2 nécessite moins d'énergie pour induire une réaction de décomposition, et les électrons secondaires achèvent 90% du procédé de déposition. La FEBID assistée par O_2 était insensible à la densité d'électrons, et l'efficacité d'un électron a pu être multipliée par 20 par rapport à la FEBID conventionnelle.

Les conditions pour éviter l'incorporation du C dans le matériau pendant la FEBID assistée par O_2 sont une haute réactivité à l'Oxygène du précurseur, faible coefficient de collage, une basse tension d'accélération, un faible temps d'irradiation (< 6 µs) et un haut temps de remplissage de couche (> 60 µs). L'O_2 additionnel peut multiplier par 7 le taux de croissance des matériaux déposés. Les molécules d'O_2 et les précurseurs mènent une compétition d'occupation de surface, qui influence l'efficacité du procédé de déposition.

Des limitations du procédé liées à l'eau résiduelle dans le MEB ont été démontrées et caractérisées en fonction de la chimie du précurseur. Elles apparaissent sous forme d'incorporation d'Oxygène dans les matériaux déposés. Le flux de collision de l'eau est la principale responsable de l'efficacité de la FEBID conventionnelle.

MOTS CLES

Déposition induite par FEB, nano-déposition locale, matériaux purs, assistance par gaz, mécanisme de déposition, efficacité de réaction, chimie de précurseur.

TABLE OF CONTENTS

ANNEXES

ACKNOWLEDGMENTS

SCIENTIFIC PUBLICATIONS

RÉSUMÉ

CHAPTER 1
INTRODUCTION

1.1 General

Reaching the nano-scale (1 nanometer = $^1/_{1000000}$th millimeter) in technology fields is a logical continuation of the progress of knowledge and of the miniaturisation that ruled high technology semiconductor industries since the 1950's with the production of the first integrated transistor.

Powered by the leitmotiv "smaller = faster = cheaper = better", companies permanently put in effort in producing smaller components. In 2007, the transistor density reached 1 billion per mm^2 on the most performing computer micro-processor. The production of reliable microelectronic chips at an ultra-large scale with such a precision is one of the most impressive industrial successes of the 21st century.

The nano-scale is today reached in many other fields than microelectronics as well: materials (Carbon nanotubes, nano-foams), quanta electronics (quantum dots and wires), optics (plasmonics, near field optics), bio-chemistry (functionalized nanoparticles), since new interesting phenomena, unknown in the microscale, emerged. These phenomena require to be understood before applying them to daily devices. Micro-scale production tools are no more suited to such structures.

New rapid prototyping techniques are hence required for nanostructure high precision production, modification and investigation. Concrete applications are as example: deposition of periodic patterns of pure Gold on a SiO_2 substrate and production of pure metal particles of given 3-D shape for optic and plasmonic theory validations, selective etching of Copper connections in prototype chips, deposition of phase shift material with a given refractive index and thickness for photomask repair; deposition of Tungsten or diamond for nano-mechanics.

These applications involve specific properties of materials, and it is expected that the rapid prototyping technique produces the identical materials, or etches away only a specific material. The production of structures of unknown properties requires time-consuming characterisation and tailoring of the theoretical models, which should be avoided.

The challenges for nano-rapid-prototyping techniques are hence that they have to combine nano-scale resolution in three dimensions, large versatility in terms of materials that can be structured (due to the large variety of useful materials), production of pure materials, and highly selective etching.

At present, the most suited equipments for the above-mentioned tasks are those based on the interaction of beams of particles (ions or electrons) with matter and adsorbed molecules. These beams can be focused to spots of a few nanometers and are widely used for high resolution (~2-5 nm) imaging since the late 1970's in scanning electron and ion microscopes, and are the most suited tools for local structuring the nano-world.

1.2 Focused Particle Beam Induced Processing (FPBIP)

FPBIP is a room temperature high resolution (sub–100 nm) local nano-structuration of matter, which can be either positive (i.e. matter is added to an existing surface) or negative (i.e. matter is taken away from an existing substrate). During FPBIP, specifically chosen gaseous chemical molecules (the "precursors"), are injected in a high vacuum chamber of a Scanning Electron Microscope (SEM). These molecules propagate through the vacuum and adsorb on the surface of a sample placed in the chamber.

When irradiated by the focused particle beam, the molecules might acquire energy, and decompose by liberating fragments. These fragments can either react with the substrate atoms to from a volatile product which will desorb from the surface, thus resulting in focused beam etching; or decompose in a solid and non volatile material, resulting in focused beam induced deposition. These different reactions are presented in Figure 1-1 in the case of a Focused Electron Beam Induced Processing (FEBIP).
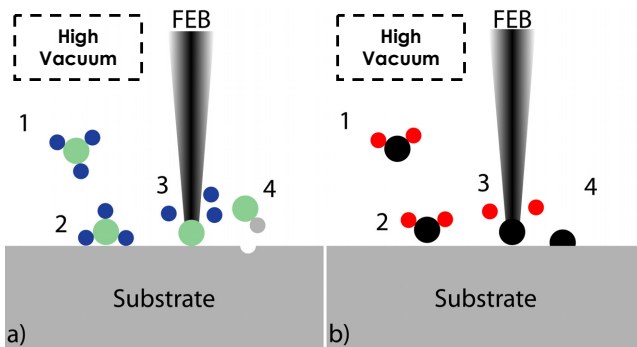
Figure 1-1: Steps of the two different FPBIP reactions possible. Precursor molecules diffuse through vacuum (1), and adsorb on substrate surface (2), and get ionized and fragmented under the FEB (3). The volatile ligands are pumped away, and the remaining fragments might form a volatile entity with atoms of the substrate (4 a), or might remain as solid material on the surface (4 b).

Although very attractive, the deposition mechanism behind FPBIP is complex and not yet fully understood. The main limitation of FPBIP is that the deposits obtained by decomposing precursor molecules are contaminated: they do not only contain the element of interest but also other elements of the starting molecule, usually C, O, H and halogens. This arises from a non optimal decomposition process. These contaminants affect adversely the materials properties, and hence the targeted applications. The particle beam induced deposition of pure materials is very challenging and constitutes today one of the main topic of research around the technique.

Compared to electrons, ions have a large mass (one 10 keV Gallium ion is about 30000 times heavier than a 10 keV electron), and lead to permanent structural defects and implantations in the irradiated structures. Ion beams could hence never lead to the production of pure materials. Additionally, ion beam induced chemistry is not selective enough to allow for high precision and selective depth etching of multi-layer samples (with layer thicknesses below 50 nm) of different materials. Ion beam processing was however preferred to Electron beam processing in the 1980's and 1990's since the processing times were lower, and less contaminants were incorporated in the material.

Due to these limitations, electron beams, that do not interact with matter in such a destructive way, are today preferred for FPBID. It is the only technique that could potentially lead to the deposition of pure materials and selective etching if further developments are done.

1.3 Motivation of this thesis: FEBID of pure SiO_2

Among many materials, SiO_2, or silica, is very interesting and widely used as insulation, passivation and optical films in industry. The properties of SiO_2 depend greatly on the concentration of impurities in the material and of its density. The highest quality amorphous SiO_2, the fused silica, is optically

transparent from deep ultra violet to infrared wavelengths (193 nm to 10 μm). The DUV grade synthetic fused silica used for photomasks has a density of 2.2 (Schott® Lithosil Q0).

FEBID of DUV fused silica at the nano-scale is a motivating and long date challenge, which would allow the production of nano-optical structures for visible light such as photonic crystals, and the repair of industrial photomasks and nano-imprint masks.

Gas assisted FEBID was applied and studied, and allowed lowering to undetectable values the concentrations of contaminants in Si-materials obtained by conventional FEBID of Si-precursors in a standard high vacuum SEM. The latter material presented identical optical properties than fused silica, and an intermediate density of 2.2.

The idea was based on the injection of a second gas, molecular Oxygen, simultaneously to the precursor vapours, which reacted and volatilized in real time the contaminants during the deposition process. The FEB process consisted hence in the deposition of SiO_2 and etching of contaminants at the same time. The understanding of the O_2 assisted FEBID process was approached by means of experiments varying paramount parameters and scanning different precursor chemistries.

This work constitutes a step forward to the development of FEBID processes for pure material deposition by gas assistance, and provided further indications to the understanding of the deposition mechanism behind FEBID.

Limitations of conventional high-vacuum systems were highlighted and demonstrated to clearly influence the deposition process. Necessary

optimisations of conventional FEBID equipments are proposed to lead to the full control of the deposition process and the production of pure materials.

1.4 Structure of the script

Chapter 2 is a literature survey. I decided to dedicate the two first sub-chapters to the history of Scanning Electron Microscopes (SEMs), and to the history and development of FEBID through the years, from its discovery due to the decomposition of contamination molecules, to the production of 2- and 3-D structures containing interesting elements. The few theoretical models developed to describe FEBID are briefly summarized. The two last sub-chapters address the problems related to contamination origins in FEBID materials. Sub-chapter 2.4 reports the sources of contamination in FEBID materials, first that due to the chamber contamination in conventional SEMs, and that due to the precursor molecule itself. The last sub-chapter presents finally the different solution developed and reported by researchers until this day to lower contamination in FEBID materials.

In Chapter 3 are shown the equipments used during this thesis to produce and characterize the materials deposited. Modifications brought to a Cambridge Stereoscan S100 SEM to allow for the simultaneous injection of two controlled flows are presented. Other evolutions of the setup consisted in the development of an *in-situ* reflectometry tool to control the deposition processes of optical materials, and the optimization of liquid Nitrogen traps. Specificities related to this thesis such as microscope periodic maintenance, effect of Oxygen on electron emission, or background vacuum composition are addressed. Finally, the different precursors used and their properties are listed and compared.

Chapter 4, 5 and 6 report the detailed study of the effects of the different parameters on the deposited chemical compositions, and growth rates. The

results and main message are summarized in a global image in a preamble before chapter 4.

In chapter 4 are presented the effects of additional Oxygen on the chemical compositions of the materials deposited under constant irradiation conditions and precursor flows. With suited irradiation dwell and replenishment times, Oxygen clearly lowered the contaminants concentration in the deposited materials to undetectable values over a [O_2]/[precursor] flow, specific to each precursor. The materials are characterized in terms of chemical composition, atomic sub-structure, and optical properties.

Chapter 5 reports results of experiments performed to understand the effect of the irradiation conditions on the growth kinetics during Oxygen assisted FEBID. Does the growth rate follow the electron emission of the substrates over which the materials are produced? Are the scanning parameters important and do they influence the chemical composition and growth rate? Based on the answers to these questions given by the experimental results, particularities of O_2 assisted FEBID such as predominant contribution of the secondary electrons, or highest efficiency of the process at low dwell times and high replenishment times are studied.

In Chapter 6 are compared the different effects that variations of the precursor and Oxygen flows induce on the deposition mechanism. Does Oxygen influence the growth rate and how? What gas flow limits the growth rate? Is the deposition rate dependent of the precursor flow, and how? The related experiments allowed demonstrating that the O_2 and precursor molecules undergo surface coverage competition on the substrate surface, and the process dynamics depended on the precursor molecule reactivity. Parasitic side-reactions driven by residual water were demonstrated to clearly limit the deposition reactions.

In Chapter 7, based on the results obtained in Chapter 4, 5, and 6, the FEBID efficiencies in terms of atom deposition rates obtained are compared to the flows of impinging precursor and Oxygen flows (calculated by flow simulations), to the residual flows of water and Oxygen, and to the electron flow irradiating the surface. The respective roles of residual water and additional Oxygen are then discussed. The atom deposition rate per electron was multiplied by 20 in O_2 assisted FEBID, compared to conventional FEBID. Finally, a decomposition process is proposed for each precursor molecule used.

Nano-scale optical structures obtained by FEBID of SiO_2 and their characterization are presented in Chapter 8.

In Chapter 9, the work achieved during this thesis is summarized and guide lines for future research are proposed. Controlling precisely the vacuum composition is a paramount necessity to lead to the understanding of the FEBID processes, and top pure materials, however requires technical optimization of the deposition equipment.

CHAPTER 2
LITERATURE SURVEY

The aim of this chapter is to give a general overview of FEBIP and the deposition equipments, starting form the first observations due to decomposition of contamination, to the recent industrial applications, requiring high quality materials of purest chemical composition. The chapter is divided in different parts, each of them addressing a different aspect:

2.1 Scanning Secondary Electron Microscope History (pp. 2-2)

2.2 FEBID history (development and applications) (pp. 2-7)

2.3 FEBID description: historical models (pp. 2-12)

2.4 Contamination origins in FEBID materials (pp.2-16)

2.5 How to lower contamination in FEBID materials (pp. 2-18)

2.6 FEBID and alternative techniques (pp. 2-26)

2.7 Target of this thesis (pp. 2-27)

In the first part, a short overview of the development of SEMs is presented. I found interesting to show how SEMs were developed from the 1930's and ended up to the products as we know them today only in the 1970's.

The FEBID history sub-chapter includes the first observations of the phenomena, the first applications and the three theoretical phenomenological models.

The third part explains where the contamination found in the FEBID materials originate from and the influences of these parasitic elements on the material properties.

Finally, ways to lower the contamination in the deposited structures are presented.

2.1 SEM history

The idea of an electronic microscope emerged as early as 1926, when Busch showed how axially-symmetric electric and magnetic fields could influence charged particles trajectories, and could lead to the focusing of beams of charged particles.[1] The discovery opened the way to geometrical electron optics, and mainly two teams of German researchers investigated the field.

A first step of this development was the construction in 1932 of a setup which demonstrated that electrons emitted from a cathode could be focused using two lenses on a screen in vacuum bell jars, see Figure 2-1.[2]
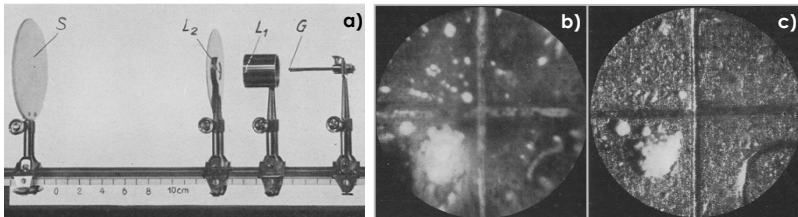
Figure 2-1: Electron beam setup constructed by Brüche et al. (a) Picture of the system placed in a vacuum bell jar, with G the emitting cathode, Li the electron lenses, and S the screen. (B) and (C) respectively electron and optical micrograph of the cathode (magnification 150 times).

Knoll and Ruska were the first to construct a Transmission Electron Microscope (TEM) and to publish their results obtained.[3, 4] At the time, the Focused Electron Beams (FEB) were focused to spots of a few hundreds of micrometers.

The TEM straightforwardly lead the researchers to think about another system that would build its image using electrons emitted from an irradiated surface. An anonymous report of 1932 clearly stated that two different engineer teams were developing in parallel the electron microscope based on electrons emitted from a surface.[5]

The first setup which allowed producing images using either primary (i.e. transmitted here) or secondary electrons (i.e. emitted from a surface) was reported by Knoll *et al* in 1933, and settled the basis of modern SEMs (for secondary electron microscopes). In Figure 2-2 is shown what is believed to be

one of the very first secondary electron micrographs of a surface (in this case the cathode grid).[6]
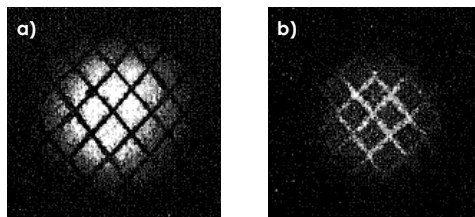
Figure 2-2: Comparison of images of a cathode grid using primary (a) and secondary electrons (b).

In a logical progression of his work, Knoll proposed in 1935 an amelioration to his first TEM, that included a scanning of the beam, which resulted in the first STEM.[7] This allowed acquiring images of larger fields of view, at different magnifications. By changing the ratio of the scan amplitudes, the magnification could be varied, as Zworykin had demonstrated in 1934.[8] In the late 1930's, von Ardenne, a private consultant contracted by Siemens and Halske AG, theoretically described a new setup in which he integrated two additional lenses to Knoll's STEM, in order to demagnify the FEB cross-over in the electron gun, which confined the FEB to spots of 50-100 nm.[9] The described setup could be used as scanning transmission electron microscope with bright and dark filed modes, as well as scanning secondary electron microscope. Since then, this concept was applied to SEMs (for scanning secondary electron microscopes) as we know them today. Von Ardenne constructed the setup, and demonstrated the formation of probes down to 4 nm diameter. The microscope is shown in details in Figure 2-3.

As presented in inset "c", a set of lenses focused the electrons emitted from a cathode. The deviation coil of the FEB column and that of the cathode ray tube are synchronized by the sawtooth signal B. The irradiated surface S emits electrons under irradiation that are collected by P. This signal is then amplified and injected in the grid of the cathode ray tube, hence controlling the brightness of the signal for each point of the image. Insets "d" and "e" present

respectively an optical micrograph of a post stamp and a secondary electron micrograph of a detail of this sample. The achieved resolution at 23 kV was about 250 nm. The acquisition time of such an image was 20 min.
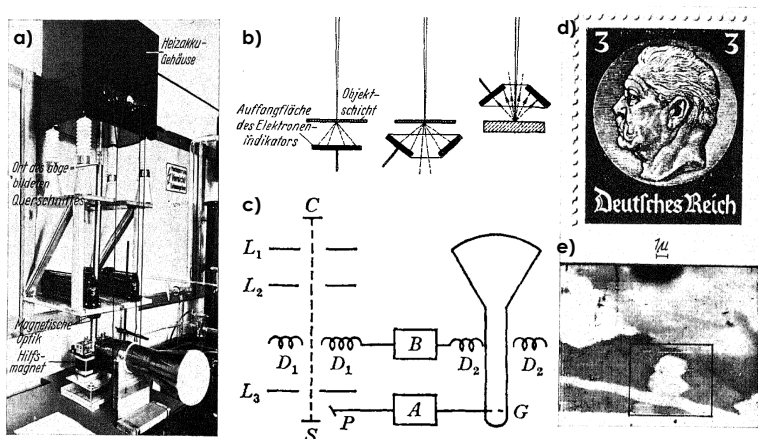
Figure 2-3: SEM principle as imagined constructed and used in 1938 by von Ardenne. (a) Optical micrograph of the electronic microscope. (b) Different irradiation possibilities. (c) Simplified illustration of the SEM, so-called raster microscope. L_x are lenses, D_x deviation coils, B a signal generator. S is the sample, P the electron detector, A an amplificator, and G the input of a cathode ray tube.(d) Postal stamp scheme, and (e) SEM image of the stamp.

This setup was constructed and used for surface imaging, backscattering and secondary emission studies as examples, and was known as the "Universal Microscope".[10-13] The imaging resolution achieved was in the order of micrometers when using a 50 Hz TV scan mode, and tens of nanometers when using higher dwell time image scanning modes.

Von Ardenne continued the development and optimization of his SEM, and obtained a patent in 1937 for a double deflection system. He published a book in 1940, in which he proposed to use an electron multiplier based on beryllium copper dynodes that had the advantage to support being opened to atmosphere. Resolution problems related to backscattered electrons were also addressed, and he already proposed the use of low acceleration voltages for ultimate resolution, since he understood the different interactions of the different electrons with matter, see Figure 2-4. His progresses were then stopped

by the war, and there is only little doubt that his work could have lead to an efficient SEM. His prototype was destroyed in air raid on Berlin in 1944, and he did not resume his research on SEMs after the war.
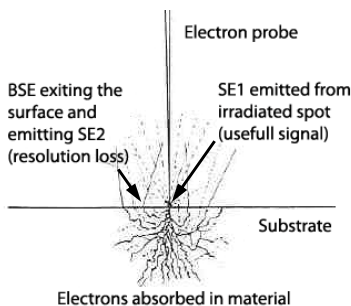
Figure 2-4: Von Ardenne's understanding of electron-matter interactions in 1940. SE and BSE states for secondary and back-scattered electrons respectively

The very first SEM entirely devoted to surface and topographical analysis as used today, and integrating all the features previously mentioned, appeared in 1942, and had already a resolution of 50 nm.[14] Zworykin's team had been active since 1938 in the development of SEMs, and was following the progress of the German engineers. They based their work on what was published. However, the low signal to noise ratio of their SEM and the poor image contrast were not to the advantage of convincing scientists of the importance of SEMs compared to TEMs. The strategy applied by Zworkin to lower the noise was to use a higher electron density gun, a field emission gun, and a slow scanning. They finally gave up the project, due to the lack of amelioration of their system after numerous unsuccessful optimizations.

The mid 1940's were poor in scientific research related to SEMs. In the 1950's, Charles Oatley understood that the main issues of SEMs compared to TEMs was the poor image quality, and decided to give SEMs a second chance. He basically suited von Ardenne's idea of the copper beryllium detector that was lacking Zworkin's microscope, and the advances of Zworkin's team in the field of electron guns to build a new microscope.

This constituted the main breakthrough at the time, see Figure 2-5. Further optimizations included the optimization of the deflection systems, image construction, aberrations corrections, and secondary electron detectors. Oatley's team then started investigating potential applications of their microscope, which already included etching and microfabrication, microelectronics. [15-23]
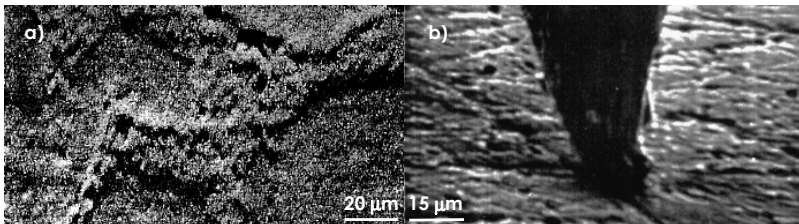
Figure 2-5: Comparison of images obtained by Zworykin, and that obtained by Oatley by changing the secondary electron detector

In these years, the idea of launching commercially SEMs emerged. In 1962, the Cambridge Instrument Company was contracted to produce the very first commercial SEM: the Stereoscan 1. Market estimation ordered by Oatley at the time resulted in the following, 6 to 10 machines would answer the worldwide market.

The production of relatively low-cost SEMs increased this demand, and it soon became the easiest machine for micro- and nano-investigations, as we know them today: complete and user friendly setups with imaging possibilities, controlled by computer, multi degree of freedom stages, *in-situ* analyze techniques, load-lock systems, and large chambers for full wafer inspection are few examples of the progresses accomplished in the last decades.

2.2. FEBID history

2.2.1 FEBID discovery

The first reports of FEBID of contamination in scientific papers appeared between 1910 and the 1940's, in the same time that scientists were developing setups based on electron beams.[24-30] Whenever electrons were flying through high vacuum (10^{-5} to 10^{-6} mmHg) and irradiating a surface, brownish-dark deposits of unknown material were locally deposited on the phosphorescent screens and growing with time. It was at the time an uncontrolled and undesired side-effect, since the contamination films produced would then prevent from high quality analyses and measurements by continually increasing the dimensions of the observed structures with time (~30 Å per minute), see Figure 2-6.[29]

Starting form the 1950's, and following the development of SEMs, the number of papers reporting FEB induced contamination importantly increased. In these years, numerous analytical techniques were based on particle (ions, α particles, ultra violet photons, etc…) interaction with matter, and all the studies related to one of these vacuum techniques reported the local growth of such contamination, which was known since 1910 to be present in vacuum systems. Systems based on FEBs could hence not be an exception.
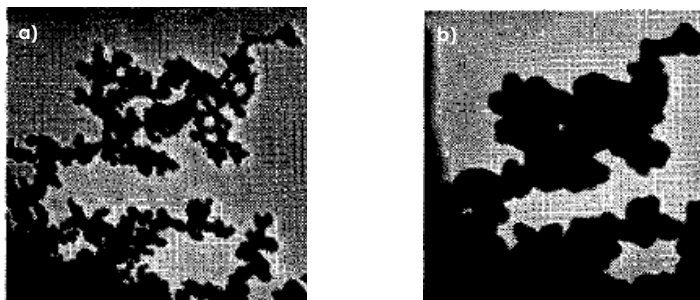
Figure 2-6: Effect of FEB induced contamination growth during TEM observation (magnification = 20000 X) of Shawinigan Acetylene Black, at (a) t = 0 min and (b) t = 12 min of exposition.

Whereas some reports state contamination was mainly polymerized Carbon,[26, 28, 31, 32] others showed that it contained Silicon, Carbon, Oxygen and Hydrogen atoms.[33, 34] FEB induced growth of contamination was understood to emanate from the interaction of electrons with adsorbed molecules, of (still) unknown origin. The process behind the molecule feeding to the deposition area was also not yet understood. The main problem being that contamination was specific to each equipment, and no real precise study could be performed.

2.2.2 Contamination applications

FEBID of contamination was however attractive to some researchers, who studied the properties of the deposited materials, and found applications based on the results obtained.

Stewart showed in 1934 that the films were made conductive after a thermal annealing in inert gas.[28] Other researches showed that ageing the deposits in air increased their resistivity and reduced their dielectric constant.[35-40]

König reported 3-D shell production by growing contamination on NaCl crystals. The material obtained was resistant to water dissolution, and supported heat annealing in vacuum up to 500 °C, but did not survive the same heat treatment in air, see Figure 2-7.[27] This thermal behavior was observed in some other studies as well.[26, 28]

Figure 2-7: Studies of contamination behaviour on NaCl crystals in a TEM. Scale bar indicates in all cases 1 μm.
(a) Contamination covered crystals.
(b) Same area after dissolving NaCl in water. Only 3-D contamination shells remain.
(c) Same area after thermal annealing to 500 °C in vacuum, showing thermal resistance of the shells.
(d) Same area after thermal annealing in air, showing that contamination shells burnt.

Some other materials appeared to be photoactive, and were used as base media to record the presence or the trace of electrons.[41]

In order to increase the deposition rate, organic molecules were deliberately introduced in the chambers by placing an adhesive tape piece, paraffin particles, or supplying oil vapours to the chamber.[42-45] Many papers can be found reporting the production of 2 and 3-dimensional structures of contamination.

Hillier showed that the contamination deposits were acid and alkalies solution resistant, which was in agreement with the work of Hirsch.[46] Such structures resisted electroplating conditions, and allowed the fabrication of 80 nm wide apertures in metallic films, see Figure 2-8.[47]
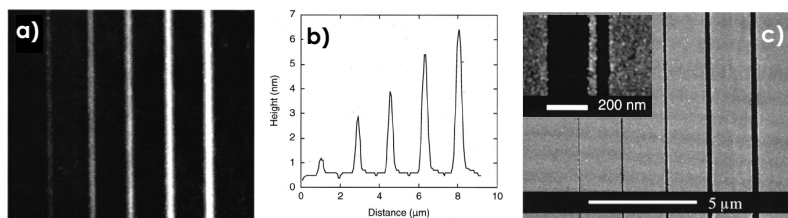
Figure 2-8: Use of contamination as masking material for electrodeposition. (a) SEM micrograph (top view) of deposited lines. (b) AFM profile of the lines. (c) Structures after Au electrodeposition showing widths of 70 nm.

The resolution of the pattern transfer in metallic film was lowered below 8 nm, the latter line roughness being attributed to the metallic film granularity.[48-50] FEBID could also be used as static memory device, as proposed by gray-scale images produced with resolutions of 30 and 25 nm.[51-56] Contamination Carbon was also used as insulating layer in microelectronics.[57, 58]

Three-dimensional deposits could be produced by spotting the beam for longer deposition times. Contamination "super-tips" could be produced on standard cantilevers, and offered higher resolution than conventional Si tips due to their high aspect ratio and nanometer scale diameters, for scanning probe microscopy.[59-64] The resolution could be increased to 10 nm due to their small apex.[65, 66]

2.2.3 FEBID of metal-containing materials

Starting from the 1960's, other gases than organic vapours were injected in the vacuum chambers. The idea of nano-structuring materials different from C was obviously interesting, and volatile metal complexes were used to create functional structures. A wide range of materials containing Au, Al, Ge, Si, Pd, Pt, Co, Cr, Cu, Fe, Mo, Ni, Os, Re, Rh, and Ru were deposited with FEBID.[67, 68] However, the limitation of FEBID, which is still not resolved yet, quickly arose. The materials deposited in high vacuum systems did not consist of pure material, and were contaminated. The undefined and uncontrolled material sub-structure and properties required time-consuming investigations. The applications were then tailored to the material properties. Applications such as conductive supertips (see Figure 2-11 b),[69-71] magnetic supertips,[72] local electrical contacts,[73, 74] X-Ray masks,[75, 76] integrated nano electron field emitters (see Figure 2-9),[77-81] electric devices,[82-84] photonic crystals for infrared–light [85], optical devices for SNOM,[86] nano-tweezers (see Figure 2-10) were developed since these materials obtained had satisfying properties,[87] interdigited electrodes with 5 nm gap[88] and sensors (see Figure 2-11 a).[89, 90]
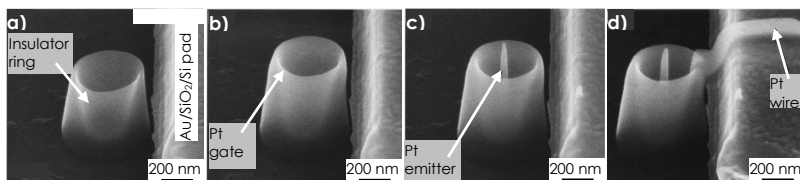
Figure 2-9: SEM micrographs (tilt view) of the different steps of fabrication of a field emitter.
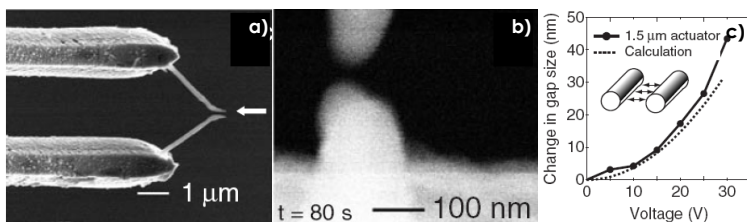
Figure 2-10: Micrographs of Nano-tweezers. (a) First deposition. (b) Step by step tuning of the gap. (c) Gap vs. voltage characteristic.
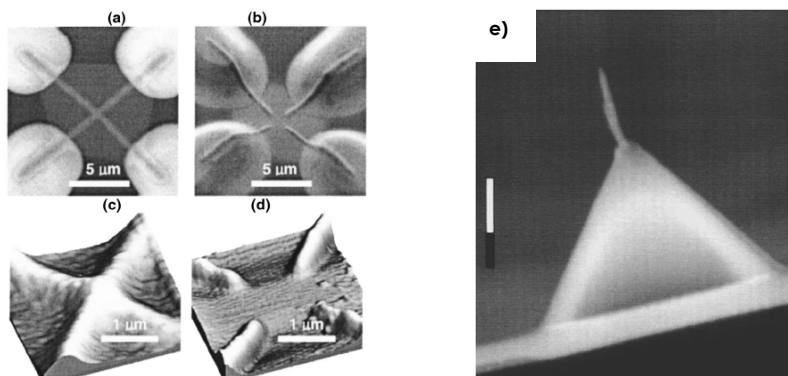
Figure 2-11: Nano-hall sensor (a) to (d), showing top and tilted 3D views of different configurations. Inset (e), super conductive tip containing gold. Bar = 1 μm

Industrial applications of FEBID emerged only in the years 2000, as a niche market. Industries were not interested in building prototype structures by FEBIP, but were looking for machines able to repair prototype chips and photomasks, containing sub-100 nm scale features. With decreasing size, the price of prototypes and masks increased drastically, and low-cost repair techniques were interesting. Due to the complexity of the materials involved and the need of high selectivity during the processing, focused ion beam processing that was used until then by industries, was no more competitive.

The versatility of FEBIP, demonstrated by the numerous structuration possibilities, was perfectly suited to the task. A few applications are: deposition of SiO_2, of phase shift material (given refractive index), selective etching of Copper and Chromium, which all require well defined properties. However, the materials to be processed had specific properties, and the materials to be deposited were expected to reached conductivity, chemical resistance, and optical properties of the corresponding bulk materials.

In order to overcome contamination problems, modifying a SEM was hence not sufficient. FEBIP for industrial applications required dedicated machines, suited for FEBIP and not for imaging. The first industrial mask repair machine was commercially available and applied to industrial applications only in 2003.[91-96]

2.3 FEBID description: historical models

In the 1960's, a few researchers proposed theoretical descriptions of the FEB deposition mechanism. Collecting results that were reported between 1939 and 1981, it can be observed that the contamination growth rate decreased with increasing FEB primary energy, for acceleration voltages between 10 eV and 1 MeV.[33, 46, 97, 98]

In 1940, Mayer published how he could actually control the growth rate of contamination in his setups, since he observed reproducible increase of growth rate as function of the electrons energy between 6 to 25 eV.[41] All these results indicated a maximum of contamination efficiency at low FEB energies, and allowed the researchers to believe that the growth rate was function of the ionizing power of the primary electrons. Experiments performed on heated sample indicated lower deposition rates at high temperature.

The contamination growth rate also showed to be dependant of the FEB probe size (diameter), indicating a dependence of the process on electron density. This hypothesis was further strengthened by results showing that it also depended on the density of the substrate over which the material was grown.[99-102] See Figure 2-12.
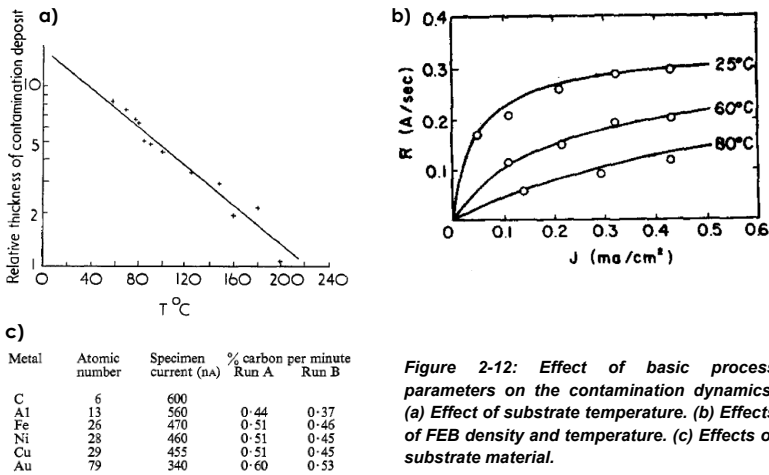
Figure 2-12: Effect of basic process parameters on the contamination dynamics. (a) Effect of substrate temperature. (b) Effects of FEB density and temperature. (c) Effects of substrate material.

Metal	Atomic number	Specimen current (nA)	% carbon per minute Run A	Run B
C	6	600		
Al	13	560	0·44	0·37
Fe	26	470	0·51	0·46
Ni	28	460	0·51	0·45
Cu	29	455	0·51	0·45
Au	79	340	0·60	0·53

2.3.1 Christy's model [103, 104]

Christy was the first to report a theoretical explanation of FEB induced deposition of contamination in his microscope based on the electron flux, the residence time of the molecules on the surface, and the molecule cross section.[103] The vapours present in the chamber were that of a silicon oil.

He separated clearly two different situations: one in which the process was limited by the amount of molecules arriving to the deposition area (precursor limited), and the other situation in which the process was limited by the electron density (electron limited). One equation was obtained for each case, giving the film growth rate R:

$$R = \frac{\upsilon F}{1 + \dfrac{1}{\sigma \tau f}} \quad \text{when} \quad F < \frac{\sigma}{\alpha} f + \frac{1}{\alpha \tau} \quad \rightarrow \text{Precursor limited regime}$$

$$R = \frac{\sigma}{\alpha} \upsilon f \quad \text{when} \quad F \geq \frac{\sigma}{\alpha} f + \frac{1}{\alpha \tau} \quad \rightarrow \text{Electron limited regime}$$

with σ the cross section for cross-linking collision, f is the number of electrons per unit area per unit time, F the number of oil molecules impinging the surface per unit area per unit time, τ the mean residence time of the molecules on the surface, α and ν are the area and the volume of a molecule respectively.

His experimental data was satisfyingly fitted by these two equations. Experiments performed with high electron flows and/or low temperature (στf >> 1) showed that the growth was proportional to νF, see Figure 2-13.

In the opposite situation (low f and high T), the growth rate appeared to be approximately στfνF, which depended on the current density and temperature.
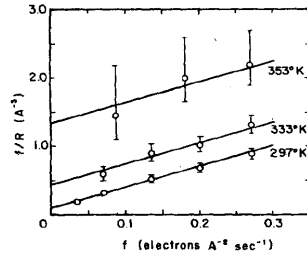
Figure 2-13: Experimental results vs. theoretical predictions (lines) of the growth rate as function of the electron flux in the electron limited regime.

2.3.2 Müller's model [56, 105]

Müller obtained in 1971 interesting annular shape deposits while depositing with a static beam. He suggested that surface diffusion of the molecules might be a significant parameter in FEBID, and added to Christy's model a surface diffusion component λ·ΔN, where λ is the surface diffusion path of the molecules, and N the number of molecules on the surface. The number of molecules on the surface could hence be written as:

$$\frac{\delta N}{\delta t} = F - \frac{N}{\tau} + \lambda \cdot \Delta N - \frac{f}{e} \cdot \sigma N$$

With e the electron charge and other symbols retained from Christy's model. Setting the equation to zero at equilibrium and resolving for an axially symmetric beam resulted in the following solution:

$$N_{surface} \approx \frac{const}{f_0 \times D^2}$$

Where f_0 is the beam electron flow and D the beam diameter. This relation could describe the experimental doughnut shape deposits he obtained, see Figure 2-14.
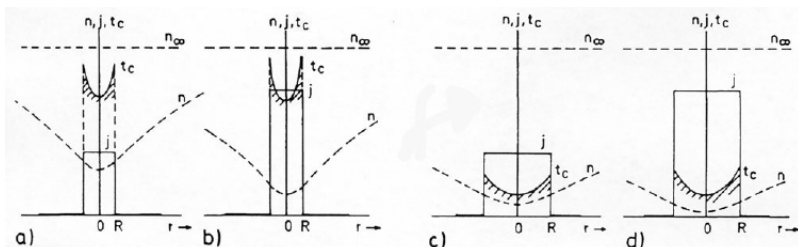
Figure 2-14: Theoretical results of Müller representing the contamination rate depletion k as function of beam parameters. (a) to (b): doubling the FEB current and keeping the diameter constant. (c) to (d) effect of doubling the spot size and current. Depletion of molecule concentration visible.

Müller also defined a reduced diffusion length ρ of the species on the surface:

$$\varrho = \sqrt{\frac{a\upsilon\tau \cdot \tau_1}{4(\tau + \tau_1)}}$$

With τ the molecule residence time and τ_1 the molecule residence time under irradiation (approximated to 10 % of τ), a the average distance between to adsorption sites, and ν the molecule diffusion speed. The diffusion rate was function of D/ρ.

Müller managed to fit his experimental data with ρ = 100 nm. By approximating τ to 3 μs, he approached the mean diffusion distance on the surface to 2 μm, which corresponded to an area of 100 nm in diameter. The migration path of 100 nm previously determined was not sufficient (i.e. was too short) to explain his results. He proposed that electron density effects might be significant.

2.3.3 Scheuer and Koops model [106]

Compared to the model of Christy, this model assumes that adsorbed molecules might undergo FEB dissociation, and the number of monolayers on the surface is limited to 1. A factor n/n_0 limits the process to one monolayer coverage, was introduced into Christy's equations, and the resulting equation of the film growth rate was:

$$R = \frac{\upsilon s F}{1 + \dfrac{n_0 + s\tau F}{n_0 \sigma \tau f}}$$

With s the sticking probability of the molecule (put to 1), η_0 the molecular density of a monolayer, and the other symbols similarly defined than in Christy's model. This model holds only for the deposition of large films.

2.4 Contamination origins in FEBID materials

The contamination detected in FEBID materials has three origins: the residual gases from the vacuum chamber that are incorporated in the material during growth, the adsorbed contamination present at the substrate surface, and the non-volatile elements originating from the precursor molecule itself.

2.4.1 Contamination sources in vacuum chambers

In 1953 and 1954, Ennos and co-workers precisely determined the origins of contamination in vacuum systems: they were identified as organic species originating from oil or grease from vacuum components such as pump oil, stopcocks, gaskets, greasy metal surfaces, O-rings, sample holder and other mechanical components.[31, 107] These pollution sources were known since 1913 to degrade vacuum quality and influence reactions occurring in the process chambers.[108-110]

Additionally to these heavy molecules, other gaseous contaminants (residual gases) were detected in the process chambers. In 1963, a study reported that hydrocarbons were clearly not the most predominant contaminants in vacuum systems, since 80 % of the background pressure (10^{-5} Torr) was gaseous water. The remaining 20 % were distributed between N_2, O_2, CO and hydrocarbons (partial pressures between $5 \cdot 10^{-7}$ to 10^{-6} Torr each).[111-113]

2.4.3 Contamination incorporation in FEBID materials

Light residual gases, mainly O and C, from the vacuum chamber were usually incorporated in the deposited materials. Although the problem was not mentioned or quantified clearly in the publications and might be undetected when using organic molecules (containing O and C atoms), it was clearly noticeable when Oxygen- and/or Carbon-free molecules were used. Such precursors decomposed under focused beams (either electron or ion) in Carbon and/or Oxygen containing materials (from 5 to 30 at %), revealing the contamination incorporation phenomena: AsH_3,[114, 115] $AuCl_3$,[116] $Al(C_4H_9)_3$,[117] $AlCl_3$,[116] $Al(CH_3)_3$,[114, 115, 118-120] SiH_2Cl_2,[121, 122] $SnCl_2$ and $Sn(CH_3)_4$,[104, 123, 124] $Pt(PF_3)_4$,[125, 126] $(CH_3C_5H_4)(CH_3)Pt$ and $(CH_3)_3(C_5H_5)Pt$,[127-130] WF_6,[121, 131-135] WCl_6 (which deposited $W_7Cl_2C_1O_2$),[134, 136, 137] $Cr(C_6H_6)_2$ (which deposited $Cr_2C_9O_3$),[134] $[RhCl(PF_3)_2]_2$,[138, 139] C_8H_8,[140] and $TiCl_4$.[141, 142] All the materials deposited from these molecules, additionally to containing Oxygen or Carbon from residual gases, contained as well all the elements present in the starting molecule.

Results reported for W, Mo, Re, Cr and Fe showed that carbonyls, even though containing only volatile ligands, mainly decomposed resistive carbide materials.[76, 132, 143-150] Halogen atoms were also detected in the materials deposited from halogen containing molecules such as WF_6, WCl_6, SnH_2Cl_2, $SnCl_4$ or $TiCl_4$. [116, 122, 124, 131, 132, 141]

The final chemical composition of the FEBID material depended of the SEM used for the experiment, operating pressure, pumping efficiencies, precursor

flow, gas injection system position, and FEB parameters. The contaminants concentration is impossible to predict from one machine to the other.

2.5 Methods to lower contamination in FEBID materials

2.5.1 Optimization of process chambers

Efforts were applied to lower and prevent SEMs from contamination and different solutions were found as function of the contamination type. Hydrocarbons concentration could be lowered by replacing standard pump oils by low vapour pressure oils (Fomblin type), which had also the advantage of not polymerizing.[151, 152] The ultimate solution of oil-free pumps appeared in 1964.[153, 154]

New vacuum components were developed during the 1950's, that did not contain any O-ring, and prevented hence from polymer degassing. These new components assured chamber background pressures of 10^{-8} to 10^{-6} mmHg and supported baking to a few hundreds of degrees Celsius.[155-166] These components were later mounted on ultra high vacuum systems, that could be baked. A few studies performed in ultra high vacuum systems showed that pure materials such as Si and Ge could be obtained by FEBID.[167-169] The depositions of Si were performed after baking the chamber during 24 h (background pressure of 10^{-10} Torr after baking), and the sample to 1000 °C prior to the deposition. No traces of O or C could be found in the deposited materials. Baking the process chamber at lower temperatures, 200 °C showed to be efficient as well and lead to the deposition of pure Ge, however with a longer baking time of 3 days.

Heating the sample while exposing it to a reducing H_2-Ar mixture allowed to decontaminate the substrate surface prior to the deposition.[170] Heating the substrate up to 200 °C showed to reduce by 80 % the contamination growth

rate,[31, 107] which was attributed to the desorption of contamination molecules. Poly-cristalline films of Au were deposited at 150 °C.[171] It was equivalently demonstrated that heating the substrate during or after the deposition could lead to a purification of the deposited material.[116, 141, 142, 172-176] Post deposition thermal annealing by heating the sample of by electron irradiation allowed less efficiently to desorb contaminants.[88, 141, 142, 177] *In-situ* sample cleaning with O_2 plasmas followed by a 300 °C annealing allowed to reduce the resistivity of W containing materials two times.[178, 179]

Cold traps (first filled with liquid air and then with liquid nitrogen) placed in the surroundings of the sample allowed decreasing the hydrocarbon contamination to lower values as well.[180-185] Although these systems were efficient for trapping part of the high weight molecules, residual gases (H_2O, O_2, N_2 etc…), could not be pumped efficiently from the SEM chambers.

In 2006, none (apart the mask repair tool from NaWotec GmbH) of the commercial FEBIP equipments available from the main manufacturers were equipped with heatable sample stages, bakable chambers, or cold traps, which were obviously well-known devices and essential to improve the quality of the deposits.

2.5.2 Precursor chemistry

Among all the results reported in literature, two solutions based on the precursor chemistry are reported to increase the material purity of the materials usually deposited with metal complexes: the use of carbonyls and halogenated precursors, and the use of simple but reactive molecules.

The average metal content obtained by FEBID at room temperature with organo-metallics and corbonyls or halogenated molecules are respectively 8-20 at.% and 50-80 at.%.[125, 186, 187] The deposits morphology indicated that they

had different sub-structures: organo-metallics usually decomposed in smooth (sub 2 nm roughness) deposits consisting of metal nano-crystals embedded in a carbonaceous matrix,[85] whereas carbonyls and halogenated molecules decomposed in polycrystalline materials.[171, 188-191]

One of the possible reasons is the lower thermal stability of halogenated and carbonyls molecules, which increase the probability of clean thermal decomposition. Autocatalytic effects were observed with $W(CO)_6$ and $(Co(CO)_4)_2$ around 120 °C already.[192-195] Using WF_6, and attempting to improve the W concentration of the deposits by heating the sample, Si substrates were etched at 150 °C. This was attributed to the decomposition of the molecule at that temperature, which liberated F atoms that reacted with the Si substrate to form the volatile SiF_4.

Exotic precursor chemistries lead to the deposition of poly-crystalline materials of high purity. The only report of a room temperature FEBID of a 100 % pure material in a high vacuum unbakable SEM using low currents, is that of pure gold, obtained form $AuPF_3Cl$.[188-190] This was certainly due to the low decomposition temperature of the precursor (estimated to 30 °C).

Other simple and reactive (pyrophoric) molecules such as hydrides showed to decompose, in a clean ultra high vacuum chamber, in crystalline films of Si and Ge.[167-169] Recent more complex molecules (acetylacetonates as example) originating from the fields of CVD and PECVD, and used for FEBID, did not improve the deposit quality obtained under standard high vacuum conditions. Derivates of organo-metallics obtained by replacing H atoms by F atoms or Carbon containing ligands by phosphines allowed increasing the material metal concentration, but did not allow for pure metal deposition.[139, 196]

Carbonyls and fluorophosphines are efficient molecules, but their high toxicity prevents from using them without high safety. Hydrides and simple molecules are generally pyrophoric, and hence not preferentially used.

2.5.3 Deposition parameters

In a general way, depositions at high currents (i.e. higher temperature increase) lead to purer deposits.[125, 195, 197, 198] The main disadvantage of this solution is the increase of deposit size, and hence the loss of resolution, together with the increase of beam current.

2.5.4 Additional gases

Another strategy appeared more efficient to increase the deposits purity. In 1954 already, French researchers observed that contamination films could be locally etched by flowing in the process chamber a controlled flux of air. This way, the Carbon reacted under the FEB to form volatile species that could desorb from the surface, see Figure 2-15.[199] The etch rate was proportional to the air flux.

Figure 2-15: Optical micrographs showing the effect of FEB irradiation of contamination with an air flux. Contamination spots produced by spotting a 27 μm FEB (density 0.007 A/cm^2) during 20 min and:
(a) no air flux
(b) an air flux of 0.14 mg/s
(c) an air flux of 0.025 mg/s.

Inset (d) shows a contamination spot identical to that in (a), that was post-irradiated by a focused FEB (6 μm diameter) during 4 min in presence of an additional air flow. The bright spot indicates the place where the contamination was locally etched by the focused FEB.

Other researchers later published the water assisted FEB etching of resist that allowed the production of nanometer scale structures. A few other papers report the same strategy.[200-205]

Hirsch demonstrated that etching of Carbon films could be achieved by cooling the sample in the chamber and irradiating locally with electrons. The phenomenon was attributed to the condensation of water on the film that could oxidize Carbon when activated by electrons. The etching process was in competition with the C build-up, and both were function of electron density.[206]

More recently, O_2, H_2O and H_2 were successfully used in order to etch other structures of Carbon such as amorphous films and diamond like Carbon.[201, 207-209] The main products of the reaction between Carbon and these additional gases are thought to be CO_2, CO, and CH_4 (only when H_2 is injected).

The idea of influencing the FEBID material chemical composition by using reactive gases was then straightforward: mixing a reactive gas together with the vapours of a precursor could lead to the deposition of pure materials, since the contaminants would be etched in real time during the deposition process. The process could also lead to the production of oxides or pure metals by adding oxidant or reducing gases to the precursor vapours.

One of the main issues of this idea was the large pressure increase that would induce the injection of two gases in the chamber, leading to the loss of resolution and technical problems. A major technical improvement appeared in 1968, that allowed higher pressures in the chamber without affecting the electron emission: the differential pumping system.[210] The idea is to pump the electron gun and column through a separate pumping unit than the process chamber, so that the chamber pressure can be increased to 10^{-2} mbar, and the molecule diffusion between the column and the chamber is limited by apertures, see Figure 2-16.[211] The pressure obtained in the gun was lowered to 10^{-8} mbar, which additionally increased the FEB quality, and lowered the gun contamination level.[212]
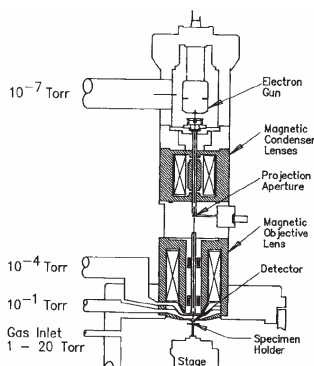
Figure 2-16: Principle of differential pumping system in a SEM

In 1983, FEBID of clean SiO_2 and Si_3N_4 films was obtained by electron assisted CVD mixing SiH_4 with O_2 (or NO_2), and SiH_4 with N_2 (or NH_3) respectively. The process chamber was an ultrahigh vacuum system, and the deposition were assisted by a relatively low temperature annealing (between 50 to 150 °C).[213, 214]

Nakano *et al* used the same idea to deposit by FEBID at room temperature, pure and high quality SiO_2, by mixing Si_2H_6 and O_2. Pure SiO_2 films were obtained only for $[O_2]/[Si_2H_6]$ injected flows superior to 2.[215] This is the very first result published that reports the production of a pure oxide using a room temperature FEBID process, in a ultra-high vacuum bakable setup. The study of pure SiO_2 FEB induced deposition was then reported sporadically. Adding reactive gases to molecules less reactive than silanes, such as organosilanes, also lead to the purification of the deposits, and some researchers obtained pure SiO_2.[216-220] However, neither the importance of the precursor chemistry (sometimes not motioned), nor that of the [Oxidant]/[precursor] ratio were ever presented.

Folch [186, 221] was the first to report gas (O_2 and $Ar+H_2O$ mixtures) assisted FEBID to increase the metal content of a gold structure in an environmental SEM, see

Figure 2-17. He demonstrated that the Au content of the deposits obtained from (CH₃)₄Au(acac) precursors depended on the water partial pressure in the SEM, and could be increased from 3 to 50 at %. The structure of the deposit was shown to consist in Au polycrystalline cores. However, pure gold could not be deposited.
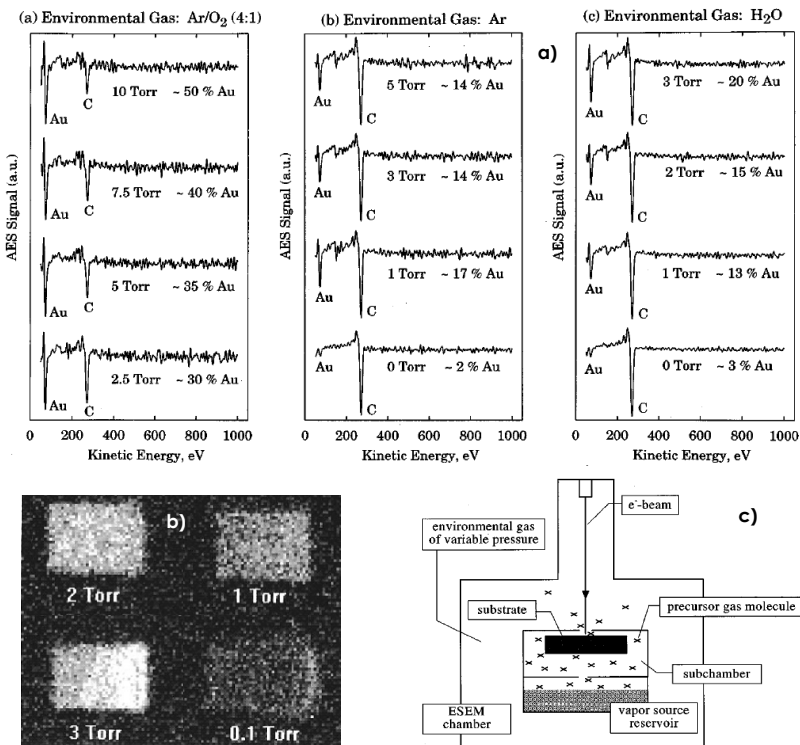
Figure 2-17: Results obtained by Folch et al. (a) Elements signals as function of additional gas and gas pressure. (b) Auger signal of Au as function of the H_2O partial pressure used during the deposition in an environmental cell. (c) Scheme of the environmental cell.

Molhave performed the same experiments, with another precursor, the dimethyl-gold-hexafluoroacetylacetonate (CH₃)₂Au(hfac), and demonstrated that H_2O was more efficient than O by comparing the oxidation efficiencies of

H_2O and O + H mixed in a 1:2 ratio. This suggested that water was more efficient than Oxygen as oxidizing agent.[222, 223] The tips deposited with water consisted of a dense core of Au surrounded by a cladding consisting of nano Au crystals embedded in a carbonaceous matrix, and the tips deposited with nitrogen consisted of nanocrystals embedded in a C matrix, see Figure 2-18.
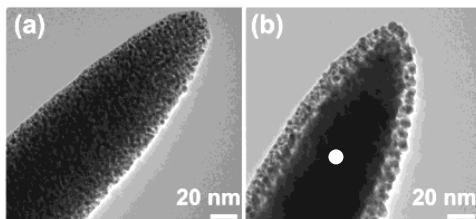
Figure 2-18: TEM investigations of tips deposited by organometallic precursor of gold, and (a) addiitonal nitrogen gas, and (b) additinal H_2O vapours. White spot indicate dense Au core.

In 2004, Wang *et al* applied the same strategy to the deposition of Platinum, and used the $Pt(PF_3)_4$ precursor mixed with Oxygen.[126] However, they observed that the higher the O_2 flux, the higher the O_2 incorporated in the material. No increase of the Pt content could be measured, see Figure 2-19.
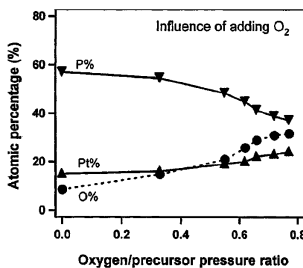
Figure 2-19: Elements chemical composition deposited from $Pt(PF_3)_4$ and additional Oxygen

The only report of a reducing gas assisted FEBID reaction is that of CH_4 mixed with H_2, which was reported to deposit diamond–like Carbon.[224]

Summary of ways to lower contamination in FEBID materials

- Gas assisted FEBID allowed producing SiO_2 using SiH_4 molecules, in a ultra high vacuum chamber. Pure materials could not be obtained from more common molecules in environmental cells such as organometalics.

- There is no detailed and systematic study of gas assisted room temperature FEBID of a pure oxide from standard organosilanes.

- Gas assisted FEBID mechanism appears complex, and no real description can be found in literature.

- The dependence of the injected gas ratios was never systematically studied and reported.

2.6 FEBID and other nano-scale prototyping techniques

As versatile 2- and 3-dimensional local and single step nano-fabrication technique, FEBIP has only few competitors allowing the additive and negative nano-scale structuration.

2.6.1 Focused Ion Beam Induced Deposition

The principle behind Focused Ion Beam Induced Deposition is the same as FEBIP, the electrons being replaced by ions. The ions used are mainly Ga^+, due to the large brilliance of the source. Research in the field of ion sources was done in the 1990's.[225-228] Similar materials were deposited with FIBs than with FEBs, using the same molecules and strategies to lower contamination: W, Au, Pt, C, Si, SiO_2. [229-237]

The high mass of ions compared to that of electrons induced structural defects in the irradiated surface, and FIBs are widely used for local etching of materials. FIBIP was widely used and preferred to FEBIP since the processes were faster with ions than with electrons, and FIBIP represented the ultimate tool for IC circuit and mask investigation and repair.[238-241] As FEBIP, FIBIP was applied for nano-prototyping applications.[238, 242-244]

However, the permanent and unavoidable ion implantation in the materials processed with FIBs influences the materials properties, which do not meet industrial requirements.[245-250] Today, FEBIP is preferred to FIBIP since electrons appear as the only solution to local deposition of pure material.

2.6.2 Scanning Tunneling Microscope Induced Deposition

In order to increase the resolution achievable with FEBIP, the use of low current and low voltage electrons emitted by tunnel effect from a sharp probe was proposed. Typical resolution obtained with this technique was 10 nm. Noble metals, magnetic materials were produced using this technique.[251-256] The reproducibility of the structures appeared to be delicate, certainly due to parasitic deposition on the tip used during the process.[257] Electrons in STMs were also used local source for the oxidation of Si surfaces in ambient atmospheres.[258-262]

2.7 Target of this thesis

This thesis focused on the FEBID of pure and high quality silica from molecular Oxygen and by selecting robust organosilanes chemistries, in an optimized standard contaminated high-vacuum equipment. The challenge of depositing pure materials in an optimized standard high-vacuum instrument is motivating since it represents a simplest solution to ultra-high vacuum bakable equipments.

The work aimed on studying the different materials obtained as function of the controlled $[O_2]/[precursor]$ ratios injected in the chamber, and determining the deposition mechanism behind O_2 assisted FEBID.

What ratio gives which material? Is it possible to deposit pure SiO_2 from organosilanes? Does the amount of Oxygen required vary with the different molecules? If pure silica is obtained, what are its optical and chemical properties?

Does the O_2 assisted FEBID mechanism follow the same tendencies than conventional FEBID? What are the effects of all the parameters on the deposited materials, in terms of chemical composition and growth rate?

The understanding of the mechanisms ruling the FEBID oxidation reactions as function of the main parameters of the technique represents a step forward to the generalization of the concept of gas assisted FEBID to other materials, such as metals as example.

2.8 Bibliography of Chapter 2

1. H. Busch, "*Calculation of the channel of the cathode rays in axial symmetric electromagnetic fields*", Annalen Der Physik, **1926**, *81*, 974-993.

2. E. Bruche, and H. Johannson, "*Electron optics and electron microscopes*", Naturwissenschaften, **1932**, *20*, 353-358.

3. M. Knoll, and E. Ruska, "*Article on the geometric electron optics Pi*", Annalen Der Physik, **1932**, *12*, 641-661.

4. M. Knoll, and E. Ruska, "*Comments on geometric electron optics I*", Annalen Der Physik, **1932**, *12*, 607-640.

5. Anonymous, "*Electron microscope*", Zeitschrift Des Vereines Deutscher Ingenieure, **1932**, *76*, 704-704.

6. M. Knoll, and G. Lubszynski, "*Microscopic electron illustration through secondary electrons*", Physikalische Zeitschrift, **1933**, *34*, 671-674.

7. M. Knoll, "*Charge potential and secondary emissions of electron irradiated bodies*", Physikalische Zeitschrift, **1935**, 36, 861-869.

8. V.K. Zworykin, "*The iconscope - A modern version of the electric eye*", Proceedings of the Institute of Radio Engineers, **1934**, *22*, 16-32.

9. M. von Ardenne, "*The scanning electron microscope: Theoretical fundamentals*", Zeitschrift Für Physik A, **1938**, *109*, 553-684.

10. M. von Ardenne, "*The scanning electron microscope: Practical construction*", Zeitschrift für Technische Physik, **1938**, *19*, 407-416.

11. M. von Ardenne, "*The mapping of the finest single particles, in particular of molecules, with the universal-electron microscope*", Zeitschrift Fur Physikalische Chemie-Abteilung a-Chemische Thermodynamik Kinetik Elektrochemie Eigenschaftslehre, **1940**, *187*, 1-12.

12. M. von Ardenne, "*Heating-super microscope with the universal-electron mocroscope*", Kolloid-Zeitschrift, **1941**, *97*, 257-272.

13. M. von Ardenne, and H.H. Weber, "*Electron microscopic analysis of muscle protein "myosin"*", Kolloid-Zeitschrift, **1941**, *97*, 322-325.

14. V. Zworykin, J. Hillier, and R. Snyder, "*A scanning electron microscope*", ASTM bulletin, **1942**, *117*, 15-23.

15. C.W. Oatley, D. McMullan, and K.C.A. Smith, "*The Development of the Scanning Electron-Microscope*", Advances in Imaging and Electron Physics, **1985**443-482.

16. C.W. Oatley, "*The Early History of the Scanning Electron-Microscope*", Journal of Applied Physics, **1982**, *53*, R1-R13.

17. R.F.W. Pease, and W.C. Nixon, "*High Resolution Scanning Electron Microscopy*", Journal of Scientific Instruments, **1965**, *42*, 81-&.

18. A.D.G. Stewart, and A. Boyde, "*Ion Etching of Dental Tissues in a Scanning Electron Microscope*", Nature, **1962**, *196*, 81-&.

19. T.E. Everhart, and R.F.M. Thornley, "*Wide-Band Detector for Micro-Microampere Low-Energy Electron Currents*", Journal of Scientific Instruments, **1960**, *37*, 246-248.

20. O.C. Wells, "*Correction of Errors in Electron Stereomicroscopy*", *British Journal of Applied Physics*, **1960**, *11*, 199-201.

21. T.E. Everhart, "*Simple Theory Concerning the Reflection of Electrons from Solids*", *Journal of Applied Physics*, **1960**, *31*, 1483-1490.

22. K.C.A. Smith, and C.W. Oatley, "*The Scanning Electron Microscope and Its Fields of Application*", *British Journal of Applied Physics*, **1955**, 6, 391-399.

23. D. McMullan, J. Thewlis, A.W. Agar, D. Gabor, M.E. Haine, H.G. Lubszynski, R. Feinberg, and D. McMullan, "*An Improved Scanning Electron Microscope for Opaque Specimens*", *Proceedings of the Institution of Electrical Engineers-London*, **1953**, *100*, 245-259.

24. E.F. Burton, R.S. Sennett, and S.G. Ellis, "*Specimen Changes Due to Electron Bombardment in the Electron Microscope*", *Nature*, **1947**, *160*, 565-567.

25. E. Gehrcke, and R. Seelinger, "*Über Oberflächenladungen auf Leitern im Vakuum*", *Verhandlungen der Deutschen Physikalische Gesellschaft*, **1913**, *15*, 438-450.

26. J. Hillier, "*On the Investigation of Specimen Contamination in the Electron Microscope*", *Journal of Applied Physics*, **1948**, *19*, 226-230.

27. H. Konig, "*Die Rolle Der Kohle Bei Elektronenmikroskopischen Abbildungen*", *Naturwissenschaften*, **1948**, *35*, 261-265.

28. R.L. Stewart, "*Insulating films formed under electron and ion bombardment*", *Physical Review*, **1934**, *45*, 0488-0490.

29. J.H.L. Watson, "*An Effect of Electron Bombardment Upon Carbon Black*", *Journal of Applied Physics*, **1947**, *18*, 153-161.

30. J.H.L. Watson, "*Specimen Contamination in Electron Microscopes*", *Journal of Applied Physics*, **1948**, *19*, 110-111.

31. A.E. Ennos, "*The Origin of Specimen Contamination in the Electron Microscope*", *British Journal of Applied Physics*, **1953**, *4*, 101-106.

32. K.M. Poole, "*Electrode Contamination in Electron Optical Systems*", *Proceedings of the Physical Society of London Section B*, **1953**, 66, 542-547.

33. A. Kumao, H. Hashimoto, and K. Shiraishi, "*Studies on Specimen Contamination by Transmission Electron-Microscopy*", *Journal of Electron Microscopy*, **1981**, *30*, 161-170.

34. M. Wendt, "*The Role of Contamination Layers in Electron-Probe Microanalysis*", *Kristall Und Technik-Crystal Research and Technology*, **1980**, *15*, 1367-1375.

35. B.H. Choi, S.K. Jung, S.I. Kim, S.W. Hwang, J.H. Park, Y. Kim, E.K. Kim, and S.K. Min, "*Electrical properties of electron-beam exposed silicon dioxides and their application to nano-devices*", *Japanese Journal of Applied Physics Part 1-Regular Papers Short Notes & Review Papers*, **1998**, *37*, 6996-6997.

36. L.E. Babcock, and R.W. Christy, "*Electron-Beam-Deposited Thin Polymer Film - Electrical Properties Vs Bombarding Current*", *Journal of Applied Physics*, **1972**, *43*, 1423-&.

37. L. Holland, and L. Laurenson, "*Electrical Properties of Silicone Films Polymerized by Electron Bombardment*", *Vacuum*, **1964**, *14*, 325-&.

38. R.W. Christy, "*Electrical Properties of Thin Polymer Films . Part 2 . Thickness 50-150 A*", *Journal of Applied Physics*, **1964**, *35*, 2179-&.

39.   H.T. Mann, "*Electrical Properties of Thin Polymer Films . Part I . Thickness 500-2500 A*", *Journal of Applied Physics*, **1964**, *35*, 2173-&.

40.   I. Haller, and P. White, "*Polymerization of Butadiene Gas on Surfaces under Low Energy Electron Bombardment*", *Journal of Physical Chemistry*, **1963**, *67*, 1784-&.

41.   L. Mayer, "*Photocontrol of Growth Rate of Thin Polymer Films Formed by Electron Bombardment*", *Journal of Applied Physics*, **1963**, *34*, 2088-&.

42.   W. Ding, D.A. Dikin, X. Chen, R.D. Piner, R.S. Ruoff, E. Zussman, X. Wang, and X. Li, "*Mechanics of hydrogenated amorphous carbon deposits from electron-beam-induced deposition of a paraffin precursor*", *Journal of Applied Physics*, **2005**, *98*.

43.   J. Romer, M. Plaschke, and J.I. Kim, "*Alignment of AFM images using an iterative mathematical procedure*", *Ultramicroscopy*, **2000**, *85*, 99-105.

44.   M. Plaschke, J. Romer, and J.I. Kim, "*Alignment of in-situ AFM images using microstructured reference points*", *Ultramicroscopy*, **1998**, *75*, 77-83.

45.   M. Antognozzi, A. Sentimenti, and U. Valdre, "*Fabrication of nano-tips by carbon contamination in a scanning electron microscope for use in scanning probe microscopy and field emission*", *Microscopy Microanalysis Microstructures*, **1997**, *8*, 355-368.

46.   E.H. Hirsch, "*Image Formation by Electron Bombardment of Metal Targets*", *British Journal of Applied Physics*, **1960**, *11*, 547-550.

47.   T. Djenizian, L. Santinacci, and P. Schmuki, "*Electron beam-induced carbon masking for electrodeposition on semiconductor surfaces*", *Applied Physics Letters*, **2001**, *78*, 2940-2942.

48.   W. Fritzsche, J.M. Kohler, K.J. Bohm, E. Unger, T. Wagner, R. Kirsch, M. Mertig, and W. Pompe, "*Wiring of metallized microtubules by electron beam-induced structuring*", *Nanotechnology*, **1999**, *10*, 331-335.

49.   A. Bezryadin, and C. Dekker, "*Nanofabrication of electrodes with sub-5 nm spacing for transport experiments on single molecules and metal clusters*", *Journal of Vacuum Science & Technology B*, **1997**, *15*, 793-799.

50.   A.N. Broers, W.W. Molzen, J.J. Cuomo, and N.D. Wittels, "*Electron-Beam Fabrication of 80-a Metal Structures*", *Applied Physics Letters*, **1976**, *29*, 596-598.

51.   H.W.P. Koops, J. Kretz, and M. Weber, "*Combined Lithographies for the Reduction of Stitching Errors in Lithography*", *Journal of Vacuum Science & Technology B*, **1994**, *12*, 3265-3269.

52.   Y. Ochiai, H. Watanabe, J. Fujita, M. Baba, S. Manako, and S. Matsui, "*Nanometer-Scale Direct Carbon Mask Fabrication Using Electron-Beam-Assisted Deposition*", *Japanese Journal of Applied Physics Part 1-Regular Papers Short Notes & Review Papers*, **1993**, *32*, 6147-6152.

53.   T. Takahashi, Y. Arakawa, and M. Nishioka, "*Insitu Patterning of Contamination Resists in Metalorganic Chemical Vapour-Deposition for Fabrication of Quantum Wires*", *Applied Physics Letters*, **1991**, *58*, 2372-2374.

54.   E.I. Rau, "*Microrecording and Information Reproduction with Sem*", *Scanning*, **1988**, *10*, 207-209.

55.   W.W. Molzen, A.N. Broers, J.J. Cuomo, J.M.E. Harper, and R.B. Laibowitz, "*Materials and Techniques Used in Nanostructure Fabrication*", *Journal of Vacuum Science & Technology*, **1979**, *16*, 269-272.

56.   K.H. Muller, "*Speed-Controlled Electron-Microrecorder .2*", *Optik*, **1971**, *33*, 331-&.

57.   N. Miura, T. Numaguchi, A. Yamada, M. Konagai, and J. Shirakashi, "*Room temperature operation of amorphous carbon-based single-electron transistors fabricated by beam-induced deposition techniques*", Japanese Journal of Applied Physics Part 2-Letters, **1998**, *37*, L423-+.

58.   N. Miura, H. Ishii, J. Shirakashi, A. Yamada, and M. Konagai, "*Electron-beam-induced deposition of carbonaceous microstructures using scanning electron microscopy*", Applied Surface Science, **1997**, *114*, 269-273.

59.   M. Castagne, M. Benfedda, S. Lahimer, P. Falgayrettes, and J.P. Fillard, "*Near field optical behaviour of C supertips*", Ultramicroscopy, **1999**, *76*, 187-194.

60.   M. Yamaki, T. Miwa, H. Yoshimura, and K. Nagayama, "*Efficient Microtip Fabrication with Carbon Coating and Electron-Beam Deposition for Atomic Force Microscopy*", Journal of Vacuum Science & Technology B, **1992**, *10*, 2447-2450.

61.   D. Keller, D. Deputy, A. Alduino, and K. Luo, "*Sharp, Vertical-Walled Tips for Sfm Imaging of Steep or Soft Samples*", Ultramicroscopy, **1992**, *42*, 1481-1489.

62.   H.Y. Ximen, and P.E. Russell, "*Microfabrication of Afm Tips Using Focused Ion and Electron-Beam Techniques*", Ultramicroscopy, **1992**, *42*, 1526-1532.

63.   D.J. Keller, and C.C. Chou, "*Imaging Steep, High Structures by Scanning Force Microscopy with Electron-Beam Deposited Tips*", Surface Science, **1992**, *268*, 333-339.

64.   T. Fujii, M. Suzuki, M. Miyashita, M. Yamaguchi, T. Onuki, H. Nakamura, T. Matsubara, H. Yamada, and K. Nakayama, "*Micropattern Measurement with an Atomic Force Microscope*", Journal of Vacuum Science & Technology B, **1991**, *9*, 666-669.

65.   K.I. Schiffmann, "*Investigation of fabrication parameters for the electron-beam-induced deposition of contamination tips used in atomic force microscopy*", Nanotechnology, **1993**, *4*, 163-169.

66.   M. Weber, H.W.P. Koops, and W. Gortz, "*Scanning Probe Microscopy of Deposits Employed to Image the Current-Density Distribution of Electron-Beams*", Journal of Vacuum Science & Technology B, **1992**, *10*, 3116-3119.

67.   N. Silvis-Cividjian, and C.W. Hagen, *Electron-beam-induced nanometer-scale deposition*, in *Advances in Imaging and Electron Physics, Vol 143*. 2006. p. 1-235.

68.   S.J. Randolph, J.D. Fowlkes, and P.D. Rack, "*Focused, nanoscale electron-bearn-induced deposition and etching*", Critical Reviews in Solid State and Materials Sciences, **2006**, *31*, 55-89.

69.   C. Schossler, J. Urban, and H.W.P. Koops, "*Conductive supertips for scanning probe applications*", Journal of Vacuum Science & Technology B, **1997**, *15*, 1535-1538.

70.   W. Gortz, B. Kempf, and J. Kretz, "*Resolution Enhanced Scanning Force Microscopy Measurements for Characterizing Dry-Etching Methods Applied to Titanium Masked Inp*", Journal of Vacuum Science & Technology B, **1995**, *13*, 34-39.

71.   K.L. Lee, D.W. Abraham, F. Secord, and L. Landstein, "*Submicron Si Trench Profiling with an Electron-Beam Fabricated Atomic Force Microscope Tip*", Journal of Vacuum Science & Technology B, **1991**, *9*, 3562-3568.

72.   M.R. Koblischka, and U. Hartmann, "*Recent advances in magnetic force microscopy*", Ultramicroscopy, **2003**, *97*, 103-112.

73.   K. Molhave, T.M. Hansen, D.N. Madsen, and P. Boggild, *"Towards pick-and-place assembly of nanostructures"*, *Journal of Nanoscience and Nanotechnology*, **2004**, *4*, 279-282.

74.   K. Molhave, D.N. Madsen, S. Dohn, and P. Boggild, *"Constructing, connecting and soldering nanostructures by environmental electron beam deposition"*, *Nanotechnology*, **2004**, *15*, 1047-1053.

75.   K.T. Kohlmann, L.M. Buchmann, and W.H. Brunger, *"Repair of Open Stencil Masks for Ion Projection Lithography by E-Beam Induced Metal-Deposition"*, *Microelectronic Engineering*, **1992**, *17*, 427-430.

76.   H.W.P. Koops, R. Weiel, D.P. Kern, and T.H. Baum, *"High-Resolution Electron-Beam Induced Deposition"*, *Journal of Vacuum Science & Technology B*, **1988**, *6*, 477-481.

77.   J. Kretz, M. Rudolph, M. Weber, and H.W.P. Koops, *"3-Dimensional Structurization by Additive Lithography, Analysis of Deposits Using Tem and Edx, and Application to Field-Emitter Tips"*, *Microelectronic Engineering*, **1994**, *23*, 477-481.

78.   K. Murakami, and M. Takai, *"Characteristics of nano electron source fabricated using beam assisted process"*, *Journal of Vacuum Science & Technology B*, **2004**, *22*, 1266-1268.

79.   O. Yavas, C. Ochiai, M. Takai, A. Hosono, and S. Okuda, *"Maskless fabrication of field-emitter array by focused ion and electron beam"*, *Applied Physics Letters*, **2000**, *76*, 3319-3321.

80.   M. Takai, T. Kishimoto, H. Morimoto, Y.K. Park, S. Lipp, C. Lehrer, L. Frey, H. Ryssel, A. Hosono, and S. Kawabuchi, *"Fabrication of field emitter array using focused ion and electron beam induced reaction"*, *Microelectronic Engineering*, **1998**, *42*, 453-456.

81.   X. Yang, M.L. Simpson, S.J. Randolph, P.D. Rack, L.R. Baylor, H. Cui, and W.L. Gardner, *"Integrated tungsten nanofiber field emission cathodes selectively grown by nanoscale electron beam-induced deposition"*, *Applied Physics Letters*, **2005**, *86*.

82.   I.W. Rangelow, T. Gotszalk, N. Abedinov, P. Grabiec, and K. Edinger, *"Thermal nano-probe"*, *Microelectronic Engineering*, **2001**, *57-8*, 737-748.

83.   H.W.P. Koops, E. Dobisz, and J. Urban, *"Novel lithography and signal processing with water vapour ions"*, *Journal of Vacuum Science & Technology B*, **1997**, *15*, 1369-1372.

84.   H.W.P. Koops, E. Munro, J. Rouse, J. Kretz, M. Rudolph, M. Weber, and G. Dahm, *"Miniature Low-Voltage Beam Systems Producable by Combined Lithographies"*, *Nuclear Instruments & Methods in Physics Research Section a-Accelerators Spectrometers Detectors and Associated Equipment*, **1995**, *363*, 1-9.

85.   H.W.P. Koops, O.E. Hoinkis, M.E.W. Honsberg, R. Schmidt, R. Blum, G. Bottger, A. Kuligk, C. Liguda, and M. Eich, *"Two-dimensional photonic crystals produced by additive nanolithography with electron beam-induced deposition act as filters in the infrared"*, *Microelectronic Engineering*, **2001**, *57-8*, 995-1001.

86.   O. Sqalli, I. Utke, P. Hoffmann, and F. Marquis-Weible, *"Gold elliptical nanoantennas as probes for near field optical microscopy"*, *Journal of Applied Physics*, **2002**, *92*, 1078-1083.

87.   P. Boggild, T.M. Hansen, C. Tanasa, and F. Grey, *"Fabrication and actuation of customized nanotweezers with a 25 nm gap"*, *Nanotechnology*, **2001**, *12*, 331-335.

88. G.C. Gazzadi, and S. Frabboni, "*Fabrication of 5 nm gap pillar electrodes by electron-beam Pt deposition*", *Journal of Vacuum Science & Technology B*, **2005**, *23*, L1-L3.

89. G. Boero, I. Utke, T. Bret, N. Quack, M. Todorova, S. Mouaziz, P. Kejik, J. Brugger, R.S. Popovic, and P. Hoffmann, "*Submicrometer Hall devices fabricated by focused electron-beam-induced deposition*", *Applied Physics Letters*, **2005**, *86*.

90. H.W.P. Koops, J. Kretz, M. Rudolph, M. Weber, G. Dahm, and K.L. Lee, "*Characterization and Application of Materials Grown by Electron-Beam-Induced Deposition*", *Japanese Journal of Applied Physics Part 1-Regular Papers Short Notes & Review Papers*, **1994**, *33*, 7099-7107.

91. K. Edinger, H. Becht, R. Becker, V. Bert, V. Boegli, M. Budach, S. Göhde, J. Guyot, T. Hofmann, O. Hoinkis, A. Kaya, H.W.P. Koops, P. Spies, B. Weyrauch, and J. Bihr, "*A novel electron-based photomask repair tool*", *Proceedings of SPIE - The International Society for Optical Engineering*, **2003**, *5256*, 1222-1231.

92. K. Edinger, H. Becht, J. Bihr, V. Boegli, M. Budach, T. Hofmann, H.W.P. Koops, P. Kuschnerus, J. Oster, P. Spies, and B. Weyrauch, "*Electron-beam-based photomask repair*", *Journal of Vacuum Science & Technology B*, **2004**, *22*, 2902-2906.

93. T. Liang, E. Frendberg, D. Bald, M. Penn, and A. Stivers "*E-beam mask repair: Fundamental capability and applications*", *Proceedings of SPIE - The International Society for Optical Engineering*, **2004**, *5567*, 456-466.

94. T. Liang, E. Frendberg, B. Lieberman, and A. Stivers, "*Advanced photolithographic mask repair using electron beams*", *Journal of Vacuum Science & Technology B*, **2005**, *23*, 3101-3105.

95. T. Liang, and A. Stivers "*Damage-free mask repair using electron beam induced chemical reactions*", *Proceedings of SPIE - The International Society for Optical Engineering*, **2002**, *4688*, 375-384.

96. T. Liang, A. Stivers, M. Penn, D. Bald, C. Sethi, V. Boegli, M. Budach, K. Edinger, and P. Spies "*Demonstration of damage-free mask repair using electron beam-induced processes*", *Proceedings of SPIE - The International Society for Optical Engineering*, **2004**, *5446*, 291-300.

97. G.F. Bahr, E.H. Zeitler, and Kobayash.K, "*High-Voltage Electron Microscopy*", *Journal of Applied Physics*, **1966**, *37*, 2900-&.

98. J.J. Trillat, and R. Merigoux, "*On the effects produced by the bombardment of a metallic surface area by fast electrons*", *Journal De Physique Et Le Radium*, **1939**, *10*, 245-249.

99. H. Akahori, "*Contamination Dependence on the Electron Beam Irradiation*", *Journal of Electron Microscopy*, **1963**, *12*, 269-270.

100. D.R. Beaman, and J.A. Isasi, "*Electron Beam Microanalysis .2. Experimental Considerations and Qualitative Analysis*", *Materials Research and Standards*, **1971**, *11*, 12-&.

101. R.L. Patterson, and C.M. Wayman, "*Study of Contamination Rates in an Electron Microscope*", *Review of Scientific Instruments*, **1963**, *34*, 1213-&.

102. G.V. Ranzetta, and V.D. Scott, "*Specimen Contamination in Electron-Probe Microanalysis and Its Prevention Using a Cold Trap*", *Journal of Scientific Instruments*, **1966**, *43*, 816-&.

103. R.W. Christy, "*Formation of Thin Polymer Films by Electron Bombardment*", *Journal of Applied Physics*, **1960**, *31*, 1680-1683.

104.   R.W. Christy, *"Conducting Thin Films Formed by Electron Bombardment of Substrate"*, Journal of Applied Physics, **1962**, *33*, 1884-&.

105.   K.H. Muller, *"Speed-Controlled Electron-Microrecorder .1"*, Optik, **1971**, *33*, 296-&.

106.   V. Scheuer, H. Koops, and T. Tschudi, *"Electron beam decomposition of carbonyls on silicon"*, Microelectronic Engineering, **1986**, *5*, 423-430.

107.   A.E. Ennos, *"The Sources of Electron-Induced Contamination in Kinetic Vacuum Systems"*, British Journal of Applied Physics, **1954**, *5*, 27-31.

108.   I. Langmuir, *"Chemical reactions at very low pressures. II. The chemical clean-up of nitrogen in a tungsten lamp"*, Journal of the American Chemical Society, **1913**, *35*, 931-945.

109.   I. Langmuir, *"Chemical reactions at very low pressures. I. The clean-up of oxygen in a tungsten lamp"*, Journal of the American Chemical Society, **1913**, *35*, 105-127.

110.   I. Langmuir, *"Chemical reactions at low pressures"*, Journal of the American Chemical Society, **1915**, *37*, 1139-1167.

111.   R.K. Hart, T.F. Kassner, and J.K. Maurin, *"Contamination of surfaces during high-energy electron irradiation"*, Phil Mag, **1970**, *12*, 453-467.

112.   H.G. Heide, *"Die Restgas zusammensetzung im Elektronenmikroskop"*, Zeitschrift für Angewandte Physik, **1963**, *XVII*, 70-72.

113.   A.T. Marshall, *"Residual-Gas Analysis in a Sem"*, Journal of Microscopy-Oxford, **1984**, *133*, 119-120.

114.   T. Takahashi, Y. Arakawa, M. Nishioka, and T. Ikoma, *"Mocvd Selective Growth of Gaasc Wire and Dot Structures by Electron-Beam Irradiation"*, Journal of Crystal Growth, **1992**, *124*, 213-219.

115.   T. Takahashi, Y. Arakawa, M. Nishioka, and T. Ikoma, *"Selective Growth of Gaas Wire Structures by Electron-Beam Induced Metalorganic Chemical Vapour-Deposition"*, Applied Physics Letters, **1992**, *60*, 68-70.

116.   M. Shimojo, S. Bysakh, K. Mitsuishi, M. Tanaka, M. Song, and K. Furuya, *"Selective growth and characterization of nanostructures with transmission electron microscopes"*, Applied Surface Science, **2005**, *241*, 56-60.

117.   R.L. Kubena, F.P. Stratton, and T.M. Mayer, *"Selective Area Nucleation for Metal Chemical Vapour-Deposition Using Focused Ion-Beams"*, Journal of Vacuum Science & Technology B, **1988**, *6*, 1865-1868.

118.   K. Gamo, and S. Namba, *"Maskless Focused Ion Beam-Assisted Deposition of Metal-Films"*, Journal of the Electrochemical Society, **1985**, *132*, C356-C356.

119.   K. Gamo, N. Takakura, N. Samoto, R. Shimizu, and S. Namba, *"Ion-Beam Assisted Deposition of Metal Organic Films Using Focused Ion-Beams"*, Japanese Journal of Applied Physics Part 2-Letters, **1984**, *23*, L293-L295.

120.   F.G. Rudenauer, W. Steiger, and D. Schrottmayer, *"Localized Ion-Beam Induced Deposition of Al-Containing Layers"*, Journal of Vacuum Science & Technology B, **1988**, *6*, 1542-1547.

121.   T. Ichihashi, and S. Matsui, *"Insitu Observation on Electron-Beam Induced Chemical Vapour-Deposition by Transmission Electron-Microscopy"*, Journal of Vacuum Science & Technology B, **1988**, *6*, 1869-1872.

122.   S. Matsui, and M. Mito, *"Si Deposition by Electron-Beam Induced Surface-Reaction"*, Applied Physics Letters, **1988**, *53*, 1492-1494.

123.   A.G. Baker, and W.C. Morris, *"Deposition of Metallic Films by Electron Impact Decomposition of Organometallic Vapours"*, *Review of Scientific Instruments*, **1961**, *32*, 458-&.

124.   H.O. Funsten, J.W. Boring, R.E. Johnson, and W.L. Brown, *"Low-Temperature Beam-Induced Deposition of Thin Tin Films"*, *Journal of Applied Physics*, **1992**, *71*, 1475-1484.

125.   J.D. Barry, M. Ervin, J. Molstad, A. Wickenden, T. Brintlinger, P. Hoffman, and J. Meingailis, *"Electron beam induced deposition of low resistivity platinum from Pt(PF3)(4)"*, *Journal of Vacuum Science & Technology B*, **2006**, *24*, 3165-3168.

126.   S. Wang, Y.M. Sun, Q. Wang, and J.M. White, *"Electron-beam induced initial growth of platinum films using Pt(PF3)(4)"*, *Journal of Vacuum Science & Technology B*, **2004**, *22*, 1803-1806.

127.   H.W.P. Koops, A. Kaya, and M. Weber, *"Fabrication and characterization of platinum nanocrystalline material grown by electron-beam induced deposition"*, *Journal of Vacuum Science & Technology B*, **1995**, *13*, 2400-2403.

128.   S. Lipp, L. Frey, C. Lehrer, E. Demm, S. Pauthner, and H. Ryssel, *"A comparison of focused ion beam and electron beam induced deposition processes"*, *Microelectronics and Reliability*, **1996**, *36*, 1779-1782.

129.   H. Morimoto, T. Kishimoto, M. Takai, S. Yura, A. Hosono, S. Okuda, S. Lipp, L. Frey, and H. Ryssel, *"Electron-beam-induced deposition of Pt for field emitter arrays"*, *Japanese Journal of Applied Physics Part 1-Regular Papers Short Notes & Review Papers*, **1996**, *35*, 6623-6625.

130.   Y.K. Park, M. Takai, C. Lehrer, L. Frey, and H. Ryssel, *"Microprobe analysis of Pt films deposited by beam induced reaction"*, *Japanese Journal of Applied Physics Part 1-Regular Papers Short Notes & Review Papers*, **1998**, *37*, 7042-7046.

131.   D.A. Bell, J.L. Falconer, Z.M. Lu, and C.M. McConica, *"Electron-Beam-Induced Deposition of Tungsten"*, *Journal of Vacuum Science & Technology B*, **1994**, *12*, 2976-2979.

132.   R.B. Jackman, and J.S. Foord, *"Electron-Beam Stimulated Chemical Vapour-Deposition of Patterned Tungsten Films on Si(100)"*, *Applied Physics Letters*, **1986**, *49*, 196-198.

133.   S. Matsui, and T. Ichihashi, *"Insitu Observation on Electron-Beam-Induced Chemical Vapour-Deposition by Transmission Electron-Microscopy"*, *Applied Physics Letters*, **1988**, *53*, 842-844.

134.   S. Matsui, and K. Mori, *"New Selective Deposition Technology by Electron-Beam Induced Surface-Reaction"*, *Journal of Vacuum Science & Technology B*, **1986**, *4*, 299-304.

135.   S. Matsui, and K. Mori, *"Insitu Observation on Electron-Beam Induced Chemical Vapour-Deposition by Auger-Electron Spectroscopy"*, *Applied Physics Letters*, **1987**, *51*, 646-648.

136.   M. Komuro, and H. Hiroshima, *"Lateral tunnel junction produced by electron-beam-induced deposition"*, *Journal of Vacuum Science & Technology B*, **1997**, *15*, 2809-2815.

137.   M. Komuro, and H. Hiroshima, *"Fabrication and properties of dot array using electron-beam-induced deposition"*, *Microelectronic Engineering*, **1997**, *35*, 273-276.

138.   F. Cicoira, P. Hoffmann, C.O.A. Olsson, N. Xanthopoulos, H.J. Mathieu, and P. Doppelt, *"Auger electron spectroscopy analysis of high metal content micro-*

structures grown by electron beam induced deposition", *Applied Surface Science*, **2005**, *242*, 107-113.

139. F. Cicoira, K. Leifer, P. Hoffmann, I. Utke, B. Dwir, D. Laub, P.A. Buffat, E. Kapon, and P. Doppelt, "*Electron beam induced deposition of rhodium from the precursor [RhCl(PF3)(2)](2): morphology, structure and chemical composition*", *Journal of Crystal Growth*, **2004**, *265*, 619-626.

140. T. Bret, S. Mauron, I. Utke, and P. Hoffmann, "*Characterization of focused electron beam induced carbon deposits from organic precursors*", *Microelectronic Engineering*, **2005**, *78-79*, 300-306.

141. S.H. Kim, and G.A. Somorjai, "*Stereospecific Ziegler-Natta model catalysts produced by electron beam-induced deposition of TiCl4: Deposition kinetics, film structure, and surface structure*", *Journal of Physical Chemistry B*, **2002**, *106*, 1386-1391.

142. S.H. Kim, C.R. Tewell, and G.A. Somorjai, "*Surface characterization of the TiClx/MgCl2 model Ziegler-Natta polymerization catalysts: Adsorption site studies using mesitylene thermal desorption*", *Langmuir*, **2000**, *16*, 9414-9420.

143. M. Takeguchi, M. Shimojo, K. Mitsuishi, M. Tanaka, and K. Furuya, "*Nanostructures fabricated by electron beam induced chemical vapour deposition*", *Superlattices and Microstructures*, **2004**, *36*, 255-264.

144. P.D. Rack, S. Randolph, Y. Deng, J. Fowlkes, Y. Choi, and D.C. Joy, "*Nanoscale electron-beam-stimulated processing*", *Applied Physics Letters*, **2003**, *82*, 2326-2328.

145. H. Jiang, C.N. Borca, B. Xu, and B.W. Robertson, "*Fabrication of 2-and 3-dimensional nanostructures*", *International Journal of Modern Physics B*, **2001**, *15*, 3207-3213.

146. D. Welipitiya, A. Green, J.P. Woods, P.A. Dowben, B.W. Robertson, D. Byun, and J.D. Zhang, "*Ultraviolet and electron radiation induced fragmentation of adsorbed ferrocene*", *Journal of Applied Physics*, **1996**, *79*, 8730-8734.

147. J.S. Foord, and R.B. Jackman, "*Studies of Adsorption and Electron-Induced Dissociation of Fe(Co)5 on Si(100)*", *Surface Science*, **1986**, *171*, 197-207.

148. J.S. Foord, and R.B. Jackman, "*Chemical Vapour-Deposition on Silicon - Insitu Surface Studies*", *Chemical Physics Letters*, **1984**, *112*, 190-194.

149. R.W. Bigelow, J.G. Black, C.B. Duke, W.R. Salaneck, and H.R. Thomas, "*Analysis of Thin-Films Arising from Electron-Beam-Induced, Ion-Beam-Induced and Photon-Beam-Induced Decomposition of Cr(Co)6 and Al(Ch3)3*", *Thin Solid Films*, **1982**, *94*, 233-247.

150. O.G. Fritz, "*Conducting Film Formed by Electron Bombardment of Tungsten Hexacarbonyl Vapour in Vacuum*", *Journal of Applied Physics*, **1964**, *35*, 2272-&.

151. U.R. Bance, I.W. Drummond, D. Finbow, E.H. Harden, and P. Kenway, "*Hydrocarbon Contamination in Vacuum Dependent Scientific Instruments*", *Vacuum*, **1978**, *28*, 489-496.

152. G. Love, V.D. Scott, N.M.T. Dennis, and L. Laurenson, "*Sources of Contamination in Electron-Optical Equipment*", *Scanning*, **1981**, *4*, 32-39.

153. R.K. Fitch, and K. Moseley, "*Evaluation of a Mcnarry-Type Omegatron on an Oil-Free High-Vacuum Pump and an Oil Diffusion Pump*", *Nuovo Cimento*, **1967**, *5*, 216-&.

154. E.M. Rudnitskii, and G.S. Selyakh, *"High-Vacuum Unit for Oil-Free Operation with Magnetic Discharge Pump"*, Instruments and Experimental Techniques, **1964** 1144-&.

155. L. Holland, *"Bakeable Ultra-High Vacuum Systems"*, Journal of Scientific Instruments, **1962**, *39*, 247-&.

156. J.A. Turner, G.R. Hoffman, and R.M. Pickard, *"Ultra-High Vacuum System"*, Journal of Scientific Instruments, **1962**, *39*, 26-&.

157. R.B. Thorness, and A.O. Nier, *"All-Metal Valve for Ultra-High Vacuum Use"*, Review of Scientific Instruments, **1961**, *32*, 807-&.

158. G. Lewin, *"Ultra-High Vacuum"*, Endeavour, **1961**, *20*, 85-&.

159. H.U.D. Wiesendanger, and R.A. Pasternak, *"An Ultra-High Vacuum System Using an Oil-Diffusion Pump with a Non-Refrigerated Isolation Trap"*, Experientia, **1960**, *16*, 467-468.

160. G.L. Munday, *"Ultra High Vacuum Technology"*, Nuclear Instruments & Methods, **1959**, *4*, 367-375.

161. M.A. Biondi, *"High-Speed Nonrefrigerated Isolation Traps for Ultra High-Vacuum Systems"*, Review of Scientific Instruments, **1959**, *30*, 831-832.

162. L.D. Hall, *"Electronic Ultra-High Vacuum Pump"*, Review of Scientific Instruments, **1958**, *29*, 367-370.

163. D.G. Bills, and F.G. Allen, *"Ultra-High Vacuum Valve"*, Physical Review, **1955**, *99*, 646-646.

164. D. Alpert, and R.S. Buritz, *"Ultra-High Vacuum .2. Limiting Factors on the Attainment of Very Low Pressure"*, Journal of Applied Physics, **1954**, *25*, 202-209.

165. H.H. Pattee, *"A Demountable Ultra-High Vacuum Joint"*, Review of Scientific Instruments, **1954**, *25*, 1132-1133.

166. J.J. Lander, *"Ultra-High Vacuum Ionization Manometer"*, Review of Scientific Instruments, **1950**, *21*, 672-673.

167. J.H. Campbell, J. Lozano, A.F. Aguilera, J.H. Craig Jr, and K.H. Pannell, *"Electron irradiation effects on digermane adsorbed on Si(100) surfaces"*, Applied Surface Science, **1997**, *108*, 345-350.

168. F. Hirose, and H. Sakamoto, *"Low-temperature Si selective epitaxial growth using electron-beam-induced reaction"*, Japanese Journal of Applied Physics Part 1-Regular Papers Short Notes & Review Papers, **1995**, *34*, 5904-5907.

169. J. Lozano, J.H. Craig Jr, and J.H. Campbell, *"A TPD, HREELS, and XPS study of electron-induced deposition of germanium on Si(100)"*, Applied Surface Science, **1999**, *137*, 197-203.

170. S. Ketharanathan, R. Sharma, P.A. Crozier, and J. Drucker, *"Electron beam induced deposition of pure, nanoscale Ge"*, Journal of Vacuum Science & Technology B, **2006**, *24*, 678-681.

171. J. Kouvetakis, R. Sharma, B.L. Ramakrisna, J. Drucker, and P. Seidler, *Electron beam assisted chemical vapour deposition of gold in an environmental TEM*, in *Film Synthesis and Growth Using Energetic Beams*, H.A. Atwater, et al., Editors. 1995. p. 323-328.

172. K. Watanabe, M. Hosoya, K. Hara, J. Yoshino, H. Munekata, and H. Kukimoto, *"Inducement of Gaas Growth by Electron-Beam Irradiation on Gaas Covered by Native-Oxide"*, Journal of Crystal Growth, **1995**, *150*, 612-615.

173. C. Schoessler, and H.W.P. Koops, "*Nanostructured integrated electron source*", *Journal of Vacuum Science and Technology B: Microelectronics and Nanometer Structures*, **1998**, *16*, 862-865.

174. H.W.P. Koops, C. Scho?ssler, A. Kaya, and M. Weber, "*Conductive dots, wires, and supertips for field electron emitters produced by electron-beam induced deposition on samples having increased temperature*", *Journal of Vacuum Science and Technology B: Microelectronics and Nanometer Structures*, **1996**, *14*, 4105-4109.

175. C. Schoessler, A. Kaya, J. Kretz, M. Weber, and H.W.P. Koops, "*Electrical and field emission properties of nanocrystalline materials fabricated by electron-beam induced deposition*", *Microelectronic Engineering*, **1996**, *30*, 471-474.

176. S. Frabboni, G.C. Gazzadi, and A. Spessot, "*TEM study of annealed Pt nanostructures grown by electron beam-induced deposition*", *Physica E-Low-Dimensional Systems & Nanostructures*, **2007**, *37*, 265-269.

177. S. Frabboni, G.C. Gazzadi, L. Felisari, and A. Spessot, "*Fabrication by electron beam induced deposition and transmission electron microscopic characterization of sub-10-nm freestanding Pt nanowires*", *Applied Physics Letters*, **2006**, *88*.

178. H. Hiroshima, N. Suzuki, N. Ogawa, and M. Komuro, "*Conditions for fabrication of highly conductive wires by electron-beam-induced deposition*", *Japanese Journal of Applied Physics Part 1-Regular Papers Short Notes & Review Papers*, **1999**, *38*, 7135-7139.

179. P.C. Hoyle, J.R.A. Cleaver, and H. Ahmed, "*Ultralow-Energy Focused Electron-Beam-Induced Deposition*", *Applied Physics Letters*, **1994**, *64*, 1448-1450.

180. M. Baker, "*Etude de la contamination dans un système de pompage*", *Le Vide*, **1967**, *127*, 22-27.

181. E.K. Brandis, "*Reduction of C contamination in the SEM*", *SEM*, **1971** 505-510.

182. T. Komoda, and N. Morito, "*Experimental Study on the Specimen Contamination in Electron Microscopy*", *Journal of Electron Microscopy*, **1960**, *9*, 77-80.

183. R. Ruhle, and E. Zehender, "*Die Beurteilung Von Objekten Im Elektronenmikroskop, Die Wahrend Der Beobachtung Geschwenkt Werden Konnen (Mit Kurzfilmen)*", *Angewandte Chemie*, **1952**, *64*, 561-561.

184. R. Ruhle, and E. Zehender, "*Die Beurteilung Von Objekten Im Elektronenmikroskop, Die Wahrend Der Beobachtung Geschwenkt Werden Konnen*", *Optik*, **1953**, *10*, 111-115.

185. E. Yoda, and B.M. Siegel, "*Reduction of Contamination in Reflection Electron Diffration*", *Journal of Applied Physics*, **1962**, *33*, 1419-&.

186. A. Folch, J. Tejada, C.H. Peters, and M.S. Wrighton, "*Electron-Beam Deposition of Gold Nanostructures in a Reactive Environment*", *Applied Physics Letters*, **1995**, *66*, 2080-2082.

187. Y. Ochiai, J. Fujita, and S. Matsui, "*Electron-beam-induced deposition of copper compound with low resistivity*", *Journal of Vacuum Science & Technology B*, **1996**, *14*, 3887-3891.

188. I. Utke, P. Hoffmann, B. Dwir, K. Leifer, E. Kapon, and P. Doppelt, "*Focused electron beam induced deposition of gold*", *J. Vac. Sci. Technol. B*, **2000**, *18*, 3168-3171.

189. P. Hoffmann, I. Utke, F. Cicoira, B. Dwir, K. Leifer, E. Kapon, and P. Doppelt, *Focused electron beam induced deposition of gold and rhodium*, in *Materials Development for Direct Write Technologies*, D.B. Chrisey, et al., Editors. 2000. p. 171-177.

190. T. Utke, B. Dwir, K. Leifer, F. Cicoira, P. Doppelt, P. Hoffmann, and E. Kapon, *"Electron beam induced deposition of metallic tips and wires for microelectronics applications"*, Microelectronic Engineering, **2000**, *53*, 261-264.

191. I. Utke, A. Luisier, P. Hoffmann, D. Laub, and P.A. Buffat, *"Focused-electron-beam-induced deposition of freestanding three-dimensional nanostructures of pure coalesced copper crystals"*, Applied Physics Letters, **2002**, *81*, 3245-3247.

192. R.R. Kunz, and T.M. Mayer, *"Electron-Beam Induced Surface Nucleation and Low-Temperature Decomposition of Metal-Carbonyls"*, Journal of Vacuum Science & Technology B, **1988**, *6*, 1557-1564.

193. T.M. Mayer, R.R. Kunz, and T.E. Allen, *"Thin-Film Nucleation and Growth Using Low-Energy Electron-Beams"*, Abstracts of Papers of the American Chemical Society, **1987**, *194*, 96-PHYS.

194. R.R. Kunz, and T.M. Mayer, *"Catalytic Growth-Rate Enhancement of Electron-Beam Deposited Iron Films"*, Applied Physics Letters, **1987**, *50*, 962-964.

195. I. Utke, T. Bret, D. Laub, P.A. Buffat, L. Scandella, and P. Hoffmann, *"Thermal effects during FEBID of nanocomposite magnetic-Co-containing tips"*, Microelectron. Eng., **2004**, *73-74*, 553-558.

196. A. Luisier, I. Utke, T. Bret, F. Cicoira, R. Hauert, S.W. Rhee, P. Doppelt, and P. Hoffmann, *"Comparative study of Cu-precursors for 3D focused electron beam induced deposition"*, Journal of the Electrochemical Society, **2004**, *151*, C590-C593.

197. M. Weber, M. Rudolph, J. Kretz, and H.W.P. Koops, *"Electron-beam induced deposition for fabrication of vacuum field emitter devices"*, Journal of Vacuum Science and Technology B: Microelectronics and Nanometer Structures, **1995**, *13*, 461-464.

198. M. Rueb, H.W.P. Koops, and T. Tschudi, *"Electron beam induced deposition in a reducing image projector"*, Microelectronic Engineering, **1989**, *9*, 251-254.

199. R. Castaing, and J. Descamps, *"Sur La Contamination Des Echantillons Dans Le Microanalyseur a Sonde Electronique"*, Comptes Rendus Hebdomadaires Des Seances De L Academie Des Sciences, **1954**, *238*, 1506-1508.

200. M.T. Postek, *"An approach to the reduction of hydrocarbon contamination in the scanning electron microscope"*, Scanning, **1996**, *18*, 269-274.

201. D. Wang, P.C. Hoyle, J.R.A. Cleaver, G.A. Porkolab, and N.C. Macdonald, *"Lithography Using Electron-Beam-Induced Etching of a Carbon-Film"*, Journal of Vacuum Science & Technology B, **1995**, *13*, 1984-1987.

202. H. Konuma, *"Rate of Carbon Contamination on Copper, Iron and Aluminum Targets in Gas-Flows by an Electron-Microprobe"*, Mikrochimica Acta, **1983**, *2*, 99-108.

203. J.S. Duerr, and R.E. Ogilvie, *"Electron-Probe Microdetermination of Carbon in Ferrous Alloys"*, Analytical Chemistry, **1972**, *44*, 2361-&.

204. G. Dupouy, F. Perrier, and L. Durrieu, *"Microscopie Electronique - Lobservation Des Objets En Milieu Gazeux - Application a Letude De La Contamination Dans Le Microscope Electronique"*, Comptes Rendus Hebdomadaires Des Seances De L Academie Des Sciences, **1962**, *254*, 3786-&.

205.   H.G. Heide, *"Elektronenmikroskopie Von Objekten Unter Atmospharendruck Oder Unter Drucken, Welche Ihre Austrocknung Verhindern"*, *Naturwissenschaften*, **1960**, *47*, 313-317.

206.   P. Hirsch, M. Kassens, M. Puttmann, and L. Reimer, *"Contamination in a Scanning Electron-Microscope and the Influence of Specimen Cooling"*, *Scanning*, **1994**, *16*, 101-110.

207.   J. Taniguchi, I. Miyamoto, N. Ohno, K. Kantani, M. Komuro, and H. Hiroshima, *"Electron beam assisted chemical etching of single-crystal diamond substrates with hydrogen gas"*, *Japanese Journal of Applied Physics Part 1-Regular Papers Short Notes & Review Papers*, **1997**, 36, 7691-7695.

208.   J. Taniguchi, I. Miyamoto, N. Ohno, and S. Honda, *"Electron beam assisted chemical etching of single crystal diamond substrates"*, *Japanese Journal of Applied Physics Part 1-Regular Papers Short Notes & Review Papers*, **1996**, *35*, 6574-6578.

209.   K. Kobashi, S. Miyauchi, K. Miyata, K. Nishimura, and J.J. Rocca, *"Etching of polycrystalline diamond films by electron beam assisted plasma"*, *Journal of Materials Research*, **1996**, *11*, 2744-2748.

210.   A.R. Taylor, C.A. Baechler, and M.A. Holcomb, *"Improved Vacuum System for Electron Microscopes"*, *Review of Scientific Instruments*, **1968**, *39*, 780-&.

211.   N. Baumgarten, *"Environmental Sem Premieres"*, *Nature*, **1989**, *341*, 81-82.

212.   P. Bonhomme, M. Troyon, C. Cheret, and Laberrig.A, *"Differential Pumping Device for Reduction of Contamination Levels in an Electron Microscope"*, *Journal of Microscopy-Oxford*, **1970**, 9, 983-&.

213.   D.C. Bishop, K.A. Emery, J.J. Rocca, L.R. Thompson, H. Zarnani, and G.J. Collins, *"Silicon-Nitride Films Deposited with an Electron-Beam Created Plasma"*, *Applied Physics Letters*, **1984**, *44*, 598-600.

214.   L.R. Thompson, J.J. Rocca, K. Emery, P.K. Boyer, and G.J. Collins, *"Electron-Beam Assisted Chemical Vapour-Deposition of Sio2"*, *Applied Physics Letters*, **1983**, *43*, 777-779.

215.   K. Nakano, T. Horie, and H. Sakamoto, *"Low-temperature growth of SiO2 films by electron-induced ultrahigh vacuum chemical vapour deposition"*, *Japanese Journal of Applied Physics Part 1-Regular Papers Short Notes & Review Papers*, **1996**, *35*, 6570-6573.

216.   E.J. Sanchez, J.T. Krug, and X.S. Xie, *"Ion and electron beam assisted growth of nanometric SimOn structures for near-field microscopy"*, *Review of Scientific Instruments*, **2002**, *73*, 3901-3907.

217.   W. Brezna, M. Fischer, H.D. Wanzenboeck, E. Bertagnolli, and J. Smoliner, *"Electron-beam deposited SiO2 investigated by scanning capacitance microscopy"*, *Applied Physics Letters*, **2006**, *88*.

218.   H.D. Wanzenboeck, M. Fischer, J. Gottsbachner, S. Mueller, W. Brezna, M. Schramboeck, and E. Bertagnolli *"Focused electron beam induced deposition of silicon dioxide"*, *ECS Transactions*, **2005**, *1*, 69-77.

219.   H.D. Wanzenboeck, M. Fischer, G. Hochleitner, W. Brezna, J. Smoliner, and E. Bertagnolli, *"High quality silicon dioxide by EBID"*, *Abstract Book of the first international workshop on electron beam induced Depsoition*, **2006**24-25.

220.   H.D. Wanzenboeck, M. Fischer, R. Svagera, J. Wernisch, and E. Bertagnolli, *"Custom design of optical-grade thin films of silicon oxide by direct-write*

electron-beam-induced deposition", *Journal of Vacuum Science and Technology B: Microelectronics and Nanometer Structures*, **2006**, *24*, 2755-2760.

221.   A. Folch, J. Servat, J. Esteve, J. Tejada, and M. Seco, "*High-vacuum versus "environmental" electron beam deposition*", *Journal of Vacuum Science & Technology B*, **1996**, *14*, 2609-2614.

222.   D.N. Madsen, K. Molhave, R. Mateiu, A.M. Rasmussen, M. Brorson, C.J.H. Jacobsen, and P. Boggild, "*Soldering of nanotubes onto microelectrodes*", *Nano Letters*, **2003**, *3*, 47-49.

223.   K. Molhave, D.N. Madsen, A.M. Rasmussen, A. Carlsson, C.C. Appel, M. Brorson, C.J.H. Jacobsen, and P. Boggild, "*Solid gold nanostructures fabricated by electron beam deposition*", *Nano Letters*, **2003**, *3*, 1499-1503.

224.   S. Kiyohara, H. Takamatsu, and K. Mori, "*Microfabrication of diamond films by localized electron beam chemical vapour deposition*", *Semiconductor Science and Technology*, **2002**, *17*, 1096-1100.

225.   J. Orloff, "*High-Resolution Focused Ion-Beams*", *Review of Scientific Instruments*, **1993**, *64*, 1105-1130.

226.   Z. Li, F. Holmes, and J. Orloff, "*Energy-Distribution Measurement of a Gallium Liquid-Metal Ion-Source Modulated at High-Frequency by a Focused Laser-Beam*", *Journal of Vacuum Science & Technology B*, **1991**, *9*, 2593-2595.

227.   L. Zhou, and J. Orloff, "*Design of a High-Resolution Focused Ion-Beam System Using Liquid-Metal Ion-Source*", *Journal of Vacuum Science & Technology B*, **1990**, *8*, 1721-1724.

228.   G. Benassayag, J. Orloff, and L.W. Swanson, "*Focused Droplet Beam from a Gold Liquid-Metal Ion-Source*", *Journal De Physique*, **1986**, *47*, 389-397.

229.   A. Stanishevsky, K. Edinger, J. Orloff, J. Melngailis, D. Stewart, A. Williams, and R. Clark, "*Testing new chemistries for mask repair with focused ion beam gas assisted etching*", *Journal of Vacuum Science & Technology B*, **2003**, *21*, 3067-3071.

230.   A.A. Iliadis, S.N. Andronescu, W. Yang, R.D. Vispute, A. Stanishevsky, J.H. Orloff, R.P. Sharma, T. Venkatesan, M.C. Wood, and K.A. Jones, "*Pt and W ohmic contacts to p-6H-SiC by focused ion beam direct-write deposition*", *Journal of Electronic Materials*, **1999**, *28*, 136-140.

231.   J. Yanagisawa, Y. Wang, T. Hada, K. Murase, and K. Gamo, "*Low-energy focused Si ion beam deposition under oxygen atmosphere*", *Nuclear Instruments & Methods in Physics Research Section B-Beam Interactions with Materials and Atoms*, **1999**, *148*, 42-46.

232.   K. Edinger, J. Melngailis, and J. Orloff, "*Study of precursor gases for focused ion beam insulator deposition*", *Journal of Vacuum Science & Technology B*, **1998**, *16*, 3311-3314.

233.   J. Funatsu, C.V. Thompson, J. Melngailis, and J.N. Walpole, "*Laser assisted focused-ion-beam-induced deposition of copper*", *Journal of Vacuum Science & Technology B*, **1996**, *14*, 179-180.

234.   J.S. Ro, C.V. Thompson, and J. Melngailis, "*Mechanism of Ion-Beam-Induced Deposition of Gold*", *Journal of Vacuum Science & Technology B*, **1994**, *12*, 73-77.

235.   Y. Takahashi, Y. Madokoro, and T. Ishitani, "*Growth of Tungsten Film by Focused Ion-Beam Induced Deposition*", *Japanese Journal of Applied Physics Part 2-Letters*, **1991**, *30*, L518-L520.

236.   T. Tao, W. Wilkinson, and J. Melngailis, "*Focused Ion-Beam Induced Deposition of Platinum for Repair Processes*", *Journal of Vacuum Science & Technology B*, **1991**, 9, 162-164.

237.   G.M. Shedd, H. Lezec, A.D. Dubner, and J. Melngailis, "*Focused Ion-Beam Induced Deposition of Gold*", *Applied Physics Letters*, **1986**, *49*, 1584-1586.

238.   K. Gamo, and S. Namba, "*Recent Advance of Focused Ion-Beam Technology in Maskless Deposition and Patterning*", *Nuclear Instruments & Methods in Physics Research Section B-Beam Interactions with Materials and Atoms*, **1991**, *59*, 190-196.

239.   C.R. Musil, J.L. Bartelt, and J. Melngailis, "*Focused Ion-Beam Microsurgery for Electronics*", *Ieee Electron Device Letters*, **1986**, *7*, 285-287.

240.   J. Melngailis, C.R. Musil, E.H. Stevens, M. Utlaut, E.M. Kellogg, R.T. Post, M.W. Geis, and R.W. Mountain, "*The Focused Ion-Beam as an Integrated-Circuit Restructuring Tool*", *Journal of Vacuum Science & Technology B*, **1986**, *4*, 176-180.

241.   J. Puretz, J. Orloff, and L. Swanson, "*An Application of Focused Ion-Beams to Electron-Beam Testing of Integrated-Circuits*", *Proceedings of the Society of Photo-Optical Instrumentation Engineers*, **1984**, *471*, 38-46.

242.   H. Ximen, R.K. Defreez, J. Orloff, R.A. Elliott, G.A. Evans, N.W. Carlson, M. Lurie, and D.P. Bour, "*Focused Ion-Beam Micromachined 3-Dimensional Features by Means of a Digital Scan*", *Journal of Vacuum Science & Technology B*, **1990**, *8*, 1361-1365.

243.   J. Melngailis, "*Focused Ion-Beam Technology and Applications*", *Journal of Vacuum Science & Technology B*, **1987**, *5*, 469-495.

244.   Y.K. Park, T. Nagai, M. Takai, C. Lehrer, L. Frey, and H. Ryssel, "*Comparison of beam-induced deposition using ion microprobe*", *Nuclear Instruments & Methods in Physics Research Section B-Beam Interactions with Materials and Atoms*, **1999**, *148*, 25-31.

245.   Z. Cui, P.D. Prewett, and J.G. Watson, "*Focused ion beam biased repair of conventional and phase shift masks*", *Journal of Vacuum Science & Technology B*, **1996**, *14*, 3942-3946.

246.   T. Liang, and A. Stivers, "*Damage-free mask repair using electron beam induced chemical reactions*", *Proceedings of SPIE - The International Society for Optical Engineering*, **2002**, *4688*, 375-384.

247.   H. Nakamura, H. Komano, K. Norimatu, and Y. Gomei, "*Silicon-Oxide Deposition into a Hole Using a Focused Ion-Beam*", *Japanese Journal of Applied Physics Part 1-Regular Papers Short Notes & Review Papers*, **1991**, *30*, 3238-3241.

248.   K. Nakamura, T. Nozaki, T. Shiokawa, K. Toyoda, and S. Namba, "*Formation of High-Resistance Region in Gaas by Ga Focused-Ion-Beam Implantation*", *Japanese Journal of Applied Physics Part 2-Letters*, **1985**, *24*, L903-L904.

249.   M. Ogasawara, M. Kariya, H. Nakamura, H. Komano, S. Inoue, K. Sugihara, N. Hayasaka, K. Horioka, T. Takigawa, H. Okano, I. Mori, Y. Yamazaki, M. Miyoshi, T. Watanabe, and K. Okumura, "*Beam induced deposition of an ultraviolet transparent silicon oxide film by focused gallium ion beam*", *Applied Physics Letters*, **1996**, *68*, 732-734.

250.   P.D. Prewett, B. Martin, A.W. Eastwood, and J.G. Watson, "*Effects of Focused Ion-Beam Reticle Repair on Optical Lithography at I-Line and Deep-Ultraviolet Wavelengths*", *Journal of Vacuum Science & Technology B*, **1993**, *11*, 2427-2431.

251. U.R. Schoffel, H. Rauscher, and R.J. Behm, *"Scanning tunneling microscope mediated nanostructure fabrication from GeH4 on Si(111)-(7x7)"*, Applied Physics Letters, **2003**, *83*, 3794-3796.

252. U.R. Schoffel, H. Rauscher, and R.J. Behm, *"Nanostructure formation by localized decomposition of Mo(CO)(6) on Si(111)-(7x7) surfaces"*, Journal of Applied Physics, **2002**, *91*, 2853-2858.

253. H. Bruckl, J. Kretz, H.W. Koops, and G. Reiss, *"Low energy electron beam decomposition of metalorganic precursors with a scanning tunneling microscope at ambient atmosphere"*, Journal of Vacuum Science & Technology B, **1999**, *17*, 1350-1353.

254. W.W. Pai, J.D. Zhang, J.F. Wendelken, and R.J. Warmack, *"Magnetic nanostructures fabricated by scanning tunneling microscope-assisted chemical vapour deposition"*, Journal of Vacuum Science & Technology B, **1997**, *15*, 785-787.

255. E.E. Ehrichs, R.M. Silver, and A.L. Delozanne, *"Direct Writing with the Scanning Tunneling Microscope"*, Journal of Vacuum Science & Technology a-Vacuum Surfaces and Films, **1988**, *6*, 540-543.

256. R.M. Silver, E.E. Ehrichs, and A.L. Delozanne, *"Direct Writing of Submicron Metallic Features with a Scanning Tunneling Microscope"*, Applied Physics Letters, **1987**, *51*, 247-249.

257. A.D. Kent, T.M. Shaw, S. Vonmolnar, and D.D. Awschalom, *"Growth of High-Aspect-Ratio Nanometer-Scale Magnets with Chemical-Vapour-Deposition and Scanning-Tunneling-Microscopy"*, Science, **1993**, *262*, 1249-1252.

258. J.A. Dagata, J. Schneir, H.H. Harary, C.J. Evans, M.T. Postek, and J. Bennett, *"Modification of Hydrogen-Passivated Silicon by a Scanning Tunneling Microscope Operating in Air"*, Applied Physics Letters, **1990**, *56*, 2001-2003.

259. J.A. Dagata, W. Tseng, J. Bennett, E.A. Dobisz, J. Schneir, and H.H. Harary, *"Integration of Scanning Tunneling Microscope Nanolithography and Electronics Device Processing"*, Journal of Vacuum Science & Technology a-Vacuum Surfaces and Films, **1992**, *10*, 2105-2113.

260. J.A. Dagata, W. Tseng, J. Bennett, C.J. Evans, J. Schneir, and H.H. Harary, *"Selective-Area Epitaxial-Growth of Gallium-Arsenide on Silicon Substrates Patterned Using a Scanning Tunneling Microscope Operating in Air"*, Applied Physics Letters, **1990**, *57*, 2437-2439.

261. G. Eres, F.Y.C. Hui, T. Thundat, and D.C. Joy, *"Direct epitaxial growth of thin-film structures"*, Journal of Vacuum Science & Technology B, **1997**, *15*, 2934-2939.

262. Y.Y. Wei, and G. Eres, *"Self-limiting behavior of scanning-electron-beam-induced local oxidation of hydrogen-passivated silicon surfaces"*, Applied Physics Letters, **2000**, *76*, 194-196.

CHAPTER 3
EXPERIMENTAL SETUPS

In this Chapter are presented the equipments that allowed the production and investigation of the structures produced.

In the last part of the chapter are presented the four different molecules used as Silicon precursors, with related properties.

3.1 Deposition Scanning Electron Microscope

3.1.1 Microscope specifications - overview

The SEM used during this thesis was a Cambridge Setereoscan S100. It was originally produced in the early 1980's, and was the first commercial SEM delivered with a turbomolecular pump. Detailed views of the machine are shown in Figure 3-1 and Figure 3-2.
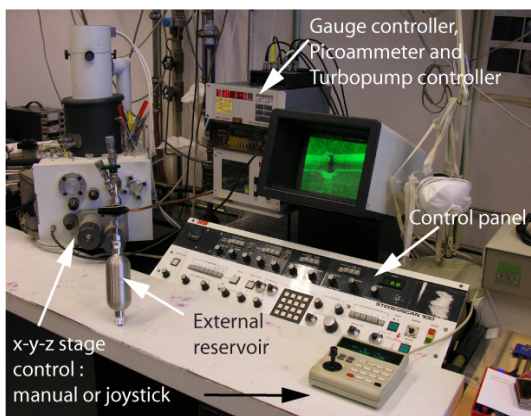

Figure 3-1: Image of the FEBID equipment
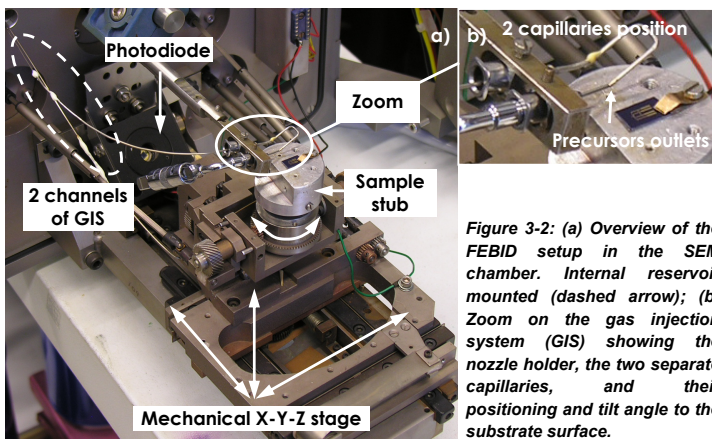
Figure 3-2: (a) Overview of the FEBID setup in the SEM chamber. Internal reservoir mounted (dashed arrow); (b) Zoom on the gas injection system (GIS) showing the nozzle holder, the two separate capillaries, and their positioning and tilt angle to the substrate surface.

The electron gun was a thermionic hairpin tungsten filament, which could be operated between 2 to 25 kV (with intermediate acceleration voltages of 3, 5, 10 and 15 kV). Operating the gun at the three lower acceleration voltages required the replacement of the anode. The FEB diameter as function of the FEB probe current was already measured at 25 kV,[1, 2] but had to be measured for 10 kV. The measurements were done with the standard knife-edge method, using a dedicated measurement device, see Figure 3-3 a). The current in the sample stub was collected as the FEB was scanned over the device; see Figure 3-3 b). The FEB profiles were extracted by derivation and fitted with Gaussians. The $1/e^2$ diameter could then be measured and is reported as function of the FEB probe current in Figure 3-3 c).
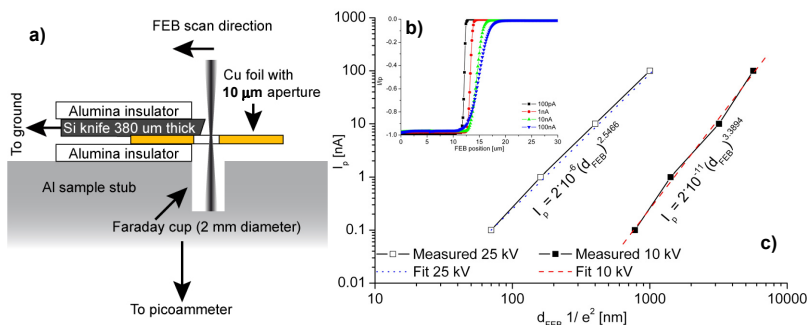
Figure 3-3: Knife-edge measurements of the FEB diameter at 10 kV. (a) Measurement device and technique; (b) experimental current vs. FEB position results for FEB currents of 0.1, 1, 10 and 100 nA; (c) FEB current Ip as function of FEB $1/e^2$ diameter for acceleration voltages of 10 and 25 kV.

This SEM was not competitive for ultra-high resolution investigations or experiments, but was perfectly suited to the physico-chemical studies of FEBID using different precursor chemistries. A two-channel custom-tailored gas injection system (GIS) was mounted and allowed for the injection of volatile compounds. The gas lines always remained at room temperature, and the precursor flows depended on their vapour pressure at the latter temperature, the GIS components dimensions, and the pumping efficiency.

3.1.2 Pumping unit

The pumping unit consisted of a dry primary membrane pump, a turbomolecular pump and a custom cryo-pumping system. The dry primary pump prevented from oil contamination in the SEM, and assured a 2 mbar vacuum. The turbopump was a lubricated pump, operated at 1000 Hz. This pumping unit assured a background pressure of $1 \cdot 10^{-6}$ mbar.

The cryo-pumping unit consisted of a liquid nitrogen trap at the primary pump inlet which condensed the molecules and prevented from chemical reactions of the injected gases with the primary pump mechanical components, see Figure 3-4 a). It was only used when the SEM was operated. However, the membranes of the pump were slowly degraded and had a lifetime of about 6 months depending on the injected gases. A second liquid nitrogen trap, a cold finger, was placed in the SEM chamber, see Figure 3-4 b). It was connected to an external LN reservoir via a liquid feed-through flange. This finger assisted the pumps during FEBID, by condensing the gaseous molecules and hence lowering the chamber pressure, to $5 \cdot 10^{-7}$ mbar.
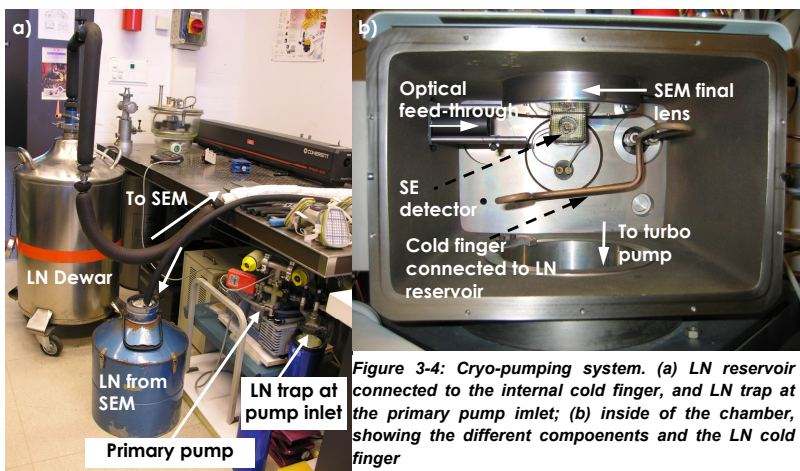
Figure 3-4: Cryo-pumping system. (a) LN reservoir connected to the internal cold finger, and LN trap at the primary pump imlet; (b) inside of the chamber, showing the different compoenents and the LN cold finger

After FEBID experiments, and prior to opening the SEM chamber, gaseous N_2 at room temperature was injected in the cold finger in order to warm it up and desorb the precursor molecules, that were then collected in the trap placed at the primary pump inlet. This prevented water condensation on the finger and operator exposition to chemicals, when opening the chamber. The liquid nitrogen consumption allowed for 7 to 8 hours of work.

3.1.3 Background vacuum composition

The composition of the background vacuum was measured with a quadrupole Residual Gas Analyzer (RGA) operating at 100 eV. RGA's do not correct for the different ionization efficiencies of the gases. However, since the electron impact cross sections of H_2O, N_2 and O_2 are comparable at this energy (2.538, 2.621 and 2.615 $Å^2$), the peak ratios were directly relate to the partial pressure ratios as first approximation. The latter appeared to be justified since the sum of mass 14 and 28 (representing N_2) were 4 times larger than the sum of pressures at mass 16 and 32 (O_2), which is the expected ratio of air composition, see Figure 3-5.

70 % of the $1 \cdot 10^{-6}$ mbar achieved without the help of liquid nitrogen traps was due to gaseous water vapour in the chamber. This value was obtained by summing the partial pressures of masses 17 and 18 (OH and H_2O). This concentration decreased to 60 % when the traps were used.
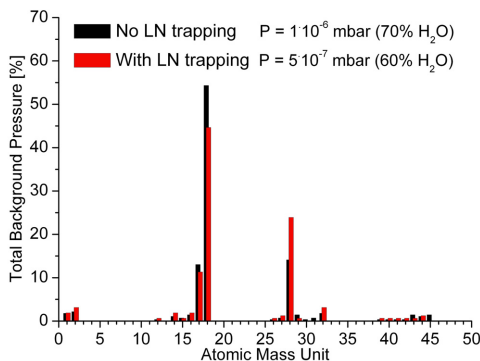
Figure 3-5: Vacuum composition as function of the use of the liquid nitrogen traps

3.1.4 Gas injection system

The gas injection system (GIS) was a custom-tailored 2 channel delivery setup. It was modified during this thesis in order to allow the simultaneous injection of controlled and oriented flows of two different gases. The nozzles delivered the molecules under an 80° angle with respect to the surface normal, and the final distance between the nozzles exit and the FEB spot was about 80 ± 10 µm. An overview of the exit nozzles positioning is presented in Figure 3-6 a).

Depending on the precursor vapour pressure, the latter was loaded either in an internal reservoir (vapour pressures < 1 mbar) or in an external reservoir, see Figure 3-6. The external reservoirs consisted of glass domes (providing visual control of the remaining level) connected to an "On/Off" security valve assuring tightness during manipulation and storage. Internal reservoirs were mounted from stainless steel components with a recipient, a tube, and a bent output. The internal reservoir was plugged in an exit nozzle, which was then manually positioned, see Figure 3-6 b), and Figure 3-7 b).
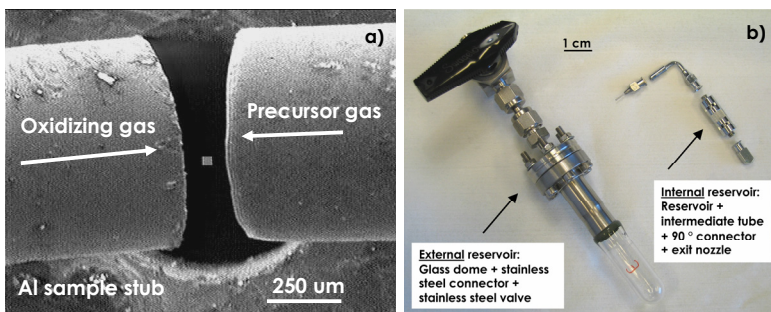
Figure 3-6: (a) SEM micrograph (top view) of the disposition of the two exit nozzles of the GIS (b) The two types of precursor reservoirs

External reservoirs were fixed to one of the two external gas lines (see Figure 3-7 a). The molecules were then brought in the SEM chamber via a gas feed-through flange, and delivered to the deposition area by one of the two stainless steel capillaries (600 / 800 µm inner / outer diameters). The capillaries exit was introduced in custom holders that were then manually positioned, see

Figure 3-7 b). Manual needle valves mounted on the external gas lines allowed to control the precursor flow injected. The precursor reservoirs were always at room temperature. A security "On/Off" valve was mounted on the precursor injection line upstream of the needle valve.
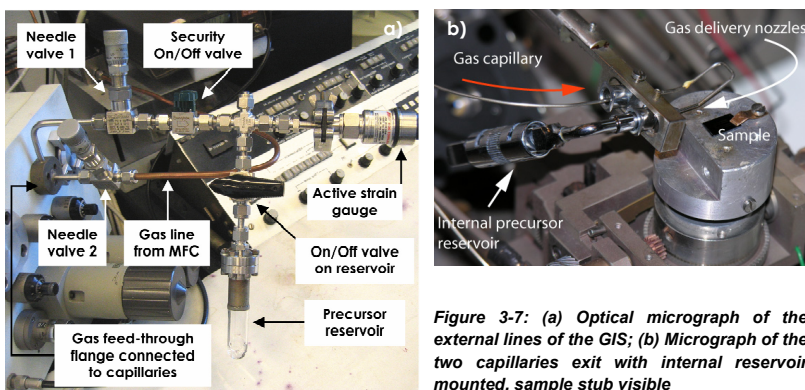
Figure 3-7: (a) Optical micrograph of the external lines of the GIS; (b) Micrograph of the two capillaries exit with internal reservoir mounted, sample stub visible

Since the needle valve conductance is gas dependent, the precursor flow as function of the needle valve aperture had to be measured for each precursor. This was done by inserting a liquid nitrogen trap after the needle valve, and condensing the molecules travelling through the GIS (see Figure 3-8). The molecule flux could then be determined by weighting the trap as function of time.

In this thesis, one of the GIS channels was used to inject organo-silane vapors and the second one to inject molecular O_2. The latter gas was controlled with a Brooks® 5850E mass flow controller (MFC, 10 sccm full scale), and the needle valve NV_2 on the Oxygen line remained 100% open. The stability of the O_2 flux was assured by the constant value displayed on the MFC controller.
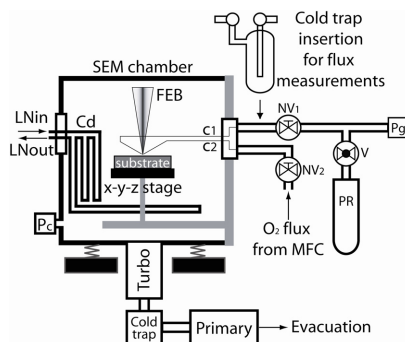
Figure 3-8: Side-cut cartoon of the FEBID SEM. NV stands for needle valve, Pc for pressure gauge chamber, Pg for pressure gauge gas line, PR for precursor reservoir, Cd for condenser and c_x for capillary

3.1.5 Contamination issues

The absence of differential pumping system allowed the injected molecules to diffuse in the gun head and column. The filament was exposed to precursor and O_2 molecules, and its lifetime varied from 2 to 6 hours, depending on the injected O_2 flows. Each new filament mounted in the gun was gradually heated over 3 hours to saturation, in order to evaporate the surface native oxide. This assured stable and reproducible emission current during the experiments. For experiments involving additional O_2, "ageing" of the filament had to be done by pulsing Oxygen in the chamber. The filament current appeared sensitive to the first three Oxygen injections, and then remained stable, see Figure 3-9.
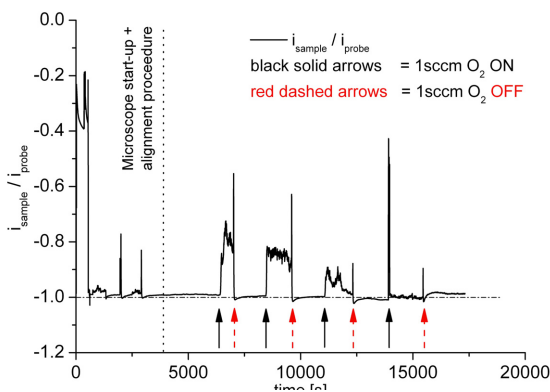
Figure 3-9: Sample current detected in a Faraday Cup as function of time and injection of Oxygen

The column was periodically cleaned (from 1 week to 1 month depending on the precursor gases) since its components got slowly coated with silica insulating films, that influenced their ideal properties and prevented from fine FEB tuning.

The chamber pressure was measured with a Penning gauge, consisting of an anode and a cathode with a 5000 V potential applied between them. Precursor molecules could diffuse between the anode and the cathode of the gauge and get decomposed by the ionization current, and the growing films slowly affected the pressure value. Hence, the anode and the cathode of the Penning gauge had to be periodically cleaned (every 2 weeks) in order to keep the pressure measurements reproducible.

3.1.6 FEB control

The FEB control was done either by using one of the built-in scan strategies (50 Hz TV scan, Line profile scan, 3 imaging scans, and spot mode), or using a lithography software installed on a secondary computer, NPGS (Nanopattern Generation Software, version 7.1), purchased from JC Nabity Lithography Systems.

The TV scan was used for large films production (micrometer scale) at different magnifications (from 1 kX to 16 kX). After tuning and aligning the FEB, the magnification was set for a given time, and the deposit was produced from the scanning FEB.

Tips were grown by setting the magnification to its maximum, and turning the spot mode on and off after a given time. The turning off had to be immediately followed by a zoom out in order to avoid parasitic depositions over the structure. NPGS was used for the production of 2 and 3 dimensional structures of complex geometries. The advantage of NPGS is the possibility of controlling all the irradiation parameters, and scanning the FEB along a specific pattern.

3.1.6.1 TV Scan

The built-in TV scan mode is a 50 Hz PAL standard. Each frame has 625 lines, which are divided in two fields, each of them having 288 active lines. The time per line is standard to the PAL system and is 69.4 µs, but the FEB is actually scanning the line only during 52 µs. The 17.4 µs remaining are used to synchronize the FEB with the electronics.

The TV scan offers the lowest dwell times on our equipment, and was used for most of the experiments. The dwell time could be determined for each magnification. As the scanned area decreases with increasing magnification, the FEB scan speed v_{FEB} decreases consequently to keep the acquisition rate constant, which leads to an increase of the dwell time. v_{FEB} is calculated by dividing the scanned line length (l_{scan}) by the time needed to scan the line.
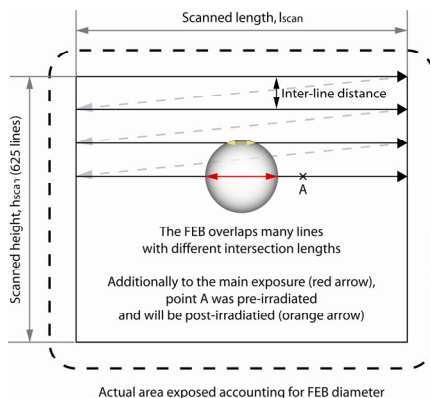
Figure 3-10: Illustration of the TV scan in strategy in the S100

This allowed determining the FEB speed at different magnifications. The total dwell time D_T of a point in the irradiated area must however consider that the FEB overlaped many different field lines due to its diameter. Each point was hence irradiated prior to and subsequent to the scan of the line to which it belonged, see Figure 3-11 . The number of overlapped lines can be calculated by dividing d_{FEB} by the inter-line distance (given by the scanned area height divided by (625*2)). D_T is hence the sum of the dwell times D_i, specific to the

relative distance of the FEB to the point considered in the area. The intersection lengths with d_{FEB} can be calculated and the resulting total dwell time determined using the v_{FEB} obtained earlier.
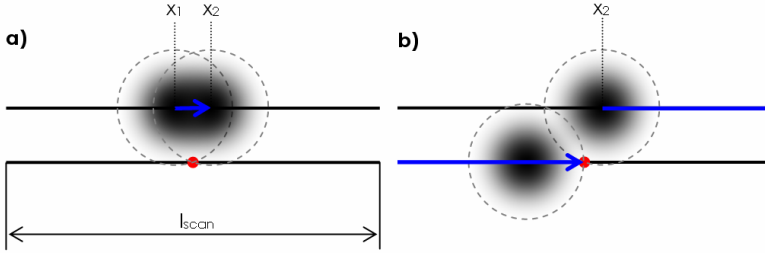
Figure 3-11: (a) Parasitic irradiation of point (red dot) due to overlap of FEB with lines, dwell time D_i and Gaussian irradiation intensity. x1 and x2 are the coordinates of the FEB center at the beginning and at the end of exposure (length of exposure showed by blue arrow). x2 – x1 = $l_{overlap}$ [µm] (b) Scan length (blue arrow) remaining after irradiation due to overlapping and next FEB scan. Length = l_{scan} – d_{FEB} + $l_{overlap}$

The dwell and replenishment times between each exposure can be expressed as:

$$D_i = \frac{4\sqrt{\left(\frac{d_{FEB}}{2}\right)^2 - l_{to\ line\ overlap}^2}}{v_{FEB}} \quad Eq.3\text{-}1$$

$$R_i = \frac{l_{scan} - d_{FEB} + l_{overlap}}{v_{FEB}} + 17.4 \quad Eq.3\text{-}2$$

The dwell time over a frame is hence a pulsed exposure, combining irradiation by electrons and replenishment times. The irradiation of a point centred in a 40 x 50 µm² rectangle scanned by a 125 nA FEB (5.8 µm diameter, Gaussian distribution) is represented in Figure 3-12.
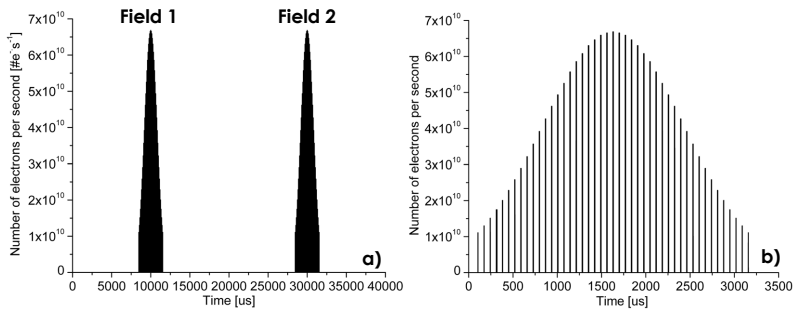
Figure 3-12: Pulsed irradiation of a point centred in a 40 x 50 μm^2 pattern during the scanning of one frame in TV mode. (a) Overview of the irradiation during the two interlaced fields, (b) zoom in irradiation during field 1. The highest irradiation corresponds to when the FEB is scanning the line on which the point is located, and the smaller ones originate from the FEB overlapping frames lines

The largest dwell times and lowest replenishment times corresponding to that of a point located on the line actually scanned by the FEB, are reported as function of the magnification, for a 10 kV 125 nA FEB in Table 3-1.

Magnification	Scanned area [μm²]	Maximum Dwell Time [μs]	Minimum Replenishment time [μs]
1 kX	100 x 80	3.02	66.38
2 kX	50 x 40	6.03	63.37
4 kX	25 x 20	12.06	57.37
8 kX	12.5 x 10	24.12	45.27
16 kX	6.25 x 5	48.24	21.14

Table 3-1: Integrated dwell times and replenishment times as function of the image magnification during constant TV scanning.

3.1.6.2 NPGS: Nano Pattern Generation Software

There are three basic steps to the pattern generation process: pattern design, parameter run file creation, and pattern writing with optional auto or semi-automatic alignment for multilevel lithography. Patterns are created using DesignCAD. Once a pattern is designed, the Run File Editor is used to record the

exposure conditions for the different drawing elements in the pattern. For each drawing layer, the following parameters may be uniquely specified in the Run File Editor:

- "Origin Offset": allows the entire pattern to be shifted

- "Magnification": must match the magnification of the SEM during exposure

- "Center-to-Center" and "Line Spacing": distance between adjacent exposure points and passes of the beam, respectively (see Figure 3-13)

- "Dwell time": exposure time of one point related to the beam current and the dose.

See Figure 3-13.
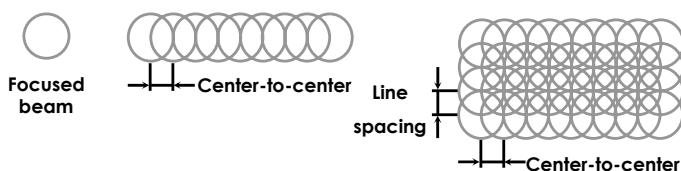
Figure 3-13: Definitions of center-to-center and line-spacing parameters. The center-to-center is the spacing along a line or arc for any orientation of the structure, and the "line spacing" is the spacing in the perpendicular direction for wide lines, arcs, or filled areas.

3.1.6.3 Alternative methods to scan the FEB

Patterns could also be produced by scanning the sample instead of the FEB itself. A "stick - slip" table, based on piezo-actuators, allowed for nanometrical displacements on two axis. Patterns could be defined on the computer interface together with the scanning parameters.

3.1.7 SEM operation protocol

Prior to any experiment, the oxygen gas line was connected from the MFC to the needle valve, and the precursor reservoir connected to its specific gas line. The two needle valves were opened and the system was left to pump through the night, in order to evacuate the gas lines from residual gases. The pressure

obtained after the night was $1 \cdot 10^{-6}$ mbar, which indicated that the gas line were tight and the experiments could be performed.

3.1.8 In situ control tools during operation

3.1.8.1 Current monitoring

Developed by a former PhD student, this tool allowed monitoring the sample current in real time during any deposition process. It is based on the fact that the secondary and backscattering yields depend both on the material and the topography of the structures. The deposition of a material or the selective etching of a material of a multilayer substrate will induce changes in the current absorption efficiency. The evolution of the sample current contains the information related to these changes, and gives hence information about the FEB induced process.[3]

3.1.8.2 Co-aligned Ar⁺ laser beam

A 514 nm wavelength beam of an Ar⁺ laser could be co-aligned with the FEB in the SEM chamber.[4] The laser was installed on a separate anti-vibration table, and a monomode optical fibre brought 40% of the laser power to an optical feed-through in the side-wall of the SEM chamber, see Figure 3-14. After a warm-up time of 30 to 45 minutes, the alignment remained stable.

Outside the chamber, two lenses collimated the laser beam in order to lower the beam divergence. An optical setup was installed in the SEM chamber that channelled the light to the FEB spot by total reflections in prisms. Finally, the light was reflected and deviated to the sample surface by a mirror (incidence angle of 45°), and a final lens produced a $10 \times 15\ \mu m^2$ spot on the sample (measured by knife-edge).
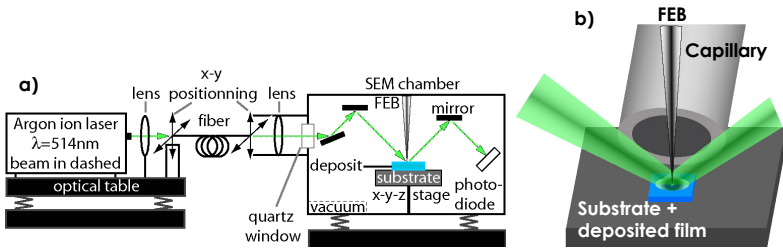
Figure 3-14: Co-focused Ar⁺ laser beam with FEB. (a) side view of the system; (b) 3D representation of the system

Ink spots were used as markers in order to fine-tune the laser spot position. The spots produced with black pens could be locally melt and marked using a 200 mW power laser beam. The vertical position of the laser spot could be varied by changing the sample height, whereas the lateral position could be tuned by varying the fiber exit position using its x-y fine positioning. After reflection on the sample, the beam was sent to a photodiode by a reflection on a horizontal mirror fixed to the last electron lens. The reflectivity of large growing deposits (at magnification 1 kX) was monitored *in-situ* with usually a 50 mW laser power. The power incident on the sample was 2.5 mW due to the coupling losses and multiple reflections. The temperature increase induced was negligible. In order to prevent from damaging the scintillator, the latter was turned off when light was injected in the chamber. The Optical setup is shown in Figure 3-15.
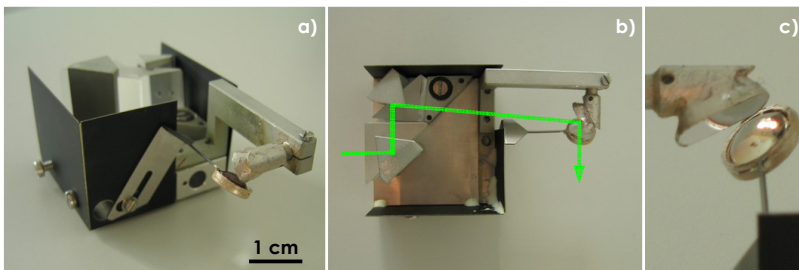
Figure 3-15: Optical setup for in situ reflectometry. (a) Overview; (b) Top view with optical path highlighted; (c) zoom on the last focusing lens assuring a spot size of 10 x 15 μm^2.

3.2 Ex–situ analysis techniques

After FEBID experiments, the SEM was vented with dry N_2, and the samples taken out with no particular protection against ambient air. The produced structures were characterized optically, chemically, and topographically by various μ-probe *ex-situ* analyses.

3.2.1 Thickness measurement / Surface topography

Thickness line profiles of films could be measured using a standard Tencor Alphastep stylus profilometer see Figure 3-16 a). The stylus had a diameter of 50 um, and an apex curvature of 10 μm approximately. Three-dimensional accurate topography imaging of structures smaller than 100 x 100 μm² was performed with a Nanosurf® atomic force microscope (AFM), see Figure 3-16 b). The AFM head could scan ranges up to 100 um with a nanometer axial resolution. It is piloted by computer. The sample positioning is done manually by two micrometric screws, and visual feed-back. Investigations could only be performed in contact mode with this AFM.
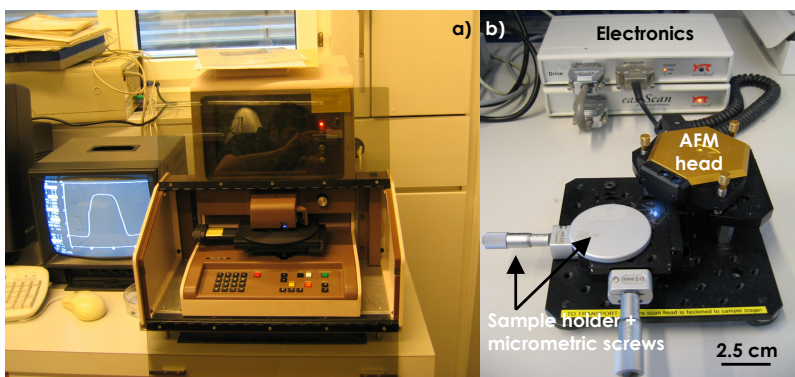
Figure 3-16: (a) Stylus profilometer for 2-D profiling; (b) High-resolution AFM for topographical imaging

3.2.2 Optical observation

Basic optical observations (up to 1 kX magnification) of the structures produced were done on an optical microscope (Zeiss Axiotech Vario 25 HD), see Figure 3-17. A CCD camera coupled with an acquisition software installed on a computer allowed to save micrographs of the structures in transmission mode, reflection mode (for which bright and dark field modes were available), and differential interferometric contrast mode (for which a additional polarizer had to be placed in the optical path of light).
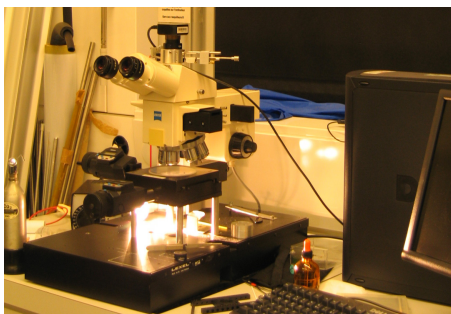
Figure 3-17: Optical Microscope for ordinary optical investigations

3.2.3 High resolution imaging – Chemical composition

High resolution imaging was run in field–emission–gun SEMs (FEI XL 30 FEG and XL 30 SFEG) installed in the Interdisciplinary Centre for Electron Miscroscopy (EPFL), see Figure 3-18 a). These microscopes offer respectively 25 and 5 nm resolution and various sample tilting and rotation possibilities. These SEMs are equipped for back scattering and secondary electron imaging. Chemical compositions of the FEBID materials were measured in the same SEMs since they are equipped with Electron Dispersive X-ray Spectroscopy (EDX) systems (Noran® Six for the FEG and Inca® for the SFEG).
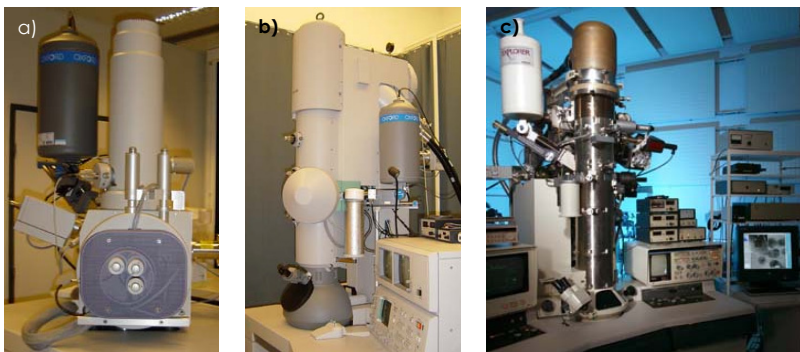
Figure 3-18: Microscope facilities in CIME. (a) XL 30 SFEG; (b) CM 300; (c) HF 2000

Higher resolution imaging and EDX investigations took place in transmission electron microscopes (TEM) after sample preparation, mainly in a FEI CM–300 TEM, operated at 300 kV. Ultrahigh resolution TEM, scanning TEM (STEM) and Electron Energy Loss Spectroscopy (EELS) analyses were done in a Hitachi HF– 2000, operated at 200 kV. TEM analyses were performed by a staff person from CIME, see Figure 3-18 b) and c).

3.2.4 Infrared Spectroscopy

Microscopic Fourier Transform Infrared Spectroscopy (μ–FTIR) was performed in a Perkin Elmer Spotlight 300 infrared microscope, installed in the Powder Technology Laboratory, EPFL. The wavenumber scale available is 500 to 4000 cm^{-1}. The microscope allows for investigations in reflection mode and in Attenuated Total Internal Reflection (ATR) mode. Resolution of a few micrometers is achievable. The investigation standard window size was usually 80 x 80 um^2, which allowed avoiding border effects. Each spectrum was taken with an average of 128 measurements.

3.2.5 X-Ray photoelectron spectroscopy

X-Ray Photoelectron spectroscopy measurements were performed with an Axis Ultra from Kratos, equipped with a monochromatic aluminum X-Ray (Al Kα)

source. The investigations were done using a 15 kV beam of 10mA current and a circular aperture (100 μm in diameter) centered and included in the deposit. The sample surface was cleaned by Argon ion sputtering (30 s, 2 kV) prior to each quantitative measurement. The equipment is located in the Metallurgical Chemistry Laboratory, EPFL.

3.2.6 Deep Ultraviolet Optical Transmission

The 193 nm wavelength optical transmission of the deposited materials was measured using an Aerial Measurement Investigation Standard (AIMS) MSM 193 (Zeiss), see Figure 3-19. It consists of a 193 nm wavelength excimer Ar-F laser, coupled to a DUV optical microscope. It is controlled by computer, and the software allows recording map images of the optical transmission through structures.

Figure 3-19: AIMS MSM 193 installed at NRG

3.3 Organosilane precursors

Different organosilane precursors were used as Silicon source during this work. They were chosen as function of their properties such as vapour pressure at room temperature, sticking coefficient, and molecular formula. The four molecules that were extensively studied during this thesis are reported in Table 3-2.

Name	Abbreviation	CAS N°	Molecular Formula
Tetraisocyanatosilane	TICS	3410–77–3	$Si(NCO)_4$
Tetraethoxysilane	TEOS	78–10–4	$Si(OCH_2CH_3)_4$
Tetramethoxysilane	TMOS	681–84–5	$Si(OCH_3)_4$
Tetramethylsilane	TMS	75–76–3	$Si(CH_3)_4$

Table 3-2: Main Silicon precursors used

Some properties of the above mentioned molecules are reported in Table 3-3.

Name	Pvap [mbar] @ 23 °C	Bp [°C]	Mp [°C]	C : Si	O : Si	H : Si	N : Si	Physical form @ 23 °C
TICS	1.3	186	28	4	4	0	4	Solid - Liquid
TEOS	2.2	169	-77	8	4	20	0	Liquid
TMOS	16	121	-2	4	4	12	0	Liquid
TMS	887	27	-99	4	0	12	0	Liquid

Table 3-3: Main properties of the chosen precursors

TEOS and TMOS belong to the alkoxysilanes, which are widely used in Chemical Vapor Deposition processes for the production of pure SiO_2 films. These two molecules were chosen since they appear to be suited candidates for CVD and PECVD of SiO_2. However, the decomposition pathways are complex, and side reactions such as oligomerisation are unavoidable.[5-10] In CVD and PECVD processes, TMOS requires more energy to be decomposed in SiO_2 than TEOS. TEOS leads to larger deposition rates.[11, 12] Since TMOS contains half the number of Carbon atoms of TEOS, it was interesting to compare the two molecules.

On the contrary of alkoxysilanes, alkylsilanes are Oxygen-free molecules. They are considered to be intermediate molecules between silanes and organosilanes molecules. They are generally used for the deposition of partially hydrogenated SiC films.[13-15] They however require less Oxygen and lower energies to be decomposed in SiO_2.[16] The decomposition pathways are less complex than that of TEOS and TMOS, since simpler and more reactive intermediate products are formed.[17-22] TMS does not polymerize with its own monomers, and oligomerisation reactions are avoided, as well as SEM contaminations.

TICS is a modern molecule, first synthesized in 1940.[23] It is part of the isocyanates family. The interesting properties of this molecule are: Hydrogen-free, and Oxygen containing, but it contains only Si-N bonds, that are weaker than Si-O. It requires very low energy to be decomposed to SiO_2, in presence of water, compared to TMS, TEOS and TMOS.[24-26] It was already applied to the deposition of SiO_2 films by CVD at temperatures as low as 100 °C.[27] The films deposited were Hydrogen free.

With respect to the molecules boiling point, representative of the evaporation enthalpy of a molecule adsorbed on the same molecule, TICS is expected to have the largest sticking coefficient, in front of TEOS, TMOS and TMS.

3.4 Precursor manipulation

The different silicon precursors used have different toxicities and sensitivities to moisture: TMOS and TICS are lethal; TMOS and TEOS hydrolyze with moisture. For all these reasons, all the precursors were stored and manipulated in a dry N_2 atmosphere of a glove box, Figure 3-20 a). The glove box was let to purge till the relative humidity in the chamber had decreased below 0.01 %. The precursors where kept in the glove box in order to prevent from accidental exposure to moisture.

A custom vacuum system was mounted, that allowed the transfer of gaseous precursors from their original cylinder into their specific reservoir, see Figure 3-20 b). The latter setup is based on a condensation mechanism: the precursor cylinder and the precursor reservoir are mounted on the setup. The system is evacuated by using a primary pump, until the reservoir and cylinder limits. The pump is then isolated, and the precursor reservoir is cooled using a slurry. The valve to the precursor cylinder is then opened in the same time than the valve of the reservoir, so that the molecules condense in the reservoir. The valves were closed after a given time.
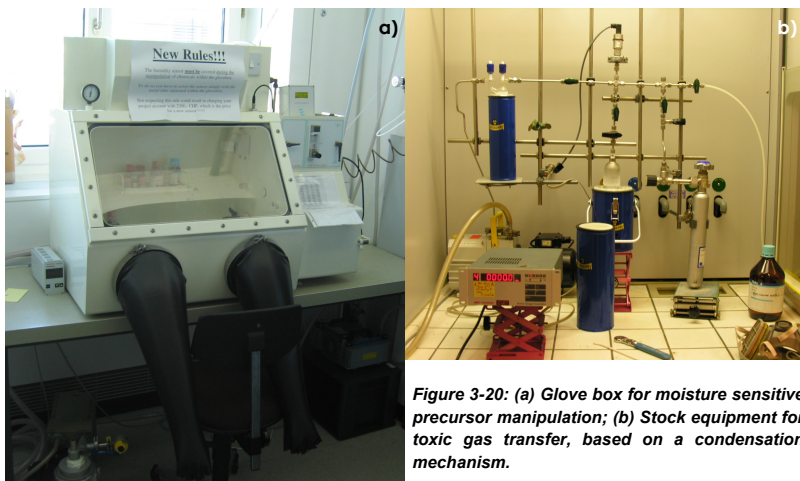
Figure 3-20: (a) Glove box for moisture sensitive precursor manipulation; (b) Stock equipment for toxic gas transfer, based on a condensation mechanism.

Although the purest compounds were purchased, they still contained dissolved gases from the production steps. The liquid precursors could be purified by an average of seven freeze-pump-thaw cycles. Usually, no gas bubbles were observed by eye after 4 cycles, three were additionally added for security. The reservoir was then mounted on the microscope GIS precursor line.

3.5 Bibliography of Chapter 3

1.   T. Bret, *Physico-chemical Study of the Focused Electron Beam Induced Deposition Process*. 2005, EPFL: Lausanne. p. 238.

2.   F. Cicoira, *Electron Beam Induced Deposition of Rhodium Nanostructures*. 2002, EPFL: Lausanne. p. 165.

3.   T. Bret, I. Utke, A. Bachmann, and P. Hoffmann, "*In situ control of the focused-electron-beam-induced deposition process*", *Applied Physics Letters*, **2003**, *83*, 4005-4007.

4.   A. Perentes, T. Bret, I. Utke, P. Hoffmann, and M. Vaupel, "*Real-time reflectometry-controlled focused-electron-beam-induced deposition of transparent materials*", *Journal of Vacuum Science & Technology B*, **2006**, *24*, 587-591.

5.   M. Hirota, N. Saito, T. Ishizaki, and A. Fuwa, "*Theoretical analysis for thermal chemical vapor deposition from Tetraethoxysilane using a semi-empirical molecular orbital method*", *Nippon Kinzoku Gakkaishi/Journal of the Japan Institute of Metals*, **1999**, *63*, 931-937.

6.   K. Okuyama, T. Fujimoto, T. Hayashi, and M. Adachi, "*Gas-phase nucleation in the tetraethylorthosilicate (TEOS)/O3 APCVD process*", *AIChE Journal*, **1997**, *43*, 2688-2697.

7.   J.H. Lee, D.S. Kim, and Y.H. Lee, "*Room temperature deposition of silicon dioxide films by ion-assisted plasma enhanced chemical vapor deposition*", *Journal of the Electrochemical Society*, **1996**, *143*, 1443-1451.

8.   E.J. Kim, and W.N. Gill, "*Low pressure chemical vapor deposition of silicon dioxide films by thermal decomposition of tetra-alkoxysilanes*", *Journal of the Electrochemical Society*, **1995**, *142*, 676-682.

9.   B.G. Todd, J.B. Hudson, and P.K.C. Wu "*Decomposition kinetics of tetraethoxysilane on SiO2*", *Materials Research Society Symposium Proceedings*, **1993**, *282*, 543-548.

10.   M.L.P. da Silva, and J.M. Riveros, "*A comparative study of gas-phase ion/molecule reactions in Si(OCH3)(4) and Si(OC2H5)(4)*", *International Journal of Mass Spectrometry*, **1997**, *165*, 83-95.

11.   K.H.A. Bogart, S.K. Ramirez, L.A. Gonzales, G.R. Bogart, and E.R. Fisher, "*Deposition of SiO2 films from novel alkoxysilane/O-2 plasmas*", *Journal of Vacuum Science & Technology a-Vacuum Surfaces and Films*, **1998**, *16*, 3175-3184.

12.   E.J. Kim, and W.N. Gill, "*Low-Pressure Chemical-Vapor-Deposition of Silicon Dioxide Films by Thermal-Decomposition of Tetra-Alkoxysilanes*", *Journal of the Electrochemical Society*, **1995**, *142*, 676-682.

13.   M. Veres, M. Koo?s, N. Orso?s, S. To?th, M. Fu?le, M. Mohai, and I. Berto?ti, "*Incorporation of Si in a-C:Si:H films monitored by infrared excited Raman scattering*", *Diamond and Related Materials*, **2006**, *15*, 932-935.

14.   M. Shajahan, Y.H. Mo, and K.S. Nahm "*Growth of SiC nanorods and microcrystals by carbon nanotubes-confined reaction*", *Materials Science Forum*, **2004**, *457-460*, 329-332.

15.   M. Shajahan, Y.H. Mo, A.K.M.F. Kibria, K.C. Kim, K.S. Nahm, and E.K. Suh, *"Low-temperature RTCVD growth and characterization of silicon-carbide nanorods through carbon nanotubes"*, Journal of the Korean Physical Society, **2002**, *41*, 789-794.

16.   K.V. Guinn, and J.A. Mucha *"Chemical vapor deposition of SiO2 from ozone-organosilane mixtures near atmospheric pressure"*, Materials Research Society Symposium Proceedings, **1993**, *282*, 575-580.

17.   X.M. Li, B.D. Eustergerling, and Y.J. Shi, *"Mass spectrometric study of gas-phase chemistry in a hot-wire chemical vapor deposition reactor with tetramethylsilane"*, International Journal of Mass Spectrometry, **2007**, *263*, 233-242.

18.   R.C. Sharma, and M. Koshi, *"Hot filament-dissociation of (CH3)3SiH and (CH3)4Si, probed by vacuum ultra violet laser time of flight mass spectroscopy"*, Spectrochimica Acta - Part A: Molecular and Biomolecular Spectroscopy, **2006**, *65*, 787-791.

19.   G.A. Zaharias, H.L. Duan, and S.F. Bent, *"Detecting free radicals during the hot wire chemical vapor deposition of amorphous silicon carbide films using single-source precursors"*, Journal of Vacuum Science and Technology A: Vacuum, Surfaces and Films, **2006**, *24*, 542-549.

20.   J.L. Jauberteau, I. Jauberteau, and J. Aubreton, *"Intermediate species in a 2.45 GHz microwave plasma sustained in an argon-tetramethylsilane gas mixture"*, International Journal of Mass Spectrometry, **2003**, *228*, 49-59.

21.   M.A. Bica de Moraes, S.F. Durrant, and F.P. Rouxinol, *"Electron emission enhanced chemical vapor deposition (EEECVD) for the fabrication of diverse silicon-containing films"*, Thin Solid Films, **2001**, *398-399*, 591-596.

22.   R. Basner, R. Foest, M. Schmidt, F. Sigeneger, P. Kurunczi, K. Becker, and H. Deutsch, *"Electron impact ionization of tetramethylsilane (TMS)"*, International Journal of Mass Spectrometry and Ion Processes, **1996**, *153*, 65-78.

23.   G.S. Forbes, and H.H. Anderson, *"Cyanates of silicon, phosphorus and boron. instability of certain ternary boron compounds"*, Journal of the American Chemical Society, **1940**, *62*, 761-763.

24.   I. Idris, and O. Sugiura, *"Hydrogen-Free Plasma-Enhanced Chemical-Vapor-Deposition of Silicon Dioxide Using Tetra-Isocyanate-Silane (Si(Nco)(4))"*, Japanese Journal of Applied Physics Part 2-Letters, **1995**, *34*, L772-L774.

25.   I. Idris, and O. Sugiura, *"Film characteristics of low-temperature plasma-enhanced chemical vapor deposition silicon dioxide using tetraisocyanatesilane and oxygen"*, Japanese Journal of Applied Physics Part 1-Regular Papers Short Notes & Review Papers, **1998**, *37*, 6562-6568.

26.   S. Wickramanayaka, Y. Nakanishi, and Y. Hatanaka, *"On the chemistry of a-SiO2 deposition by plasma enhanced CVD"*, Applied Surface Science, **1997**, *114*, 670-674.

27.   H. Taniguchi, and O. Sugiura, *"Low-Temperature Chemical-Vapor-Deposition of Silicon Dioxide Using Tetra-Isocyanate-Silane (Si(Nco)(4))"*, Japanese Journal of Applied Physics Part 2-Letters, **1994**, *33*, L1485-L1488.

PREAMBLE TO CHAPTERS 4, 5, 6 AND 7

The role of this preamble is to give the reader a general overview of the global deposition mechanism underlying O_2 assisted FEBID, summarizing the results of Chapters 4, 5, 6 and 7. The O_2 assisted FEBID involves flows of four different entities: precursor molecules, additional Oxygen molecules, residual gases molecules and electrons. The determination of the deposition mechanism required to independently study the influence of each of these flows on the deposition process.

Additional Oxygen influenced strongly the chemical composition of the FEBID material deposited, by decreasing the C content down to zero above a $[O_2]/[precursor]$ threshold ratio, specific to each molecule (Chapter 4). The growth rates were affected as well, and were either decreased (factor of 0.6) or increased (factors up to 7) till a saturation value, as function of the precursor reactivity to O_2 (Chapters 5 and 6). These effects are shown in Figure P-1, in the case of an increase of growth rate with Oxygen.
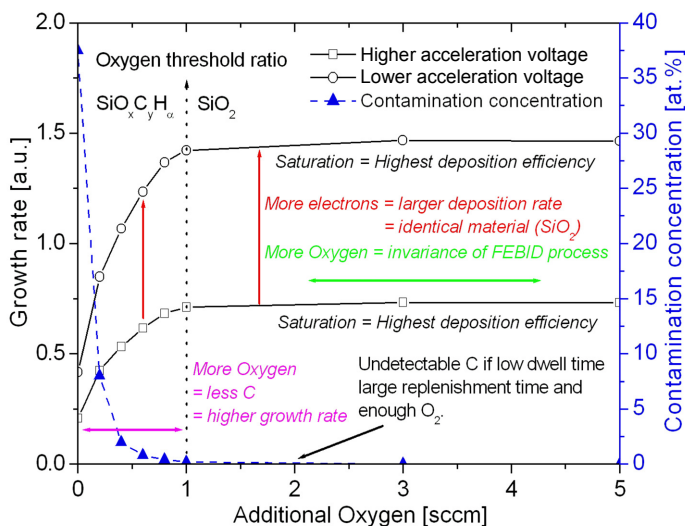
Figure P-1: O_2 assisted FEBID mechanism, showing the growth rate and contamination concentration as function of additional Oxygen in the case of an increase of growth rate

Contamination free materials could be obtained from all tested organosilanes. Under suited dwell and replenishment times (respectively below 15 and above 60 µs in our setup), the threshold O_2 flow depended on the precursor chemistry and flow only, and was not influenced by the electron flow. The SiO_2 obtained was stoichiometric, amorphous, had an approximated density of 2.2 and was used for optical applications.

These results indicated a change in the deposition mechanism. O_2 assisted FEBID required less amount of energy to induce a decomposition reaction. Unlike conventional FEBID, O_2 assisted FEBID was independent of the electron density in our setup and the deposition rates obtained for pure SiO_2 films were proportional to the number of secondary electrons emitted from the substrate. For the first time, the role of the different electron types could be separated. Secondary electrons were demonstrated to achieve 90% of the deposition process, and their efficiency was multiplied by factors up to 20 (compared to conventional FEBID) in presence of Oxygen. The FEB parameters for the highest SiO_2 deposition rates were low acceleration voltage and low density of electrons. The deposition rates were electron limited.

The co-adsorption of O_2 and precursor molecules on the surface followed a competition coverage process (Chapter 6). The resulting steady state surface occupation as function of additional Oxygen and precursor flows ruled the deposition process in terms of growth kinetics and chemical composition deposited, and was responsible for the exponential behaviours of the contamination concentration and growth rates observed in Figure P-1. This competition also influenced the growth dynamics when varying the precursor flows. The oxidation efficiency was hence dependent of the precursor adsorption enthalpy and chemical reactivity.

Residual water was demonstrated to be active during conventional FEBID processes. Comparison of experimental deposition yields with impinging flows demonstrated that residual water was responsible for Oxygen incorporation and ruled the deposition process in absence of Oxygen. During O_2 assisted FEBID, Oxygen molecules were the main oxidizing agent.

CHAPTER 4
μ–Characterization of FEBID Materials

The first step of the study consisted in depositing materials by keeping the precursor and the electron flows constant, and varying the Oxygen flow. This chapter reports the characterization by standard micro-probe techniques, of the chemical composition and etch rate, optical properties at DUV and visible wavelengths, and atomic sub-structure of the materials obtained as function of the additional Oxygen flow.

It is shown that adding molecular Oxygen simultaneously to the organosilane vapours during the FEBID process allowed gradually turning the $SiO_xC_yH_\alpha$ material obtained from the precursor vapours alone, to stoichiometric SiO_2, above a [O_2]/[precursor] ratio specific to each precursor. The pure silica produced was OH and C free, had an intermediate density (2.2), was amorphous, and sufficiently transparent at 193 nm wavelength to be used to DUV applications. It and presented a similar refractive index than fused silica at 514 nm wavelength as well.

The *elements concentration vs. additional Oxygen* measured highlighted a surface competition mechanism. The chemical composition of the deposited film was influenced by the dwell and replenishment times (further discussed in Chapter 5), and the results presented here were produced by operating the SEM at 2 kX (dwell time of 6 μs and replenishment time of 63 μs), which appeared suited in terms of deposition time, and which produced films that could be investigated with standard micro-probe analysis techniques (which require a minimum interaction volume of a few cubic micrometers with the structure). The SEM was operated at 10 kV, with a relatively high current of 125 nA (diameter 5.8 μm). Deposition times varied between 15 and 120 minutes.

4.1 Chemical compositions obtained from O_2 assisted FEBID

The chemical compositions were determined using five different and complementary micro-probe techniques: Electron Dispersive X-Ray Spectroscopy (EDX), Fourier Transform Infrared Spectroscopy (FTIR), X-Ray Photoelectron Spectroscopy (XPS), Elastic Recoil Detection Analysis (ERDA) and Nuclear Reaction Analysis (NRA). All the results presented in this chapter were produced with the precursor flows reported in Table 4-1. These values are an average of three different measurements of precursor consumption, and were chosen since they allowed reasonable deposition times. The effect of additional Oxygen flow was however identical for all the precursor flows tested (see Appendix 1), and the trends presented here are general.

Precursor	Injected Flow [molecules·cm^{-2}s^{-1}]	Reservoir type
TEOS	$5.3 \cdot 10^{19}$	external
TMOS	$8.8 \cdot 10^{20}$	external
TMS	$2.5 \cdot 10^{20}$	external
TICS	$8.5 \cdot 10^{17}$	internal

Table 4-1: Precursor flows used for the experiments

A typical large area deposit obtained is shown in Figure 4-1, with the standard investigation steps performed before any micro-probe analysis.
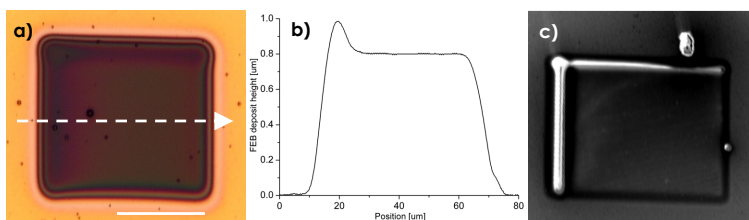
Figure 4-1: Basic investigations before EDX analyses. White bar represent 25 μm.
(a) Optical microscopy showing the thickness gradient due to TV scan; (b) Profilometer thickness measurement. Typical line profile (corresponding to the dashed arrow in (a); (c) SEM imaging for fine positioning of the investigation

The deposits surface appeared always smooth. The gold surface contained eventually grains originating form the evaporation step. The μ-analysis locations were carefully selected at places where the surface was uniform and flat.

4.1.1 Electron Dispersive X-Ray spectroscopy (EDX)

EDX was used to roughly estimate (± 5 at.%) the chemical composition of the FEBID materials. Element specific X–Rays are generated by the interactions of a FEB with matter, and are counted as function of their energy, which allows determining the elements present in the material and their respective weight and atomic concentrations. It is a rapid technique, which gives results representative of a volume corresponding to the electron range of the electrons in the material (see Appendix 5).

In order to decouple elements from the films deposited from that of the substrate, the films were deposited on Au-coated (500 nm) Si substrates. Au was an element that should not be present in the deposited films. EDX investigations were performed at 5 keV since this energy allowed exciting the Kα lines of Si, O, and C, but also the M line of the underlying Au substrate, if the FEBID film thickness was thin enough. In order to contain the entire excitation volume of the 5 kV FEB, the films had to be at least 300 nm thick. This limit thickness was determined by means of Monte Carlo simulations, taking a low density of 2.0 for the Si-containing material, see Figure 4-2. Whenever Au was detected, the results were not accounted for, since the quantifications of the elements concentration were obviously incorrect, due to the account of elements present at the Au-deposit interface.
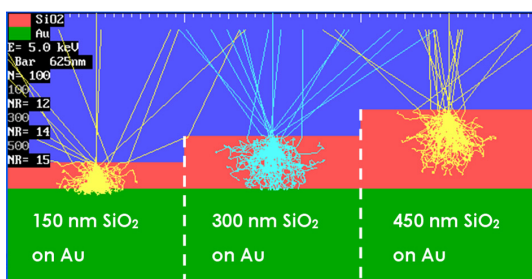
Figure 4-2: Monte-Carlo simulations of the penetration of 5 keV electrons in 150, 300 and 450 nm thick SiO$_2$.

Prior to acquiring a spectrum, the software was calibrated using a bulk Si sample, and the irradiation conditions were finely tuned, which allowed setting the X-Ray detector dead time to its optimal value of 12 %, and lower the

quantification error bars to ± 2 at%. Elemental concentrations below 1 at.% were not considered by the software factory settings, which was problematic for the quantification of elements present with lower concentrations. In these situations, the presence of the elements was imposed to the software and the respective concentration calculation could be performed with the same error than for heavier elements. Cross-investigations with different analysis techniques showed that the elements could be considered absent of the material for EDX concentrations of 0.5 at.%.

Series of films were produced using TEOS, TMOS, TMS and TICS and varying additional O_2 flow. The chemical compositions of the deposited materials as function of the $[O_2]/[precursor]$ ratio are presented in Figure 4-3. The deposits chemical composition was not function of the FEB acceleration voltage and current parameters (see Chapter 5, pp. 5-7), but was influenced by the dwell and replenishment times (see Chapter 5, pp. 5-15).
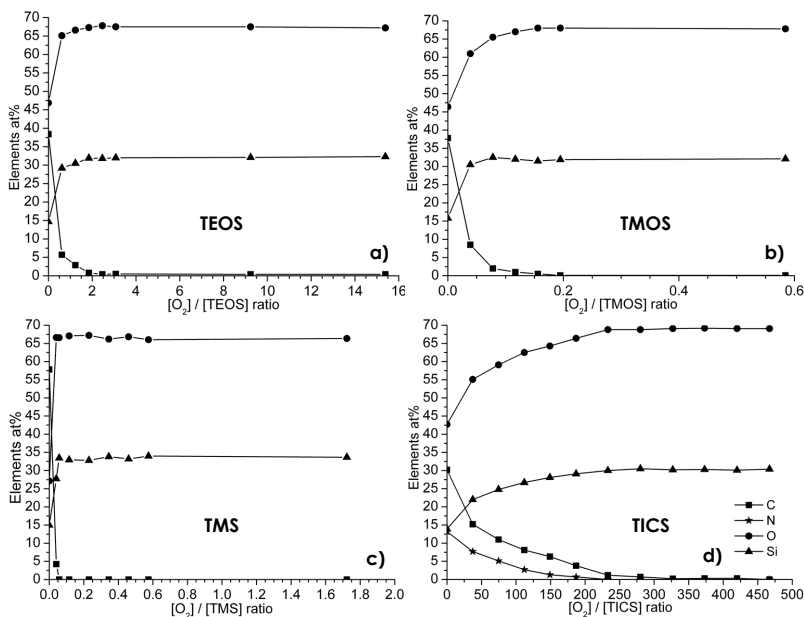
Figure 4-3: Chemical compositions of FEBID materials measured by EDX as function of precursor chemistry and injected $[O_2]/[precursor]$ injected ratios: (a) TEOS; (b) TMOS; (c) TMS; (d) TICS. Error bars: ± 2 at.%

The materials obtained using only the precursor vapours ($[O_2]$/[precursor] = 0 in Figure 4-3) could all be written, whatever the precursor flows tested, as SiO_xM_y (M = N and/or C contaminants), with 2 < x < 3 and 3 < y < 3.7. This was true for materials deposited from the Oxygen-free TMS, suggesting an Oxygen incorporation effect during the FEBID process. This is further discussed in Chapter 6, pp. 6-10. There was always sufficiently of Oxygen compared to the number of Silicon atoms to produce SiO_2.

Apart an identical Si atomic concentration of 15 at.% in the FEBID materials, the different precursor chemistries appear to decompose with specific pathways under the FEB, which are further discussed in Chapter 6.

Precursor	Atomic ratios in molecule			FEBID material at $[O_2]$/[precursor] = 0
	Si : O (# of bonds)	Si : C (# of bonds)	Si : N (# of bonds)	
TEOS	1 : 4 (4)	1 : 8 (0)	1 : 0	$SiO_{2.5}C_{3.2}$
TMOS	1 : 4 (4)	1 : 4 (0)	1 : 0	$SiO_{2.5}C_{3.2}$
TMS	1 : 0	1 : 4 (4)	1 : 0	$SiO_2C_{3.7}$
TICS	1 : 4 (0)	1 : 4 (0)	1 : 4 (4)	SiO_3C_2N

Table 4-2: Comparison of atomic ratios in the starting molecule and that in the deposited material obtained form the precursor vapours only. Numbers in parenthesis indicate the number of chemical bonds between the Si atom and a specific atom.

TEOS and TMOS decomposed in the same material, both loosing 1.5 atoms of Oxygen, 4.8 and 0.8 atoms of Carbon respectively. TMS lost 0.3 atoms of Carbon and gained 2 atoms of Oxygen. TICS lost 3 atoms of Nitrogen, 2 atoms of Carbon and 1 atom of Oxygen. The atomic ratios between the starting organosilane and the deposited material obtained with no additional Oxygen are compared in Table 4-2.

When adding molecular Oxygen to the precursor vapours, a similar behaviour was observed for all the molecules: the contaminants concentrations in the FEBID materials (C for TEOS, TMOS and TMS, C and N for TICS) decreased exponentially with increasing Oxygen flow. The contaminants concentration passed beyond the EDX detection limit above a $[O_2]$/[precursor] ratio specific to each molecule. In the case of TEOS and TMOS, a 80% Carbon concentration

decrease was induced by adding 0.2 sccm of O_2, and additional 0.4 sccm (i.e. $[O_2]/[TMOS]$ and $[O_2]/[TEOS]$ = 0.15 and 1.75 respectively) were needed to oxidize the remaining 5 at.% of C, suggesting a lower reaction efficiency. This was not observed with TMS since the C concentration dropped from 60 at.% to undetectable values already with 0.1 sccm of Oxygen (i.e. $[O_2]/[TMS]$ = 0.05), which was the smallest flow resolvable with the MFC. For TICS, the C and N concentrations also followed exponential decays. However, although the N concentration was three times lower than the C concentration in starting material, N became undetectable only at $[O_2]/[TICS]$ = 250, compared to $[O_2]/[TICS]$ = 325 for C. This suggested an oxidation efficiency function of the contaminant. As it will be presented in Chapter 6 (§ 6.1, pp. 6-2), this dependence of the elements concentration with the Oxygen flow is related to the number of molecules present at the surface, ruled by the co-adsorption following Langmuir-Hinselwood isotherms, which showed that increasing the Oxygen flow decreased exponentially the number of precursor molecules present at the surface which supply the deposition area with Si atoms. The characteristics observed were hence related to such a surface competition.

The C and N concentrations disappeared beyond the EDX detection limit above a $[O_2]/[precursor]$ threshold ratio, specific to each precursor, which are reported in Table 4-3 for the precursor flows reported in Table 4-1. This ratio depended on the precursor flow, and was larger for lower TEOS and TMOS flows, and lower for lower TMS flows. This characteristic involved side reactions due to contamination molecules in the SEM chamber, that are further discussed and explained in Chapter 6, pp. 6-12.

Precursor	$[O_2]/[precursor]$ threshold ratio	Injected Flow [molecules·cm^{-2}s^{-1}]
TEOS	1.75	$5.3 \cdot 10^{19}$
TMOS	0.15	$8.8 \cdot 10^{20}$
TMS	0.05	$2.5 \cdot 10^{20}$
TICS	325	$8.5 \cdot 10^{17}$

Table 4-3: Comparison of the amount of additional Oxygen needed to obtain pure SiO$_2$ from the different precursors.

The ratio depended as well of the dwell and replenishment time, and was larger for larger dwell times, which indicated a competition between the Oxygen consumed by the reaction and the amount of Oxygen supplied to the deposition area.

The contaminants concentrations decrease was to the advantage of the O and Si concentrations, which increased to reach stationary values above the threshold O_2 flow, and were similar for all four precursors: $SiO_{2.12}C_{0.01}$. The chemical composition remained then insensitive to additional Oxygen, indicating a complete oxidation of the deposited material. Although the latter composition mismatched the stoichiometric composition SiO_2, it was in good agreement to a reference spectrum taken on an industrial fused silica photomask substrate which resulted in $SiO_{2.1}C_{0.03}$. The residual C detected stemmed probably from the SEM chamber contamination, and the quantification errors form the X-Ray detector tuning.

The chemical composition of the materials remained stable to $Ar:O_2$ plasmas (energy < 12 eV), and ambient atmosphere, demonstrating that the C detected was not present as surface contamination, see Figure 4-4.
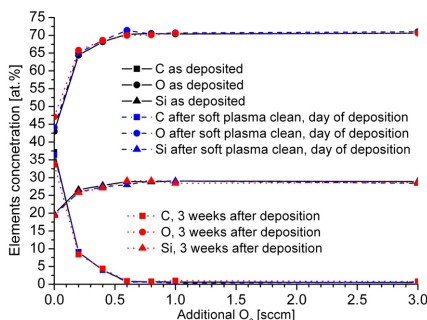
Figure 4-4: Influences of post-treatments on the chemical composition of the FEBID deposits obtained from TMOS.

A first comparison approach based on the simplest oxidation reactions, approximating that N oxidizes in NO_2 and C in CO_2 demonstrated that TMOS would be the easiest molecule to oxidize, followed by TICS, TMS and TEOS. This indicated that O_2 assisted FEBID did not follow simple rules (see Eq.4-1 to 4-4).

$$TEOS \quad Si(OC_2H_5)_4 + 10\,O_2 \;\rightarrow\; SiO_2 + 10\,H_2O + 8\,CO_2 \qquad Eq.4\text{-}1$$
$$TMS \quad Si(CH_3)_4 + 8\,O_2 \;\rightarrow\; SiO_2 + 6\,H_2O + 4\,CO_2 \qquad Eq.4\text{-}2$$
$$TICS \quad Si(NCO)_4 + 7\,O_2 \;\rightarrow\; SiO_2 + 4\,NO_2 + 4\,CO_2 \qquad Eq.4\text{-}3$$
$$TMOS \quad Si(OCH_3)_4 + 6\,O_2 \;\rightarrow\; SiO_2 + 6\,H_2O + 4\,CO_2 \qquad Eq.4\text{-}4$$
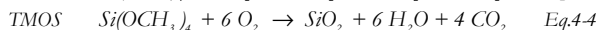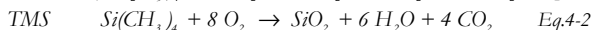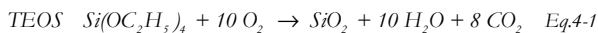
The different Oxygen threshold ratios obtained from the different molecules indicated that the amount of Oxygen needed to deposit pure SiO_2 depended on the molecule reactivity to Oxygen as well as on the fragments and contaminants reactivity to O_2. The molecules tested here originate from three different families. The comparison of the molecules different behaviour requires data concerning the growth kinetics, and deposition efficiencies that are discussed in Chapters 6 and 7. However, pure SiO_2 could be produced from all the molecules tested her, under these experimental conditions.

4.1.2 μ–Fourier Transform Infrared Spectroscopy (FTIR)

FTIR investigations are sensitive to the chemical entities vibrations in the FEBID material. It is complementary to EDX since it gives access to the Hydrogen content, and to the chemical bonds present in the material sub-structure. Wavenumbers from 550 to 4500 cm^{-1} (corresponding to wavelengths of 18 and 2 um) are selected from an infrared source by a diffraction grating, and irradiate the sample. The light reflected from the sample is recorded and an absorption spectra as function of the wavenumber can be plotted. Due to the large wavelengths used, FTIR represents also a volumic composition of the material.

It was used here to estimate and compare the chemical entities present in the $SiO_xC_yH_\alpha$ materials deposited using the four precursor vapours alone, and that of pure SiO_2, obtained with a threshold O_2 flow. The re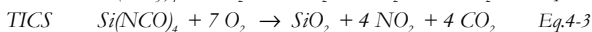sults were compared to the spectrum of a high quality commercial fused silica sample (Lithosil Q1 purchased from Schott Lithotec).

In order to prevent from optical scattering and border diffraction, the μ-FTIR microscope was operated with an investigation window of at least 75 x 75 μm^2. The spectra recorded were all taken in reflection mode, using normal incidence

of light on the sample surface, and unpolarized light. Prior to recording a spectrum over the FEBID materials, a calibration background was recorded on a gold mirror. The material specific spectra were obtained by subtracting the background to the data obtained over the FEBID material. The films were produced 100 x 80 μm² large on Au-coated Si samples. The results are presented in Figure 4-5.
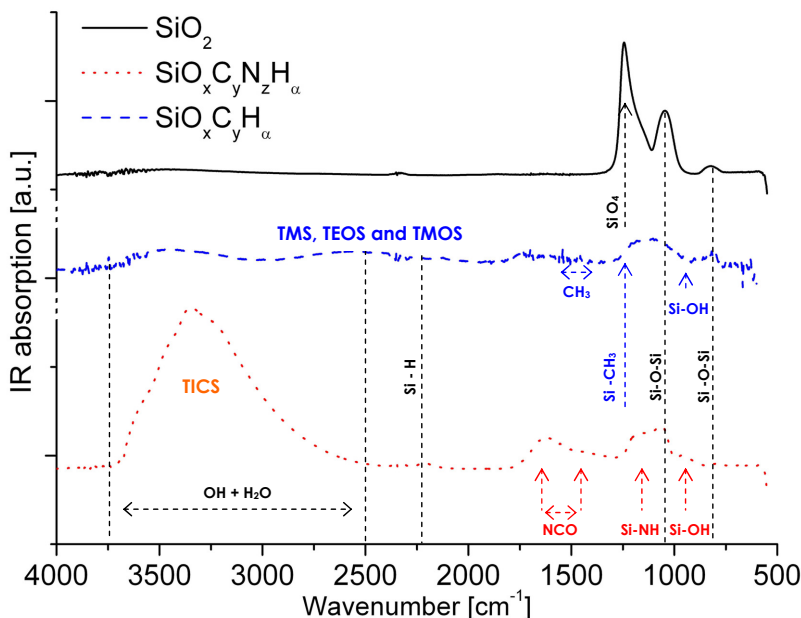
Figure 4-5: FTIR absorption spectrum for the different materials. Solid line: typical FEBID SiO₂ film; dashed line: FEBID material obtained by TEOS, TMOS and TMS alone (identical spectra, shown here for TMS only); dotted line: FEBID material obtained from TICS alone

The materials produced from TEOS, TMOS and TMS appeared similar (dashed line), but different from that produced from TICS (dotted line). All the materials deposited from the different monomers alone (referred to as the SiO$_x$C$_y$H$_\alpha$ materials) presented an undefined and complex sub-structure, as indicated by the broad absorption bands present in the dashed and the dotted lines in

Figure 4-5. On the contrary, the pure FEBID SiO_2 presented the same reflection spectra with three narrow absorption peaks.

The determination of the entities present was delicate, however similarities between the different $SiO_xC_yH_\alpha$ materials could be found. The wide absorption regions between 2500 to 3700 cm^{-1} were attributed to water and hydroxyl groups (OH) in the materials.[1, 2] The larger intensity of this peak for the material obtained from TICS might be due to the high moisture sensitivity of the molecule, indicating reactions with residual water in the SEM. This was reinforced by the presence of an absorption signal at ~950 cm^{-1}, indicating that OH groups were attached to Si atoms.[1, 3, 4] Hence, part of the Oxygen detected by EDX in these materials was incorporated in the FEBID films and bonded to the Si atom. This was further supported by the presence of peaks (of low intensity for the material obtained from TICS) at ~820 and 1060 cm^{-1}, generally assigned to the Si-O-Si symmetric and asymmetric stretching frequencies. The SiO_2 network was hence produced already with no additional Oxygen. The weak absorption signals at ~2240 cm^{-1} were assigned to Si–H.[1]

A few particularities of the materials obtained from TMOS, TEOS and TMS are the peaks at 900 cm^{-1} due to Si-CH3, that were confirmed by absorption bands at ~780, ~1385 and ~1465 cm^{-1}, assigned to the CH_3 and CH_2 deformation modes, as the broad tail between 2800 and 3000 cm^{-1}.[5] This suggested that ligand attachment to Si atoms could occur during FEB driven reactions.

The $SiO_xC_yN_zH_\alpha$ material obtained from TICS contained Si-N bonds, suggested by the peaks at ~1170 cm^{-1}, and usually assigned to the Si-NH bending mode,[6] and the weak signal at 700 cm^{-1} corresponding to the Si-N stretch deformation.[7] The shoulder between 1170 and 1650 cm^{-1} might be attributed to the excitation of NCO (~1480 cm^{-1} [7]). No real evidence could be brought concerning the presence of C=O bonds, usually located at 1700 cm^{-1}.[1]

These results demonstrated that for all the precursors tested, the silicon dioxide network was already produced under the beam without adding molecular Oxygen, certainly due to rearrangement reactions of the ionic species formed by electron irradiation and oxidation reactions driven by residual gases in the SEM chamber. Other recombination reactions involving C and N containing ligands to Si atoms were suggested to occur as well, and had to be confirmed.

The absorption spectra of all the SiO_2 materials deposited under $[O_2]/[precursor]$ threshold ratios (see solid line spectra in Figure 4-5) exhibited three narrow and distinctive absorption peaks centred at 820, 1050 and 1250 cm^{-1}. The spectral regions of hydroxyl, carbonyl and hydrocarbon groups appeared flat, which supported the idea that the material was C, N and OH free. The 820 and 1050 cm^{-1} peaks are specific to SiO_2 (Si-O-Si symmetric and asymmetric stretching respectively). The 1250 cm^{-1} peak was unusual for silica materials, since it generally appeared in literature as a low intensity shoulder of the 1050 cm^{-1} peak, resulting of a coupling between the transverse optic mode (1050 cm^{-1}) and the longitudinal optic mode in SiO_2, as proposed by Berreman.[8] However, this coupling is generally obtained using oblique incidence FTIR (typically 30° to the surface), but should not be observed under normal incidence.[9] The 1250 cm^{-1} frequency also corresponds to the presence of Si–CH$_3$ in the material,[5] but the absence of the other Si–CH$_3$ absorption signals (~780, ~1385 and ~1465 cm^{-1}) excluded this option.

A reference spectra taken, of a fused silica substrate with the same equipment and under the same experimental conditions, did not present this high absorption, indicating that it was specific to our material, see Figure 4-6.

The silica films obtained are thought to contain polymerized SiO_4 tetrahedra, which might present such absorption, as proposed by Clarks experiments.[10, 11] These entities act as scattering defects that can diffract light under angles,

creating a similar effect than oblique incidence irradiation, and shows this absorption related to the LO mode.
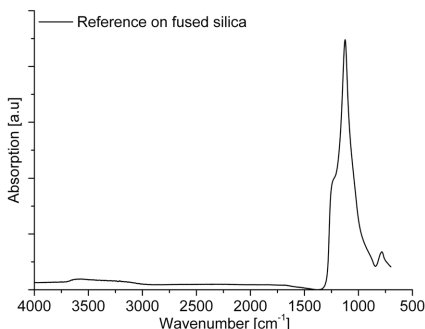
Figure 4-6: FTIR absorption spectra under normal incidence of a fused silica sample, showing no distinctive peak at 1250 cm^{-1}

4.1.3 X-Ray Photoelectron Spectroscopy (XPS)

Compared to the previous analyses presented, XPS investigations allow quantifying with high accuracy the elements concentrations present in the first 5 nm of matter, and gives additional information about the elements binding energy. The principle is to irradiate the surface with X-Ray that will emit electrons from the surface that are element–characteristic. It was useful to confirm the FTIR and EDX analyses. Since it is sensitive to the surface, the XPS equipment is coupled to an ion sputtering system, which allows getting rid of the surface contamination, originating from sample manipulation, handling and exposure to atmosphere. This layer has to be removed before any XPS analysis. The decontamination is done in-situ by a soft, thirty seconds long cleaning ion sputtering of the analyzed area.

Investigations were performed on the same films than those used for the FTIR investigations already. The latter consisted of two films deposited from TMS, (one $SiO_xC_yH_\alpha$ film obtained with 0 sccm O_2, and one SiO_2 film obtained with a threshold O_2 flow). The photoelectron emission spectra obtained for Si, O and C are reported for the two different materials in Figure 4-7 (a), (b) and (c) respectively. Due to the low signal to noise ratio, the data was treated in terms of main peak positions.

The chemical composition of the $SiO_xC_yH_\alpha$ film (previously reported in Table 4-2) was confirmed to be $SiO_{1.8}C_{3.8}$ and the suggested peaks position (284.9 eV for C, 103.1 and 102.4 for Si, 523.5 and 523.8 for O) and distribution, see solid line spectra in Figure 4-7 and solid gray lines, hint to an estimation of the deposits nature. The latter seem to contain already SiO_2, Si-C, R-Si(OCH$_3$)$_3$ or -(Si(CH$_3$)$_2$O)-type entities, and oxygenated carbonaceous chains. The presence of Si-C in this material was confirmed by Auger spectroscopy and indicates that rearrangement reactions and ligand attachment occur during the FEBID process. The latter result and the detection of SiO_2 entities are in perfect agreement with the previous FTIR analysis results.
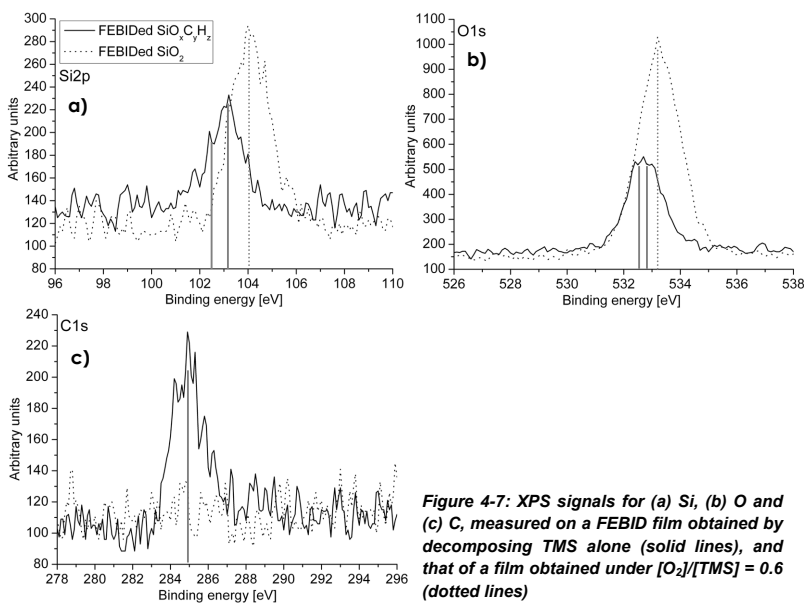
Figure 4-7: XPS signals for (a) Si, (b) O and (c) C, measured on a FEBID film obtained by decomposing TMS alone (solid lines), and that of a film obtained under $[O_2]/[TMS] = 0.6$ (dotted lines)

The XPS chemical composition of the deposited oxide (produced with $[O_2]/[TMS] = 0.6$) was measured to $SiO_{1.97}$, with no detected C, which confirmed the production of pure SiO_2 with an undetectable contamination. The insulating material made difficult the investigations and since no C was detected, the correction of the peak position could not be performed. The shifts observed

were not identical for Si (0.75 eV) than for O (0.5 eV), which suggested that they were not due only to charging effects. The spectra were interpreted as measured, and the reasonable peaks position (104 eV for Si and 533.3 eV for O) corresponded to SiO_2. Compared to EDX, XPS has higher sensitivity to light elements, and lower detection limits. This was a substantial evidence of the high purity of the SiO_2 FEB deposited from TMS and additional oxygen.

4.1.4 Elastic recoil detection analysis (ERDA) / Nuclear Reaction analysis (NRA)

ERDA and NRA are two particle beam investigation techniques that allow determining the precise concentrations of the elements incorporated in the materials. The main advantage compared to the other techniques presented previously is that it allows precise quantification of any elements (including H) in the deposited film, at a given depth (1 nm resolution). [12, 13] The high energy (MeV) ion beams used for the investigations can be focused to micrometer spots, and allow for spatial micro-analysis. ERDA and NRA have been performed at the research centre of Dresden-Rossendorf, by Frans Munnik.[14, 15] For the ERDA measurements, a He+ beam (2 MeV, focused smaller than 10 µm) was used to eject H atoms from the target. The latter were detected under a forward angle of 30°.[14] For NRA, a 1.05 MeV deuterium (d) beam has been used. C is detected through the $d + {}^{12}C = p + {}^{13}C$ reaction and O through $d + {}^{16}O = {}^{14}N + a_0$.

Elements	FEBID materials from TICS compositions [at%]		TMS FEBID material composition [at%]	
	$SiO_xC_yN_zH_\alpha$	SiO_2	$SiO_xC_yH_\alpha$	SiO_2
H	2	1	3	2
C	19	2	38	3
N	15	0	-	-
O	53	65	39	63
Si	12	32	20	32
Total	$SiO_4C_{1.5}N_{1.2}$	$SiO_{2.03}C_{0.06}H_{0.03}$	$SiO_{1.95}C_{1.9}H_{0.15}$	$SiO_{1.96}C_{0.09}H_{0.06}$

Table 4-4: chemical composition measured by ERDA and NRA of two different materials obtained from TICS and TMS. Error bars for H: ± 2 at.%.

ERDA and NRA depth profiling measurements were performed on four deposits: two $SiO_xC_yH_\alpha$, and two SiO_2, obtained from TICS and TMS (mixed with respective O_2 threshold flow for the deposition of SiO_2). The results of the atomic concentration in the deposit material for all the films are listed in Table 4-4.

The pure oxides deposited presented Hydrogen concentrations smaller than the quantification error bar, and suggested that the oxides are H-free.

Some expected and reasonable divergences were found between the EDX and the ERDA quantifications, concerning the quantification of light elements. The concentrations of the elements apart Hydrogen were constant through the deposit thickness, and were an indication that the film density was homogenous through the entire films. The H and C concentrations increased at the deposit-Au interface. The respective interface H concentrations for the $SiO_xC_yH_\alpha$ materials were larger than that measured for the SiO_2 films, produced with additional Oxygen, see Table 4-5.

Precursor	Deposit	C concentration at the deposit – Au interface [at.%]	H concentration at the deposit – Au interface [at.%]
TICS	$SiO_xC_yN_2H_\alpha$	12.2	6.5
	SiO_2	5.4	1.5
TMS	$SiO_xC_yH_\alpha$	16.8	13
	SiO_2	7.3	4

Table 4-5: H concentration at the deposit – Au interface.

This increase could not be due to the incorporation of hydroxyl groups since no Oxygen increase could be detected. The presence of these elements at this specific location was the trace of surface contamination oxidation in the very first steps of the FEBID process. Since no special care was taken to protect the substrate surface during loading in the SEM chamber, hydrocarbon contamination was expected to be covering the surface. A 5 keV EDX measurement on a standard Au-coated Si sample showed that it had an average C concentration of 18 at.%. This contamination was not desorbing during the SEM pump down, and remained as interface over the Au coating.

When the FEB was scanning the 40 x 50 µm² area, this contamination layer was partially fragmented by impinging electrons, and could react either with residual water or injected Oxygen to form volatile species such as H_2O or CO_2, and desorb from the surface, as already reported.[16, 17] O_2 appeared more efficient than residual water, since a lower H concentration was detected at the interface. However, this etching process was in competition with the deposition process, since precursor molecules were injected simultaneously.

This proposed mechanism was demonstrated by following the sample current during the first seconds of deposition. The sample current is that which is actually flowing out of the substrate under electron irradiation, and follows the surface electron emission.[18, 19] It is equal to the probe current out of which are subtracted the secondary and the backscattered yields (respectively δ and η) of the substrate material (see Chapter 5, § 5.2, pp. 5-6, and Appendix 2 and 3):

$$I_{sample} = I_{probe} \ (1\text{-}\delta\text{-}\eta) \quad Eq.4\text{-}5$$

These yields are specific to a substrate material, and the sample current is expected to follow the electron emission of the top layer. When a SiO_2 film is deposited by a 10 keV FEB on an Au surface, the sample current is expected to start from the Au theoretical electron yield, 10 % of the probe current (with δ = 0.39 and η = 0.48 see Appendix 2 and 3) to the SiO_2 electron yield, 80 % of the probe current, see Appendix 2 and 3.

Series of SiO_2 films produced form TMS and O_2 (mixed in threshold ratio) were produced, with deposition times between 1 and 10 seconds. The sample current was collected for each of these depositions, and EDX measurements were performed on the deposition sites. The surface chemical composition could hence be related to the sample current characteristic. The results are reported in Figure 4-8.
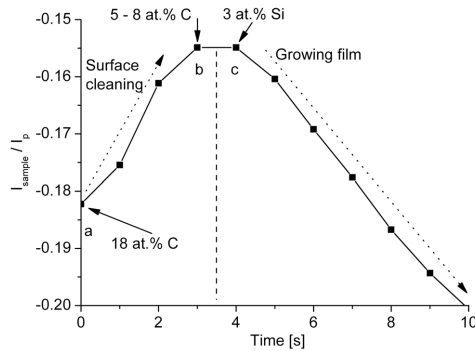
Figure 4-8: Sample current evolution during Oxygen assisted FEBID, showing the competition between deposition and etching in the first seconds, and EDX corresponding EDX analysis.

The sample current showed a different behaviour than the theoretically expected one. The current started at a larger value than that expected (20 % of probe current, instead of 10 %, point a in Figure 4-8), which was due to the surface contamination since EDX analyses showed a 18 at.% C concentration on the Au surface. C has a lower electron yield than Au, and more current is expected to remain in a bulk C substrate than Au (see Appendix 2 and 3).

The current then decreased, and reached a value corresponding to 15 % of the probe current, point b in Figure 4-8, meaning than the surface was emitting more and more electrons, and the electron yield was approaching the theoretical value of 10 %. EDX measurements showed a 5 at.% of C at this current value, demonstrating that the C was efficiently etched away. Still, no Si atom could be detected.

The current remained stable and started then decreasing, point c in Figure 4-8, and Si atoms started to be deposited on the surface. The theoretical electron yield of Au could never be reached due to the dominance of the deposition reaction.

This clearly indicated the two different reactions occurring during O_2 assisted FEBID. This effect was not detected during conventional FEBID. This behaviour might be due to the different reactivities or efficiencies of creating reactive

fragments from a contamination layer and from volatile molecules. However, it clearly indicated the deposition mechanism.

4.1.5 TEM investigations

TEM investigations were performed in order to determine the atomic sub-structure of the deposited materials. TEM is sensitive to the sample thickness, which should be smaller than 80 nm if the investigations are done at 300 kV. First, films were prepared by microtome slicing. The protocol contained some cleaning steps involving water, and the final lamellas did not contain anymore C, indicating that the structure had been modified during the preparation. To prevent this problem, the second TEM sample consisted of a 3-D free-standing deposit, produced directly on a standard Cu TEM grid, which did not necessitate any preparation to be observed since the apex and borders were thin enough.

The free-standing rod was produced using TICS and additional Oxygen ([O_2]/[TICS] = 325). The SEM was operated at 25 kV for ultimate resolution and the probe current was set to 500 pA to produce a thin rod. The grid was centred over a Faraday cup of the sample stub. After positioning the FEB between to sub-lines of the periodic grid pattern and focusing on the edge of a line, the free-standing rod was produced by scanning the FEB towards the empty volume, see Figure 4-9. The scanning speed was set to 1.5 nm·sec^{-1}, which is slightly larger than the vertical growth rate under these irradiation conditions. This assured an almost horizontal growth. The final structure was 4.5 μm long.

The low sensitivity of the materials chemical composition to the FEB parameters (see § 5.3) suggested that the produced rod had the same properties than large films.
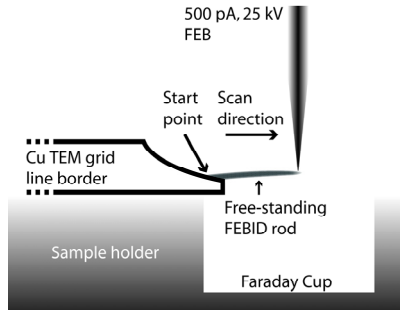
Figure 4-9: FEBID of a free-standing rod principle (not at scale).

The entire grid was placed directly in the TEM for investigations. High resolution TEM micrographs of the structure produced are presented in Figure 4-10.
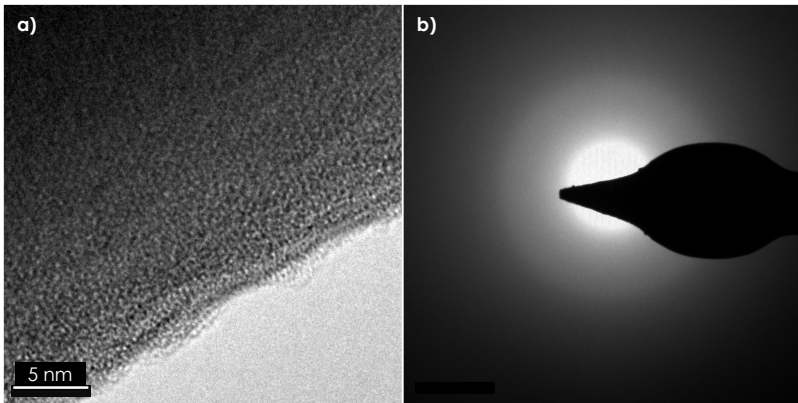
Figure 4-10: TEM (300 kV) micrographs of the deposited SiO$_2$ free-standing rod.
(a) High resolution bright field mode micrograph showing the sub-structure of the deposited SiO$_2$.
(b) Diffraction pattern of the FEBID SiO$_2$ confirming the absence of a defined structure.

Figure 4-10 a) is a high resolution bright field micrograph taken on the border of the insulating rod. The investigations were performed close to the copper grid junction, assuring a sufficient thermal and electrical conduction in order to

prevent from damaging the rod. No porosity was detected in the FEBID SiO_2 at this scale, indicating a high density material, which prevented from water diffusion into the material.

According to the grain size distribution, see Figure 4-10 a), the material appeared homogenous at this scale, but no evidence of the homogeneity through the entire section could be declared, due to the large thickness of the pillar. However, we believe that structural inhomogeneities as observed by other researchers (crystalline core, amorphous C cladding)[20, 21] should not be present in this material. The rod border shows a nano-meter scale roughness (approximately 2 nm), which satisfies the requirements for optical and plasmonic devices, as well as photolithography mask repair. The roughness might originate from beam instabilities during the deposition.

The diffraction pattern shown in Figure 4-10 b) presented a homogenous disk, free of isolated crystalline diffraction spots or rings, which allowed concluding that the deposited SiO_2 was amorphous at this scale.

Summary of Chemical Composition of FEBID materials

- Large films produced allowed to characterize FEBID material using standard micro-investigation techniques

- The chemical composition of the FEBID material obtained from the four molecules tested could be brought from $SiO_xC_yH_\alpha$ to pure and stoichiometric SiO_2 by adding molecular Oxygen. Cross-checking and complementary investigation techniques guaranteed the high quality of the SiO_2 produced

- Residual gases appear to be reactive when depositing from the precursors vapours alone, and lead to Oxygen incorporation, and creation of Si-O-Si network

- Recombination reactions were demonstrated to occur during FEBID

- Oxygen assisted FEBID was demonstrated to be a real time combination of contamination etching and deposition of pure SiO_2

- The deposited oxide is amorphous

4.2 Chemical etch rates of deposited materials

Material density is related to the atomic sub-structure of the deposited materials. It is a paramount parameter which influences the potential applications of the materials since it determines the material resistance to chemicals or the refractive index as examples. A large variety of silica is commercially available, and quartz is that with the largest density of 2.6, and the smallest chemical etch rates. The larger the density is, the lower the chemical etch rate in BHF will be.

40 x 40 µm^2 deposits where produced on a Si substrate using TEOS, TMOS and TMS, and varying the [O$_2$]/[precursor] ratios from zero to above threshold ratio for each case. In order to avoid the border thickness inhomogeneties due to the standard TV scanning (see Figure 4-1, pp. 4-2), the films were produced using NPGS (center-to-center = line spacing = 50 nm, dwell time = 13 µs), which scans homogeneously the FEB over the defined pattern. The sample was exposed to buffered hydrofluoric acid (BHF), piranha and base-piranha solutions, which are commonly used as etching and cleaning solutions. Thickness measurements of the films before and after exposure to the different solutions allowed determining the etch rates of the Si-containing materials in these solutions, which were representative of their density and chemical composition.

4.2.1 Resistance to BHF

The sample was dipped in a BHF (NH$_4$F (40%) + HF (50%) in a 7:1 ratio) for thirty seconds without stirring. The chemical reaction taking place was the following:

$$HF + SiO_2 \rightarrow SiF_4 + H_2O \quad Eq.4\text{-}6$$
$$NH_4F \rightleftarrows NH_3 + HF \quad Eq.4\text{-}7$$
$$SiF_4 + 2F^- \rightleftarrows SiF_6^{2-} \quad Eq.4\text{-}8$$
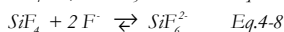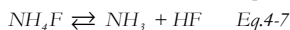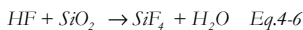
Etch rates of SiO$_2$ in BHF solutions range from 70 nm·min^{-1} for dry thermal oxide (highest density), to 300 nm·min^{-1} for the low temperature grown oxide (low density). The average etch rate as function of the precursor and the O$_2$ flow

used for the deposition are reported in Figure 4-11 a). The measured etch rates increase with the decreasing C concentration in the FEBID material. C is not degraded in BHF and could protect the Si-O bonds of the material. Deposits obtained from TEOS and TMOS behave similarly, and the corresponding curves were nearly superposed. The etch rate was quasi-constant around 170 nm·min^{-1} for $0.6 \leq$ flow $(O_2) \leq 1$, and raised up to 180 nm·min^{-1} for flow $(O_2) > 1$ sccm. This was not observed for the deposits obtained from TMS for which the etch rate saturated around 150 nm·min^{-1} for flow $(O_2) > 0.2$ sccm. The lower saturated etch rate is an indication that TMS leads to denser deposits than TEOS and TMOS, nevertheless all the structures deposited here have a lower density compared to dry thermal oxide.

4.2.2 Resistance to piranha solution

Piranha solutions consist of sulphuric acid mixed with peroxide in a 3:1 ratio. The atomic Oxygen produced by mixing these two chemicals (see Eq. 4-9) is a highly oxidizing reactive oxidizes Carbon in any form (Eq. 4-10). The concentrated H_2SO_4 absorbs the produced water and keeps the solution "dry". The sample was dipped for 10 minutes into a freshly prepared and hot piranha solution (H_2SO_4 (98%) + H_2O_2 (30%) in a 3:1 ratio). The expected chemical reactions between the solution and the organics present in the materials are:

$$H_2SO_4 + H_2O_2 \rightarrow H_3O^+ + HSO_4^- + O \quad Eq.4\text{-}9$$
$$2\,O + X\text{-}C \rightarrow CO_2 + X \quad\quad\quad Eq.4\text{-}10$$
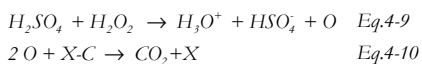
As expected, the etch rates depended proportionally on the C concentration present in the oxides. The results are reported in Figure 4-11 b). It is observed that the deposits obtained from TMS and TMOS with $[O_2]/[precursor]$ ratios above their specific threshold ratios present immeasurable etched depth after 10 minutes in piranha. In contrary, the comparable resistance for TEOS based deposits is reached for an O_2 flow 5 times higher than its respective EDXS threshold ratio for obtaining pure SiO_2. Hence, TMOS and TMS seem to decompose into cleaner material as TEOS.

4.2.3 Resistance to base-piranha solution

Base piranha solution (NH$_4$OH (28%) + H$_2$O$_2$ (30%) + distillated water in a 1:1:5 volume ratio) allows to remove low density native surface oxides. The principle is to lift-off the surface particles by slight etching of a silicon surface. The etch rates measured after 15 minutes dips are shown in Figure 4-11 c), and no measurable etching of the deposited materials could be observed. These results meant that the film top surface was dense.
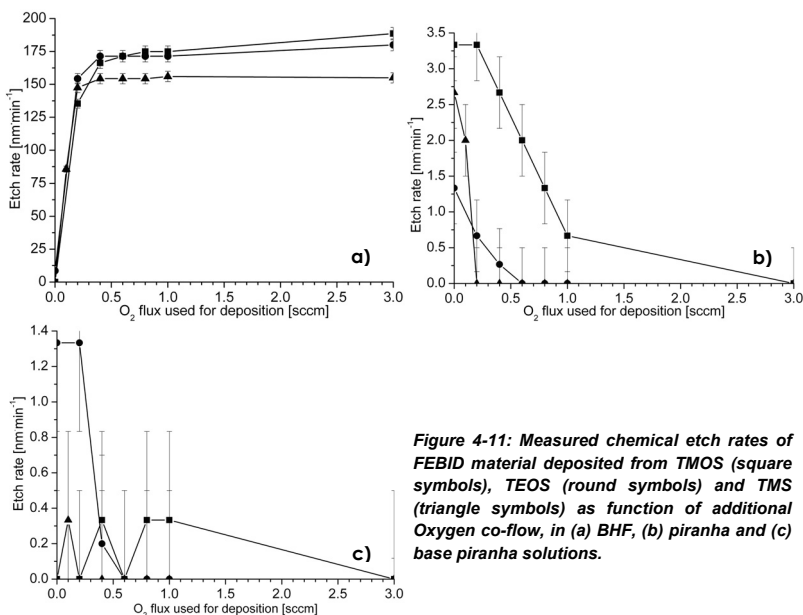
Figure 4-11: Measured chemical etch rates of FEBID material deposited from TMOS (square symbols), TEOS (round symbols) and TMS (triangle symbols) as function of additional Oxygen co-flow, in (a) BHF, (b) piranha and (c) base piranha solutions.

Summary of Chemical etch rates

- The SiO$_2$ obtained from TMS had a higher density than that obtained from TEOS and TMOS

- Good etch resistance of the oxides could be measured in piranha and base-piranha solutions.

- The three oxides obtained all presented a higher etch rate in BHF than dry thermal oxide, indicating a lower density

4.3 Optical characterization

The optical qualities of the oxides deposited from the organosilanes were evaluated using different optical techniques. The determination of the optical refractive indices of micrometer size structures of films are challenging tasks that require high resolution equipments. They were evaluated by means of deep ultra-violet (DUV, 193 nm wavelength) optical transmission measurements, and *in–situ* reflectometry and *ex–situ* micro-ellipsometry for the properties in the visible part of the spectra.

4.3.1 193 nm wavelength transmission

The optical transmission at 193 nm wavelength of pure SiO_2 deposits obtained from TMOS, TMS and TICS were measured on the AIMS tool. 10 x 10 µm² films were deposited on fused silica samples, cut out from DUV photomasks. The deposits were produced between 150 and 170 nm thick, and close to Chromium strips. The focusing of the microscope over such thin films is delicate, and was done stepwise, see Figure 4-12.
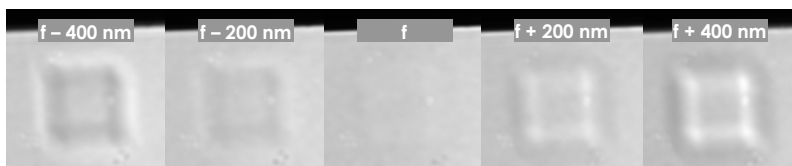
Figure 4-12: Focusing steps strategy for AIMS measurements. Black contrast is an absorbing 90 nm thick Cr strip. Deposit is a 10 x 10 um² square.

All the transmission results reported were taken in focus. The signal to noise ratio was lowered by setting the laser pulse duration to an intermediate value of 3000 pulses. The results presented in Figure 4-13 are intensity profiles of a line passing through the deposit centre, normalized to the transmission of the surrounding mask blank.
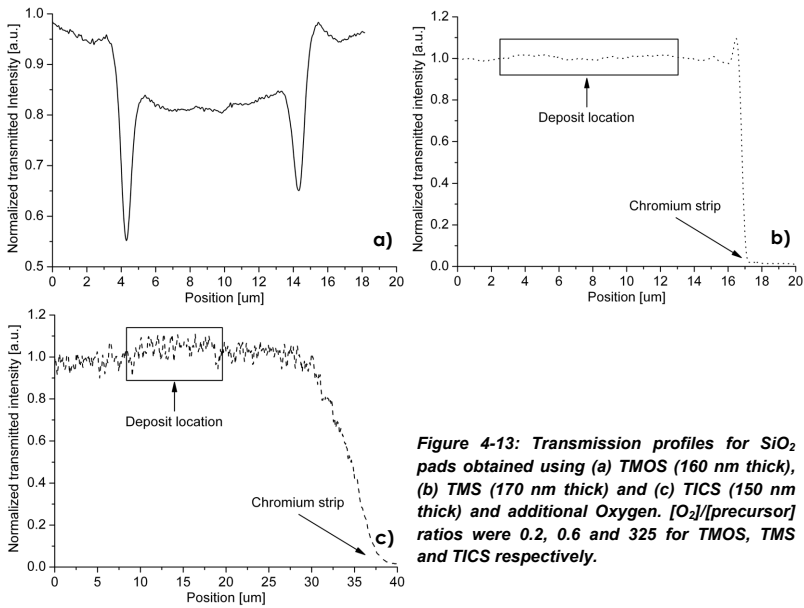
Figure 4-13: Transmission profiles for SiO$_2$ pads obtained using (a) TMOS (160 nm thick), (b) TMS (170 nm thick) and (c) TICS (150 nm thick) and additional Oxygen. [O$_2$]/[precursor] ratios were 0.2, 0.6 and 325 for TMOS, TMS and TICS respectively.

The deposits obtained from TMOS, TMS and TICS showed transmissions of 85, 99 and 108 %, respectively, normalized to the virgin photomask transmission. The higher optical transmission of the deposits obtained from TMS was probably due to a higher material density, as measured in § 4.2. The transmission measured for the deposits obtained from TICS, higher than 100 %, are thought to be due to an antireflection effect between the bulk substrate and the film. Antireflection effects occur when the index of the film is the square-root of that of the substrate, which would indicate that the silicon dioxide obtained from TICS is less dense than that obtained from the other precursors.

This effect would require precise *transmission vs. thickness* measurements, which could not be realized during this thesis.

4.3.2 514 nm wavelength reflectometry

The refractive indexes of $SiO_xC_yH_\alpha$ and SiO_2 materials at 514 nm wavelength were estimated using the *in-situ* reflectometry setup. The magnification was set to 1 kX (irradiated area of 80 x 100 µm²) in order to contain the elliptical 10 x 15 um² laser spot, and the laser power was set to 200 mW. The films were produced using TMOS, on plain Si substrates. The photodiode signal variations depended on the films growth rate and complex refractive index. The interferometry principle is represented in Figure 4-14.
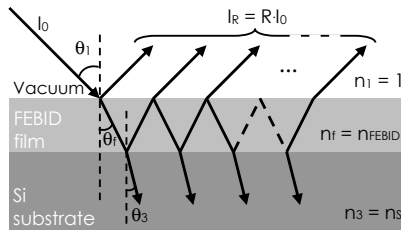
Figure 4-14: Reflectometry between three media

The total complex reflection coefficient can be calculated from Fresnel's coefficients (see Appendix 2) for the different polarizations, and is the infinite sum of all the waves reflected and transmitted through the film:

$$\tilde{r} = r_{12} + t_{12}r_{23}t_{12}e^{-2i\Phi} + t_{12}r_{23}^2t_{12}e^{-4i\Phi} + ... \quad Eq.\ 4\text{-}11$$

Where r_{xy} and t_{xy} represent respectively the reflection and the transmission coefficients between media x and y (considered purely real), and ϕ the complex attenuation and phase shift coefficient between the light reflected at the vacuum-FEBID film interface and that reflected at the FEBID film-substrate interface:

$$\tilde{\Phi} = 2\pi \frac{\tilde{n}_f d_f}{\lambda} \cdot cos(\theta_f) \quad Eq.\ 4\text{-}12$$

The complex reflection coefficient depends on the incident light polarization and can be re-written when the infinite series converge:

$$\tilde{r}^{s,p} = \frac{r_{12}^{s,p} + r_{23}^{s,p} e^{2i\Phi}}{1 + r_{12}^{s,p} r_{23}^{s,p} e^{2i\Phi}} \quad Eq.\ 4\text{-}13$$

The resulting intensity reflection coefficient as function of the polarization is hence:

$$R^{s,p} = \left|\tilde{r}^{s,p}\right|^2 = \frac{(r_{12}^{s,p})^2 + (r_{23}^{s,p})^2 + 2\,r_{12}^{s,p} r_{23}^{s,p} \cdot \cos(2\Phi)}{1 + (r_{12}^{s,p})^2 (r_{23}^{s,p})^2 + 2\,r_{12}^{s,p} r_{23}^{s,p} \cdot \cos(2\Phi)} \quad Eq.\ 4\text{-}14$$

In the case of a circularly polarized beam as that used in this study, the total reflection coefficient is given by the average of R^s and R^p:

$$R = \frac{R^s + R^p}{2} \quad Eq.\ 4\text{-}15$$

Eq. 4-16 allows calculating the reflected Intensity I_R:

$$I_R = I \cdot R \quad Eq.\ 4\text{-}16$$

A custom Matlab code supporting complex numbers was implemented (see Appendix 2) and applied to fit the experimental curves obtained. The real-time *in-situ* reflectometry setup provided the photodiode signal (I_R) as function of the deposit time. The latter could be converted to deposit thickness by profilometry of the different films produced.

The code takes as input parameter the deposit thickness, and fits the real and the imaginary part of the FEBID film, so that the calculated I_R given by Eq. 4-16 fits the experimental data. The experimental data was normalized to the reflected intensity measured at the start of the experiment (when the substrate consisted only of plain Si). The fitting was done with the approximations that no scattering occurred in the films. The results are presented in Figure 4-15.
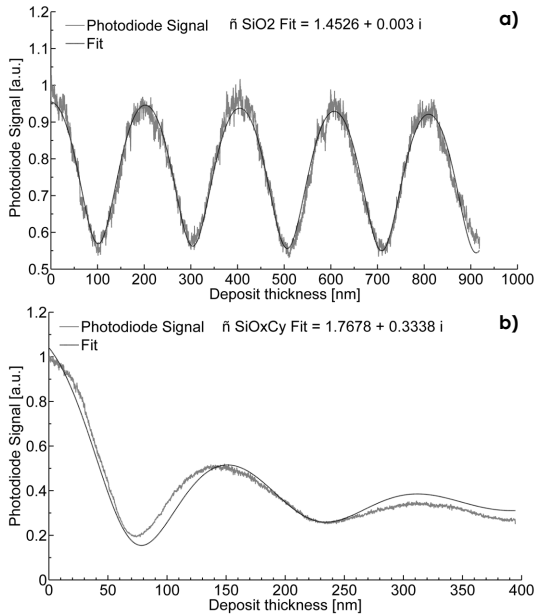
Figure 4-15: Experimental reflectometry signals acquired during the FEBID of (a) SiO₂ ([O₂]/[TMOS] = 0.6) and (b) SiOₓCᵧHₐ (TMOS alone). Dashed lines = mathematical fit using Eq. 4-6.

Compared to the $SiO_xC_yH_a$ material, the deposited SiO_2 had a low absorption (0.003) and a refractive index of 1.452. At the same wavelength, fused silica has a refractive index of 1.462 and a null absorption coefficient. The divergences are in good accordance with the chemical etch rate measured that showed a lower density for the FEBID oxide. The values are however satisfying for a custom reflectometry setup.

The contaminated material absorbed already 70 % of the incident light at a thickness of 350 nm. This was due to the presence of C incorporated in the material.

4.3.3 Micro-ellipsometry

Ex–situ spectral micro-ellipsometry investigations were performed on the same two $SiO_xC_yH_\alpha$ and SiO_2 films. The measurements were performed by Nanofilm Technologie®, with a Nanofilm NP3 micro-ellipsometer that allows for 5 x 5 μm^2 resolution, and a 10^{-3} precision of the refractive index, which was measured between 350 to 950 nm. The measurements were performed with a 55° incident angle. The data were fitted with respect to n, k and the film thickness. The results are reported in Figure 4-16.
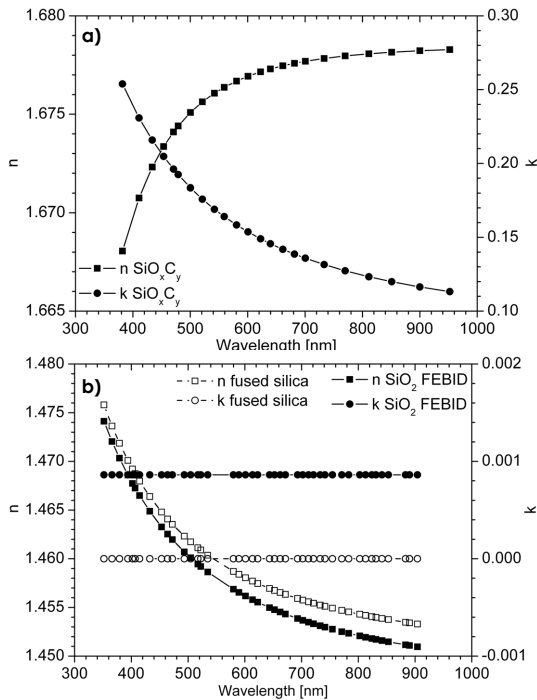
Figure 4-16: Complex refractive indices of FEBID materials obtained by Micro-ellipsometry. (a) $SiO_xC_yH_a$ obtained by decomposing TMOS vapours, and (b) SiO_2 ($[O_2]/[TMOS] = 0.6$), compared to fused Silica. Error bars: ± 0.003

The deposited SiO_2 had similar refractive index than fused silica, within the measurement error bars. The measurements were double checked by the fit of

the thickness of the films that were identical (± 5 nm) to that measured by standard profilimetry. The FEBID oxide had similar optical properties than fused silica in the visible part of the spectra, which suited this material for nano-scale optics. As shown by the DUV measurements, the silica obtained by decomposing TMOS had the lowest transmission, indicating that the SiO_2 obtained from TMS might be denser than the SiO_2 measured here. On the contrary, the $SiO_xC_yH_a$ material had a varying absorption coefficient which increased to 0.25 at 400 nm wavelength.

Summary of Optical investigations of the materials

- the deposited SiO_2 was of sufficiently dense to be used for optical applications

- the DUV optical transmission fulfill the industrial requirements for mask repair.[22-26] The three different oxides had different DUV transmissions, which might be related to differences of material density

- The deviations between the *in-situ* setup and *ex-situ* high precision micro-ellipsometry were in the order of 10%, which might be significant for optical applications, but the *in-situ* setup appeared satisfying as first estimation of the refractive index

- The materials deposited without additional Oxygen are not optically performant due to the high absorption coefficient

4.4 Conclusion of Chapter 4

Additional Oxygen increased the FEBID process efficiency in terms of chemical composition of the deposits. Pure SiO_2 could be obtained from all the four precursors, which was contamination free, and could be used for optical applications. The dynamics and the process behind O_2 assisted FEBID was influenced by the precursor chemistry. The influences of the electron flow and dwell and replenishment times on the growth dynamics and chemical composition are presented in details in the next Chapter.

4.5 Bibliography of Chapter 4

1.   A. Goullet, C. Vallee, A. Granier, and G. Turban, "Optical spectroscopic analyses of OH incorporation into SiO2 films deposited from O₂/tetraethoxysilane plasmas", Journal of Vacuum Science & Technology A, **2000**, 18, 2452-2458.

2.   P. Innocenzi, "Infrared spectroscopy of sol-gel derived silica-based films: a spectra-microstructure overview", Journal of Non-Crystalline Solids, **2003**, 316, 309-319.

3.   A. Barranco, F. Yubero, J. Cotrino, J.P. Espinos, J. Benitez, T.C. Rojas, J. Allain, T. Girardeau, J.P. Reviere, and A.R. Gonzalez-Elipe, "Low temperature synthesis of dense SiO2 thin films by ion beam induced chemical vapour deposition", Thin Solid Films, **2001**, 396, 9-15.

4.   I. Idris, and O. Sugiura, "Hydrogen-Free Plasma-Enhanced Chemical-Vapour-Deposition of Silicon Dioxide Using Tetra-Isocyanate-Silane (Si(NCO)₄)", Japanese Journal of Applied Physics Part 2-Letters, **1995**, 34, L772-L774.

5.   A. Grill, and V. Patel, "Low dielectric constant films prepared by plasma-enhanced chemical vapour deposition from tetramethylsilane", Journal of Applied Physics, **1999**, 85, 3314-3318.

6.   M.S. Kang, T.H. Chung, and Y. Kim, "Plasma enhanced chemical vapour deposition of nitrogen-incorporated silicon oxide films using TMOS/N₂O gas", Thin Solid Films, **2006**, 506, 45-49.

7.   J.O. Jensen, "Vibrational frequencies and structural determinations of tetraisocyanatosilane", Spectrochimica Acta Part a-Molecular and Biomolecular Spectroscopy, **2003**, 59, 937-947.

8.   D.W. Berreman, "Infrared Absorption at Longitudinal Optic Frequency in Cubic Crystal Films", Physical Review, **1963**, 130, 2193.

9.   C.T. Kirk, "Quantitative-Analysis of the Effect of Disorder-Induced Mode-Coupling on Infrared-Absorption in Silica", Physical Review B, **1988**, 38, 1255-1273.

10.   D.E. Clark, E.C. Ethridge, M.F. Dilmore, and L.L. Hench, "Quantitative-Analysis of Corroded Glass Using Infrared Frequency-Shifts", Glass Technology, **1977**, 18, 121-124.

11.   D.E. Clark, M.F. Dilmore, E.C. Ethridge, and L.L. Hench, "Aqueous Corrosion of Soda-Silica and Soda-Lime-Silica Glass", Journal of the American Ceramic Society, **1976**, 59, 62-65.

12.   W.A. Lanford, H.P. Trautvetter, J.F. Ziegler, and J. Keller, "New Precision Technique for Measuring Concentration Versus Depth of Hydrogen in Solids", Applied Physics Letters, **1976**, 28, 566-568.

13.   J.R. Tesmer, and M. Nastasi, "Handbook of modern ion beam materials analysis", Materials Research Society, **1995**.

14.   D. Grambole, T. Wang, F. Herrmann, and F. Eichhorn, "Hydrogen redistribution in titanium due to bending stress studied by micro ERDA", Nuclear Instruments & Methods in Physics Research Section B-Beam Interactions with Materials and Atoms, **2003**, 210, 526-530.

15.   F. Herrmann, and D. Grambole, "The New Rossendorf Nuclear Microprobe", Nuclear Instruments & Methods in Physics Research Section B-Beam Interactions with Materials and Atoms, **1995**, 104, 26-30.

16. M. Toth, C.J. Lobo, G. Hartigan, and W.R. Knowles, "Electron flux controlled switching between electron beam induced etching and deposition", Journal of Applied Physics, **2007**, 101.

17. D. Wang, P.C. Hoyle, J.R.A. Cleaver, G.A. Porkolab, and N.C. Macdonald, "Lithography Using Electron-Beam-Induced Etching of a Carbon-Film", Journal of Vacuum Science & Technology B, **1995**, 13, 1984-1987.

18. T. Bret, Physico-chemical Study of the Focused Electron Beam Induced Deposition Process. 2005, EPFL: Lausanne. p. 238.

19. T. Bret, I. Utke, A. Bachmann, and P. Hoffmann, "In-situ control of the focused-electron-beam-induced deposition process", Applied Physics Letters, **2003**, 83, 4005-4007.

20. K. Mølhave, D.N. Madsen, S. Dohn, and P. Bøggild, "Constructing, connecting and soldering nanostructures by environmental electron beam deposition", Nanotechnology, **2004**, 15, 1047-1053.

21. I. Utke, J. Michler, P. Gasser, C. Santschi, D. Laub, M. Cantoni, P.A. Buffat, C. Jiao, and P. Hoffmann, "Cross section investigations of compositions and sub-structures of tips obtained by focused electron beam induced deposition", Advanced Engineering Materials, **2005**, 7, 323-331.

22. Z. Cui, P.D. Prewett, and J.G. Watson, "Focused ion beam biased repair of conventional and phase shift masks", Journal of Vacuum Science & Technology B, **1996**, 14, 3942-3946.

23. T. Liang, and A. Stivers "Damage-free mask repair using electron beam induced chemical reactions", Proceedings of SPIE - The International Society for Optical Engineering, **2002**, 4688, 375-384.

24. H. Nakamura, H. Komano, K. Norimatu, and Y. Gomei, "Silicon-Oxide Deposition into a Hole Using a Focused Ion-Beam", Japanese Journal of Applied Physics Part 1-Regular Papers Short Notes & Review Papers, **1991**, 30, 3238-3241.

25. M. Ogasawara, M. Kariya, H. Nakamura, H. Komano, S. Inoue, K. Sugihara, N. Hayasaka, K. Horioka, T. Takigawa, H. Okano, I. Mori, Y. Yamazaki, M. Miyoshi, T. Watanabe, and K. Okumura, "Beam induced deposition of an ultraviolet transparent silicon oxide film by focused gallium ion beam", Applied Physics Letters, **1996**, 68, 732-734.

26. P.D. Prewett, B. Martin, A.W. Eastwood, and J.G. Watson, "Effects of Focused Ion-Beam Reticle Repair on Optical Lithography at I-Line and Deep-Ultraviolet Wavelengths", Journal of Vacuum Science & Technology B, **1993**, 11, 2427-2431.

CHAPTER 5

GROWTH DYNAMICS: EFFECT OF ELECTRON FLOWS

In this chapter are reported and compared the results related to the growth kinetics of the $SiO_xC_yH_\alpha$ and of the pure SiO_2 films obtained in Chapter 4, as function of the electron flows crossing the deposit surface. The precursor flows remained constant to those used in the previous chapter. The electron flows were varied by using different substrate materials and irradiation parameters (acceleration voltage, probe current). This provided explanations to the role of electrons during the deposition process.

Does the substrate atomic number influence the growth kinetics of these materials? Does the chemical composition obtained vary with the probe current and acceleration voltage? What is the dependence of the chemical compositions deposited on the dwell and replenishment times under constant precursor flows?

It is demonstrated that the deposition rate is related to the electron emission of the surface and low-energy electrons were demonstrated to be the main actors of the deposition process. Unlike conventional FEBID, the O_2 assisted FEBID process appeared insensitive to electron density in our equipment. Variations of dwell and replenishment times showed that O_2 assisted FEBID behaved similarly than other gas assisted particle induced process, with higher efficiencies at low dwell times and large replenishment times. Finally, side thermal effects leading to uncontrolled growth are presented.

5.1 Influences of substrate material

In Figure 5-1 are reported the *thickness vs. time* characteristics for series of deposits obtained under constant irradiation parameters, on an Au coated Si substrate, and on a plain Si substrate. The materials grew faster on heavy substrates. Injecting O_2 increased the deposition efficiencies (in terms of atom deposition rate per second, see Chapter 7. This trend was observed for all the precursors, and is presented in the case of TMOS alone and TMOS + Oxygen mixed in the threshold ratio, which corresponded to the highest growth rate measured. The gradual effects of increasing the O_2 flow on the growth rates are presented for the other precursors in Chapter 6.
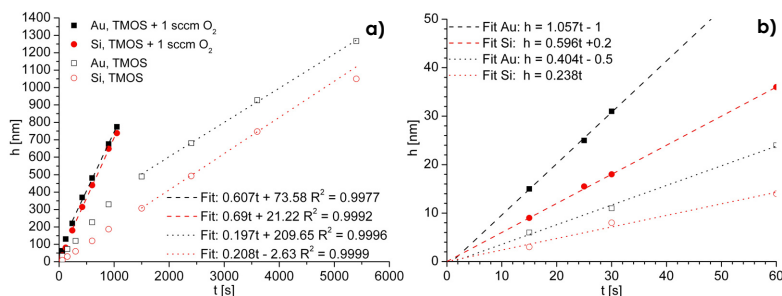
Figure 5-1: FEBID films (40 x 50 μm^2) thickness as function of deposition time, substrate material, and presence of additional Oxygen. (a) Comparison of final growth rates at [O₂] / [TMOS] = 0 and [O₂]/[TMOS] = 0.6, showing linear growth. (b) First 60 s of growth, showing higher deposition rate on Au than on Si, and influence of O₂ flow (error bars ± 5 nm).

The curves presented two distinctive regions: the initial growth rate (for thicknesses below 30 nm), and the final growth rate (thicknesses above 200 nm).

The dotted and dashed lines in Figure 5-1 a) are trendlines showing that the final growth rate was independent of the substrate material (shown by the identical slopes of the lines), and was approximately 3 times larger with Oxygen than without. The similar growth rates measured were due to the constant electron emission from the substrate above a thickness of 200 nm

approximately, since the FEB was mainly interacting with the FEBID material (see d_{BSE} in Figure 5-2), and the resulting electron emission constant, which lead to a constant number of electrons crossing the deposit interface and hence growth rate.

In the first 20 nm of growth however, the FEB materials grew faster on heavy substrates, see Figure 5-1 b). The deposited thickness varied linearly with the deposition time, and grew 1.7 times faster on Au than on Si. The growth rate ratios between the O_2 assisted depositions and the conventional depositions appeared slightly higher on Au than on Si, 2.7 and 2.6 respectively.

The following model was applied to demonstrate that these deposition rates were related to the substrate electron emission. There are three different types of electrons, see Figure 5-2 : [1]
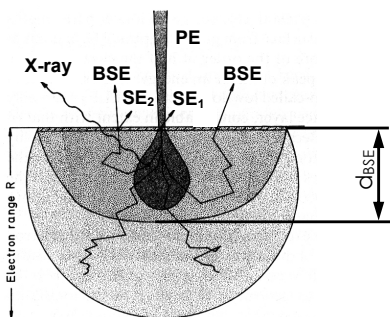
Figure 5-2: Electron beam – material interactions. SE1s are emitted from PEs at the irradiated spot, and SE2s from BSEs. Ds = maximum depth from which BSE can be re-emitted from substrate.

- the primary electrons (PE), of the incident beam,

- the back scattered electrons (BSE), which are PEs that experience large angle scattering events, and may exit the substrate at a significant distance from the incident beam. This volume of production is very large and can be estimated by the electron range R_m, defined as the length where the electron energy becomes zero. BSEs can escape the sample from a distance to the beam equal to the Bethe range R_b, and depth of approximately d_{BSE}, see Appendix 5.

- the secondary electrons (SE), are low energy electrons (< 50 eV by convention), produced by PE or BSE energy dissipation by inelastic interactions. SEs originate from less than 2 to15 nm deep in the sample, depending on the material. The total number of SE can be quantified by the SE yield δ. SE produced by the PE electrons, the SE1, have to be distinguished from that produced by back-scattered electrons, the SE2. The ratio of SE2 over SE1 is represented by the factor β, which takes into account the angular and energy distribution of BSEs, β = δ$_{BSE}$ / δ$_{PE}$. Its value ranges from 3 to 5 depending on the substrate material and acceleration energy.[2]

The secondary and the backscattered yields vary with the growing film thickness. The δ was influenced by the substrate material typically during the first 10-15 nm of growth, which corresponds to the SE extraction depth in insulators.[2] Above this thickness, it was equal to the SE yield of the deposited material. However, the total number of SE, n$_{SE}$, scaled with the number of primary and back-scattered electrons, respectively n$_{PE}$ and n$_{BSE}$ crossing the film surface, until the film was thick enough to contain the entire electron excitation volume d$_{BSE}$.[3, 4] The evolution of the number of secondary electrons with film thickness is summarized in the following equations (δ stands for the secondary electron yield of a thin layer producing only SE1, and has a η of 0):

$$General: \qquad n_{SE} = \delta_{Substrate}\ (n_{PE} + \beta n_{BSE}) \qquad Eq.5\text{-}4$$
$$d < 10\text{-}15\ nm \qquad n_{SE} = \delta_{Substrate}\ (1 + \beta_{Substrate}\eta_{Substrate})n_{PE} \qquad Eq.5\text{-}5$$
$$10\text{-}15\ nm < d < d_{BSE} \qquad n_{SE} = \delta_{Film}\ (1 + \beta\eta_{Film+Substrate})n_{PE} \qquad Eq.5\text{-}6$$
$$d_{BSE} < d \qquad n_{SE} = \delta_{Film}\ (1 + \beta\eta_{Film})n_{PE} \qquad Eq.5\text{-}7$$

The electron flow crossing the deposit surface can be written as:

$$\Phi_{e\text{-}}(t) = I_p\ (1 + \delta_{SE1}(t) + \eta_{BSE}(t) + \delta_{SE2}(t)) = I_p\ (1 + \delta_{SE1}(t) + \eta_{BSE}(t) + \beta\eta_{BSE}(t)) \quad Eq.\ 5\text{-}8$$

The following hypotheses were applied:

- Each electron type has a specific probability of decomposing the molecules, and should be assigned a cross-section

- The PE and BSE emitted at normal incidence have identical chances of decomposing a molecule, due to their similar energy

- The probability to induce a decomposition reaction at the surface for SEs and BSEs depends on their exit angle. The effective SE and BSE increase by the factor β:[3, 4]

$$\sigma_{SE} = \int_{\theta} \delta(t,\theta)\sigma_{SE}(\theta)d\theta \Rightarrow \overline{\sigma}_{SE} = \delta_{Film}(1+\beta\eta(t))\sigma_{SE} \qquad Eq.5\text{-}9$$

$$\sigma_{BSE} = \int_{\theta} \eta(t,\theta)\sigma_{BSE}(\theta)d\theta \Rightarrow \overline{\sigma}_{BSE} = \beta\eta(t)\sigma_{BSE\_Normal\ incidence} = \beta\eta(t)\sigma_{PE} \qquad Eq.5\text{-}10$$

The decomposition rate can hence be expressed as:[3]

$$R = \, \propto I_p \, (\sigma_{PE} + \delta_{SE\_film}(1+\beta\eta_{BSE}(t))\sigma_{SE} + \beta\eta_{BSE}(t)\sigma_{PE}) \quad Eq.\ 5\text{-}11$$

Equation 5-11 simplifies to:

$$R = \, \propto I_p \, ((1+\beta\eta_{BSE}(t))\cdot(\sigma_{PE}+\delta_{SE\_film}\sigma_{SE})) \quad Eq.\ 5\text{-}12$$

Hence, the growth rate ratio in the first nano-meters of growth simplifies to:

$$\frac{R_{Au}}{R_{Si}} = \frac{1+\beta\eta_{Au}}{1+\beta\eta_{Si}} \quad Eq.5\text{-}13$$

The experimental Au / Si growth rate ratios obtained without additional Oxygen and with additional Oxygen were 1.7 and 1.8 in the initial steps. Injecting in Eq.5-13 these values together with the η of Si and Au at 10 kV, 0.48 and 0.18 respectively, (see Appendix 4) leads to:

$$\frac{(1 + \beta\cdot 0.48)}{(1 + \beta\cdot 0.18)} = 1.8 \Rightarrow \beta = 5 \qquad Eq.5\text{-}14$$

$$\frac{(1 + \beta_{O2\_assisted\ FEBID}\cdot 0.48)}{(1 + \beta_{O2\_assisted\ FEBID}\cdot 0.18)} = 1.7 \Rightarrow \beta_{O2\_assisted\ FEBID} = 4 \quad Eq.5\text{-}15$$

These values of β were in perfect accordance to that already published, and demonstrated the FEB deposition with and without additional Oxygen followed the electron emission form the substrate as function of the deposit thickness. This approach did however not allow the separation of the specific contributions of high and low energy electrons.

Summary of Effect of Substrate Material

- A simple model based on an electron emission ratio was adapted to this specific situation, and resulted in reasonable values of β

- The larger was the number of emitted electrons (i.e. the heavier the substrate), the larger was the growth rate

- Oxygen increased the efficiency of the deposition process

5.2 Specific contributions of high- and low-energy electrons

In order to complete the previous model, and separate the contributions of low-energy electrons of that of high-energy electrons, the following approach was applied to Oxygen assisted FEBID. Based on the observation that lowering the acceleration voltage increased the deposition rate (see § 5.3.1), and that Oxygen assisted FEBID was independent of the electron density in our deposition equipment (see § 5.3.2), I proposed a simple model based only on the number of low-energy electrons emitted from the surface. This model fitted with good agreement the experimental results obtained for depositions produced on a transparent substrate (producing only SE1) and other depositions produced on a bulk substrate (producing SE1 and SE2), see § 5.3.3, and demonstrated the paramount role of secondary electrons during O_2 assisted FEBID.

5.2.1 Effect of acceleration voltage

Decreasing the FEB acceleration voltage increased the film deposition rate. The average growth rates for 300 nm thick films deposited from TMS on a Au-coated Si and on a plain Si substrate are reported in Figure 5-3 as function of the acceleration voltage and the additional Oxygen flow. The specific increase and saturating characteristic of these curves are due to surface coverage competition of the O_2 and precursor molecules, which are discussed and presented in details in Chapter 6, § 6.1, pp- 6-2.

The average growth rate, determined by (thickness of films in homogenous part)*(area of the film)/(deposition time), contains the information of the initial and final growth rates, but does not allow to decouple the initial growth rate from the final growth rate. The average value can only be used to discuss qualitatively the effect of the different parameters.
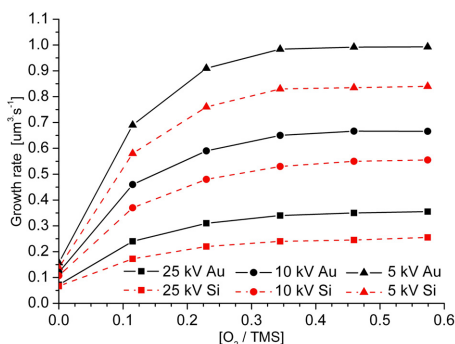
Figure 5-3: Average growth rates of 40 x 50 μm^2 films as function of the FEB acceleration voltage and the additional Oxygen flow.

Whatever the acceleration voltage, Oxygen had always an identical effect on the film growth rate, and neither the saturation level nor the film chemical composition was affected by the variation of the FEB energy. The previous trend presented in § 5.1 remained unchanged: the films grew faster on heavy substrates.

This increase of growth rate with decreasing acceleration voltage was already observed and accepted by the researchers to be due to the increasing SE yield

δ with decreasing energy.[5-9] However, the real situation in our setup is more complex, since additionally to increasing the number of secondary electrons, decreasing the acceleration voltage influences the SE1 and SE2 densities, since the diameter of the primary beam (producing SE1) increases, and the R_b (surface from which the BSE escape the sample) decreases.

The computations of electron densities variations is a complex task which requires using data (minimum extraction energy and minimum extraction depth of SE), given with large deviations, and resulting in errors easily reaching 50 %, which are not reliable for precise calculations. It also requires using simulation softwares that do not take into account the finite size of the FEB and considers it infinitely small, which is not realistic.

5.2.2 Effect of electron density

In the case of Oxygen assisted FEBID however, and for Oxygen flows corresponding to the threshold condition, the FEB processes appeared independent of the electron density. At 10 and 25 kV and for O_2 flows larger than the threshold ratio, the volume growth rate per nA was constant for probe currents of 50, 125 and 250 nA, see Figure 5-4 a). It was not affected by the change of electron density between these different currents; see Figure 5-4 b).
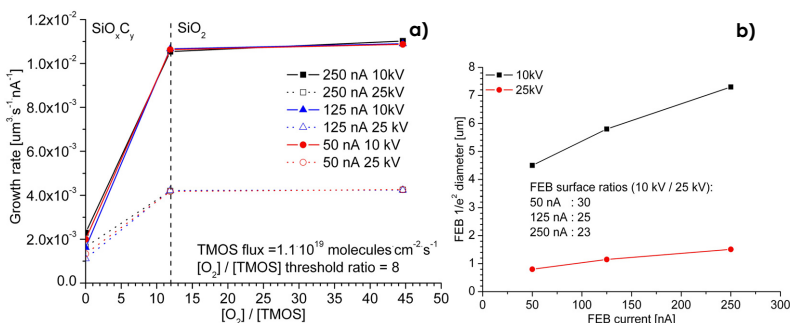
Figure 5-4: (a) Volume growth per nA, as function of the [O_2]/[TMOS] ratio; (b) FEB probe diameters for currents used in (a) as function of acceleration voltages

On the contrary, the results obtained without Oxygen showed that the volume growth rate per nA was larger for high probe currents, which demonstrated electron density effects (i.e. larger electron density = larger growth rate) on the deposition rate, as already reported. The contradictory results available in literature do not allow predicting the real influence of this parameter, which appears to depend on the precursor flows and irradiation conditions as well. [10-12]

5.2.3 Decoupling of electrons contributions

The previous result allowed proposing a simple model for O_2 assisted FEBID, based only on the number of electrons emitted as function of the acceleration voltage on specifically chosen substrates, and comparing it to the experimental results.

The decoupling between the different electron types was attempted by comparing the growth rates obtained on a substrate transparent to electrons to those obtained on a bulk sample. The transparent substrate consisted of a free-standing 60 nm thick Si_3N_4 membrane (BSE yield of 1% at 10 kV, and 0.08% at 25 kV), supported by a surrounding Si structure, used as the bulk substrate (BSE yield of 14.8 % at 10 kV and 14.5 % at 25 kV), see Figure 5-5. There were hence much lower BSEs and SE2s on the membrane than on the bulk substrate.

40 x 40 μm^2 square deposits were produced half on the membrane and half on the bulk substrate, see Figure 5-5, using a 125 nA FEB of 10 and 25 keV (respective $1/e^2$ diameters of 5.8 and 1 μm). The FEB was controlled by NPGS (center-to-center = line-spacing = 50 nm, dwell time = 13 μs). The pattern was scanned a chosen number of times in order to deposit a measurable thickness of about 60 nm. The precursor used was TMS, and TMS + O_2 mixed in a threshold ratio (highest deposition rate).
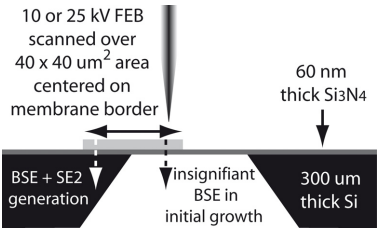
Figure 5-5: side-cut scheme of the experiment. Thickness measurements were done by AFM, after evaporation of a 50 nm thick Au layer on both sides of the sample that avoided membrane deflection during AFM scans.

The experimental deposition rates were measured by AFM on the transparent membrane and on the opaque substrate and are reported in Table 5-1, as function of the Oxygen flow and of the FEB energy.

O_2 [sccm]	Membrane		Bulk	
	10 kV	25 kV	10 kV	25 kV
0	0.15	0.07	0.30	0.18
1	3.25	1.08	4.45	1.58

Table 5-1: Measured initial growth rates per layer (0.5 second) as function of the O_2 co-flow and substrate

With no additional Oxygen, the material grew 50 and 60 % slower on the membrane than on the bulk, at 10 and 25 kV respectively. This ratio increased to 74 and 68 % with a 1 sccm O_2 flow.

The comparison of these numbers with the respective electron yields of the different substrates required the simulation of the latter using Mocasim®. The total theoretical yields of secondary electrons $\delta_{(SE\ 1\ +\ SE\ 2)}$ of the 60 nm thick membrane at 10 and 25 kV were 21 and 3 % respectively (± 3 according to Mocasim® simulations). The back-scattering coefficients of the membrane were as low as 1 and 0.08 % at 10 and 25 kV respectively.

However, the actual back-scattering yield of the membrane shown in Figure 5-5 was affected at 25 kV by BSE escaping from the underlying Si substrate, and emitted under an angle allowing them to cross the free-standing membrane and create a non negligible number of SE2 electrons, see Figure 5-6.

This happened when the Si thickness was thinner than the electron range R_m, and this number of parasitic BSE could reach 15 % depending on the position of the primary beam. The precise number of parasitic BSE electrons could not be calculated.

Majority of these BSE had grazing incidence on the membrane, which meant the probability of producing SE2 was high. Hence the results obtained on the membrane at 25 kV were not relevant of the theoretical ideal situation, and were not taken under consideration.
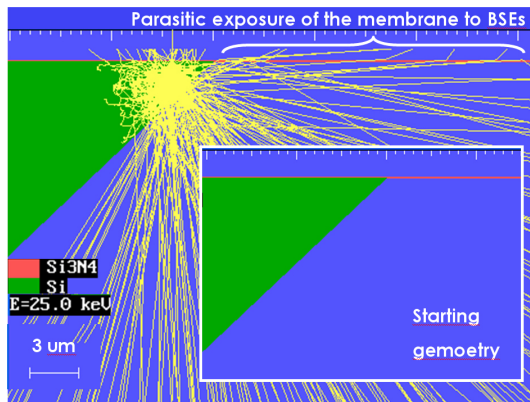
Figure 5-6: Monte-Carlo simulations of the parasitic exposure of the membrane to BSE emitted from the underlying Si substrate, for a FEB irradiating at 3 um form the membrane border.

The theoretical back-scattering yields η of the bulk substrate (60 nm Si_3N_4 over Si) were equal to 14.8 and 14.5 % at 10 and 25 kV, respectively. The SE1 yield δ_{SE1} of the bulk and of the thin membrane were similar, and was approximated by simulating the interaction of a 10 and 25 keV beam with a 20 nm thick Si_3N_4 membrane (lowest thickness accepted by Mocasim), and setting the extraction energy to 50 eV. The SE2 yields δ_{SE2} were then obtained by $\delta_{(SE1 + SE2)} - \delta_{SE1}$. These different values are summarized in the Table 5-2.

Electron yield	Membrane		Bulk	
	10 kV	25 kV	10 kV	25 kV
δ_{SE1}	0.091	0.011	0.091	0.011
δ_{SE2}	0.122	0.018	0.216	0.108
η	0.01	0.008	0.148	0.146

Table 5-2: Simulated electron yields as function of substrate and acceleration voltage

Summing SE1 and SE2 electrons on the different substrates lead to the following total number of SE emitted as function of the parameters, see Table 5-3:

SE total yield	Membrane		Bulk	
	10 kV	25 kV	10 kV	25 kV
δ	0.213	0.029	0.307	0.119

Table 5-3: Simulated total SE yield as function of substrate and acceleration voltage

Considering that secondary electrons determine the deposition rate, theoretical growth rate ratios could be calculated for all the possible combinations of substrate and acceleration voltages (apart the results at 25 kV on membrane). These total SE yield ratios are reported in Table 5-4, and compared to the experimental deposition rate values obtained during Oxygen assisted FEBID from Table 5-1.

Ratio Substrate_a $V_{acc}y$ / Substrate_b $V_{acc}x$	Theoretical	Experimental
Membrane 10 kV / Bulk 10 kV	0.69	0.74
Membrane 10 kV / Bulk 25 kV	1.73	2.03
Bulk 10 kV / Bulk 25 kV	2.5	2.8

Table 5-4: Comparison of the theoretical ratio of low-energy electrons emitted as function of the acceleration voltage and substrate, with the experimental values of growth rate measured

The theoretical numbers obtained are in satisfying accordance with the experimental results, but were always 10 % lower. As a conclusion, the total number of secondary electrons emitted was not sufficient to explain the

differences in growth rates observed, although they appeared to realize the main contribution of 90%.

This high contribution was visible as well on the optical micrographs of the films produced, see Figure 5-7. The deposits obtained with no additional Oxygen appeared with rounded corners on the bulk substrate and with a distinct thickness gradient perceptible on the film produced on the bulk substrate. This gradient is representative of proximity effects due to back-scattered electrons, and demonstrated the importance of back-scattered electrons density during conventional FEBID.

The deposits produced with additional Oxygen presented rounded corners on the bulk sample side, but straight corners at the bulk-membrane border, which indicated a large contribution of secondary electrons in these conditions, and the low influence of BSEs on the deposition process. This suggested a lower threshold activation energy with additional O_2 as well.
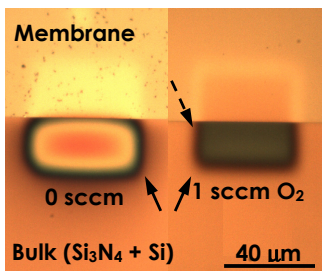
Figure 5-7: Optical micrographs (25 X) taken in reflection mode, of deposits as function of the O_2 co-flow. Solid arrows indicate rounded corners, and dashed arrows indicate the straight corners

The different contributions of high-energy and low-energy electrons might be due to the different electron ionization cross-sections of the molecules adsorbed on the surface, which show a maximum at energies close to that of SE, see Figure 5-8.[1] Angular distributions of BSE should be accounted for in an ideal model. The reactions induced by high- and low-energy electrons might also differ.

[1] Available online at
http://physics.nist.gov/PhysRefData/Ionization/index.html
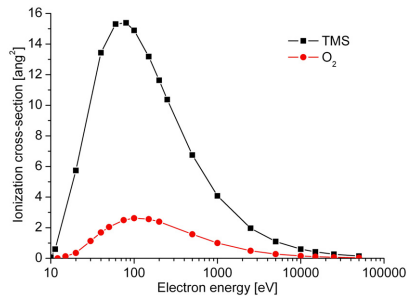
Figure 5-8: Ionization cross-sections of TMS and O_2 as function of incident electron energy

Summary of contributions of low- and high-energy electrons

- Lower acceleration voltages lead to higher deposition rates.

- Compared to conventional FEBID, O_2 assisted FEBID of films was independent of the electron density in our setup, and scaled linearly with the probe current

- The initiation of the oxidation reaction requires low amount of energy, and the process appears mainly driven by low-energy electrons

- However, high-energy electrons are not negligible, and might be the reason explaining the 10 % deviation of the theoretical values to the experimental results.

5.3 Effect of dwell and replenishment times

Dwell and replenishment times are paramount parameters of particle induced chemical processes, known to influence the efficiency of the reactions taking place under a focused beam.[13-17] The particle induced process efficiency is generally larger for short dwell times (< 1 µs) and long replenishment times (>100 µs).

The following experiment demonstrated that the oxide quality obtained by Oxygen assisted FEBID depended similarly on these parameters. Keeping the irradiation conditions constant (125 nA and 10 keV), deposits were produced with varying replenishment and dwell times, by operating the SEM in TV scan mode and varying the magnification between 2 ad 16 kX.

The precursors used were TMS and TEOS, mixed with specifically chosen Oxygen flows. The chemical compositions of the deposits were then measured and are reported in Figure 5-9, together with the respective dwell and replenishment times corresponding to each magnification

M [kX]	Maximum Dwell Time [µs]	Minimum Replenishment time [µs]
2	6.03	63.37
4	12.06	57.37
8	24.12	45.27
16	48.24	21.14
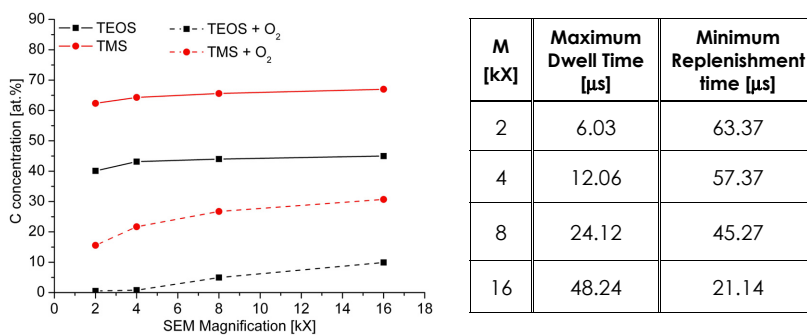
Figure 5-9: Deposited C concentration in film obtained from TEOS and TMS with and without additional Oxygen (respectively dashed and solid lines), as function of the magnification used for the deposition in TV scan mode.
The TEOS and TMS flows used for the experiments were $1.9 \cdot 10^{18}$ and $1.2 \cdot 10^{21}$ molecules$\cdot$cm$^{-2}\cdot$s^{-1}.
Additional O_2 flows were 1 and 5 sccm for TMS and TEOS respectively, corresponding to [O_2]/ [precursor] ratios of 0.01 and 400 for TMS and TEOS respectively. Deposited material: SiO_2 at 2 and 4 kX only for TEOS, and $SiO_xC_yH_\alpha$ for TMS.
Table on the right reports the maximum dwell time and the minimum replenishment time for each magnification. Data copied from Table 3-1.

The flows of the different molecules were specifically chosen to provide:

- 2 sets of data (one for TMS and one for TEOS) without Oxygen in order to compare the differences inter-precursors

- 1 set of data were pure SiO_2 was deposited at 2 kX (corresponding to the TEOS + O_2 experiment) to follow the elements concentration as function of the magnification

- 1 set of data where Oxygen was added, but the deposited material still contained C at 2 kX (corresponding to the TMS + O_2 flow here).

Using this approach, the dwell time and the replenishment time could not be chosen independently. The long replenishment time between two successive filed scans in TV scan mode remained constant whatever the magnification (about 15 ms).

The Carbon concentration decreased with increasing replenishment time and decreasing dwell time, to the advantage of the Oxygen and Silicon incorporated in the material (not shown here). This dependency of the C concentration was amplified when additional Oxygen was injected together with the precursor molecules, as shown by the larger slopes of the dashed lines in Figure 5-9.

The results obtained with no additional Oxygen showed a poor sensitivity to the variation of the dwell and replenishment times. This could be explained by accounting for the presence of residual water as oxidant agent in the experiments performed with no additional Oxygen. Water is a sticking molecule, and it is expected that the amount of adsorbed molecules is sufficient to not be consumed even at large dwell times. In Chapter 6, pp. 6-11 to 6-13, is demonstrated that residual water is the main agent responsible for the Oxygen incorporation effect in the deposited materials, which supports the explanation proposed here. The C etching from residual water should however depend on the molecule reactivity to water. These differences should probably be visible at identical precursor flows, which was not the case here.

The C increase as function of the dwell time was amplified in the presence of Oxygen. Oxygen and precursor molecules have different interactions with the surfaces, and Oxygen is expected to have a lower sticking coefficient than the organosilanes (residence times of 10^{-11} and 10^{-5} seconds respectively).[18] Hence, under electron irradiation, the consumption of Oxygen molecules is faster than the consumption of precursor molecules. The resulting C etching efficiency depends then on the number of O_2 molecules present on the surface, and once this is depleted, C starts building in the material. As shown in Figure 5-9, the deposits obtained from TEOS and additional Oxygen mixed in a threshold ratio (maximum deposition rate) consisted of pure SiO_2 at 2 and 4 kX (dwell times of 6 and 12 µs respectively), but C was detected at 8 kX (dwell time of 24 µs). The limit dwell time was hence between 12 and 24 µs. The experiments performed by NPGS (pp. 5-9, pp. 4-22) with a dwell time of 13 µs were hence resulting in similar irradiation conditions in terms of dwell time than the TV scan. The similar slopes of both curves might indicate that the phenomenon was only related to Oxygen surface coverage.

Similar experiments performed in a Nova 600 Dual beam System from FEI, showed the same trends as function of dwell and replenishment times than those observed in the S100. The only precursor available on the dal beam system was TEOS, mixed with H_2O in a 1:2 ratio.[19] The results obtained are hence not directly comparable to those obtained in the S100 with different chemistries. The results are reported in Table 5-5.

Dwell time [µs]	Replenishment time [ms]	C [at.%]	O [at.%]	Si [at.%]
0.2	20	2.29	62.21	35.5
0.5	20	4.52	65.27	30.21
1	20	6.04	64.14	29.81
0.5	10	5.24	65.41	29.34
0.5	20	4.52	65.27	30.21
0.5	30	4.09	61.76	34.15

Table 5-5: Effects of dwell and replenishment times on Chemical composition of films deposited in the FEI dual Beam system

The results indicate that lowering the dwell time to the smallest value possible, 200 ns is more efficient than increasing the replenishment time from 10 to 30 ms. The material obtained with the lowest dwell time (200 ns) and the highest replenishment time (20 ms) did not lead to the production of a C-free material, which indicated that the electron density of the FEB might be an important parameter (or limitation) in modern machines, or that the built-in mixing ratio is not suited to the deposition of pure SiO_2. A high electron density induces a large and fast consumption of the adsorbed Oxygen, and depleted regions appear, only rich in TEOS molecules. Electron density effects can then occur, which could explain that SiO_2 could not be deposited in the dual beam. However the trend was similar that that obtained in the low density S100 deposition machine.

Surface diffusion of oxidant molecules might be as well an important parameter during high dwell time depositions, as suggested by the C concentration gradient obtained in a deposit produced by decomposing in the S100, TEOS and additional Oxygen under a defocused (diameter of 40 µm) 125 nA FEB, see Figure 5-10. The replenishment time of such a deposition is decreased to 0, and the dwell time is identical to the deposition time (6 min). The resulting structure was a 3-D dome, and presented gradients of elements concentrations.
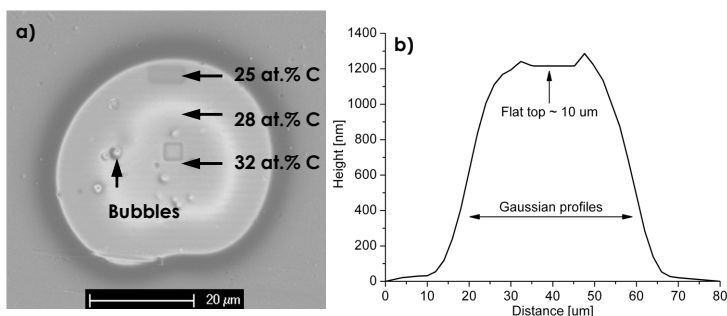
Figure 5-10: (a) SEM micrograph (top view) of the deposit obtained by defocusing the FEB to a 40 µm spot. (b) Measured profile through deposit center.

The C concentration in the deposit was larger in the center than in the surroundings, respectively 32 and 25 at.%, see Figure 5-10 a). The line profile of the deposit is shown in Figure 5-10 b).

Since the deposition was not affected by electron density effects, as presented in § 5.2.2, pp 5-8, this demonstrated that the amount of Carbon in the deposited material was affected by the surface diffusion of molecules in the case of long exposures times and zero replenishment times. The latter conditions limited the number of effective molecules supplied in the center of the deposit, which resulted in a lower C etching efficiency.

Summary of Dwell and Replenishment time

- The C concentration in the deposited films produced with and without additional Oxygen could be increased by increasing the dwell time and decreasing the replenishment time. In our SEM, with a 125 nA and 10 keV FEB, the limit dwell and replenishment times were 12 and 57 µs, respectively. In the case of O_2 assisted FEBID, the increase of Carbon was due to the consumption of the total amount of Oxygen molecules on the surface before the end of the dwell time, and the Carbon stemmed from the decomposition of the precursor molecules. When depositing from precursor vapours alone, residual water supplied enough molecules to the deposition area and lowered the incorporated C concentration

- The results showed a similar behaviour than other gas assisted focused particle beam induced reactions, and was a competition between a particle physical reaction (such as bond cleavage) occurring at low replenishment times and high dwell times, and a particle induced chemical reaction of entities (such as initiation of an oxidation reaction) occurring most likely at high replenishment times and low dwell times

- This C concentration increase was independent of the precursor used, and was only slightly amplified in presence of Oxygen, which indicated that it was most likely depending on the oxidant concentration

- Molecule surface diffusion was responsible for the lower oxidation efficiency at high dwell times and zero replenishment times, leading to higher C contents

- Trends obtained in the S100 SEM by mixing an organosilane and an oxidant agent, are similar to that obtained in modern SEMs

5.4 Side-effect of electron flows

As presented in § 5.1 and 5.2, the growth rate of pure SiO_2 was linear with time, for thicknesses up to 600 nm approximately. For larger thicknesses, uncontrolled non-linear effects occurred, and the deposits evolved three-dimensionally. With TMOS, deposits produced up to 60 min were still 2-D films. The 3-D growth started at the deposit centre as a small extrusion, which grew with time in a pyramidal shape deposit with dimensions comparable to that of the scanned area (40 x 50 μm^2). In Figure 5-11 are presented various SEM micrographs showing the transition between the two deposition regimes.
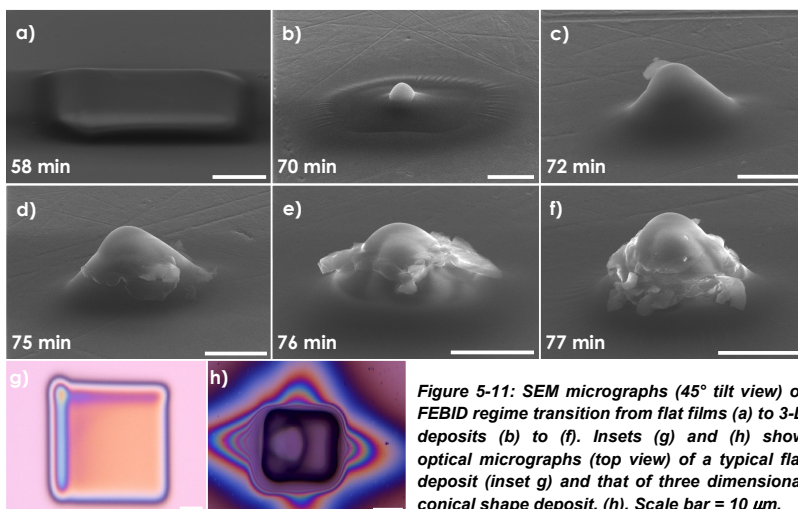
Figure 5-11: SEM micrographs (45° tilt view) of FEBID regime transition from flat films (a) to 3-D deposits (b) to (f). Insets (g) and (h) show optical micrographs (top view) of a typical flat deposit (inset g) and that of three dimensional conical shape deposit, (h). Scale bar = 10 µm.

The resulting deposit consisted of a smooth core with free-standing thin layers. The limit thickness marking the transition of the two deposition regimes was

lower at low acceleration voltages. It occurred for film thicknesses that contained the entire FEB excitation volume: 800 nm at 10 kV, and 300 nm at 5 kV. This indicated that the origin of the phenomena originated from the electron-matter interactions.

The inner part of these 3-D deposits was investigated by milling half of a deposit using a focused ion beam. The results are presented in Figure 5-12. The core consisted of solid material, without asperities, bubbles or porosities visible at this scale. The high charging of the material prevented from high-resolution imaging. Back-scattering imaging showed that the material was homogenous, so did Focused Ion Beam imaging, see Figure 5-12 b) and c).
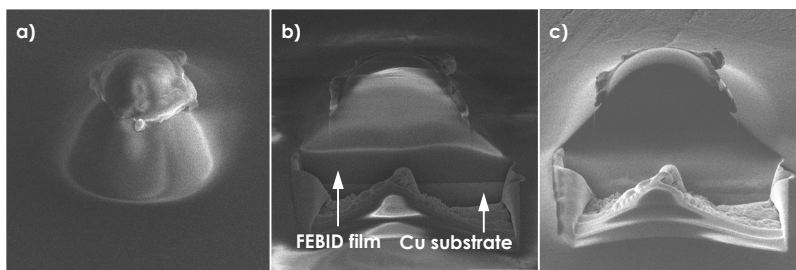
Figure 5-12: (a) As-deposited 3-D deposit. 52° tilt view SEM micrograph. (b) Back-scattered image of cross-section, showing solid core neither asperities nor porosity). Cu substrate visible. (c) Secondary electron image of cross-section, obtained by irradiating with the focused ion beam. Scale bar = 5 μm.

Although these deposits were produced using a [O₂]/[TMOS] ratio equal to the threshold ratio, Carbon could be detected by EDX, in gradually decreasing concentrations from the core to the surrounding layers (respective average concentrations of 10 and 3 at.%). Oxygen was homogenously distributed in the material with an average concentration of 72 at %. Only the Si concentration varied with the Carbon decrease, between 18 and 25 at.%. This indicated that during the 3-D deposition, the reaction was not driven only by the electrons.

SiO_2 is known to be unstable to electron irradiation. Kalceff demonstrated how complex and interesting asperities and annular outgrowths could be produced from bulk silica samples using comparable FEB conditions than those used in this study.[20-26] The rearrangement reactions are attributed to charges trapped in

the lattice, that induce high intensity electric fields which can lead to the production of peroxy linkages (creation of Si-O-O, and Si-O-O-Si), formed by incorporation of surface Oxygen in the lattice, which causes an expansion of the material, and the production of gaseous O and O_2.[20]

However, the geometries obtained here were produced from thin films, and the structural rearrangement of the 1600 μm^3 film grown in 58 minutes (shown in Figure 5-11 a) to the 10000 μm^3 pyramidal deposits grown in 77 minutes (shown in Figure 5-11 f) would necessarily induce the presence of visible porosities in the material. This excluded the option of structural rearrangements to explain the 3-D depositions, and suggested another mechanism such as thermal decomposition was the predominant actor of this phenomena.

The surface temperature increase induced by a stationary FEB impinging on a bulk SiO_2 surface which contains the entire excitation volume (thickness of 800 nm), was calculated using the following equation:[27]

$$\Delta T = 3 V_{acc} \cdot I_p \cdot \frac{(1-\eta)}{2\pi\varkappa(R_m + d_{FEB})} \qquad Eq.\ 5\text{-}16$$

with V_{acc} and I_p the FEB acceleration voltage and probe current, R_E the electron range in SiO_2 (1.4 μm), d_{FEB} the FEB diameter (5.8 μm), κ the thermal conductivity of SiO_2 (1.38 $W \cdot m^{-1} K^{-1}$) and η the back-scattering yield of SiO_2 at 10 kV (0.12). The resulting temperature increase under the experimental conditions used here (125 nA), was 53 K and 26 K for a 10 and a 5 kV FEB respectively. The respective temperature increase of a 5 kV beam was 26 K. With a 25 kV FEB (ΔT = 100 K approximately), no such effect was visible until a deposited thicknesses of 1200 nm, which indicated that the Au substrate was efficiently evacuating the temperature.

It is reasonable to attribute these uncontrolled outgrowths to this low thermal energy accumulated, and this is in good accordance with the previous result that demonstrated that secondary electrons had already sufficient energy to initiate a deposition reaction.

Summary of non linear growth

- The deposition process changed from a homogenous and 2-D growth to an uncontrolled 3-D growth when the thickness of the film reached the electron range R_m, due to heating of the film.

- The thermal activation energy of the oxidation reaction might be as low as 25 K approximately, which suggests that O_2 assisted FEBID was a sensitive equilibrium between electron driven reactions and thermal decomposition.

5.5 Conclusions of Chapter 5

- Additional Oxygen increased the deposition efficiency in terms of growth rate, under constant irradiation parameters

- The growth kinetics showed to follow the electron emission of the substrate, and was proportional to the number of secondary electrons. The latter type of electrons achieved 90 % of the deposition process

- The oxidation efficiency was function of the dwell and replenishment times and related to the consumption of the Oxygen molecules on the surface

- The irradiation conditions for high growth rates and low C concentration are: large number of low-energy electrons, low dwell time, and low electron density

- Thermal effects were significant only when the film thickness was large enough to contain the entire FEB excitation volume, which lead to the largest surface temperature increase. Low thermal energy, 25 K, was sufficient to initiate the thermal decomposition

5.6 Bibliography of Chapter 5

1.	L. Reimer, *Scanning Electron Microscopy, Physics of Image Formation and Microanalysis*, Second edition, Springer-Verlag, Optical Sciences Series, Vol. 45, 1998.

2.	H. Seiler, *"Secondary Electron Emission in the Scanning Electron Microscope"*, *Journal of Applied Physics*, **1983**, *54*.

3.	T. Bret, *Physico-chemical Study of the Focused Electron Beam Induced Deposition Process*. 2005, EPFL: Lausanne. p. 238.

4.	H. Kanter, *"Contribution of Backscattered Electrons to Secondary Electron Formation"*, *Physical Review*, **1961**, *121*, 681-&.

5.	M. Takai, W. Jarupoonphol, C. Ochiai, O. Yavas, and Y.K. Park, *"Processing of vacuum microelectronic devices by focused ion and electron beams"*, *Applied Physics a-Materials Science & Processing*, **2003**, *76*, 1007-1012.

6.	S. Lipp, L. Frey, C. Lehrer, B. Frank, E. Demm, S. Pauthner, and H. Ryssel, *"Tetramethoxysilane as a precursor for focused ion beam and electron beam assisted insulator (SiOx) deposition"*, *Journal of Vacuum Science & Technology B*, **1996**, *14*, 3920-3923.

7.	K.L. Lee, and M. Hatzakis, *"Direct Electron-Beam Patterning for Nanolithography"*, *Journal of Vacuum Science & Technology B*, **1989**, *7*, 1941-1946.

8.	K.T. Kohlmannvonplaten, J. Chlebek, M. Weiss, K. Reimer, H. Oertel, and W.H. Brunger, *"Resolution Limits in Electron-Beam-Induced Tungsten Deposition"*, *Journal of Vacuum Science & Technology B*, **1993**, *11*, 2219-2223.

9.	P.C. Hoyle, J.R.A. Cleaver, and H. Ahmed, *"Ultralow-Energy Focused Electron-Beam-Induced Deposition"*, *Applied Physics Letters*, **1994**, *64*, 1448-1450.

10.	R.W. Christy, *"Formation of Thin Polymer Films by Electron Bombardment"*, *Journal of Applied Physics*, **1960**, *31*, 1680-1683.

11.	S. Matsui, and T. Ichihashi, *"Insitu Observation on Electron-Beam-Induced Chemical Vapour-Deposition by Transmission Electron-Microscopy"*, *Applied Physics Letters*, **1988**, *53*, 842-844.

12.	V. Scheuer, H. Koops, and T. Tschudi, *"Electron beam decomposition of carbonyls on silicon"*, *Microelectronic Engineering*, **1986**, *5*, 423-430.

13.	M. Fischer, H.D. Wanzenboeck, J. Gottsbachner, S. Muller, W. Brezna, M. Schramboeck, and E. Bertagnolli, *"Direct-write deposition with a focused electron beam"*, *Microelectronic Engineering*, **2006**, *83*, 784-787.

14.	C. Santschi, M. Jenke, P. Hoffmann, and J. Brugger, *"Interdigitated 50 nm Ti electrode arrays fabricated using XeF2 enhanced focused ion beam etching"*, *Nanotechnology*, **2006**, *17*, 2722-2729.

15.	K.T. Kohlmann, L.M. Buchmann, and W.H. Brunger, *"Repair of Open Stencil Masks for Ion Projection Lithography by E-Beam Induced Metal-Deposition"*, *Microelectronic Engineering*, **1992**, *17*, 427-430.

16.	H.C. Petzold, and P.J. Heard, *"Ion-Induced Deposition for X-Ray Mask Repair - Rate Optimization Using a Time-Dependent Model"*, *Journal of Vacuum Science & Technology B*, **1991**, 9, 2664-2669.

17.	M. Amman, J.W. Sleight, D.R. Lombardi, R.E. Welser, M.R. Deshpande, M.A. Reed, and L.J. Guido, *"Atomic force microscopy study of electron beam written*

contamination structures", Journal of Vacuum Science & Technology B, **1996**, *14*, 54-62.

18. J.H. de Boer, *The dynamical character of adsorption*, Clarendon Press, Vol. 2nd ed., 1968.

19. FEI_technician, *Personal communication*, **2007**.

20. M.A.S. Kalceff, *"Cathodoluminescence microcharacterization of the defect structure of irradiated hydrated and anhydrous fused silicon dioxide", Physical Review B*, **1998**, *57*, 5674-5683.

21. M.A.S. Kalceff, and M.R. Phillips, *"Electron-Irradiation-Induced Outgrowths from Quartz", Journal of Applied Physics*, **1995**, *77*, 4125-4127.

22. M.A.S. Kalceff, M.R. Phillips, and A.R. Moon, *"Electron irradiation-induced changes in the surface topography of silicon dioxide", Journal of Applied Physics*, **1996**, *80*, 4308-4314.

23. M.A.S. Kalceff, G.J. Thorogood, and K.T. Short, *"Charge trapping and defect segregation in quartz", Journal of Applied Physics*, **1999**, *86*, 205-208.

24. M.A. Stevens-Kalceff, *"Electron-irradiation-induced radiolytic oxygen generation and microsegregation in silicon dioxide polymorphs", Physical Review Letters*, **2000**, *84*, 3137-3140.

25. J.P. Vigouroux, J.P. Duraud, A. Lemoel, C. Legressus, and D.L. Griscom, *"Electron Trapping in Amorphous Sio2 Studied by Charge Buildup under Electron-Bombardment", Journal of Applied Physics*, **1985**, *57*, 5139-5144.

26. M.A.S. Kalceff, *Irradiation induced specimen damage in an Environmental Scanning Electron Microscope*, in *Microbeam Analysis 2000, Proceedings*. 2000. p. 265-266.

27. I. Utke, J. Michler, P. Gasser, C. Santschi, D. Laub, M. Cantoni, P.A. Buffat, C. Jiao, and P. Hoffmann, *"Cross section investigations of compositions and sub-structures of tips obtained by focused electron beam induced deposition", Advanced Engineering Materials*, **2005**, *7*, 323-331.

CHAPTER 6
GROWTH DYNAMICS, EFFECTS OF GAS FLOWS

In the previous chapters, it was demonstrated that additional Oxygen allowed decreasing the contamination in the deposited materials, whatever the precursor tested, and that the O_2 assisted deposition mechanism differed from conventional FEBID. The activation of the oxidative deposition process had a much lower threshold value of electrons, and secondary electrons mainly contributed to the deposition process. The deposition dynamics were therefore electron limited.

This chapter addresses aspects of the growth kinetics related to the gas flows present in the chamber, under constant irradiation conditions (125 nA, 10 kV and 2 kX magnification). The latter parameters, already used in the previous chapters, revealed to be best suited for the study of deposition rates and compositions of the FEBID materials, and allowed producing materials from $SiO_xC_yH_\alpha$ to pure SiO_2 in reasonable deposition times.

Here, it is demonstrated that additional Oxygen influences the growth rates of the FEBID materials, either by boosting it (factor of 7) or by attenuating it (factor of 0.6). The effect depends on the reactivity to O_2 of the molecules, and the respective surface coverage of O_2 and precursors present on the surface. The surface occupation resulting of the co-adsorption of the two gases followed a surface competition. The latter provided explanations to the deposition mechanism and to the effect of additional Oxygen on the deposited chemical composition shown in Chapter 4.

The quantitative influence of the precursor flow variation on the deposition dynamics, mechanism and amount of Oxygen needed to deposit pure SiO_2 are presented and highlighted limitations due to this surface coverage of molecules influencing the FEBID efficiency.

6.1 Average growth rate as function of additional Oxygen

Gas assisted FEBID differs from conventional FEBID due to the presence of a second gas injected in the deposition area. I found necessary to briefly present the differences between the surface coverage phenomena related to the adsorption of a single gas, and that related to the co-adsorption of two different gases on a surface.

6.1.1 Background of (co-)adsorption of (two) gases on a surface

The adsorption dynamics of a single gas on a surface follows adsorption isotherms (such as the Langmuir-Hinselwood). The resulting surface coverage as function of the precursor flow impinging on the surface presents generally a rapid uptake with increasing flow, and then saturates. The saturation region indicates a total coverage of the surface by the molecules,[1] and is reached for a flow, specific to the molecule adsorption entropy. When a flow of electron is locally consuming this adsorbed phase, depending on the reaction efficiency and the molecules dynamics on the surface, the reaction can be either electron limited (i.e. there are always enough precursor molecules adsorbed and diffusing to the deposition area and the deposition rate is constant), or precursor limited (precursors molecules do not have the time to replenish the deposition area with fresh molecules, which leads to a depletion of the layer, and decrease of growth rate).

In gas-assisted FEBID, a second gaseous molecule is injected with the precursor molecules. When two gases co-adsorb on the same surface, the adsorption mechanism remains the same for each of them, however, the coverage of each molecule depends on the coverage of the other molecule. According to Langmuir-Hinselwood adsorption isotherm models, the specific surface coverage θ of each molecule resulting of the co-adsorption of two different molecules (Precursor and Oxygen as example) depends on their partial pressures and their enthalpies of adsorption by the following equations:[2]

$$\theta_{Precursor} = \frac{K_{Precursor}P_{Precursor}}{1+K_{Precursor}P_{Precursor}+K_{Oxygen}P_{Oxygen}} \quad Eq.6\text{-}1$$

$$\theta_{Oxygen} = \frac{K_{Oxygen}P_{Oxygen}}{1+K_{Precursor}P_{Precursor}+K_{Oxygen}P_{Oxygen}} \quad Eq.6\text{-}2$$

With P_x the partial pressures of gas x, and K_x the equilibrium constants for the adsorption of gas x. If a reaction happens to occur (initiated by electrons), the adsorption equilibrium remains undisturbed by the occurrence of such events between the two gases, and the reaction rate v is function of the product of the two coverages:[2]

$$v = k_r \theta_{Precursor}\theta_{Oxygen} \quad Eq.\ 6\text{-}3$$

$$k_r = k_0 \cdot e^{\frac{-Er}{RT}} \quad Eq.\ 6\text{-}4$$

The determination of the adsorption constants K_x, is difficult in FEBID processes, due to the numerous potential decomposition pathways of the precursor molecules. However, the previous equations highlight the main issue: depending on the different adsorption constants of each gas, there will be a surface coverage competition between the molecules.

Studies related to CVD of SiO_2 (generally obtained by mixing Oxygen, Ozone and Silanes) have reported such competition phenomena, and used the previous model to fit the experimental data successfully.[3-8] This surface competition appeared in the deposition rates which followed an increase, saturation and decrease behaviour as function of the additional O_2 flow.[9] These three regions are respectively attributed to the filling of the surface sites by the different molecules (increase of growth rate), the production of a filled layer (saturation), and the over-occupation of one gas, leading to a lack of the other reactant and hence a decrease of the growth rate.[7] The maximum deposition rate is obtained when the two molecules are present on the surface in the ratio that allows for the highest deposition efficiency. The latter is reached when the minimum number of molecules required by the chemical reaction is present on the surface. If one of the reactants happens to be in excess with respect to this balance, the deposition rate decreases. This balance depends

on the precursor chemistry, its adsorption enthalpy, and on the amount of O_2 required to fully oxidize the Si atoms and by-products.

This surface competition was demonstrated by adding an inert gas (Ar, N) together with the reactive mixture. This resulted in a lower deposition rate, due to the surface occupation by the inert gas which lowered the probability that a precursor and an Oxygen molecule would adsorb on two neighbouring sites and react together.[9, 10]

It is expected that such surface coverage competitions occur during FEBID processes involving different gases. An ideal and complete model would be more complex for a standard unbakable high vacuum SEM than for a CVD or PECVD setup, since it should account for the main residual gas flows (N_2, H_2O, O_2) additionally to the injected flows of precursors and reactive gases. This would require the determination of the different adsorption and decomposition constants of all these gases at room temperature. The adsorption site density of a standard sample should then be determined as function of the molecules present on its surface (presence of surface contamination, presence of adsorbed water layers [11]), and the reactivity of the latter molecules between one another, which are generally unknown.

An illustration of this complexity was obtained during an attempt of depositing pure nickel from the tetrakis(trifluorophosphine)Nickel $Ni(PF_3)_4$ precursor. Injecting additional H_2 flows did not lead to the purification of the deposited material, but resulted in Oxygen incorporation, which was attributed to Hydrogen induced surface water desorption.[12]

The precise study of these surface phenomena require well defined controlled vacuum and surface conditions that are not obtainable in standard FEBID equipments. They represent a great challenge for surface chemistry, and appear totally necessary for the development of rigorous models, controlled and well defined FEB processes. These studies are the steps missing to understand FEBID and lead to the production of pure materials.

6.1.2 Effect of additional Oxygen on Si-material growth rate

The growth rate of the films obtained from TEOS, TMOS and TMS increased, on the contrary to that obtained from TICS, with increasing O_2 flow, and reached a plateau, more or less well defined, for O_2 flows above 1 sccm. For Oxygen flows superior to 7.5 sccm, the measured growth rate decreased (~10 % of saturation value) for TEOS, TMOS and TICS, but appeared constant for TMS. This increase of deposition rate was observed for magnifications from 1 to 8 kX (respective dwell times of 3 and 24 µs), and observed for acceleration voltages of 5, 10 and 25 kV, and FEB currents between 1 and 250 nA. The average growth rates in the case of films produced at 2 kX (scanned area of 40 x 50 µm²) under constant irradiation conditions (10 kV and 125 nA) are presented in Figure 6-1.
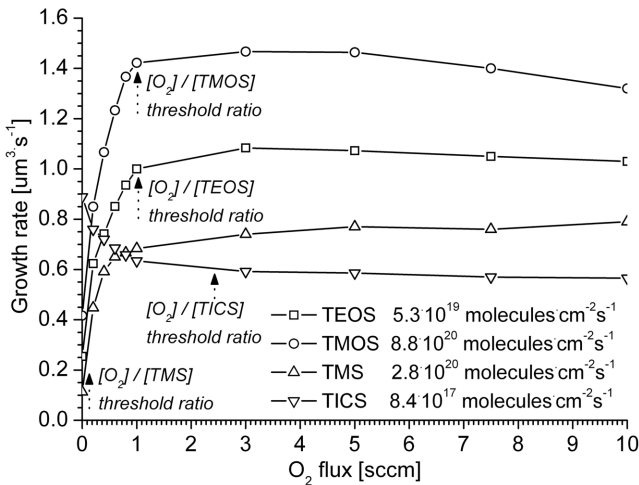
Figure 6-1: Average volume growth rate as function of additional O_2 flow and precursor. Black arrows indicate O_2 flow needed to deposit pure SiO_2 from each of the precursors. FEB parameters: 125 nA, 10 kV. Error bars: ± 0.025

At saturation, the initial growth rates of TEOS, TMOS, TMS and TICS were multiplied by 4.2, 3.6, 7, and 0.6, respectively. The multiplication factors indicated that each molecule had a specific decomposition mechanism, and a specific adsorption enthalpy. Oxygen boosted the deposition rates of TEOS,

TMOS and TMS, but decreased that of TICS. A increase of *growth rate vs. additional Oxygen* characteristic was already reported by Wang *et al.* during FEBID of Pt, but was not further explained.[13] It is however representative of a surface competition adsorption mechanism such as that presented in § 6.1.1, which induces an exponential decreasing coverage of precursor molecules as function of increasing Oxygen flow.[9] This also explained the exponentially decreasing behaviour of the embedded C concentration with increasing Oxygen, see Chapter 4, § 4.1.1 pp. 4-4.

This was further supported by the decrease in deposition rate observed for flows superior to 7.5 sccm that was attributed to an over-occupation of the Oxygen molecules on the surface. The latter blocked adsorption sites useful for precursor molecules, and hence created a lack of precursors providing Si atoms. This resulted in a decrease of the growth rate. The deposited material remained pure SiO_2.

All the precursor have a specific sticking coefficient, the saturation flow always appeared at 1 sccm, and was additionally independent of the probe current and acceleration voltage (see Chapter 5, pp. 5-7). The saturation region corresponded to the maximum number of Oxygen molecules possible on the surface in order to get the largest deposition rate and/or the lowest amount of Carbon in the material. This indicated that the characteristics observed in Figure 6-1 were mainly representative of the surface occupation of the additional Oxygen since the precursor flow remained constant.

The growth rate boost and attenuation factors were related to the surface coverage of Oxygen and sticking coefficient of the different molecules only. Dotted black arrows in Figure 6-1 indicate the O_2 flows needed to obtain pure SiO_2 (undetectable C by EDX, see Figure 4-1, pp. 4-4) from the four precursors, and demonstrated that the saturation of the growth rate was not always related to the total oxidation of the FEBID material and could only be due to a

surface coverage effect. For TMS, pure SiO_2 was deposited with an O_2 flow of 0.1 sccm, whereas the growth rate still increased and saturated at 1 sccm. This was not visible for TEOS and TMOS, for which the saturation appeared at the same flow as pure SiO_2 was deposited. For TICS however, the deposition of pure SiO_2 appeared for flows superior to the saturation flow.

Hence, this indicated in the case of TMS, TEOS and TMOS, that the number of molecules participating to the deposition reaction increased by the presence of Oxygen. Since the precursor flow was not varied, this suggested that a large number of molecules were leaving the surface without decomposing when no additional Oxygen was injected. The low amount of Oxygen required to oxidize the material obtained form TMS indicated a larger reactivity of the molecule to oxygen under the FEB. These efficiencies are discussed in details in Chapter 7.

In the case of TICS however, additional Oxygen lowered the deposition efficiency. This was explained by the high reactivity of the molecule to water (see Chapter 3, pp. 3-21), on the contrary to molecular Oxygen. The amount of residual water was responsible for the large deposition efficiency with no additional Oxygen (see Chapter 7) under electron irradiation. A large amount of Oxygen was required in order to push the equilibrium of the oxidation reaction to SiO_2. Injecting water vapour would have certainly lead to larger efficiencies.

The closer the Oxygen flow was from the saturation flow, the lower the increase of growth rate was. This decrease in efficiency was observed when reporting the *deposit thickness vs. deposition time and additional Oxygen* see Figure 6-2. The highest variation of the deposition efficiency (given by the slopes of the curves) was obviously larger between the depositions at 0 and 0.2 sccm of O_2 than that observed between the 0.8 and the 1 sccm flows of O_2.

The linear characteristics observed, indicated a constant deposition rate as function of the Oxygen flow. This confirmed that for a given O_2 flow, there was a stationary surface coverage of the molecules that remained constant during the deposition time. The slight decrease in deposition rate for films thicker than 600 nm might be due to thermal effects (as presented in Chapter 5, §5.4). Higher surface temperature increases the desorption rate of the molecules which decreases the surface coverage and therefore the deposition rate.
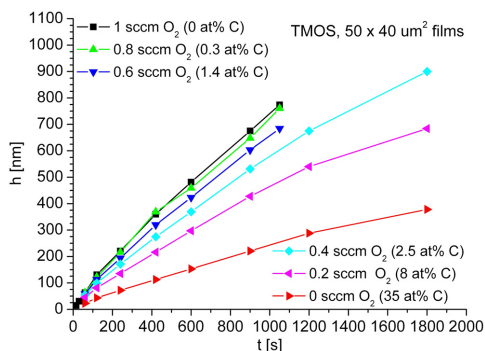
Figure 6-2: General overview of the effect of additional Oxygen on the deposit thickness as function of time. Error bars ± 5 nm.

Summary of effect of Oxygen on FEBID films growth rate

- During gas assisted FEBID, the injected molecules undergo surface coverage competition, as function of their respective flows and constants of adsorptions

- Additional Oxygen influenced the deposition rate of the FEBID materials until a saturation value, similar for all the precursors tested here: 1 sccm. Depending on the precursor properties and reactivity, Oxygen either boosted or decreased the growth rate obtained when using only the precursor vapours

- The increase of deposition efficiency suggested that a large number of molecules were leaving the substrate surface without reacting during conventional FEBID. This efficiency was increased by molecular Oxygen with reactive molecules, certainly due to its high reactivity and scavenging power

- The increase-saturation-decrease effect appeared invariant to irradiation conditions

- The largest efficiencies were reached when a maximum number of O_2 molecules were present on the surface

6.2 Precisions on the deposition mechanism

As mentioned in previous paragraphs (Chapter 5, § 5.2.2, and Chapter 6, § 6.1.2), the growth rate was higher for low acceleration voltages, but the chemical composition was not affected by these changes of electron emission, and remained purely dependant of the injected Oxygen flow. These two results provided indications to the understanding of the deposition process behind O_2 assisted FEBID:

- independently of the Oxygen flow, the growth rate of the material is only dependant of the number of electrons crossing the deposit per unit surface and their respective efficiency to induce a reaction.

➔ For a given Oxygen flow, the growth rate was hence "electron limited".

- the only way to influence the deposited chemical composition was to vary the additional Oxygen flow injected. The quantity of C incorporated in the material was only dependent of the resulting reaction between the precursor and Oxygen. Since the C decreased until or even before saturation when increasing the Oxygen flow, this indicated that there was always a sufficient number of organosilane molecules on the surface that supplied the C atoms, and that organosilanes were the main molecule present on the substrate surface. Oxygen was predominant on the surface only for flows where the growth rate decreased without influencing the chemical composition, which indicated a lack of supply of Si atoms. This is typical of coverage competition

on the substrate surface. The total number of molecules of each type depended on the adsorption enthalpies of the two molecules, and their respective local flow.

➔ The C concentration in the deposited material was "Oxygen limited".

➔ In the case of reactive molecules such as TMS, even if the FEBID material consisted of pure SiO_2, the growth increased until Oxygen reached its maximum surface coverage. The growth rate of SiO_2 was hence "Oxygen coverage limited".

- the exponential dependences observed for the growth rates and for the elements concentrations as function of additional Oxygen were typical of co-adsorption of two gases on a surface

This is illustrated in Figure 6-3.
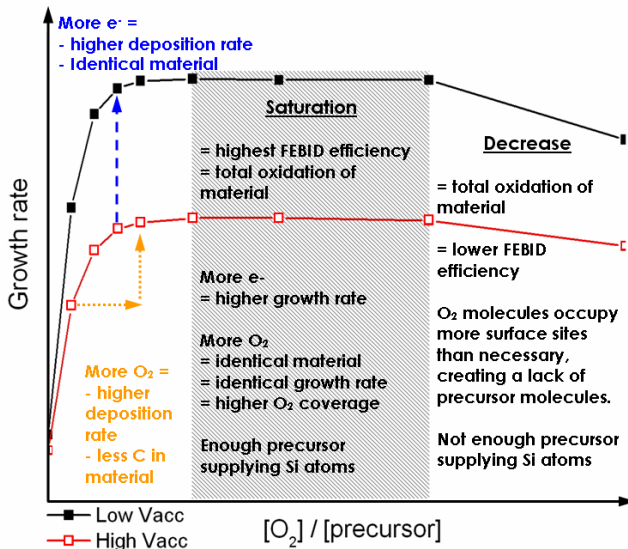
Figure 6-3: Description of the Oxygen assisted FEBID process based on experimental results

6.3 Importance of precursor flow on FEBID process

Surface coverage competition was demonstrated to depend on the precursor chemistry, sticking coefficient, and flow. The differences of precursor reactivity and deposition mechanism could be observed by varying the precursor flow and measuring the growth kinetics and the threshold amount of Oxygen required to fully oxidize the FEBID material.

6.3.1 Growth rate as function of Precursor flow

Under constant irradiation conditions, the growth rate was larger at low TEOS and TMOS flows and lower at low TMS flows. This was observed even for depositions performed without additional Oxygen. The dependency of the growth rate on the additional O_2 flow remained the same, and followed the increase – saturation characteristic, see Figure 6-7.

Figure 6-4: Effect of the precursor flow on the growth rate of 40 x 50 μm^2 films, for (a) TEOS, (b) TMOS, and (c) TMS.

Red round symbols = larger precursor flow than black square symbols.

Deposition conditions: 10 keV FEB, 125 nA. Substrate: Au coated Si.
Growth rates increase with decreasing precursor flows of TEOS and TMOS, and decreases with precursor flow for TMS.
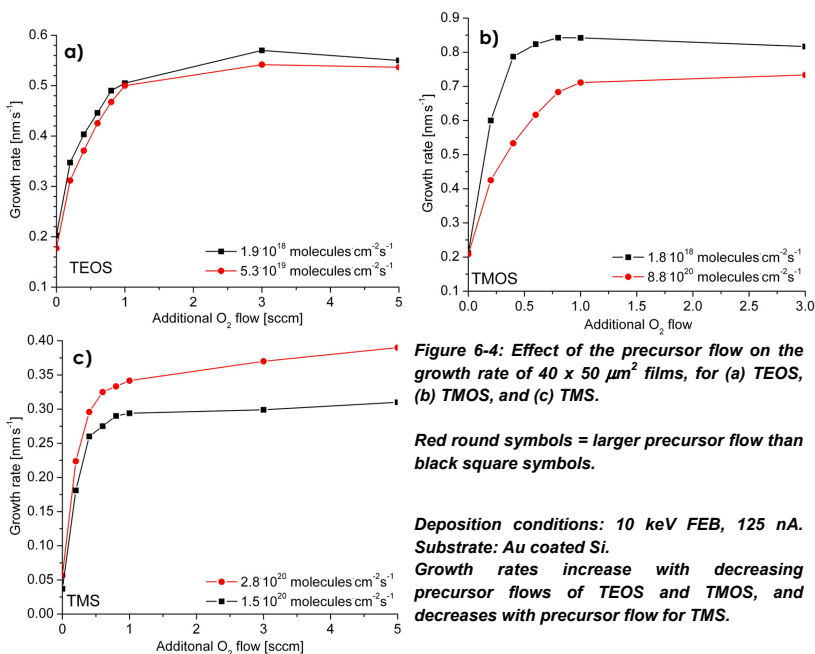
An explanation of such behaviours is proposed, based on the molecules sticking coefficients.

6.3.1.1 High sticking coefficient molecules: TEOS and TMOS

As discussed in Chapter 3, pp. 3-22, TEOS and TMOS are more sticky molecules compared to TMS. The increase of growth rate at lower flows, see Figure 6-4 a) and b), could be explained by suggesting that the number of efficient molecules decomposed was larger. The experiments were electron limited (see § 6.2), and there was always a sufficient number of precursor molecules on the surface, whatever the flow values used here. However, at high precursor flows, some of them might leave the surface without reacting or decomposing. In such situation, these molecules in excess block for a given time the adsorption sites for Oxygen molecules that can hence not participate to the deposition. The deposition was not limited by the flow of precursor, but the oxidation efficiency was influenced.

This led to a lower growth rate for large TEOS and TMOS flows. As presented in the following section 6.3.2, this led to an apparent higher $[O_2]/[precursor]$ threshold ratio at lower precursor flows. However, the realistic threshold ratio should account only for the number of useful molecules at large precursor flows. The results obtained between TEOS and TMOS were not quantitatively comparable since different precursor flows were used.

6.3.1.2 Low sticking coefficient molecule: TMS

Lowering the TMS flow resulted in lowering the growth rate, see Figure 6-4 c) and amount of Oxygen required to deposit pure SiO_2. TMS is expected to have a much lower residence time on the surface than TEOS and TMOS, and the blocking of adsorption sites should hence not be significant. The growth rate decreased with the precursor flow, and so did the amount of Oxygen required to fully oxidize the material. Compared to the sticking molecules situation, the oxidation reaction with TMS was "limited" by the number of precursor molecules impinging the substrate surface.

Another proposition based on polymerisation side reactions due to residual water could be the following. At high precursor flows, the number of monolayers striking the surface in the irradiated area is high (between 1000 and 10000 per second, see § 7.1.2). The total oxidation of the gaseous fragments is mainly driven by the gaseous additional Oxygen molecules injected in the SEM, and requires low additional O_2. This ratio is further decreased since the reaction of O_2 with silanes produces water molecules which will act as reagents.

At low precursor flows, the surface processes are thought to predominate, and there is relatively more water per organosilane molecule. As mentioned earlier, TEOS and TMOS are water sensitive and the hydrolysis product are large oligomers, containing Si-O-Si chains and/or networks, and Carbon containing ligands.[14] In FEBID, they might however consist of partially hydrolyzed and fragmented species and entrap reaction products, which are then hardly accessible for O_2 molecules. More Oxygen is therefore needed to diffuse through the fluffy network and fully oxidize the deposited material. Compared to TEOS and TMOS, TMS fragments do not follow a polycondensation reaction with residual water to form SiO_2. Hence, by lowering the TMS flow, the number of efficient residual water molecules per TMS is increased, and less additional O_2 is actually needed to obtain pure SiO_2 at low TMS flows.

As demonstrated in Chapter 7 however, the parasitic reactions with water molecules are not predominant in presence of Oxygen during O_2 assisted FEBID of SiO_2. This limited hence the possibilities of such mechanism.

6.3.2 Threshold Oxygen amount as function of precursor flow

The previous decomposition proposition was supported by the $[O_2]/[precursor]$ injected ratios needed to deposit pure SiO_2 from TEOS, TMOS and TMS as function of the injected precursor flows, which are reported in Table 6-1. As already suggested by the previous paragraph, in contrary to TMS, this ratio increased with decreasing TEOS and TMOS flows.

Precursor	Precursor flow [molecules·cm^{-2}·s^{-1}]	[O$_2$]/[precursor] threshold ratio
TEOS	$5.3 \cdot 10^{19}$	1.75
	$1.9 \cdot 10^{18}$	400
TMOS	$8.8 \cdot 10^{20}$	0.15
	$1.1 \cdot 10^{19}$	8
	$1.8 \cdot 10^{18}$	35
TMS	$1.9 \cdot 10^{20}$	0.03
	$2.8 \cdot 10^{20}$	0.05

Table 6-1: Oxygen needed to deposit pure SiO$_2$ from TEOS, TMOS and TMS as function of precursor flow

This phenomenon was double-checked by using a single capillary gas injection system, where the silane precursor and the Oxygen additional flow were injected through the same tube (instead of the two capillaries GIS delivering separately the gases that was used normally).

This setup was constructed in a way that additional Oxygen and the precursor molecules were mixed upstream of the needle valve, that was hence controlling the total flow, see Figure 6-5. The Oxygen flow was regulated by the mass flow controller. The precursor flow was dependant on the Oxygen flow, and could be determined by reservoir weighting as function of the different additional flows.
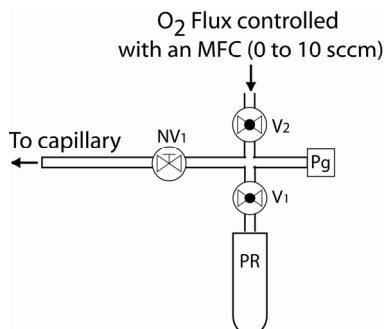

Figure 6-5: Principle of the single capillary gas injection system. PR = Precursor Reservoir, Pg = Penning gauge, V$_1$ and V$_2$ = On / Off valves, NV$_1$ = Needle Valve 1.

The precursor consumption as function of the Oxygen flow for the single capillary system is reported in Figure 6-6, together with the FEBID material Carbon concentration as function of the additional O_2 co-flow.

Undetectable Carbon contamination was obtained for an additional O_2 flow of 1 sccm, which corresponded to a $[O_2]/[TMOS]$ ratio of 10, and a TMOS flow of $1.5 \cdot 10^{19}$ molecules$\cdot$cm$^{-2}\cdot$s^{-1}.
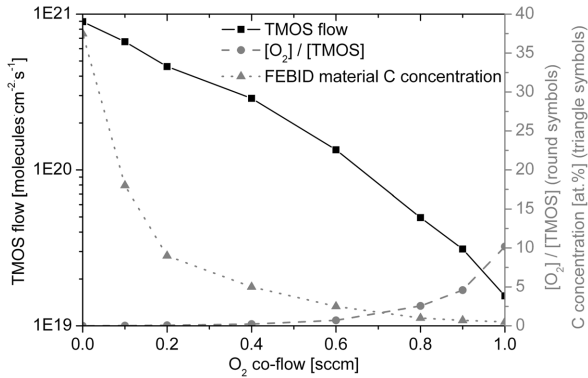
Figure 6-6: Results obtained from single capillary GIS. TMOS flow as function of additional O_2 flow (left scale, error bars 10%), resulting $[O_2]/[TMOS]$ ratio (left scale), and C concentration in the FEBID material as function of additional O_2 flow.

The $[O_2]/[TMOS]$ ratio needed to deposit pure SiO_2 from a TMOS flow of $1.5 \cdot 10^{19}$ molecules$\cdot$cm$^{-2}\cdot$s^{-1} with the single capillary setup and with the two channel setup are coherent, respectively 10 and 8, taking into account the error bars on the TMOS flux measured by weighting the reservoir. It became obvious that the precursor chemistry was a main issue in FEBID.

The variation of the threshold O_2 as function of precursor flow has however to be corrected with respect to the effective deposition rate at the corresponding flows. The larger the number of efficient precursor molecules (at low flows), the larger the amount of Oxygen has to be to deposit pure SiO_2, which corresponds to the experimental data.

This dependence of the FEBID efficiency as function of the precursor flow is further discussed and calculated in Chapter 7.

Summary of Importance of precursor flow on FEBID process

- The precursor molecules were always present in excess on the surface

- When the sticking coefficient was high, precursor molecules occupied sites of adsorption during their surface residence time, and left without decomposing. This occupation prevented from Oxygen molecules to adsorb and participate to the deposition mechanism. This led to lower deposition efficiencies

- When the sticking coefficient was low, such phenomena did not occur, and the growth dynamics followed the precursor flow.

- More additional O_2 was required at low flows of TEOS and TMOS to deposit pure SiO_2. This highlighted a lower probability for Oxygen molecules to adsorb near a precursor fragment, a larger O_2 consumption due to the presence f more efficient molecules at the surface.

- The injected threshold ratios should account for the number of efficient molecules only, and not for the total flow.

6.4 The Oxygen incorporation effect

This sub-chapter addresses an issue related to the side-reaction due to residual water molecules in the SEM chamber, see Chapter 3, pp. 3-5. The latter led to Oxygen incorporation in the FEBID films, which influenced the deposition mechanism.

The films produced by decomposing TMS (which does not contain any Oxygen atom) always showed a non-negligible Oxygen concentration that was incorporated in the film during the growth. The concentration of the incorporated Oxygen was inversely dependent on the precursor flow. The C concentration decreased with increasing O concentration. This effect was visible for all the precursors as well. The chemical compositions of the films obtained form TMOS and TMS vapours with no additional Oxygen are presented in Figure 6-7.
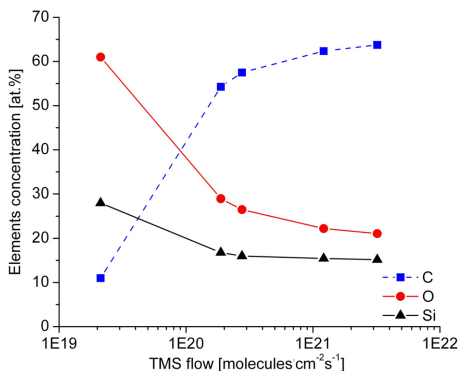
Figure 6-7: FEBID chemical composition of films obtained from TMOS and TMS as function of precursor flow. Error bars: ± 5 at.%

The Carbon concentration in the deposited films decreased with decreasing precursor flow, leading to an increase of the Silicon and Oxygen concentrations. For a flow of $2.1 \cdot 10^{19}$ molecules·cm^{-2}s^{-1}, TMS decomposed into Carbon contaminated SiO_2 (10 at.% C). This demonstrated the existence of an oxidation side reaction occurring during FEBID, which was more efficient at low precursor flows. The Carbon concentrations increased to 55 at.% for a TMS flows of $1.9 \cdot 10^{20}$ molecules·cm^{-2}s^{-1}.

FEBID films deposited with a non-purified TMS showed identical chemical compositions as function of the precursor flow, than that obtained with a purified TMS, which indicated that the oxidant source was not dissolved in the precursors. Therefore, the Oxygen presence in the deposit could only be attributed to oxidant molecules, either residual water or residual Oxygen, present in the SEM chamber, since the gas injection system was tight to $5 \cdot 10^{-7}$ mbar. The attribution of the oxidation reactions to one of these molecules was not obvious, and the literature data concerning this phenomenon is contradictory. Molhave demonstrated that water vapour was more efficient than O_2 and H_2 mixed in a 1:2 ratio, to oxidize organometallics. However, experiments of bulk Si oxidation using a Scanning Tunnelling Microscope showed that Oxygen was the main oxidant agent.[15-20]

Calculations of the FEBID efficiencies presented in Chapter 7, in which the atomic deposition rates were compared to the different flows of molecules impinging the surface, allowed determining that water was the main oxidant agent during FEBID using only precursor vapours. Furthermore, the organo-silanes and their fragments produced under FEB irradiation are moisture sensitive molecules, which react directly with water. Water has a higher sticking coefficient and hence more chances of being adsorbed on a surface than Oxygen. This is further presented in details in Chapter 7 §7.2.

6.5 Conclusion of Chapter 6

The surface competition resulting of the co-adsorption of O_2 and precursor molecules was responsible of:

- The exponential dependencies of the elements concentration and the exponentially saturating growth rate characteristics as function of O_2 flow

- The growth kinetics of the deposited films, and the amount of Oxygen required to deposit pure SiO_2 (also influenced by the sticking coefficient)

- This competition also arose during conventional FEBID, due to the residual water molecules in the chamber

6.6 Bibliography of Chapter 6

1.   R.E. Kirby, and D. Lichtman, "*Electron-Beam Induced Effects on Gas Adsorption Utilizing Auger-Electron Spectroscopy - Co and O2 on Si .1. Adsorption Studies*", *Surface Science*, **1974**, *41*, 447-466.

2.   K.J. Laidler, *Catalysis*, Emmet, P.H. edition, Reinhold Publishing Co., Vol. 1, 1954.

3.   F. Ojeda, R. Cuerno, R. Salvarezza, and L. Vazquez, "*Study of the growth mechanisms of low-pressure chemically vapour deposited silica films*", *Journal De Physique Iv*, **1999**, 9, 265-271.

4.   F. Ojeda, A. Castro-Garcia, C. Gomez-Aleixandre, and J.M. Albella, "*Growth kinetics of chemically vapor deposited SiO2 films from silane oxidation*", *Journal of Materials Research*, **1998**, *13*, 2308-2314.

5.   C. Pavelescu, and C. Cobianu, "*Correlations between the Properties and the Deposition Kinetics of Low-Temperature Chemical Vapor-Deposited Sio2-Films - the Effect of O2/Sih4 Mole Ratio*", *Journal of Materials Science Letters*, **1990**, 9, 143-144.

6.   C. Pavelescu, and C. Cobianu, "*A Mechanism for the Surface-Reaction between Silane and Oxygen at Low-Temperature and Correlations with the Properties of the Deposited Sio2-Films*", *Journal of Materials Science Letters*, **1988**, *7*, 1107-1109.

7.   C. Cobianu, and C. Pavelescu, "*Silane Oxidation Study - Analysis of Data for Sio2-Films Deposited by Low-Temperature Chemical Vapor-Deposition*", *Thin Solid Films*, **1984**, *117*, 211-216.

8.   C. Pavelescu, and C. Cobianu, "*A Mechanism for the Surface-Reaction between Silane and Oxygen at Low-Temperature*", *Journal of the Electrochemical Society*, **1984**, *131*, C319-C319.

9.   C. Cobianu, and C. Pavelescu, "*A Theoretical-Study of the Low-Temperature Chemical Vapor-Deposition of Sio2-Films*", *Journal of the Electrochemical Society*, **1983**, *130*, 1888-1893.

10.   E.A. Haupfear, E.C. Olson, and L.D. Schmidt, "*Kinetics of SiO2 deposition from tetraethylorthosilicate*", *Journal of the Electrochemical Society*, **1994**, *141*, 1943-1950.

11.   P.A. Thiel, and T.E. Madey, "*The Interaction of Water with Solid-Surfaces - Fundamental-Aspects*", *Surface Science Reports*, **1987**, *7*, 211-385.

12.   A. Perentes, G. Sinicco, G. Boero, B. Dwir, and P. Hoffmann, "*Focused Electron Beam Induced Deposition of Nickel*", *Journal of Vacuum Science & Technology B*, **2007**, *Accepted for publication*.

13.   S. Wang, Y.M. Sun, Q. Wang, and J.M. White, "*Electron-beam induced initial growth of platinum films using Pt(PF3)(4)*", *Journal of Vacuum Science & Technology B*, **2004**, *22*, 1803-1806.

14.   M.L.P. da Silva, and J.M. Riveros, "*A comparative study of gas-phase ion/molecule reactions in Si(OCH3)(4) and Si(OC2H5)(4)*", *International Journal of Mass Spectrometry*, **1997**, *165*, 83-95.

15.   J.A. Dagata, J. Schneir, H.H. Harary, C.J. Evans, M.T. Postek, and J. Bennett, "*Modification of Hydrogen-Passivated Silicon by a Scanning Tunneling Microscope Operating in Air*", *Applied Physics Letters*, **1990**, *56*, 2001-2003.

16.   J.A. Dagata, W. Tseng, J. Bennett, E.A. Dobisz, J. Schneir, and H.H. Harary, "*Integration of Scanning Tunneling Microscope Nanolithography and Electronics Device Processing*", *Journal of Vacuum Science & Technology a-Vacuum Surfaces and Films*, **1992**, *10*, 2105-2113.

17.   J.A. Dagata, W. Tseng, J. Bennett, C.J. Evans, J. Schneir, and H.H. Harary, "*Selective-Area Epitaxial-Growth of Gallium-Arsenide on Silicon Substrates Patterned Using a Scanning Tunneling Microscope Operating in Air*", *Applied Physics Letters*, **1990**, *57*, 2437-2439.

18.   G. Eres, F.Y.C. Hui, T. Thundat, and D.C. Joy, "*Direct epitaxial growth of thin-film structures*", *Journal of Vacuum Science & Technology B*, **1997**, *15*, 2934-2939.

19.   N. Kramer, J. Jorritsma, H. Birk, and C. Schoenenberger, "*Nanometer Lithography on Silicon and Hydrogenated Amorphous-Silicon with Low-Energy Electrons*", *Microelectronic Engineering*, **1995**, *27*, 47-50.

20.   Y.Y. Wei, and G. Eres, "*Self-limiting behaviour of scanning-electron-beam-induced local oxidation of hydrogen-passivated silicon surfaces*", *Applied Physics Letters*, **2000**, *76*, 194-196.

CHAPTER 7
PROPOSED DEPOSITION MECHANISM

In this chapter, the different efficiencies of the FEBID processes presented in Chapters 5 and 6, with and without additional Oxygen are quantified and compared. The results obtained at 2 kX, 125 nA and 10 kV were studied in detail, since these parameters allowed obtaining SiO_2 from all the precursors. Sporadic results based on the variation of the parameters are also included.

The contributions of the different oxidant agents present in the chamber are calculated by comparing the actual atom deposition yield measured experimentally, to the flows of the different molecules impinging the surface.

Residual water was demonstrated to be the main entity ruling the deposition rate form the plain precursors, and leading to Oxygen incorporation. When injecting Oxygen however, the latter became predominant.

The electron efficiency was shown to be multiplied by factors up to 20 in O_2 assisted FEBID compared to conventional FEBID.

This required the calculation of the actual flows of all the entities impinging in the irradiated area, which differ from the injected flows. Precursor and Oxygen flows were the approximated by means of simulations suited to our gas injection system. The flows of residual water and Oxygen were calculated as well. Decomposition pathways are then proposed for each molecule.

7.1 Precursor, Oxidant and electron flows calculations

7.1.1 Flow simulations

A more precise estimation of the number of molecules in the FEBID area during the deposition process was obtained by means of flow simulations. The molecule surface distribution depends on the GIS position and geometrical dimensions, and on the molecules mean free path in the gas phase λ (distance travelled before a collision with another molecule arises). The ratio of λ by the smallest dimension of the GIS (taken here as the capillary diameter) determines the Knudsen number, representative of the flow regime, which can then be simulated. λ can be calculated knowing the local pressure and using the following equations, and the molecule diameter d (calculated from the compound density ρ and molar weight M):[1]

$$\lambda = \frac{kT}{\sqrt{2} \cdot \pi \cdot d^2 \cdot P} \qquad Eq.\ 7\text{-}1$$

$$d = 2 \left(\frac{3}{4\pi} \frac{M}{\varrho \cdot N_A} \right)^{\frac{1}{3}} \qquad Eq.\ 7\text{-}2$$

with k Boltzmann's constant $= 1.38 \cdot 10^{-23}$ [J·K^{-1}], T the temperature = 300 [K], N_A Avogadro's number $6.022 \cdot 10^{23}$ entities·mol^{-1}, and P the pressure in the deposition area on the substrate [Pa]. The determination of P is subtle since the effusion of the molecules from the capillary outlet creates a pressure gradient between the capillary and the substrate surface, which induces a gradient of the λ. An approximation of P consisted in calculating the pressure at the capillary outlet (i.e. the highest pressure), which will result in a minimization of λ (i.e. worst case), by the following equation ($F_{injected}$ = injected flow of precursor):

$$P = F_{injected} \cdot 10^4 \cdot (2\pi \cdot M \big/ N_A \cdot 10^{-3} \cdot kT) \qquad Eq.\ 7\text{-}3$$

In Table 7-1 are reported the different molecules diameters.

Precursor	Compound density [g·cm^{-3}]	Molar Mass [g·mol^{-1}]	Molecule diameter [nm]
TEOS	0.934	208.33	0.88
TMOS	1.023	152.22	0.78
TMS	0.648	88.22	0.76
TICS	1.442	196.16	0.76

Table 7-1: Calculation of molecule radius

The molecules mean-free path λ and the corresponding Knudsen number as function of the injected precursor flows calculated using Eq.6-1 to 6-3 are reported in Table 7-2. The values for molecular Oxygen were obtained by taking 0.29 nm as molecule length.

Molecule	Injected total flux [molecules·cm^{-2}·s^{-1}]	P at the nozzle exit [Pa]	λ [μm]	λ / D	Flow regime
TEOS	$5.3 \cdot 10^{19}$	50.1	0.23	$3.9 \cdot 10^{-4}$	Slip
	$1.9 \cdot 10^{18}$	1.8	6.35	0.01	Transient
TMOS	$8.8 \cdot 10^{20}$	714.6	0.02	$4 \cdot 10^{-4}$	Slip
	$1.1 \cdot 10^{19}$	8.6	1.78	$3 \cdot 10^{-3}$	Transient
	$1.8 \cdot 10^{18}$	1.5	10.49	$1.7 \cdot 10^{-2}$	
TMS	$2.5 \cdot 10^{20}$	169.7	0.09	$1.6 \cdot 10^{-4}$	Slip
	$1.9 \cdot 10^{20}$	115.5	0.14	$2.3 \cdot 10^{-4}$	
	$2.3 \cdot 10^{19}$	13.1	1.24	$2.1 \cdot 10^{-3}$	Transient
TICS	$8.5 \cdot 10^{17}$	0.8	20.9	3.485	Transient
O$_2$	$4.5 \cdot 10^{16}$ (0.1 sccm)	0.017	$6.60 \cdot 10^{3}$	$1.10 \cdot 10^{1}$	Molecular
	$8.9 \cdot 10^{16}$ (0.2 sccm)	0.033	$3.34 \cdot 10^{3}$	5.56	
	$1.8 \cdot 10^{17}$ (0.4 sccm)	0.067	$1.65 \cdot 10^{3}$	2.75	
	$2.7 \cdot 10^{17}$ (0.6 sccm)	0.100	$1.10 \cdot 10^{3}$	1.83	
	$3.6 \cdot 10^{17}$ (0.8 sccm)	0.133	$8.25 \cdot 10^{2}$	1.38	Transient
	$4.5 \cdot 10^{17}$ (1 sccm)	0.167	$6.60 \cdot 10^{2}$	1.10	
	$1.3 \cdot 10^{18}$ (3 sccm)	0.482	$2.28 \cdot 10^{2}$	0.3	
	$2.2 \cdot 10^{18}$ (5 sccm)	0.815	$1.35 \cdot 10^{2}$	0.2	

Table 7-2: Molecule mean free path as function of injected flow. D = capillary diameter 600 μm.

The precursor flows used during this thesis were all in the transient or slip regime, on the contrary of the Oxygen flows that were all in the molecular flow regime. The simulation of the transient and slip regimes based on Monte-Carlo simulations are complex since they involve complex and inelastic molecule-molecule interactions. However, Utke *et al* developed a custom simulation code that delivered excellent results for the simulations of molecular flow regimes, and satisfying results for the transient regimes (accuracy ± 10 %).[1]

The distributions of the molecules used here were calculated with the same software, and applying the following parameters and dimensions:

- capillary diameter and height to the surface: 600 and 100 μm respectively

- capillary angle to the substrate surface: 10°

The results are presented in Figure 7-1 in terms of fraction of the injected molecule flow, impinging on a pixel on the surface as function of its position.
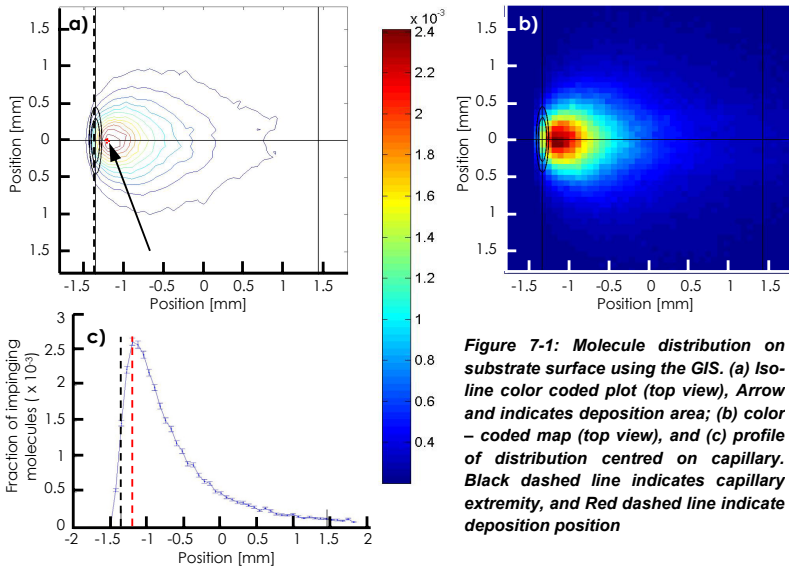

Figure 7-1: Molecule distribution on substrate surface using the GIS. (a) Iso-line color coded plot (top view), Arrow and indicates deposition area; (b) color – coded map (top view), and (c) profile of distribution centred on capillary. Black dashed line indicates capillary extremity, and Red dashed line indicate deposition position

The actual precursor flow impinging in the 40 x 50 μm^2 deposition area F_{DA_Prec} could be determined from these results:

$$F_{DA\_Prec} = frac_{in\ zone\ of\ interest} \cdot \frac{capillary\ area}{pixel\ size} \cdot F_{injected} \qquad Eq.\ 7\text{-}4$$

- $frac_{in\ zone\ of\ interest}$ the fraction given by the color code in Figure 7-1: according to these simulations and to the relative position of the FEB deposits to the capillary (approximately 80 μm) during the experiments, the deposits were produced in the region where the maximum fraction (i.e. $2.4 \cdot 10^{-3}$) of the injected flow impinges the surface.

- capillary area the exit surface of the GIS capillaries, $\pi \cdot r^2 = \pi \cdot (300 \cdot 10^{-3})^2$ [mm²]

- pixel size the sampling size used for the simulations, 0.0735^2 [mm²]

- $F_{injected}$ the injected molecule flow [molecules·cm⁻²·s⁻¹]

7.1.2 Precursor flow

Assuming that the precursor flow exiting the capillary was equal to that injected in the capillary allowed calculating and correcting the precursor flows for each oraganosilane using Eq.7-4. The results are reported in Table 7-3.

Precursor	Injected total flux [molecules·cm⁻²·s⁻¹]	Flow impinging in FEBID zone [molecules·cm⁻²·s⁻¹]	Flux impinging in irradiated area F_{DA_Prec} [molecules·s⁻¹]
TEOS	$5.3 \cdot 10^{19}$	$6.6 \cdot 10^{18}$	$1.3 \cdot 10^{14}$
	$1.9 \cdot 10^{18}$	$2.4 \cdot 10^{17}$	$4.8 \cdot 10^{12}$
TMOS	$8.8 \cdot 10^{20}$	$1.1 \cdot 10^{20}$	$2.2 \cdot 10^{15}$
	$1.1 \cdot 10^{19}$	$1.4 \cdot 10^{18}$	$2.8 \cdot 10^{13}$
	$1.8 \cdot 10^{18}$	$2.3 \cdot 10^{17}$	$4.5 \cdot 10^{12}$
TMS	$2.5 \cdot 10^{20}$	$3.1 \cdot 10^{19}$	$6.3 \cdot 10^{14}$
	$1.9 \cdot 10^{20}$	$2.4 \cdot 10^{19}$	$4.8 \cdot 10^{14}$
	$2.3 \cdot 10^{19}$	$2.9 \cdot 10^{18}$	$5.8 \cdot 10^{13}$
TICS	$8.5 \cdot 10^{17}$	$1.1 \cdot 10^{17}$	$2.1 \cdot 10^{12}$

Table 7-3: Correction of precursor flows for GIS geometry and irradiated surface.
Errors bars are ± 10 %

These flows could be converted in terms of monolayers per second, assuming that the adsorbed molecules arrange in a hexagonal dense pattern on the surface, and assuming that the projection of each molecule on the surface is a circular area of radius equal to that of the molecule (obtained by Eq.7-4). The resulting monolayer flows as function of the precursor molecule and injected flows are reported in Table 7-4.

Precursor	Monolayer density [molecules·cm^{-2}]	Flow impinging in FEBID zone [molecules·cm^{-2}·s^{-1}]	Monolayer flow in FEBID area [monolayers·s^{-1}]
TEOS	8.2·10^{12}	6.6·10^{18}	8·10^{5}
		2.4·10^{17}	2.9·10^{4}
TMOS	1.1·10^{13}	1.1·10^{20}	1·10^{3}
		1.4·10^{18}	1.3·10^{5}
		2.3·10^{17}	2.1·10^{4}
TMS	1.1·10^{13}	3.1·10^{19}	2.8·10^{6}
		2.4·10^{19}	2.2·10^{6}
		2.9·10^{18}	2.6·10^{5}
TICS	1.1·10^{13}	1.1·10^{17}	1·10^{4}

Table 7-4: Monolayer flows corresponding to injected molecule flows.

The number of monolayers impinging the surface was high; however, the real number of molecules actually adsorbed on the surface was unknown. Compared to TICS, TEOS and TMOS, TMS is expected to have a lower sticking coefficient and hence residence time on the surface.

7.1.3 Oxygen flow

The same approach was applied to correct the flows of injected Oxygen. The correction factor was taken directly from the Monte Carlo flow simulations, see Table 7-2. Due to the symmetric GIS, the flow fraction impinging in the FEBID area was the same than that for the precursor flows, 2.4·10^{-3} of the total injected flow, see Figure 7-1. The corrections for Oxygen co-flows are reported in Table 7-5.

	Injected flow		Flow impinging in FEBID zone [molecules·cm^{-2}·s^{-1}]	Flow impinging in irradiated area (40 x 50 µm^2) [molecules·s^{-1}]
	[sccm]	[molecules·cm^{-2}·s^{-1}]		
O$_2$ flow	0.1	4.5·10^{16}	5.6·10^{15}	1.1·10^{11}
	0.2	8.9·10^{16}	1.1·10^{16}	2.2·10^{11}
	0.4	1.8·10^{17}	2.2·10^{16}	4.5·10^{11}
	0.6	2.7·10^{17}	3.4·10^{16}	6.7·10^{11}
	0.8	3.6·10^{17}	4.5·10^{16}	9.0·10^{11}
	1	4.5·10^{17}	5.6·10^{16}	1.1·10^{12}
	3	1.3·10^{18}	1.7·10^{17}	3.4·10^{12}
	5	2.2·10^{18}	2.8·10^{17}	5.6·10^{12}

Table 7-5: Correction of Oxygen flows for GIS geometry and irradiated surface. Errors bars are ± 5 %

7.1.4 Flow of Residual water and Oxygen

Additionally to the injected Oxygen, the contribution of residual water vapour had to be accounted for in the total flux of oxidant gases. The residual water concentration was 60 % of the background pressure 5·10^{-7} mbar, obtained by summing the partial pressures of OH and H$_2$O and comparing it to the total pressure (see § 3.1.3, pp. 3-5). The corresponding collision flow was calculated using the Hertz-Knudsen formula, which requires the partial pressure of water and the temperature of the chamber:[2]

$$F_{water} = \frac{P}{\sqrt{2\pi mkT}} \quad Eq.\ 7\text{-}5$$

With F$_{water}$ the water impingement flow with surfaces [molecules·m^{-2}·s^{-1}], P the partial pressure of water in the chamber 3·10^{-5} [Pa], T the temperature of the environment 300 [K], k Boltzmann's constant 1.38·10^{-23} [J·K^{-1}], and m the molecular mass of water 0.018 [kg·mol^{-1}] / 6.022·10^{23} = 2.9·10^{-26} [kg].

This lead to a water impinging flow of:

$$F_{water} = 1.1 \cdot 10^{14}\ molecules \cdot cm^{-2} s^{-1}$$

Taking the 40 x 50 µm^2 deposition area used for the large films depositions leads to local collision flow of:

$$F_{DA\_R\_H2O} = 1.1 \cdot 10^{14} \cdot (40 \cdot 10^{-4}) \cdot (50 \cdot 10^{-4}) = 2.2 \cdot 10^{9} \ molecules \cdot s^{-1}$$

The chamber background pressure was reproducibly obtained from day-to-day, and indicated that the residual water vapour concentration was similar from one experiment to the other. Additionally, the background pressure value was identical at the beginning and at the end of each experiment, which indicated that the residual water partial pressure had not been significantly (not more than $0.5 \cdot 10^{-7}$ mbar) lowered by the FEBID process. The water impingement rate could be hence considered constant during all the experiments.

The similar calculation was done for the residual Oxygen present in the SEM chamber, which represents only 5 % of the background pressure (obtained by summing the partial pressures of mass 16 and 32 amu in Figure 3-5). This partial pressure leads to a residual Oxygen impingement rate $F_{DA\_R\_O2}$ of:

$$F_{DA\_R\_O2} = 9.5 \cdot 10^{12} \cdot (40 \cdot 10^{-4}) \cdot (50 \cdot 10^{-4}) = 1.9 \cdot 10^{8} \ molecules \cdot s^{-1}$$

7.1.5 Flow of electrons

The irradiation parameters remained constant: TV scan mode, 2 kX magnification (irradiated area 40 x 50 μm^2), 125 nA and 10 kV (FEB diameter 5.8 μm). The TV scan acquisition rate was 50 Hz. During the 20 ms of the scanning of a field, the FEB is actually scanning the area during 14.9 ms, due to synchronization times (see Chapter 3, § 3.1.6.1, pp. 3-10). Hence, during 1 second of TV scanning at 2 kX, the FEB is scanning the area during 0.74 second.

The electron dose per second of scanning in the deposition area can hence be deduced as:

$$F_{e^-} = \frac{(125 \cdot 10^{-9})}{1.6 \cdot 10^{-19}} \cdot 0.74 = 5.78 \cdot 10^{11} \ electrons \cdot s^{-1}$$

Considering that the SE electrons are the main responsible for the deposition process leads to an effective flow of electrons in the deposition area of, taking 0.3 as secondary yield of Silica at 10 keV:

$$F_{DA\_SE} = 0.3 \cdot 5.8 \cdot 10^{11} = 1.7 \cdot 10^{11} \ electrons \cdot s^{-1}$$

Summary of flow calculations and corrections

- By means of simulation using existing software, realistic flows of precursor and Oxygen impinging in the deposition area were calculated

- the collision flow of residual water corresponding to the partial pressures measured was evaluated and are not negligible

- These values will be used in the following sub-chapters to explain the deposition mechanism of Oxygen assisted FEBID

- The following Table 7-6 summarizes the different flows present on the surface

Entity	Typical flow in the 40 x 50 μm^2 deposition area [molecules·s^{-1}]
Precursor flows	$10^{12} - 10^{15}$
Additional Oxygen flows	$10^{11} - 10^{12}$
Residual Water flow	10^9
Residual Oxygen flow	10^8
Electron flow	10^{11}

Table 7-6: Flows of the different entities impinging in the deposition area

7.2 FEBID deposition efficiencies

7.2.1 Efficiency definition and calculation

The experimental FEBID process yields were defined as the ratio of the number of Si or O atoms deposited per second, over the number of molecules, either precursor molecules, residual water molecules or residual Oxygen molecules, impinging the FEBID area per second. These results allowed attributing the oxidation reaction to the different oxidant agents present in the chamber during the deposition, by comparing the efficiencies to theoretical values.

The simple following relation allowed calculating the number of Si (or O) atoms deposited V_{Si} (V_O):

$$V_{Si} \ (V_O) = \frac{V_{GR} \cdot \varrho_{FEBID} \cdot Wt_{Si} \ (Wt_O) \cdot N_A}{M_{Si} \ (M_O)} \quad Eq. \ 7\text{-}6$$

with V_{GR} the volume average growth rate (see chapter 6, § 6.1.2, pp. 6-4), ρ_{FEBID} the material density, Wt_x the weight percentage of Si or O in the material, N_A Avogadro's number and M_x the molar mass of Si or O (28 and 16 g·mol⁻¹ respectively). In the following paragraphs are presented the deposition efficiencies of the FEBID processes first in the case of the Oxygen incorporation effect using TMS, then in the case of FEBID using only the precursor vapours, and finally in the case of Oxygen assisted FEBID of pure SiO_2.

Since the irradiation parameters are identical for all the experiments, the dwell and replenishment times were not accounted as parameters here.

7.2.2 Efficiency of Oxygen incorporation

The Oxygen atom incorporation rates as function of the TMS flow impinging in the irradiated area were calculated by injecting in Eq.6-6 the experimental data obtained. The atom deposition rate of O and Si were calculated. The densities of the materials deposited were estimated by writing the different chemical compositions as $(SiO_2)_xM_{1-x}$, since they contained the same Si concentration of 15 at%, and always enough Oxygen. M is a matrix containing the remaining elements (C, H, and O) that are in excess compared to SiO_2, which has an average density of 1.75 g·cm⁻³ approximately.[3] The density of SiO_2 was set to 2.2 g·cm⁻³. The results are presented in Table 7-7.

F_{DA_Prec} [molecules·s⁻¹]	V_O [atoms·s⁻¹]	V_O / F_{e^-} [atoms deposited per e⁻]	V_O / F_{DA_Prec} [atoms deposited per precursor molecule]	$V_O / F_{DA\_R\_H2O}$ [atoms deposited per residual H_2O molecule]	$V_O / F_{DA\_R\_O2}$ [atoms deposited per residual O_2 molecule]
$5.8·10^{13}$	$9.1·10^8$	0.005	$1.6·10^{-5}$	0.4	4.8
$6.3·10^{14}$	$2.2·10^9$	0.012	$3.5·10^{-6}$	1	11.6
$3.0·10^{15}$	$2.1·10^9$	0.012	$5.4·10^{-7}$	0.9	11

Table 7-7: Comparison of Oxygen incorporation rate obtained using TMS vapours only at various flows. Flows error bars are ± 5%, atom deposition rates ± 10%, and ratios at ± 10%

As function of the precursor flow, the deposition efficiencies were in the order of 1 atom deposited per 10^5 to 10^7 precursor molecules. Each electron deposited between 0.005 and 0.012 atom. The decrease of this efficiency at low precursor flows could be related to the lower probability of inducing a decomposition reaction when a lower number of molecules are present at the surface.

However, expressing these efficiencies as function of the residual water flows brought more trustful values. At the lowest TMS flow tested, the residual water flow was 2.4 times larger than the O atom deposition rate, which meant that only 42 % of the total water collision flow was converted as Oxygen atoms in the deposited material. This incorporation was certainly limited by the electron driven reactions taking place at the same time, and indicated that part of the molecules might leave the surface before having the chance to participate to the deposition reaction. The incorporation efficiency increased to 1 at larger precursor flows, which is the theoretical value expected: one Oxygen atom from residual water can only lead to the incorporation of 1 Oxygen atom in the film. The incorporation percentage increased to 100 % at higher TMS flows. This represented Oxygen concentrations of 38 and 22 at.% at TMS flows of $6.3 \cdot 10^{14}$ and $3.0 \cdot 10^{15}$ molecules·s^{-1} (impinging in the deposition area).

The same calculations based on the residual Oxygen impinging rate lead to unrealistic values ranging from 4 up to 11, meaning an efficiency for one residual Oxygen atom to incorporate an Oxygen atom in the film superior to 1. This clearly indicated that the Oxygen incorporation phenomenon was due to residual water only.

Summary of Oxygen incorporation

- with respect to the Oxygen deposition rates, the Oxygen incorporation effect can only be attributed to residual water molecules, and not residual Oxygen molecules.

7.2.3 FEBID efficiency without additional Oxygen

The densities of the materials deposited using only the different precursor vapours were estimated by using the previous approach and writing the different chemical compositions as $(SiO_2)_x M_{1-x}$, where M is a matrix containing the remaining elements (C, H, O, and N for TICS) that are in excess compared to SiO_2. The deposited materials obtained with no additional Oxygen could all

be written as $(SiO_2)_{0.45}M_{0.55}$ since they contained the same Si concentration of 15 at%, and always enough Oxygen. This lead to an approximate material density of 1.95 $g \cdot cm^{-3}$ by taking densities of 2.2 and 1.75 for SiO_2 and M respectively. The resulting FEBID yields calculations are presented in Table 7-8.

Precursor	F_{DA_Prec} [molecules·s⁻¹] ± 10 %	V_{GR} @ [O₂]/[precursor] = 0 [μm³·s⁻¹]	V_{Si} [atoms·s⁻¹] ± 0.2·10⁹	V_{Si} / F_{e-} [atoms deposited per electron]	V_{Si} / F_{DA_Prec} [atoms deposited per precursor molecule]
TMS	$6.3 \cdot 10^{14}$	0.11	$2.9 \cdot 10^9$	0.017	$1.8 \cdot 10^{-6}$
TMOS	$2.2 \cdot 10^{15}$	0.39	$4.2 \cdot 10^9$	0.024	$2.1 \cdot 10^{-6}$
TEOS	$1.3 \cdot 10^{14}$	0.25	$1.1 \cdot 10^9$	0.006	$2.3 \cdot 10^{-5}$
TICS	$2.1 \cdot 10^{12}$	0.88	$9 \cdot 10^9$	0.052	$4.3 \cdot 10^{-3}$

Table 7-8: FEBID yields obtained when depositing form the precursor vapours only. Atom deposition rate as function of impinging electron,

The results showed that the number of Si atoms incorporated in the materials for 10^6 molecules impinging the deposition area were 1.8, 2.1, 23 and 4300 for TMS, TMOS, TEOS and TICS respectively. This was visible in the deposition yields per secondary electron, which higher for TICS than the other molecules. The latter molecule was hence the most efficient in terms of deposition rate per injected molecule.

This demonstrated different decomposition mechanisms and reactivities of the precursors. Expressing these yields as function of the residual water flow resulted in yield values that are reported in Table 7-9.

Precursor	$F_{DA\_R\_H2O}$ [molecules·s⁻¹] ± 10 %	V_{Si} [atoms·s⁻¹] ± 10 %	V_{Si} / $F_{DA\_R\_H2O}$ [atoms deposited per residual water molecule]
TMS	$2.2 \cdot 10^9$	$2.9 \cdot 10^9$	0.5
TMOS	$2.2 \cdot 10^9$	$4.5 \cdot 10^9$	2.1
TEOS	$2.2 \cdot 10^9$	$1.1 \cdot 10^9$	1.4
TICS	$2.2 \cdot 10^9$	$9 \cdot 10^9$	4.1

Table 7-9: FEBID yields for depositions using only the precursor vapours; as function of the precursor and residual H_2O impinging flow in the irradiated area $F_{DA\_R\_H2O}$.

The residual gaseous water appeared significant for all the precursors, and the resulting efficiency was in all cases close to the theoretical value of 2: each

Oxygen atom can bond a maximum of two Si atoms: Si-O-Si. This ratio can be lowered if the deposition process is not perfect. Hence the values obtained for TMS, TEOS and TMOS were in good accordance to what is theoretically expected. TEOS and TMOS are moisture sensitive and undergo polymerisation reactions that produce Si-O-Si networks with residual water, which might explain the ratio value close to the ideal case.

The efficiency obtained for TICS was double the theoretical ratio. TICS is very reactive to water, and is a hygroscopic molecule. The FTIR investigations (§ 4.2) showed that the material deposited from TICS contained a large amount of water, and EDX investigations showed that Oxygen concentration was three times larger than the Si concentration. Hence, considering that not all the Oxygen atoms are bonded to Si atoms, and that the incorporation of H_2O in the FEBID film can occur during the deposition without completely reacting, the measured efficiency of 4 still had a reasonable value.

Summary of Efficiencies of FEBID without additional Oxygen

- Si atom deposition rates were compared to the flows of precursors and residual water

- The efficiencies of Si deposition as function of the residual water flow show good agreement to the theoretical expected value of 2.

- Variations of this ratio were explained by means of molecule reactivity and behaviour when exposed to water.

7.2.4 Efficiencies of FEBID of pure SiO_2

The density of all the oxides (i.e. materials deposited above the specific $[O_2]/[precursor]$ ratios) was set to 2.2, which is an intermediate density for silica, in accordance to the chemical etch rates measured in Chapter 4, § 4.2. The weight percentage of Si in the SiO_2 obtained from all the precursors was 43 % according to EDX measurements. In the Table 7-10 are presented the FEBID process yields for the deposition of pure SiO_2 from the different precursors.

Precursor	F_{DA_Prec} [molecules·s⁻¹] ± 10 %	V_{GR} @ [O₂]/[precursor] = threshold ratio [µm³·s⁻¹]	V_{Si} [atoms·s⁻¹] ± 0.2·10¹⁰	V_{Si} / F_{DA_Prec} [atoms deposited per precursor molecule]
TMOS	$2.2 \cdot 10^{15}$	1.46	$3.0 \cdot 10^{10}$	$1.3 \cdot 10^{-5}$
TMS	$6.3 \cdot 10^{14}$	0.74	$1.5 \cdot 10^{10}$	$2.4 \cdot 10^{-5}$
TEOS	$1.3 \cdot 10^{14}$	1.08	$2.0 \cdot 10^{10}$	$1.5 \cdot 10^{-4}$
TICS	$2.1 \cdot 10^{12}$	0.59	$1.2 \cdot 10^{10}$	$5.7 \cdot 10^{-3}$

Table 7-10: Yield of FEBID of SiO₂ as function of the precursor. F_{DA_Prec} is the flow of molecules actually impinging on the 40 x 50 um² area irradiated by the FEB, V_{GR} the measured Growth rate of the materials.

For TMOS, TMS, TEOS and TICS, the average number of precursor molecules useful for the FEBID of pure SiO₂ over 10⁶ precursor molecules injected were 13, 24, 150 and 5700, respectively, which were low in terms of process efficiency, however reasonable compared to results published in literature.

As the two previous situations, these efficiencies were larger when expressed in terms of the injected Oxygen or residual H₂O flows, see Table 7-11.

Precursor	F_{DA_O2}	$F_{DA\_R\_H2O}$	V_{Si} [atoms·s⁻¹] ± 0.2·10⁹	V_{Si} / F_{e-} [atoms deposited per electron]	V_{Si} / F_{DA_O2} [atoms deposited per O₂ molecule]	V_{Si} / $F_{DA\_R\_H2O}$ [atoms deposited per residual H₂O molecule]
	[molecules·s⁻¹] ± 10 %					
TICS	$2.8 \cdot 10^{12}$	$2.2 \cdot 10^{-9}$	$1.2 \cdot 10^{10}$	0.071	$4.3 \cdot 10^{-3}$	5.4
TEOS	$1.1 \cdot 10^{12}$	$2.2 \cdot 10^{-9}$	$2.0 \cdot 10^{10}$	0.117	$1.8 \cdot 10^{-2}$	9
TMOS	$1.1 \cdot 10^{12}$	$2.2 \cdot 10^{-9}$	$3.0 \cdot 10^{10}$	0.176	$2.7 \cdot 10^{-2}$	13.6
TMS	$1.1 \cdot 10^{11}$	$2.2 \cdot 10^{-9}$	$1.5 \cdot 10^{10}$	0.088	$1.4 \cdot 10^{-1}$	6.8

Table 7-11: FEBID yields for SiO₂ depositions at threshold [O₂] / [precursor] ratios; as function of the O₂, the H₂O and the electron impinging flows in the irradiated area, F_{DA_O2}, F_{DA_H2O} and F_{e-}.

The deposition efficiencies obtained when considering the residual water as main oxidant agent were much larger than the theoretical ratio of 2 Furthermore, in the case of FEBID of SiO₂, the oxidation of the non-volatile side-products produced should be accounted for, and the production of pure SiO₂ is expected to require more Oxygen. Although a single water molecule can lead to the production of oligomers containing 2 or 3 Si atoms with polymerizing molecules such as TEOS and TMOS,[4] the actual numbers of 13.6 and 9 were

unrealistic. This was further supported by the efficiencies obtained with the simple and non-polymerizing molecules TMS and TICS, where one H_2O molecule should have fixed 6.8 and 5.4 atoms of Silicon respectively.

The efficiencies obtained when considering the additional Oxygen as main oxidant agent were all lower than 1, and were for TICS, TEOS, TMOS and TMS, 0.0043, 0.018, 0.027 and 0.14 respectively. TMS, that had the lower efficiency when depositing form the molecule alone, had the highest efficiency of deposition in presence of Oxygen. Although these efficiencies are low, they are more reasonable to consider than those obtained with residual water. The non-volatile fragments remaining on the substrate surface are unknown, and their reactivity to Oxygen might be low.

Compared to conventional FEBID, the electron efficiencies measured were multiplied by 19.5, 7.3, 5.1 and 1.36 for TEOS, TMOS, TMS and TICS respectively. This increase can be due to the lower threshold energy required to initiate the deposition reaction, the sensitivity of the molecules to react with Oxygen. TEOS will liberate more water than TMOS or TMS, and it is expected to lead to larger deposition rates.

The CN bond in TICS is a high polarity bond, that makes the molecule reactive to water, but not to Oxygen. This could explain why so much Oxygen was needed to totally oxidize the FEBID material obtained from TICS. TMS is a molecule that reacts with H_2O and O_2, with no distinction. The low 0.14 deposition efficiency is explained since the material contained 4 times more C than Si that had also to be oxidized.

Summary of Efficiencies of FEBID of pure SiO_2

- Si atom deposition rates of pure SiO_2 were compared to the flows of precursors, additional Oxygen and residual water.

- The efficiencies of Si deposition as function of the residual water flow show improbable values, meaning that residual water was certainly not significant during the deposition of pure SiO_2.

- Efficiencies calculated based on the additional O_2 flow appeared more realistic, and varied between 0.004 and 0.14 depending on the molecule.

- The main oxidant power during O_2 assisted FEBID of SiO_2 was provided by additional Oxygen.

7.3 Oxygen flow side effect

Additionally to providing oxidant agent to the deposition area, increasing the Oxygen flow increased the chamber pressure. This indirectly influenced the number of collisions of the Oxygen and of the background molecules with the surface, following Hertz-Knudsen formula. This was verified by depositing a film from TMS with and without using the chamber liquid nitrogen traps. The resulting Oxygen concentration obtained when no traps were used (P = $1 \cdot 10^{-6}$ mbar, 80 % of residual water) was 20 at.%, which fell to 35 at.% when the traps were filled with liquid nitrogen (P = $5 \cdot 10^{-7}$ mbar, 60 % of residual water). This was due mainly to the increase of residual water collision flow with increasing chamber pressure.

In Figure 7-2 is presented the chamber pressure as function of the different flows injected. The number of collisions could however not be calculated since the pressure values reported in Figure 7-2 are that given by the Penning gauge, which are gas dependent. Qualitatively, multiplying the Oxygen flow by 2 should have increased the number of collisions by two as well.
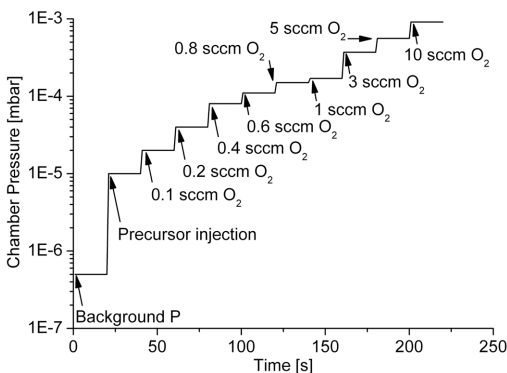
Figure 7-2: Chamber pressure increase as function of injected flows of precursor and Oxygen

7.4 Proposed deposition mechanism

Based on the previous results, the following decomposition mechanism was proposed for Oxygen assisted FEBID:

- The molecules diffused through vacuum and adsorbed on the surface

- The fragments produced by the focused electron beam were identical to that obtained by mass spectrometry of the molecules.

- The fragments produced had different reactivities to residual water. If additional Oxygen was present in the chamber, the lifetime of the fragments was greatly decreased.

- Once the fragments produced, recombination reactions and compactation reactions could occur, driven by the electrons. During these reactions, non – volatile side-products were embedded in the material. When additional Oxygen was added, these reactions were minor, the deposition efficiency larger, and the non-volatile species oxidized to gases, that could further assisted the deposition process. The lifetime of the fragments was lowered in presence of Oxygen, due to its high scavenging power.

- The amount of Oxygen needed to obtain SiO_2 from a given molecule depended of the reactivity to Oxygen of the fragments, and the by-products produced.

In the following sections are presented the suggested hypothetical decomposition pathways of the different molecules used during this study.

7.4.1 Decomposition of alkoysilanes

The material obtained using TEOS and TMOS with no additional O_2 flux was identical in terms of chemical composition measured by EDX: $SiO_{2.5}C_{3.2}$. Potential structural entities were determined by XPS investigations and were SiO_2, Si-C, $R-Si(OCH_3)_3$ or $-(Si(CH_3)_2O)-$ type entities, and Oxygenated Carbonaceous chains. It is reasonable to think that polymerization reactions similar to those observed in gas phase reactions of the pure precursors [4-6]

occur equally during FEBID. Electron impact on TEOS and TMOS monomers create excited cationic species which undergo chain propagating polymerization reactions with TEOS and TMOS monomers, resulting in the production of excited oligomers containing Si-O-Si networks, which can further decompose. However, these reactions might be limited by impinging electrons which lower the diffusion and rearrangement probabilities by cleaving and recombining directly adsorbed entities, as suggested by the detection of Si-C and Si-CH$_3$ (see Chapter 4).

Additionally to the creation of Si-O-Si networks by polymerization reactions presented above, the presence of SiO$_2$ in the FEBID material obtained with no additional O$_2$ flux can also be explained by hydrolysis reactions. The moisture sensitive TEOS and TMOS cations produced under the FEB [5, 6] could easily react to SiO$_2$ with residual water molecules in the chamber. The higher number of C atoms in the TEOS monomer compared to the TMOS intuitively suggests a higher C concentration in deposits obtained from TEOS than those obtained from TMOS (under similar deposition parameters). We believe that this would occur at similar precursor fluxes. In this study though the gaseous TEOS vapour flux was 200 times lower compared to that of TMOS. There are hence 200 times more residual water molecules which can contribute to condensation and/or oxidation reactions when using TEOS in our equipment, which lowers the expected C concentration. This hydrolysis reaction mechanism as function of the precursor flux could be a reason why Lipp et al [7] obtained lower C containing FEB deposits from TMOS (SiO$_{1.05}$C$_{0.45}$) since their precursor flux was approximately 1000 times inferior to ours (10^{17}molecules·cm^{-2}s^{-1}) while operating at equivalent chamber pressure.

The observation by XPS of Oxygenated Carbonaceous chains in the material could consist of entrapped by-products resulting from the hydrolysis, rearrangement, oxidation and dissociation reactions presented above and might be OC$_2$H$_5$, C$_2$H$_4$, H$_3$CCHO for TEOS and CH$_2$OH, CH$_3$O, CH$_2$O for TMOS.[4, 6, 8] Additional O$_2$ flux injected during deposition processes assist the real-time oxidation of all these by-products. The H$_2$O and CO$_2$ molecules produced can further react with fragments, in an avalanche type reaction, producing each

several reactive species. The large difference in the $[O_2]$/[precursor] ratios needed to produce pure SiO_2 from TEOS and TMOS (respectively 0.15 and 1.75) is attributed to the difficulty of oxidizing the heavy oligomers formed by TEOS cations polymerization, which is higher than for TMOS reactants.[4]

7.4.2 Decomposition of TMS

Tetramethylsilane (TMS) contains only Si–C and C–H bonds and has a low sticking coefficient compared to TEOS and TMOS. The FEBID material obtained from pure TMS vapours contains 27at% O, coming from residual water molecules in the SEM chamber. Comparable observations where previously reported.[9-11]

The study of electron activation of TMS and successive reactions in the presence of residual gases (e.g. water) explained the ease of oxidation of this precursor, compared to TEOS and TMOS. The electron ionization mass spectrum of TMS [12] shows that the trimethylsilyl cation $(CH_3)_3Si^+$ is the predominant entity produced under electron irradiation.

Although it is inert against TMS molecules, it quickly decomposes to CH_3Si^+ and forms silanol species such as $(CH_3)_3SiOH_2^+$ or $CH_3SiOH_2^+$ when remaining in the gaseous phase [13, 14] and in presence of water or Oxygen molecules.[9, 15] These reactions can equivalently be induced by electron impact,[16] and the presence of residual water together with the reactivity of the cation lead to O incorporation and the formation of SiO_2 entities in the FEBID material. The high amount of C (60at%) in the material obtained from pure TMS vapour indicated that by-products produced by the electron bombardment and oxidation of the TMS cations might be entrapped in the deposit, as suggested by Faber.[10]

The FEBID material was completely oxidized to SiO_2 with a very low additional Oxygen flow compared to TEOS, TMOS and TICS.

This was attributed to the high reactivity and the non-polymerizing behaviour of trimethylsilyl- and methylsilyl-cations, which eased the deposition of a well structured and pure SiO_2. Additionally, the by-products formed require less O_2 to be oxidized: $(CH_3)_3Si^+$ decomposes to CH_3Si^+ by liberating CH_3 or C_2H_4, followed

by H_2 which can recombine with an O atom and further assist the oxidation reactions.

7.4.3 Decomposition of TICS

TICS presented the highest deposition yield when no additional Oxygen was added to the precursor vapours. The lack of data concerning the ionization of the molecule prevents from understanding completely its deposition mechanism. The high growth rate obtained with the low molecule flow could be due to the fact that compared to TEOS, TMOS and TMS who form positive ions under low energy electron irradiation[4], the electron capture by TICS leads to the formation of negative ions, similarly to halogenated compounds[17]. Hence, during the FEBID process, negative TICS ions formed by the outer part of the Gaussian FEB are attracted towards the center of the FEB irradiated substrate surface which is charged positively due to electron ejection. This induces hence a higher molecule supply and growth rate (at equivalent precursor fluxes) when using TICS than TEOS, and a higher Oxygen supply is thus necessary in order to totally oxidize the growing deposit.

A second hypothesis was that when reacting with residual water in CVD processes (substrate at 100 °C), TICS formed HNCO, which is a volatile compound.[18] The material deposited from TICS with no additional Oxygen was $SiNC_2O_3$, demonstrating that already 3 N atoms had left compared to the starting molecule. The resulting N might be attached to a NCO group, which are known to be very stable at room temperature.[19] The chemical composition however demonstrated that NCO groups were not the predominant entity produced under the FEB, since only 1 of the 2 C and one of the 3 O would be used. The remaining elements should be bonded to the Si atom, since they would form volatile species that would leave already the deposit (CO, CO_2). TICS and its fragments do not polymerize in high weight oligomers. The remaining possibility was that the C is bounded to the Si atom and require a lot of additional Oxygen to be oxidized.

Summary

- Residual water in the SEM chamber was demonstrated to be the agent influencing the deposited chemical composition of the films, and appeared as a large limitation of FEBIP of pure materials. The resulting oxidation efficiency was inversely proportional to the precursor flow

- The importance of the Oxygen incorporation depends on the reactivity of the precursor fragments produced

- This observation was double checked using a second gas injection system based on a single capillary

- This phenomena demonstrated the different reactivities of the different molecules under the beam to additional Oxygen. Condensation reactions of alkoxysilanes appeared as a limitation to the deposition of pure SiO_2

- The highest performance molecule tested was TMS, and combined low sticking coefficient, non condensation behaviour, and high reactivity to Oxygen

7.5 Bibliography of Chapter 7

1. I. Utke, V. Friedli, S. Amorosi, J. Michler, and P. Hoffmann, "Measurement and simulation of impinging precursor molecule distribution in focused particle beam deposition/etch systems", Microelectronic Engineering, **2006**, 83, 1499-1502.

2. P. Atkins, and J. de Paula, *Atkins' Physical Chemistry*, Oxford, 2006.

3. I. Utke, V. Friedli, J. Michler, T. Bret, X. Multone, and P. Hoffmann, "Density determination of focused-electron-beam-induced deposits with simple cantilever-based method", Applied Physics Letters, **2006**, 88.

4. M.L.P. da Silva, and J.M. Riveros, "A comparative study of gas-phase ion/molecule reactions in Si(OCH3)(4) and Si(OC2H5)(4)", International Journal of Mass Spectrometry, **1997**, 165, 83-95.

5. J. Holtgrave, K. Riehl, D. Abner, and P.D. Haaland, "Ion Chemistry in Tetraethylorthosilicate (C2h5o)(4)Si", Chemical Physics Letters, **1993**, 215, 548-553.

6. E. Tabei, S. Mori, F. Okada, S. Tajima, K. Ogino, Y. Okawara, and S. Tobita, "Metastable Ion Study of Organosilicon Compounds .5. Tetramethoxysilane and Trimethoxymethylsilane", Organic Mass Spectrometry, **1992**, 27, 702-708.

7. S. Lipp, L. Frey, C. Lehrer, E. Demm, S. Pauthner, and H. Ryssel, "A comparison of focused ion beam and electron beam induced deposition processes", Microelectronics and Reliability, **1996**, 36, 1779-1782.

8. E. Tabei, S. Mori, F. Okada, S. Tajima, K. Ogino, H. Tanabe, and S. Tobita, "Metastable Ion Study of Organosilicon Compounds .6. Triethoxymethylsilane and Tetraethoxysilane", Organic Mass Spectrometry, **1993**, 28, 412-421.

9. Y. Catherine, and A. Zamouche, "Glow-Discharge Deposition of Tetramethylsilane Films", Plasma Chemistry and Plasma Processing, **1985**, 5, 353-368.

10. E.S. Faber, R.N. Tauber, and B. Broyde, "Deposition of Silicon by Electron Irradiation of Tetramethylsilane", Journal of Applied Physics, **1969**, 40, 2958-&.

11. A. Walkiewicz-Pietrzykowska, J. Espinos, and A. Gonzalez-Elipe, "Type of precursor and synthesis of silicon oxycarbide (SiOxCyH) thin films with a surfatron microwave oxygen/argon plasma", JVSTA, **2006**, 24, 988-994.

12. T.J. Odiorne, P. Vouros, and D.J. Harvey, "Chemical Ionization Mass-Spectrometry Using Tetramethylsilane", Journal of Physical Chemistry, **1972**, 76, 3217-&.

13. E. Tabei, S. Mori, F. Okada, S. Tajima, and S. Tobita, "Metastable Ion Study of Organosilicon Compounds .4. 1,1,1,3,3,3-Hexamethyldisilazane andd 1,1,3,3-Tetramethyldisilazane", Mass Spectrometry, **1991**, 39, 19-27.

14. S. Tobita, K. Nakajima, S. Tajima, and A. Shigihara, "Loss of H-2 from Metastable Ch3sih2+ Ions", Rapid Communications in Mass Spectrometry, **1990**, 4, 472-475.

15. S. McGinnis, K. Riehl, and P.D. Haaland, "Ion Chemistry in Tetramethylsilane (Ch3)4si", Chemical Physics Letters, **1995**, 232, 99-102.

16. G.S. Groenewold, M.L. Gross, M.M. Bursey, and P.R. Jones, "Unimolecular and Collision-Induced Decompositions of Gas-Phase Group IVA Enium Ions (Ch3)3M+", Journal of Organometallic Chemistry, **1982**, 235, 165-175.

17. Wilkerso.Be, and J.G. Dillard, "Resonant Electron Capture in Silicon Tetraisocyanate and Silicon Tetrachloride", Journal of the Chemical Society D-Chemical Communications, **1969**212-&.

18. A. Fujimoto, and O. Sugiura, "A deposition mechanism of SiO2 chemical vapour deposition using tetra-isocyanate silane and water", Japanese Journal of Applied Physics Part 1-Regular Papers Short Notes & Review Papers, **2000**, 39, 5164-5168.

19. R. Nemeth, J. Kiss, and F. Solymosi, "Surface chemistry of HNCO and NCO on Pd(100)", Journal of Physical Chemistry C, **2007**, 111, 1424-1427.

CHAPTER 8

APPLICATIONS

As illustration, prototype structures produced during this thesis that were designed and computed by two applied optics laboratories are presented.

The versatility of FEBID is shown and applied to complex structures.

8.1 Tip deposition

8.1.1 Tip definition

The production of functional structures required to scan a low current and spotted FEB along a given pattern. This situation was completely opposite than the deposition of films, and calibration structures had to be performed as function of the beam current and additional Oxygen. When spotting a FEB on a given point, the produced deposit grows vertically and laterally with time. The resulting deposits usually contain two distinctive regions: a cone at the top, and a quasi-cylindrical core, see Figure 8-1. The tips are usually larger than the FEB diameter, due to electron scattering.[1]

The cone was shown to originate from forward scattering of primary electrons from the first grains of material. The cone dimensions depend of the deposited material density and primary electron beam energy, that both determine the scattering phenomenon occurring in the tip apex. A precise and complete theoretical model of the tip deposition is presented elsewhere.[1]
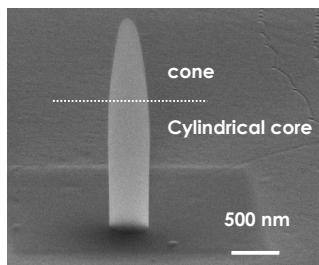
Figure 8-1: SEM micrograph of a standard tip deposited from TMOS. (tilt angle 45 °)

8.1.2 Effect of additional O_2 on tips growth rate and chemical composition

The vertical growth rate and the tip diameter increased with additional Oxygen, see Figure 8-2 a), and seemed to saturate for Oxygen flows superior to 1 sccm. This indicated a higher density of the material grown with Oxygen assistance, leading to higher electron scattering in the conical part and hence larger dimensions. Additional Oxygen helped to decrease the Carbon content in the tips, and the material was C-free for flows of Oxygen superior to 1 sccm. Due to the small small irradiated spot, the molecules could always fill the depleted region and supply sufficient of Oxygen and Silicon atoms to lead to the deposition of pure SiO_2. The *height vs. time* characteristic was linear for heights up to 40 µm, see Figure 8-2 b).
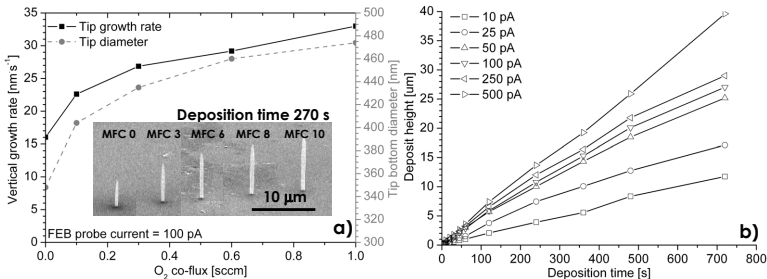
Figure 8-2: (a) Vertical growth rates and tip diameter as function of additional Oxygen; (b) Tip height as function of deposition time and FEB current. FEB acceleration voltage was set to 25 kV for all experiments.

Based on these results, photonic structures designed by external laboratories could be produced.

8.2 SiO₂ filled sub-wavelength apertures

Sub-wavelength apertures in opaque metallic films are extensively used to create confined electro-magnetic sources applied to the bio-molecule detection.[2] The usual poor transmission of sub-wavelength apertures can be

boosted by creating a periodic corrugation around the aperture, or filling the aperture with a material of higher refractive index than air.

The apertures (80 to 500 nm in diameter in 150 nm thick gold film) were produced by custom focused electron beam lithography recipe based on a lift-off process using a negative tone resist, see Figure 8-3.[3]
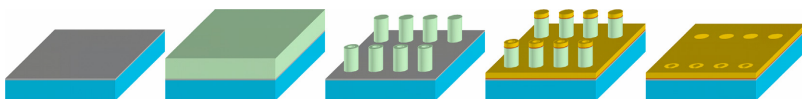
Figure 8-3: E-beam lithography lift-off process based on a negative tone resist for sub-wavelength structure fabrication

The sample was then placed in the S100, and using NPGS, a precise positioning and alignment could be performed over an aperture, which could be then filled by spotting the FEB in the aperture, see Figure 8-4.
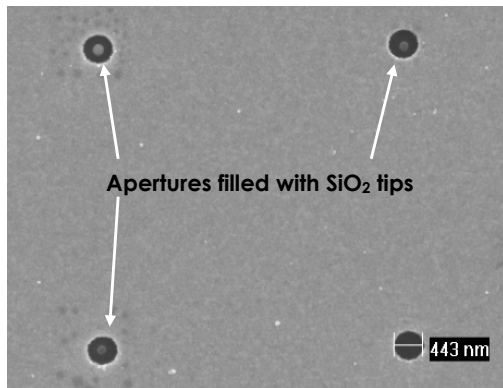
Figure 8-4: SEM micrograph (top view) of sub-wavelength apertures filled with FEBID SiO$_2$

The apertures produced allowed reaching excitation volumes of a few hundreds of ato-liters.[4] The filled sub-wavelength apertures are currently under investigations.

8.3 Surface Plasmon enhancement of transmission through sub-wavelength apertures

The structures presented here consist of a plasmonic approach to enhance the transmission of the sub-wavelength apertures. The excitation of surface plasmons (i.e. surface charge waves excited under precise irradiation conditions, and propagating a few hundred of nanometers at the surface of a metallic film) is done by creating an array of nanometer-scale bumps of precise dimensions, arranged in a periodic structure.[5-7] This constitutes the second approach to enhance the transmission of sub-wavelength apertures.

The first three pictures presented here, Figure 8-5 to Figure 8-7, show images of such plasmonic crystals, consisting of a circular array of SiO_2 pads deposited on a gold layer. The sub-wavelength aperture in the center was performed after the deposition of the pads, by focused ion milling. The pattern dimensions were calculated by Norik Janunts and Olivier Martin, from the nanophotonic laboratory, EPFL.
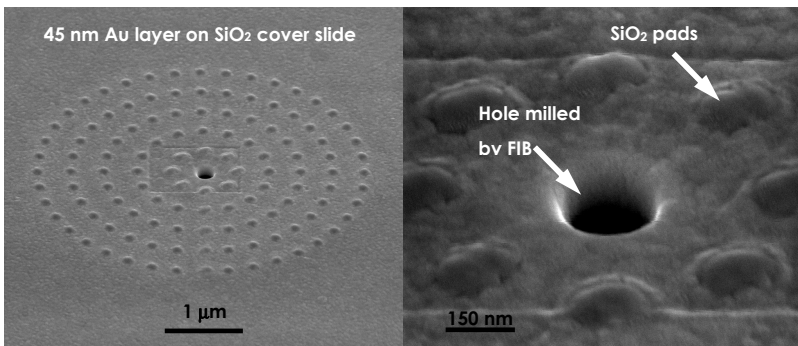
Figure 8-5: 45 ° tilt SEM micrographs of the circular geometry plasmonic structure. Bumps are SiO2 deposited with NPGS, and central hole milled by FIB post deposition

The second plasmonic structure consisted in replacing the central hole by a SiO_2 tip. A second structure consisted in placing a center defect.
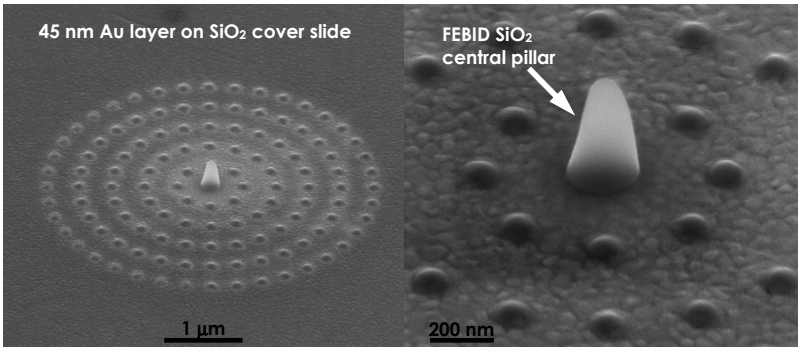
Figure 8-6: 45 ° tilt SEM micrographs of the circular geometry plasmonic structure. Bumps are SiO₂ deposited with NPGS, and central pillar.

Similar structure was produced by replacing the circular array by a square array, see Figure 8-7.
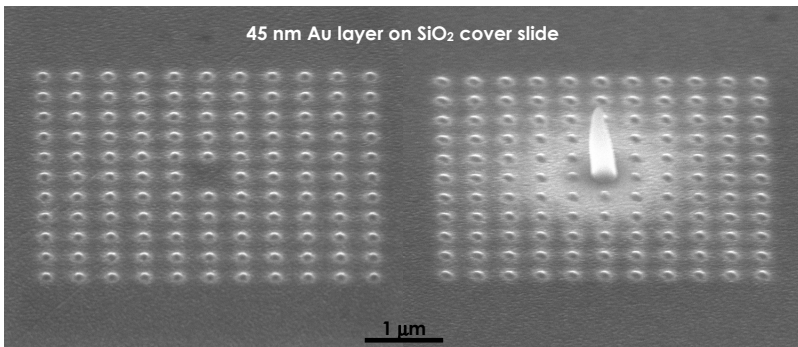
Figure 8-7: 45 ° tilt SEM micrographs of the square geometry plasmonic structure, with and without central pillar.

Structures with identical geometries were produced by FIB milling, which produced indents in the metallic film instead of bumps. All the structures were measured in order to compare the performance of the bumps and of the indents, and to demonstrate the surface effect of plasmons. The present results are shown in Figure 8-8. Apparently, indents are more efficient to create localized spectral filtering. The interpretations of the results are under investigation.
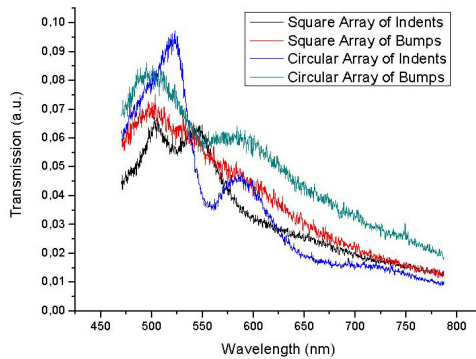
Figure 8-8: Normalized transmission of structures of bumps and structures of indents as function of wavelength

8.4 Photonic crystals

Another laboratory designed structures based on the periodic variation of the refractive index in two dimensions, acting as a multi-dimensional Bragg reflector, or photonic crystal.[8, 9] If the refractive index is high enough, a photonic band gap for visible light can be created by tuning the structure parameters correctly. See Figure 8-9.
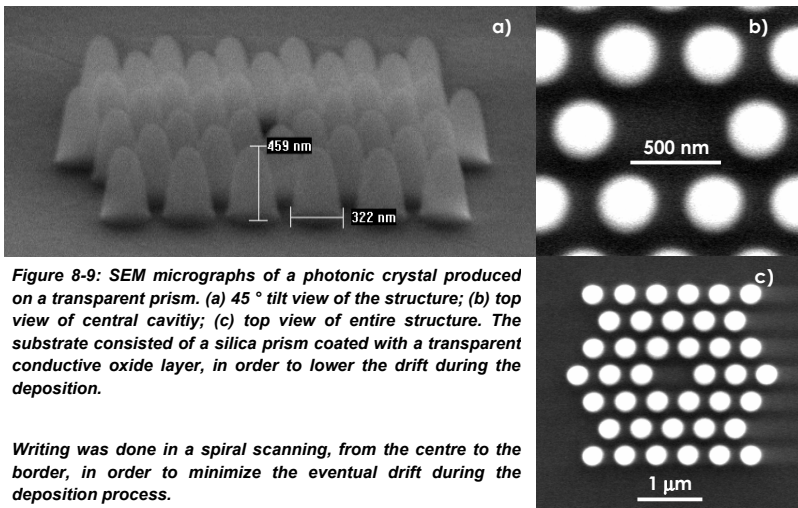
Figure 8-9: SEM micrographs of a photonic crystal produced on a transparent prism. (a) 45 ° tilt view of the structure; (b) top view of central cavitiy; (c) top view of entire structure. The substrate consisted of a silica prism coated with a transparent conductive oxide layer, in order to lower the drift during the deposition.

Writing was done in a spiral scanning, from the centre to the border, in order to minimize the eventual drift during the deposition process.

8.5 Prototype structures

This sub-chapter presents a few prototype structures produced with the only purpose of demonstrating the versatility of FEBID. In Figure 8-10 are presented lines produced by scanning a focused FEB with a given speed. For speeds below 15 nm.s-1, the structure produced was 3-D. The lower the scan speed, the larger the take-off angle. This could be used as 3-D connectors for prototype chips.

Other 3-D prototype structures consisted of SiO_2 super tips, presenting large aspect ratios above 75, see Figure 8-10. No charging of the material or drift due to charging of the SiO_2 under irradiation could be detected. This was certainly due to gaseous radicals discharging the surface in real time.
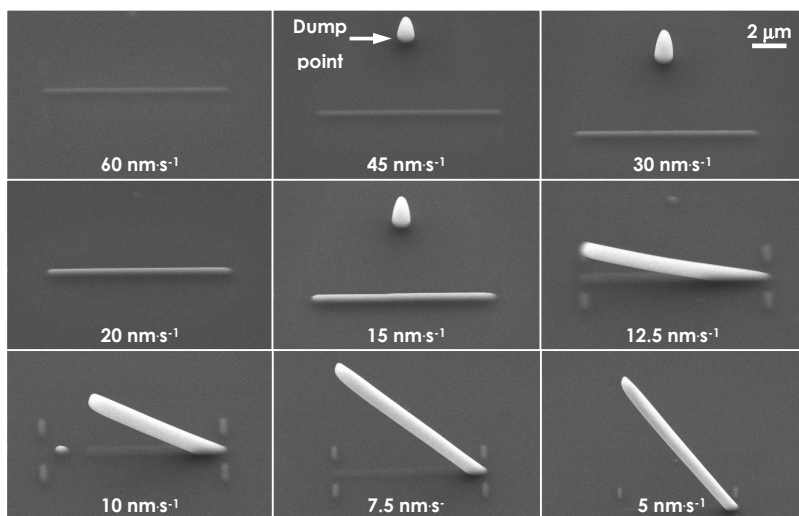
Figure 8-10: SEM micrographs (45 ° tilt vies) of SiO₂ lines produced by scanning the FEB at different speeds, from right to left.
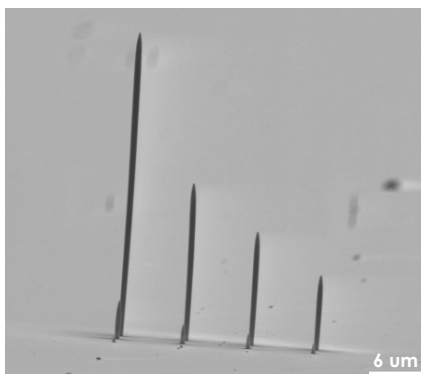
Figure 8-11: SEM micrograph (80 ° tilt vies) of an array of SiO₂ tips produced under constant irradiation parameters, but with varying time. Largest tip is about 35 um high, and 500 nm in diameter.

More complex 3-D structures for feasibility demonstration could be produced by controlling the beam with NPGS, see Figure 8-12.
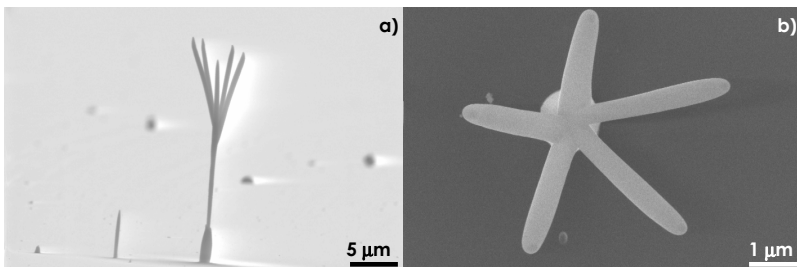

Figure 8-12: 3-D nano-palm tree made of SiO₂. (a) 85 ° tilt view, and (b) top view

8.6 Photomask repair

As showed in the Chapter 4, § 4.3, the deposits obtained from the precursors were transparent at 193 nm wavelength, which is a wavelength used in industrial photolithography processes. The deposited SiO₂ obtained from TMS

showed an almost 100 % transmission at the latter wavelength, and fulfilled the mask repair requirements.

TMS would lead to production of highly transparent repairs, resistant to chemical etching, and would not lead to equipment contamination, as the TEOS molecule used today. An attempt of implementation of the TMS recipe in an industrial e-beam mask repair tool was however unsuccessful. The main reasons were technical limitations that did not allow reducing the TMS flow and increasing the Oxygen flow to suited values.

8.7 Masks for wet etching

When investigating the sample produced for the chemical wet etching experiments (Chapter 4, § 4.2), I discovered that a broken SiO_2 tip, laying on the substrate surface, had actually protected the Si surface from BHF etching.

The resulting pattern transfer in the Si presented a sharp apex under the tip extremity, of dimensions of a few nanometers, see Figure 8-13.
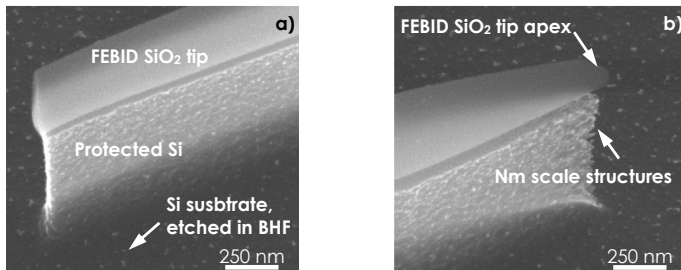
Figure 8-13: Broken SiO_2 tip used as mask during BHF etching of Si. (a) rear extremity, (b) top extremity). 45° tilt views.

8.8 Bibliography of Chapter 8

1.   T. Bret, *Physico-chemical Study of the Focused Electron Beam Induced Deposition Process*. 2005, EPFL: Lausanne. p. 238.

2.   T.W. Ebbesen, H.J. Lezec, H.F. Ghaemi, T. Thio, and P.A. Wolff, *"Extraordinary optical transmission through sub-wavelength hole arrays", Nature*, **1998**, *391*, 667-669.

3.   A. Perentes, I. Utke, B. Dwir, M. Leutenegger, T. Lasser, P. Hoffmann, F. Baida, M.-P. Bernal, M. Russey, J. Salvi, and D. Van Labeke, *"Fabrication of arrays of sub-wavelength nano-apertures in an optically thick gold layer on glass slides for optical studies", Nanotechnology*, **2005**, *16*, S273-S277.

4.   M. Leutenegger, M. Gosch, A. Perentes, P. Hoffmann, O.J.F. Martin, and T. Lasser, *"Confining the sampling volume for Fluorescence Correlation Spectroscopy using a sub-wavelength sized aperture", Optics Express*, **2006**, *14*, 956-969.

5.   D. Van Labeke, F.I. Baida, and J.M. Vigoureux, *"A new structure for enhanced transmission through a two-dimensional metallic grating", Journal of Microscopy-Oxford*, **2004**, *213*, 140-143.

6.   T. Thio, K.M. Pellerin, R.A. Linke, H.J. Lezec, and T.W. Ebbesen, *"Enhanced light transmission through a single subwavelength aperture", Optics Letters*, **2001**, 26, 1972-1974.

7.   T. Thio, H.J. Lezec, and T.W. Ebbesen, *"Strongly enhanced optical transmission through subwavelength holes in metal films", Physica B*, **2000**, *279*, 90-93.

8.   E. Yablonovitch, T.J. Gmitter, K.M. Leung, R.D. Meade, A.M. Rappe, K.D. Brommer, and J.D. Joannopoulos, *"3-Dimensional Photonic Band-Structure", Optical and Quantum Electronics*, **1992**, *24*, S273-S283.

9.   E. Yablonovitch, T.J. Gmitter, and K.M. Leung, *"Photonic Band-Structure - the Face-Centered-Cubic Case Employing Nonspherical Atoms", Physical Review Letters*, **1991**, *67*, 2295-2298.

CHAPTER 9
CONCLUSIONS AND PERSPECTIVES

This Chapter is a summary of the work accomplished in this thesis, recalling all the main messages and results obtained.

In a second section are reported optimizations and research direction that could lead to the understanding of the gas assisted FEBID mechanism, and the deposition of pure materials other than oxides. More technical optimizations based on the improvement of the deposition system are proposed to lead to reliable and fully understood and controlled processes.

9.1 Conclusions

Oxygen assisted FEBID was demonstrated to be suited to the deposition of high quality silicon dioxide. The global FEBID mechanism was affected by the presence of molecular Oxygen: growth rates could be multiplied by 7 and electron efficiencies by 20 in the best case. Precursor chemistry and chemical reactivity appeared as paramount parameters, influencing this enhanced mechanism. For low sticking and reactive molecules, the deposition process required low energy to be efficient, and increase of efficiency (growth rate, purity) was related to a larger and better consumption of the precursor molecules on the surface. Residual water in standard SEMs was of efficient assistance when no Oxygen was injected, able of etching 90 % of the C incorporated in the growing film.

The maximization of the efficiency in terms of material purity and growth rate requires the following parameters:

- lowest dwell time, largest replenishment time (6 and 60 µs respectively in our machine)

- low acceleration voltage (large SE emission)

- low FEB density

- reactive molecule with low sticking coefficient

- suited flows of Oxygen and precursor allowing the optimal coverage of each gas in ideal ratios on the surface. The less complex the precursor molecule was, the less Oxygen was needed to obtain pure SiO_2. TMS appeared as the best candidate

In the following paragraphs are reported detailed summaries of the main achievements.

9.1.1 Deposition equipment and evolutions

- A standard SEM was used and modified to allow the simultaneous injection of two controlled flows of gases. The system worked perfectly, and leads to reproducible results. The final field of view was 200 x 200 μm^2 approximately.

- An optical in-situ setup was developed to follow in real time the growth of optical films. The setup produced satisfying signals that could be easily fitted to quickly extract the optical properties of the materials.

- The external liquid nitrogen dewar assured a good circulation of LN in the cold finger, which increased the vacuum quality.

9.1.2 Precursor chemistries

TEOS, TMOS, TMS and TICS were used as precursors, and pure SiO_2 could be deposited from all of them under suited irradiation conditions.

- Sticking molecules appeared more efficient in terms of growth rates

- In presence of Oxygen however, low sticking is preferred since it leads to lower threshold Oxygen flows.

- Low sticking molecules such as TMS induced undetectable contamination of the microscope, compared to TEOS and TMOS

9.1.3 Effect of Oxygen on the growth kinetics

- Injecting Oxygen allowed influencing the growth rate up to a certain saturation value, corresponding to the maximum surface coverage of the two gases, and resulting in the deposition of SiO_2.

- Oxygen assisted FEBID appears similar than other gas assisted particle processes: the highest efficiency were obtained at low dwell times and high replenishment times.

- Contrary to conventional FEBID using only the precursor vapors, oxygen assisted FEBID was independent of the electron density- The larger the number of electrons, the larger the growth rate

- Low energy electrons appeared to have sufficient energy to initiate the oxidation reaction during O_2 assisted FEBID

- Thermal effects appeared significant only when the film was thick enough that the FEB interacted completely with the deposited material

9.2 Perspectives

Gas assisted FEBID was demonstrated to be a potential generalization of the FEBID technique for the deposition of pure materials. Pure SiO_2 should be producible in a standard SEM using only the residual water as oxidant flow using simple and reactive molecules such as SiH_4 or SiH_2Cl_2. Water vapour might be a more efficient oxidant agent than O_2, but would lead to the contamination of the machine and poor vacuum quality (unless a non-wetting coating is applied on the components).

Other oxides, such as Al_2O_3, TiO_2, and HfO_2, interesting for their high refractive indices, should be easily deposited using the same approach.

However, limits of standard machines were clearly demonstrated in terms of water contamination. This is a main issue for the generalisation of gas assisted FEBID of metals for example with H_2 assistance, since the oxidant and reducing reactions will simultaneously occur under the FEB.

Gas mixtures for the deposition of pure materials other than oxides can only be obtained in water and oxygen free setups, which require technical optimisations of the existing FEBID machines.

A few technical optimizations of the conventional FEBID machines that would allow for a better control of the deposition process and deposited materials would be:

- continuous monitoring of the amount of residual gases during the experiments

- increasing the surface of the cold finger in the chamber, to further improve the vacuum quality

- silanization of the entire microscope so that water does not stick to surface, and would hence be more easily pumped away

- bakable chamber

- bakable capillaries, in order to avoid cross contamination issues between the different precursors

- *in-situ* cleaning of the chamber and substrate in reducing or oxidizing atmospheres

- *in-situ* pressure gauge at the outlet of capillary to control the flow of molecules effusing form the capillary

- turbo pump on the S100 gun in order to avoid changing the filament daily, and weekly cleaning of the column. A first attempt with a 30000 rpm turbo showed however that the mechanical vibrations induced large image instabilities.

ANNEXES

Annex 1: Effect of additional Oxygen on chemical composition of deposited material

Whatever the precursor flow, additional Oxygen had always the same effect on the deposited chemical composition, and pure SiO_2 could always be deposited with the flows tested here. The latter were varied between 10^{18} and 10^{20} molecules·cm^{-2}·s^{-1}. However, the [O_2]/[precursor] threshold ratio depended on the precursor flow. It was larger for lower TEOS and TMOS flows, and smaller for lower TMS flows. See Figure i and Figure ii.
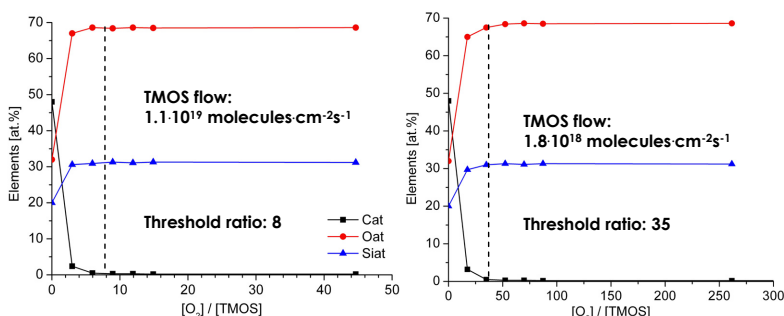
Figure i: Chemical composition and threshold ratios as function of the TMOS flow
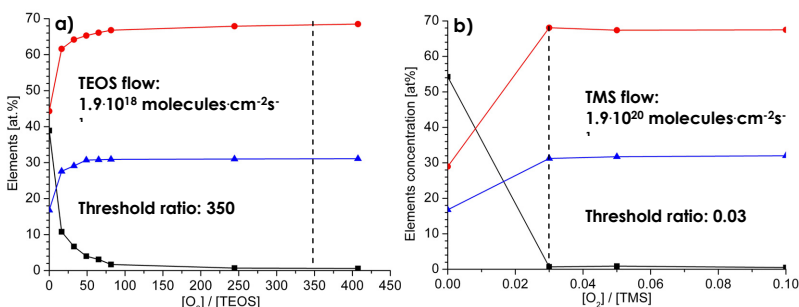
Figure ii: Chemical composition and threshold ratio as function of (at) TEOS and (b) TMS flow

Annex 2: Fresnel coefficients, Matlab code for fitting

The reflection coefficients of Fresnel at the interface of two media are defined as follows for the different polarizations:

$$r_{12}^s = \frac{n_1 cos\theta_1 - n_2 cos\theta_2}{n_1 cos\theta_1 + n_2 cos\theta_2}$$

$$r_{12}^p = \frac{n_2 cos\theta_1 - n_1 cos\theta_2}{n_2 cos\theta_1 + n_1 cos\theta_2}$$
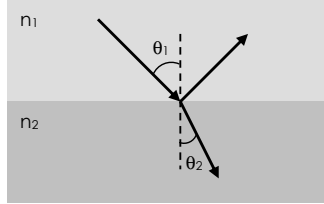
The following code was implemented and allowed to fit the experimental results. Scattering was not included.

```
function nf = fitReflecto(e_data,I_data)

%   Start Values
      nf0R = 1.5;
      nf0C = 0;
      A0 = 1; % Constant
      B0 = 0; % Offset

P = lsqcurvefit(@signalReflecto,[nf0R nf0C A0 B0],e_data,I_data);
plot(e_data,I_data,e_data,signalReflecto(P,e_data));

      nf = P(1) + i*P(2);
      A=P(3)
      B=P(4)
return

function I = signalReflecto(P,e_data)
% Fitting of Intensity signal
% Complex nf
      nfR = P(1);
      nfC = P(2);
      nf = (nfR+i*nfC);

% Parameters
      n0 = 1;
      lambda = 514;
      theta0 = 45*pi/180;
      ns = 4.17;

%   Angle
      thetaf = asin(n0*sin(theta0)/nfR);
```

```
%   Attenuation Coefficient

    beta = 2*pi*nf*cos(thetaf)/lambda*e_data;

%   Multiple Reflection
    rp = (fresnel_rp(theta0,n0,nfR) +
    fresnel_rp(thetaf,nfR,ns)*exp(2*i*beta))./...
        (1 +
    fresnel_rp(theta0,n0,nfR)*fresnel_rp(thetaf,nfR,ns)*exp(2*i*beta
    ));
    rs = (fresnel_rs(theta0,n0,nfR) +
    fresnel_rs(thetaf,nfR,ns)*exp(2*i*beta))./...
        (1 +
    fresnel_rs(theta0,n0,nfR)*fresnel_rs(thetaf,nfR,ns)*exp(2*i*beta
    ));

%   Intensity
    RP = rp.*conj(rp);
    RS = rs.*conj(rs);

    I = P(3)*(RP+RS)/2+P(4);
return


%----------------------------
%-------Other functions--------
%----------------------------

function rp = fresnel_rp(theta1,n1,n2)
    theta2 = asin(n1*sin(theta1)/n2);
    rp = (n2*cos(theta1)-
    n1*cos(theta2))/(n2*cos(theta1)+n1*cos(theta2));
return

function rs = fresnel_rs(theta1,n1,n2)
    theta2 = asin(n1*sin(theta1)/n2);
    rs = (n1*cos(theta1)-
    n2*cos(theta2))/(n1*cos(theta1)+n2*cos(theta2));
return
```

Annex 3: Secondary electron yields δ

The data related to Secondary emission yields of a given material that can be found in literature present large deviations from one paper to the other. [1, 2] Additionally to paramount parameters such as extraction depth or minimal extraction energy; surface roughness, presence of native oxide or contamination layer can greatly influence the measured value. The SE yield is however always larger on heavy substrates, whatever the energy. Their

The following table reports the SE total yield (SE1 + SE2) of the material mostly used in this thesis, that were calculated with Mocasim®, by taking the standard extraction depth, and calculating with the minimum and the maximum value of extraction energy. Carbon and Copper are given as intermediate materials.

Element	Z	δ @ E_0 [keV]		
		5	10	25
C	6	0.27	0.14	0.59
Si (SiO_2)	14	0.36	0.29	0.14
Cu	29	0.49	0.33	0.16
Au	79	0.54	0.39	0.20

Annex 4: Back-scattering yields η

Back-scattered electrons are less sensitive than SE to surface properties, and are hence easier to measure accurately. As the SE yield, the BSE yield increases with the atomic number of the substrate. Depending on the substrate density, it increases or decreases with the FEB energy.

D.C. Joy published in 2001 a database, regrouping results of backscattering yields published until 2001.[1] Interesting values for this thesis are reported in the following table.

Element	Z	η @ E_0 [keV]		
		5	10	25
C	6	0.08	0.07	0.05
Si (SiO_2)	14	0.17	0.16	0.15
Si_3N_4	-	0.13	0.12	0.11
Cu	29	0.34	0.32	0.31
Au	79	0.45	0.46	0.49

Annex 5: Back-scattering range R_b

The back-scattering range R_b is the largest distance from the focus spot, from which BSE can exit the material.

R_b is function of the electron range R_m, which is the largest distance that a BSE can travel in the material before loosing all its energy.

R_b and R_m are given by:[3, 4]

$$R_b = \frac{C \cdot R_m \cdot \gamma}{1+\gamma} \qquad Eq.A\text{-}1$$

$$R_m = 2.76 \cdot 10^{-4} \cdot \frac{A \cdot E_0^{\frac{5}{3}}}{Z^{\frac{8}{9}} \cdot \varrho} \qquad Eq.A\text{-}2$$

With C a constant empirically fixed as 1.1, and $\gamma = 0.19 \cdot Z^{2/3}$; E_0 the beam energy, A the substrate atomic mass, Z the substrate atomic number, and ρ the material density. The back-scattering ranges are given for Si, SiO_2, Si_3N_4 and Au in the following table.

Element	Rb [nm] @ E_0 [keV]		
	5	10	25
C	176	556	2547
Si (SiO_2)	232	750	3738
Si_3N_4	160	510	2575
Cu	98	309	1414
Au	68	197	983

Bibliography of Annexes

1.   D.C. Joy, "*A Database on Electron-Solid Interactions*", *Scanning*, **1995**, *17*, 270-275.

2.   K.S. Sim, and J.D. White, "*New technique for in-situ measurement of backscattered and secondary electron yields for the calculation of signal-to-noise ratio in a SEM*", *Journal of Microscopy-Oxford*, **2005**, *217*, 235-240.

3.   K. Kanaya, and S. Okayama, "*Penetration and Energy-Loss Theory of Electrons in Solid Targets*", *Journal of Physics D-Applied Physics*, **1972**, *5*, 43-&.

4.   L. Reimer, *Scanning Electron Microscopy, Physics of Image Formation and Microanalysis*, Second edition, Springer-Verlag, Optical Sciences Series, Vol. 45, 1998.

SCIENTIFIC PUBLICATIONS

2007

- **Perentes A**, G. Sinicco, G. Boero, B. Dwir and Hoffmann P, *Focused Electron Induced Deposition of Nickel*, Journal of Vacuum Science and Technology B, accepted for publication

- **Perentes A** and Hoffmann P, *Oxygen assisted Focused electron beam induced deposition of SiO₂: Growth Dynamics*, Journal of Vacuum Science and Technology B, accepted for publication

- **Perentes A**, Hoffmann P, and Munnik F, *Focused electron beam induced deposition of DUV SiO₂*, Proceedings of SPIE - The International Society for Optical Engineering **6533** (23rd European Mask and Lithography Conference, Uwe F. W. Behringer, Editor): article number 65331Q, 2007.

- **Perentes A**, Hoffmann P, *Focused electron beam induced deposition of Si-based materials from SiOₓCᵧ to stoichiometric SiO₂: chemical compositions, chemical etch rates, and deep ultraviolet optical transmissions*, Chemical Vapor Deposition **13 (4)**: 176-184, 2007.

2006

- **Perentes A**, Bret T, Utke I, Hoffmann P and Vaupel M, *Real-time reflectometry-controlled focused-electron-beam-induced deposition of transparent materials*, Journal of Vacuum Science and Technology B **24 (2)**: 587-591, 2006

- Leutenegger M, Gosch M, **Perentes A**, Hoffmann P, Martin OJF, Lasser T *Confining the sampling volume for Fluorescence Correlation Spectroscopy using a sub-wavelength sized aperture*, Optics Express **14 (2)**: 956-969, 2006

- Poujet Y, Roussey M, Salvi J, Baida Fl, Van Labeke D, **Perentes A**, Santschi C, Hoffmann P, *Super-transmission of light through subwavelength annular aperture arrays in metallic films: Spectral analysis and near-field optical images in the visible range*, Photonics and Nanostructures – Fundamentals and Applications **4 (1)**: 47-53, 2006

- Poujet Y, Salvi J, Salut R, Baida F, Van Labeke D, **Perentes A**, Santschi C, Hoffmann P, *Enhanced transmission of light through coaxial nano-structures in a silver film: Theory and first experimental results*, Proceedings of SPIE – The International Society for Optical Engineering **6195**: article number 61951M, 2006.

2005

- **Perentes A**, Utke I, Dwir B, Leutenegger M, Lasser T, Hoffmann P, Baida F, Bernal MP, Russey M, Salvi J, Van Labeke D, *Fabrication of arrays of sub-wavelength nano-apertures in an optically thick gold layer on glass slides for optical studies*, Nanotechnology **16 (5)**: S273-S277, 2005

- Hoffmann P, Utke I, **Perentes A**, Bret T, Santschi C, Apostolopoulos V, *Comparison of fabrication methods of sub-100 nm nano-optical structures and devices*, Proceedings of SPIE - The International Society for Optical Engineering **5925**: article number 592506, 2005.

- Salvi J, Roussey M, Baida FI, Bernal MP, Mussot A, Sylvestre T, Maillotte H, Van Labeke D, **Perentes A**, Utke I, Sandu C, Hoffmann P, Dwir B, *Annular aperture arrays: study in the visible region of the electromagnetic spectrum,* Optics Letters **30 (13)**: 1611-1613 2005

- Brintlinger T, Fuhrer M, Melngailis J, Utke I, **Perentes A**, Hoffmann P, Abourida M, Doppelt P, *Electrodes for carbon nanotube devices by focused electron beam induced deposition of gold,* Journal of Vacuum Science and Technology B **23 (6)**: 3174-3177 2005

2004

- **Perentes A**, Bachmann A, Leutenegger M, Utke I, Sandu C, Hoffmann P, *Focused electron beam induced deposition of a periodic transparent nano-optic pattern,* Microelectronic engineering **73-74**: 412-416, 2004

- Best poster award received at the TNT 2004 international conference in Segovia, Spain

RÉSUMÉ

Alexandre PERENTES   26 years old
12, rue de Schlierbach   Single
FR - 68300 Saint-Louis   Swiss - Greek
Tél: + 41 76 437 22 28
E-mail: alexandre.perentes@epfl.ch

Education

PhD in Nanostructuration of Materials (2007)
Master in Science in Micro-engineering (2003)
Swiss Federal Institute of Technology EPFL, Lausanne, Switzerland

Key Skills

Technical and specialized (Advanced theoretical and practical knowledge)

- Micro- and Nano-scale production technologies:

- Focused electron and ion beam induced processing techniques (lithography, selective deposition and etching), Photo-lithography
- Clean-room standard equipments and processes for integrated devices production and research.
- Standard machining techniques for micro-devices

- Micro- and Nano-scale investigation techniques for surface characterization:

- Surface topography and chemical composition

Management

- IP evaluation and valorization solutions.

Professional experiences and industrial collaborations

- NaWotec (2006 – 2007): technology transfer and optimization of a FEB chemical process. Resulted in industrial implementation of an EPFL-like process.
- Intel Corporation (2006): evaluation and optimization of a FEB process and performances, done in EPFL.
- Focused Electrons and Ions (2005): development of a FEB driven process for the deposition of a specific material for industrial applications, done in EPFL.

- Microelectronic Systems Laboratory, EPFL (2001) : Internship for the fabrication of an integrated chemical gas sensor (1 month).
- Switcher SA (2000): Stock handling and management (during summer).

Academic / Teaching experiences (2003 – 2007)

- Management of an applied scientific research project as PhD student
  → <u>Main achievements</u>: development of a process for the deposition of pure oxides,

  understanding of the developed process, and implementation to industry.
- Adviser for 5 master and semester projects for undergraduate students on various topics (chemistry, integrated devices, optics).
- Meeting organization for project advancement, project budget handling
- Lecturer and examination expert for Bachelor and Master students for the following topics: Surface chemistry, Nanotechnologies, Microstructures technology

Informatics

- Modeling using Matlab, Microcal Orgin, Femlab (Comsol)
- Windows and Macintosch operative systems
- Excellent knowledge of Microsoft office, Project and Adobe products family
- Databases such as Active Directory, File Maker, EndNote
- Web sites construction by Dreamwaver ® or Jahia ®
- General knowledge on networks (substitute informatics manager in the institute)

Languages

- French, (mother tongue)
- English (excellent skills)
- German and Greek (spoken and written, easily perfectible)
- Spanish, Italian (beginner, basic)

Grants

- Swiss national funding for scientific research, project numbers 200021-10333311 (2003 – 2006) and 200020-113458 (2006 – 2007).
- Best poster award, TNT conference 2004
- Student Support, EIPBN conference 2007